Experimental and Computational Mechanics of Arteries in Health and Disease: An Exploration of Complex Structures and Simple Mathematical Models

A DISSERTATION

SUBMITTED TO THE FACULTY OF THE

UNIVERSITY OF MINNESOTA

BY

RYAN R. MAHUTGA

IN PARTIAL FULFILLMENT OF THE REQUIREMENTS

FOR THE DEGREE OF

DOCTOR OF PHILOSOPHY

ADVISOR: VICTOR H. BAROCAS

MAY 2021

DEDICATION

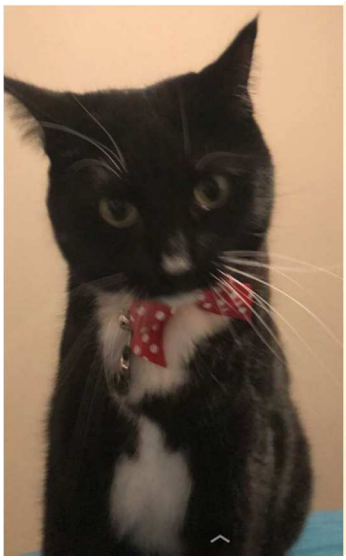

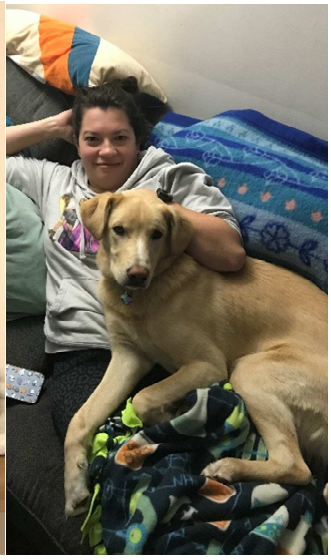

ABSTRACT

Aortic aneurysm, or dilatation of the aorta, is a clinically significant pathology as the risk of potentially fatal rupture (through-thickness failure) or dissection (delamination of the layers) is the fifteenth leading cause of death in the U.S. [1], with just under 10,000 deaths occurring in 2017 [2]. Current diagnostics for assessing aneurysm risk are aortic size and growth rate [1, 3]. These criteria correlate with aneurysm risk but are not direct measures of tissue strength. These criteria are especially inadequate for rare disorders involving genetic anomalies, where population sizes are relatively small and disease severity can vary widely between individuals. Therefore, it is important that we recognize and understand the underlying pathology that makes one aneurysm different from another, especially in terms of mechanics as this is what dictates aneurysm rupture risk. In this thesis I explore several testing methods for assessing aortic properties in animal models of health and disease. I evaluate the simple ring pull test as a high-throughput mechanical testbed for circumferential mechanics and explore the use of ultrasound for the assessment of complex aortic structures including vessel bifurcations and the aortic arch. These techniques offer unique insights as screening tools for understanding mechanics and for evaluating therapeutics. In order to further understand how the different mechanics in healthy and diseased tissues arise, I created a novel micromechanical model of pathophysiologic remodeling. Using this model, I was able to show pathological differences in mechanical properties despite similar clinical growth parameters. I further developed a technique to model more complex geometries using a multiscale coupling to finite element models. These methods create a unique and useful tool for evaluating remodeling with complex geometries utilizing complex microstructural remodeling scenarios leading to improved understanding of the mechanics of healthy and diseased tissues, as well as being a convenient way to assess tissue-engineered therapies.

TABLE OF CONTENTS

LIST OF TABLES

LIST OF FIGURES

CHAPTER 1: INTRODUCTION

Importance of Cardiovascular Disease and Aortic Aneurysm:

Cardiovascular disease continues to be the leading cause of death worldwide, accounting for over 500 million deaths in 2019 [4]. The focus of this thesis is on diseases that affect the aorta, which is the main blood vessel leaving the heart (Fig. 1). The aorta travels the length of the torso and is responsible for moving oxygenated blood throughout the body, meaning that failure in this vessel is often fatal. In fact, aortic aneurysm, or enlargement of the aorta, is a particularly dangerous pathology causing over 17,000 deaths per year in the U.S., making it the 15th most prevalent cause of death [5]. Aortic aneurysm results from abnormal and often unstable growth. However, aneurysm itself is not typically a problem -the vessel can grow larger, provided it still is able to carry blood from the heart to the rest of the body. The issues arise when the abnormal growth results in the aorta failing either through outright rupture or through delamination of the aortic layers (dissection). Current techniques for assessing the risk of such failures focus on tracking aortic diameter and growth rate [6], neither of which is a direct measure of how strong the vessel is. Further, these metrics do not employ any information about the underlying pathology. For example, aortic aneurysm is particularly prevalent in genetic disorders that affect connective tissues of the body such as Marfan Syndrome, Loeys-Dietz Syndrome, Familial Thoracis Aortic Aneurysm, and vascular Ehlers-Danlos Syndrome [1]. With each of these disorders, the underlying material, that is the extracellular matrix (ECM), of the aorta is directly affected. Additionally, aortic aneurysms tend to form near complex geometric structures, such as ascending aortic aneurysms that form on the curvature of the arch near the coronary branches, descending aortic aneurysms that form near the left subclavian artery branch, and abdominal aortic aneurysms that form near the renal branches and the iliac bifurcation. The proximity and location of aneurysms are part of the clinical classifications of aortic aneurysms (DeBakey or

Stanford) [7]. Thus, clinical criteria for assessing aortic aneurysm mechanics are insufficient, and a more detailed understanding of the underlying pathology is necessary to deduce new clinically measurable metrics in order to improve patient outcomes.

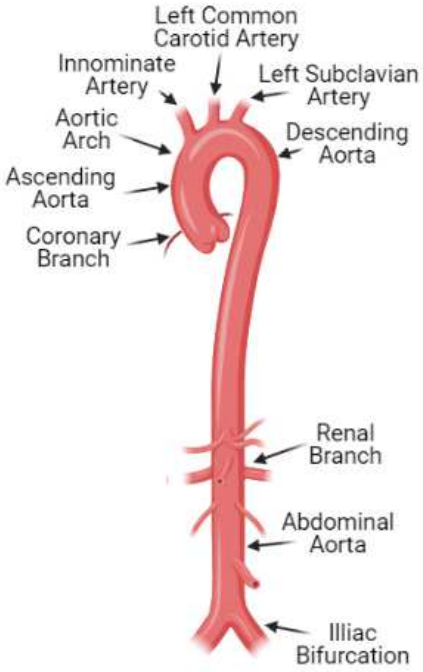

Figure 1. Aortic Anatomy

Major Knowledge Gaps:

Aortic aneurysms tend to form near complex geometric structures. This means that describing the mechanics of the ascending aorta is not as simple as treating it as a straight, pressurized tube. In fact, it is very difficult to extract the ascending aorta and aortic arch to do most physiologically relevant inflation-type experiments, especially in mouse models. *Thus, there is a need for new ways to assess complex geometric arterial structures like the ascending aorta and aortic arch in order to broaden our understanding of exactly how these structures concentrate stresses and influence remodeling.*

The aorta in a baby is typically 0.7-1 cm in diameter [8], and over the course of one's life reaches a size near 2.5-3.5cm [3], with aortic aneurysms having a diameter >4.5cm [3]. In

addition, given the difference in heights between a baby and an adult, the aorta must lengthen immensely during development. Thus, the aorta is capable of large-scale growth and maintaining a stable size, which are fundamentally different growth modes. Normal and abnormal growth and remodeling of the aorta, however, are driven by the same players: the cells and the extracellular matrix (discussed in more detail in Chapter 2). Thus, we might expect growth to be described by some universal remodeling law(s). To date, there have been many attempts to formulate such universal laws, some of which can accurately capture and predict where, how, and when aneurysm may occur on a continuum scale, but none can accurately predict development, homeostatic remodeling, and aneurysm in a single model. Existing models typically employ a phenomenological bulk growth response and fundamentally neglect certain aspects of the physics and biology of the problem, and many disregard failure entirely. Therefore, there remains a need to capture underlying physics to explain why some connective tissue disorders lead to aneurysm, as well as to provide techniques for assessing the patency and strength of the underlying ECM in disease. *Thus, it remains important to computationally model and experimentally validate vascular mechanics, growth, and remodeling in health and disease to understand the underlying mechanisms of aortic aneurysm.*

Summary of Accomplishments:

- *Chapter 3: Mechanical Characterization of Arteries using the Ring Pull Assay*

  This chapter focused on developing new criteria to use the ring-pull test for assessment of aortic properties. We combined computational models with experimental validation to define equations for relating the ring-pull to the planar uniaxial test. The main contribution of this work was to suggest the use of large pins relative to the diameter of the aorta to reduce the bending of the sample and to focus stress near the center region, rather than near the pins, for correct assessment of failure properties. This work also demonstrated a simple set of equations for relating the ring-pull to the uniaxial extension test given specific sample

geometry and pin size. We further developed a Matlab code to perform the stress analysis and the correction of properties which we made available via GitHub. This work contributes a new technique for analyzing the simple ring-pull test allowing for more direct property comparisons between geometrically different aortic samples. This work provides a thorough analysis protocol for assessing property differences in health and disease which has numerous applications, probably most notably in therapy screening for aortic disease in mouse models.

This work resulted in my undergraduate mentee (Carl Schoephoerster) being accepted as an undergraduate student paper finalist at the 2019 Summer Biomechanics, Bioengineering, and Biotransport Conference (SB3C) in Seven Springs, PA. I presented portions of this work as a SB3C2017 poster in Tucson, AZ, and as a virtual lightning talk at SB3C2020. This work culminated in a first-author publication in the Society of Experimental Mechanics official journal *Experimental Mechanics* [9].

- *Chapter 4: Arterial Inflation Testing*

  Arterial diseases, including aneurysm, tend to form near complex geometric structures making it difficult to parse out the mechanistic effects of geometry from the underlying material. This chapter focuses on testing complex geometric arterial structures to decouple the geometry from the underlying material behavior. The technique we demonstrated utilizes ultrasound to visualize through the structure giving full field images of the deformation which we can use to create tissue specific 3D models. We applied this methodology both to bifurcations and to mouse aortic arch mechanics, where we demonstrated the ability to gain unique insights into what's happening near branch points and to visualize through-thickness parameters. This work utilizes ultrasound for full-field measurements during inflation testing. This work is significant because vascular disease tends to affect complex, branching structures which can have very different behavior on the luminal side versus the exterior, adventitial side. Further, it is also very important we consider the tissue compressibility as

tissue is not truly incompressible, and this compressibility can affect the stress state of the vessel.

This work resulted in my undergraduate mentee (John Carruth) winning the undergraduate student paper competition at SB3C2016 in Washington, D.C. I presented portions of this work at the 2016 Biomedical Engineering Society (BMES) meeting in Minneapolis, MN and at SB3C2017 in Tucson, AZ.

- *Chapter 5: Microstructural Growth and Remodeling of the Aorta in Health and Disease*

  The arterial microstructure is a network of fibers from the fibrous extracellular matrix of collagen and elastin to the internal cellular actomyosin networks. To properly understand aortic remodeling, we must understand how these various fiber types interact and influence one another. To do this, I created a discrete-fiber model of the aortic media. Using this model, I simulated various remodeling scenarios including hypertension and several modes of medial degradation including loss of smooth muscle contractility and fragmentation of elastin. This work highlighted the importance of the microstructure as we were able to match clinical criteria for size and growth rate of vessels, but the vessels had major differences in mechanics and failure. This technique offers insight into aortic remodeling and failure that many continuum models cannot, and it demonstrates a unique tool for studying disease progression linked to clinical outcomes.

  This work resulted in acceptance to the Ph.D. student paper competition at the World Congress of Biomechanics (WCB) 2018 in Dublin, IRE. Portions of this work were also presented at SB3C2019 in Seven Springs, PA as a podium talk and at SB3C2020 as a virtual lightning talk. This work was also shared with the broader community at the 2019 Elastin, Elastic Fibers and Microfibrils Gordon Conference in Manchester, NH. This work culminated

in a first-author publication in American Society of Mechanical Engineers (ASME) *Journal of Biomechanical Engineering* [10].

- *Chapter 6: The Holzapfel-Gasser-Ogden Model for Network Mechanics*

  The major drawback with using network models for mechanical simulations is that they are computationally expensive when applied to finite-element simulations as one has to compute network solutions for each Gauss point. To get around this computational issue, in this work we propose a new coupling technique where we fit network behavior to a model of the HGO-type to allow for simple finite element solution. We were able to show 1000x speedup with our technique while still maintaining the additional information gathered on network attributes subjected to specified deformations. This technique offers a straightforward method for understanding the ECM as a fiber network. The simple implementation and intuitive nature of this method should help drive fiber network multiscale modeling, particularly in understanding growth and remodeling.

  This work resulted in a second-author publication in the *Journal of Elasticity*.

- *Chapter 7: Multiscale Remodelling of Tissue-Engineered Constructs*

  Growth and remodeling frameworks should be able to predict bulk growth of a tissue, compositional changes in a tissue, and the overall tissue mechanics. Many frameworks do this well, but few are able to capture the underlying architecture and the failure mechanics. In this work, we demonstrated a discrete-microstructural growth and remodeling framework that leverages our previous work coupling the network simulations to the HGO model to perform finite element simulations. We validated our code against a simple collagen gel experiments. This technique offers

many unique insights into remodeling including fiber architecture and failure which are important in assessing clinical outcomes from multiscale models.

I will co-present this work at SB3C2021 as a virtual podium talk. This work is currently in preparation for submission to an archival journal.

CHAPTER 2: BACKGROUND

The Healthy Aorta – Vascular Structure and Function

The aorta is the largest artery in the vascular system and directs the blood flow leaving the heart to the distributing arteries, which, in turn, funnel blood to the peripheral vasculature. The aorta is an innervated elastic artery responsible for adding capacitance to the cardiovascular system [11]. It accommodates the large impulse of blood ejected from the left side of the heart during systole and regulates the flow rate to the rest of the arterial system. The aorta is thus capable of large deformations throughout the cardiac cycle.

To handle the pressures and deformations of the cardiac cycle, the aorta is made up of three distinct layers. The *tunica intima* or *intima* is the innermost layer of the artery. It consists of a basement membrane and a loose array of collagen and elastin fibers covered by an endothelial sheet that is directly in contact with the blood flow. The endothelial sheet serves as a selective barrier to the blood flow and prevents the adhesion of most molecules, circulating cells, and platelets in order to prevent thrombosis and clotting. The endothelial layer also mediates contraction of smooth muscle cells in the artery through release of nitric oxide and other vasoactive chemicals [11].

The second layer of the aorta is the *tunica media* or *media*. The media is the thickest layer, comprising between 50-75% of the arterial wall [12], and is composed of elastin and collagen fibers, smooth muscle cells, and fibroblasts. The media tends to organize as ~50 elastin/collagen sheets with smooth muscle and interlammelar collagen fibers between them [13, 14]. This repeated structure is known as the medial lamellar unit (MLU). This structure allows the artery to expand in order to store energy, but it also provides for active contraction of the smooth muscle cells in the collagenous layers as a response to local blood pressure [15].

The outermost layer of the aorta is the *tunica adventitia* or *adventitia*. The adventitia is a collagen-rich layer that acts a sleeve around the artery, giving the artery its strength and

preventing it from expanding too much. The collagen layer of the adventitia is interspersed with primarily fibroblasts and nerve cells. These innervations protrude through the adventitia into the media and are thought to signal smooth muscle cells. The adventitia also plays host to the vasa vasorum, or the small vessels that supply blood to the outer layers of the artery that are beyond the diffusion limit within the arterial wall [11].

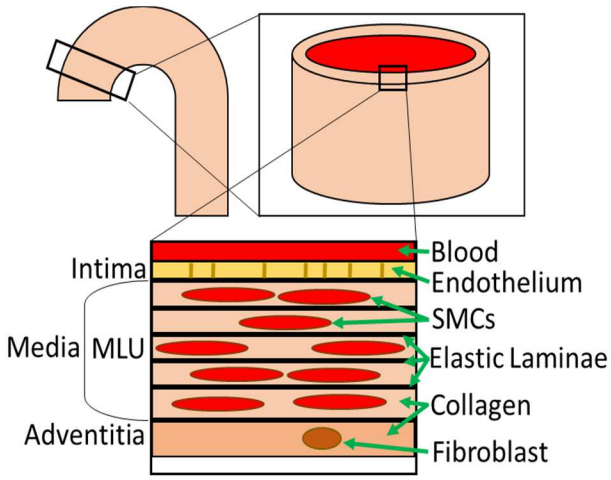

Figure 2. Aortic Structure

Cells and The Extracellular Matrix – Growth, Remodeling, and Stability

A step down in scale from the arterial wall layers are the cells and the extracellular matrix (ECM). The aortic wall is made up of many different constituents, but those most important in tissue mechanics, growth, remodeling, and stability are collagen, elastin, smooth muscle cells (SMCs), endothelial cells, fibroblasts, and a variety of glycoproteins (GPs) and glycosaminoylycans (GAGs) [16]. The ECM in the aorta consists of two main fiber types: collagen and elastin. Collagen fibers give the tissue most of its strength. Collagen is secreted by cells including fibroblasts and smooth muscle cells and can degraded by many mechanism, but the most common are matrix metalloprotease (MMP) activity and phagocytosis. The rate of collagen degradation and secretion is intrinsically variable, depending on the system of interest and the local microenvironment ranging anywhere from a few minutes (in cases of disease or

injury), to a few days (in the case of the periodontal ligament), to a few hundred days (in the case of skin) [16].

Elastin, on the other hand, gives tissue most of its elasticity. Elastin is a small protein that forms elastin fibers that tend to form sheets within artery walls [16]. Elastin is most commonly cross-linked by the conversion of lysine to aldehydes by lysyl oxidase (LOX), and by the extracellular glycoprotein fibrillin-1 [17]. Elastin is very hydrophobic and therefore remains stable in the ECM, meaning that the typical lifecycle for elastin in the ECM is on the order of years [16].

The aorta has several cell types, including fibroblasts, smooth muscle cells, endothelial cells, and immune cells. The different types of cells each perform different task, but they are each known to react to loading. It is widely believed that arteries tend to remodel to maintain a long-term preferred stress state [16]. In many cases, it is assumed that SMCs and fibroblasts primarily respond to tension, while endothelial cells along the lumen respond to shear stress due to the flow rate of blood, signaling fibroblasts and SMCs. In any case, the effect is that SMCs and fibroblasts react by degrading, reorganizing, and/or synthesizing collagen to return the system to the preferred stress state. Further, SMCs also have been shown to operate on a continuum between a contractile phenotype and a synthetic phenotype. This phenotypic switching is particularly important in development and disease [18].

The last constituents we will discuss are the glycoproteins (GPs) and glycosaminoglycans (GAGs). The most common mechanical function for GPs and GAGs is the binding of water into tissues. This functionality gives tissue its incompressible, and viscous nature [16]. GPs and GAGs also tend to function as major matrix linking molecules and mediate many cellular responses as discussed below. There are many glycoproteins and glycosaminoglycans that modulate ECM remodeling and cellular responses to loading and damage, the most significant of these are fibronectin, tenascins, fibrillins, laminin, fibulins, fibrinogen, hyaluronic acid, and heparan sulfate. Fibronectin is a large multi-domain GP that primarily mediates the assembly of collagen

fibers into a network. Fibronectin also tends to drive cell migration and adhesion by ligand binding of integrins on cells to the collagen network [16, 17]. Tenascins, on the other hand, are GPs that limit the effect of fibronectin on cell migration. Tenascins are upregulated by high stress and tend to create inflammatory, fibrotic responses in the ECM, and they have been shown to have a role in elastin fragmentation [17]. Fibrillins are GPs that are significant to elastin fiber formation and fragmentation. Fibrillin-1 specifically has a major role in both the formation of elastin fibers and the integrin binding of cells to the matrix. Fibrillin-1 also has roles in mediating the effect of transforming growth factor beta (TGFB) leading to downstream effects on elastin [16, 17]. Another major GP is laminin. Laminin is a large GP with attached GAG chains and is important in the formation of basement membranes. Laminin is also known to modulate cell differentiation, migration, phenotype stability, and apoptosis [16, 17]. Another family of GPs are fibulins. Fibulins' main roles are in basement membrane formation and adhesion of both endothelial cells and SMCs. Fibulins also regulate the response of LOX on elastin fiber formation and fragmentation. Additionally, fibulins can mediate cell growth and differentiation, as well as angiogenesis [17]. Fibrinogen is yet another GP. Fibrinogen has its primary role in clotting and wound healing. This motif carries through to the ECM where fibrinogen is important in cell adhesion and inflammatory, fibrotic responses. Fibrinogen also binds a number of growth factors including vascular endothelial growth factor (VEGF), platelet-derived growth factor (PDGF), and transforming growth factor beta (TGFB) mediating elastin fiber stability and cell growth response [17]. Similarly, thrombospondins also lead to fibrosis and regulate cellular response to VEGF, PDGF, and TGFB within the ECM. Hyaluronic acid (HA) is a very large GAG that binds a large amount of water. It is known to give tissue its viscous, gel-like properties, and therefore has a major role in defining the underlying ground matrix mechanics [16]. Heparan sulfate is also a large GAG that binds large amounts of water, and is also known to bind and modulate the effect of fibroblast growth factor (FGF) potentially causing changes in deposition of matrix components [16].

A major cause of remodeling is circulating and interstitial signaling molecules and growth factors [16]. Common circulating molecules include acetyl choline (ACh), histamine, and thrombin, as well as a number of growth factors. These molecules, along with mechanical loading, cause endothelial cells to signal smooth muscle cells, macrophages, and fibroblasts through the release of endothelin-1 (ET-1), nitric oxide (NO), prostacyclin (PGI2), angiotensin-II (ANG-II), and many other interstitial signaling molecules. Many of these have effects on matrix remodeling, cell growth, cell migration, apoptosis, and active contraction of SMCs. Smooth muscle cells, macrophages, and fibroblasts also respond to release of ACh and norepinephrine (NE) from nerve endings protruding from nerve cells in the adventitia into the media, and are dependent on the presence of proteins, lipoproteins, glycosaminoglycans, polysaccharides, and proteoglycans like those listed above. Additionally, lysyl oxidase (LOX) and matrix metalloproteases (MMPs) have a significant effect on matrix integrity especially through the fragmentation of elastin sheets. Other factors causing changes in natural growth and remodeling processes are material property changes such as calcification, fibrosis, and elastin fragmentation, all of which cause vascular stiffening. The ECM itself also has a direct impact on the sequestering and regulation of growth factors which affect aortic remodeling. A detailed review on these aspects is given in [19].

Underlying Physiology and Pathology of Vascular Disease

The most common cause of aortic aneurysm is cystic medial degradation. Cystic medial degradation is the weakening of the media structure of the aortic wall through elastin fiber fragmentation and smooth muscle cell apoptosis [20]. This pathology can be caused by local material properties changing the underlying mechanisms of artery remodeling, such as in hypertension and atherosclerotic plaque formation [21, 22]. Cystic medial degradation can be related to age, lifestyle, or genetics. Hypertension and aortic stiffening become increasingly common with age but are also dependent on factors like smoking and obesity. Additionally, age,

smoking, and obesity can lead to higher incidence of calcifications, atherosclerotic plaques, clotting, and restenosis. Cystic medial degradation is also common in many genetic diseases including Marfan Syndrome (mutation of fibrillin-1 causing elastin fragmentation), Ehlers-Danlos Syndrome (faults in collagen synthesis and/or structure), Loeys-Dietz Syndrome (mutations in TGFB causing altered cellular behavior and ECM structure), and Familial Thoracic Aortic Aneurysm (FTAA) [17]. In these cases, cystic medial degradation occurs primarily due to malformation of the ECM due to underlying genetic mutations that affect connective tissues. Bicuspid aortic valve (BAV) tends to lead to aortic root aneurysm with severity depending on a combined effect of genetics and hemodynamics [23]. Infection or local tissue trauma is another cause of aneurysm. In most of these cases, the local microenvironment is disturbed, and it is likely that one would see upregulated fibroblast and macrophage activity, as well as significant aortic stiffening.

Another pathology that sometimes leads to aneurysm is hypertension. In hypertension, we tend to see adventitial thickening of the arteries in response to higher pressure [24–27]. In atherosclerosis, we see intimal thickening prior to the formation of fatty deposits and calcification [28, 29]. In conditions marked by high pulse wave velocity, or the speed of the pulse pressure wave due to aortic stiffening, we see increased luminal perimeter. In aneurysmal arteries, we see similar increases in luminal perimeter, along with lower cellularity and fragmentation of the elastin sheets [30, 31].

Current Testing Methods in Vascular Mechanics

Current testing methods in assessing aortic mechanics focus primarily on planar tests. Uniaxial testing using strip or dog-bone samples and biaxial tests using either cruciform or rectangular (or square) samples are used to assess mechanical properties [32–34] (Fig. 2). The benefit of this type of testing is that the analysis is straightforward. These testing methods, however, test the tissues in non-physiologic states, and are destructive to the tissue as a whole.

One alternative to using, particularly uniaxial, tests is the ring pull [35–38]. The main benefit of this type of test is that the sample preparation and testing method are simple. The downsides are that the ring pull is also not a physiologic loading scenario, and the analysis is complex. The alternative to these types of tests are inflation tests, where one inflates the entire tissue [39–44]. The benefits of the inflation test is that the tissue can be kept intact, and the analysis, if one uses a straight section, is straightforward. The drawback is that the testing apparatus is complex and requires good imaging modalities, especially for small tissues such as mouse vasculature. There are also a number of failure tests that evaluate the strength of cross-layer fibers. One such test is the peel test where one initiates a cut in the middle of a tissue, grips each side of the tissue, then peels the tissue apart [45]. Another alternative is the lap test where one initiates a cut in the middle on each side then grips the top layer on one side and the bottom layer on the other, then pulls the sample to failure [45, 46]. For a detailed review of testing methods used for determining the mechanical properties of arterial tissues see [47].

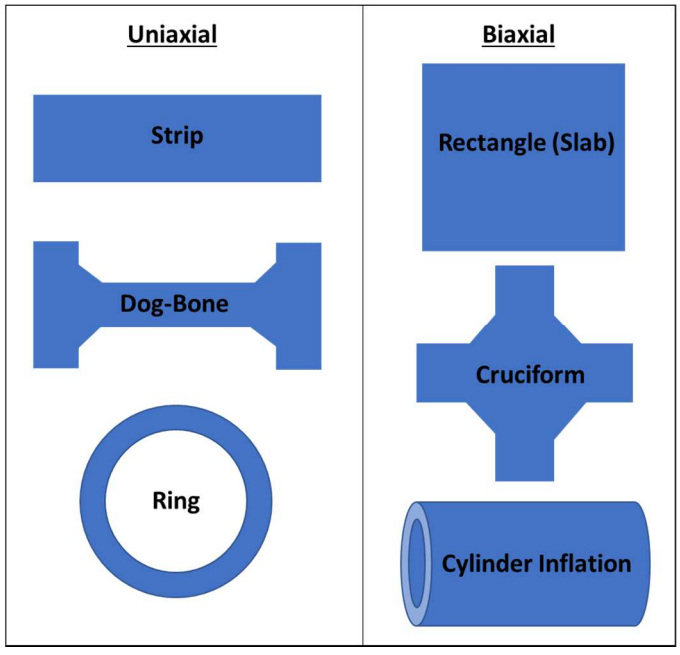

Figure 3. Existing mechanical testing methods

Key Figures in Aortic Mechanics, Growth, and Remodeling

We begin our description of continuum mechanics of arteries with a background on the key figures. Y.C. Fung is widely regarded as the father of biomechanics. He was the first mechanician to probe the viscoelastic properties of arteries and accurately model their behavior. He first described the exponential nature of tissue response to loading. The exponential model is now frequently applied to model fibers and is referred to as a "Fung-type" fiber model [16, 48, 49]. Several key figures have also emerged as knowledge experts in biomechanics following Fung. Gerhard A. Holzapfel, Thomas C. Gasser, and Ray W. Ogden first described the cylindrical constitutive framework underpinned with a constitutive equation describing tissue as having a neo-Hookean ground matrix with "Fung-type" exponential fibers [50–53]. This model is known as the Holzapfel-Gasser-Ogden, or HGO model (GOH is also sometimes used) and is described below. This model was expanded to account for four fibers (axial, circumferential, and two diagonal), and has been used extensively by Jay D. Humphrey to simulate many different types of arterial mechanics in both health and disease [54–61]. The advancement of aortic mechanics to include growth, remodeling, and maintenance of the ECM was brought to fruition by Richard Skalak, Larry A. Taber, Andrew D. McCulloch, Kumbakonam R. Rajagopal, and Jay D. Humphrey [62–71].

Current Models of Vascular Mechanics, Growth, and Remodeling

Current models of vascular growth and remodeling all center around continuum mechanics. Continuum mechanics treats tissues as time and space averages, ignoring much of the discrete minutia of tissues. The power of continuum mechanics is that it can describe systems in terms of continuously varying fields, thereby explaining many macroscopic observables remarkably well. Continuum mechanics, however, is not a closed theory. It relies on a derived mechanical framework coupled with a, typically phenomenological, constitutive equation. Thus, though we can describe many systems quite well with continuum mechanics, we do not have a means in this framework to describe a system's behavior starting from first principles on the

micro- or nano-scale [72, 73]. Further, continuum mechanics does not lend itself well to understanding fiber failure cascades such as are observed in many soft tissue experiments [13, 33, 74].

Cylindrical Arterial Framework

To begin our discussion of current vascular continuum models, we first outline the cylindrical framework that these models operate in most often. This framework follows the assumption that arteries are cylindrical in shape and subjected to uniform internal pressurization. As with any continuum system, the pressurization of an artery must satisfy the fundamental laws shown below, along with the laws of thermodynamics (zeroth law, conservation of energy, and law of increasing entropy) [72].

1. Conservation of Mass: $\frac{\partial \rho}{\partial t} + div(\rho \boldsymbol{v}) = 0$ where ρ is density and $\boldsymbol{v}$ is the material velocity tensor
2. Balance of Linear Momentum: $div(\boldsymbol{\sigma}) + \rho \boldsymbol{b} = \rho \boldsymbol{a}$ where $\boldsymbol{\sigma}$ is the Cauchy (true) stress tensor, $\boldsymbol{b}$ is the body force tensor, and $\boldsymbol{a}$ is the material acceleration tensor

It was observed by Fung that when one slices an artery down its axis, it opens up with some angle. Fung postulated that this opening was due to residual stress in the tissue, and put forth the following framework for finding the residual stress in an artery based on its opening angle [75, 76]. Fung referred to this axially cut state as "stress-free", even though we now know that the different layers would have different residual stresses due to the varied microstructure. In any case, we can use this approach as a good approximation to the residual stress in an artery. Figure 2 shows the "stress-free" configuration, the residual stress configuration, and the loaded configuration we will base our derivation on.

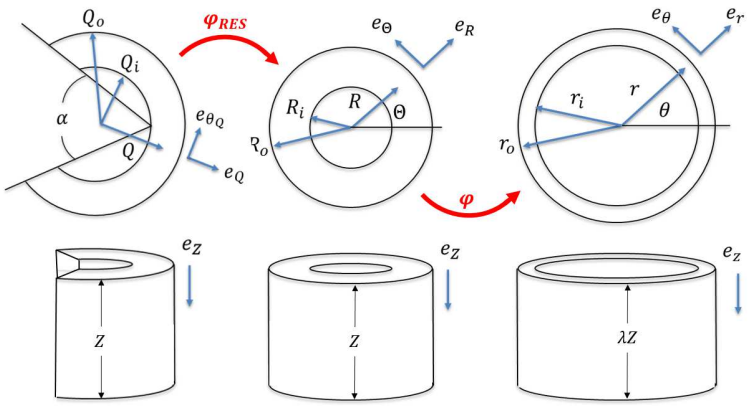

Figure 4. Deformation Mapping from "Stress-Free" (left) to Unloaded (center) to Loaded (right)

First, we can write the mapping, φ_{RES}, from the "stress-free" state to the residual stress state

$$R = R(Q);\ \Theta = k\theta_Q \text{ where } k = \frac{2\pi}{2\pi - \alpha};\ Z = z_Q$$

where R is the closed-cylinder radius, Q is the open artery radius, and α is the opening angle. We can then write the "stress-free" to residual stress deformation gradient tensor, F_{RES}.

$$F_{RES} = \frac{\partial R}{\partial Q} e_R e_Q + \frac{kR}{Q} e_\Theta e_{\theta_Q} + e_Z e_{z_Q}$$

By applying incompressibility and using the boundary condition at $Q = Q_i$, $R = R_i$, we can solve for R in terms of Q

$$J = \det(F_{RES}) = 1 = \left(\frac{\partial R}{\partial Q}\right)\left(\frac{kR}{Q}\right)(1) \rightarrow R = \sqrt{\frac{1}{k}\left(Q^2 - Q_i^2\right) + R_i^2}$$

where J is the Jacobian of the residual stress deformation gradient, F_{RES}.

We can also write the mapping from the residual stress state to the inflated state

$$r = r(R);\ \theta = \Theta;\ z = \lambda z$$

where r is the deformed radius, R is the undeformed radius, and λ is the axial z-stretch.

We then write the residual stress to loaded deformation gradient, F^*.

$$F^* = \frac{\partial r}{\partial R} e_r e_R + \frac{r}{R} e_\theta e_\Theta + \lambda e_z e_Z$$

By applying incompressibility and using the boundary condition at $R = R_i$, $r = r_i$, we can solve for r in terms of R.

$$J = \det(F^*) = 1 = \left(\frac{\partial r}{\partial R}\right)\left(\frac{r}{R}\right)(\lambda) \rightarrow r = \sqrt{\frac{1}{\lambda}\left(R^2 - R_i^2\right) + r_i^2}$$

where J is the Jacobian of the deformed deformation gradient, F^*.

We can combine deformations to get the deformation gradient, F, from the "stress-free" state to the inflated state.

$$F = F_{RES} \cdot F^* = \frac{1}{k\lambda}\left(\frac{Q}{r}\right) e_r e_Q + \frac{kr}{Q} e_\theta e_{\theta_Q} + \lambda e_z e_Z$$

In the case of artery inflation, we assume there are no external body forces on individual material elements and negligible material acceleration. Thus, we can look at a force and moment balance on a differential material element to equilibrate our momentum. The differential element is shown in Figure 4.

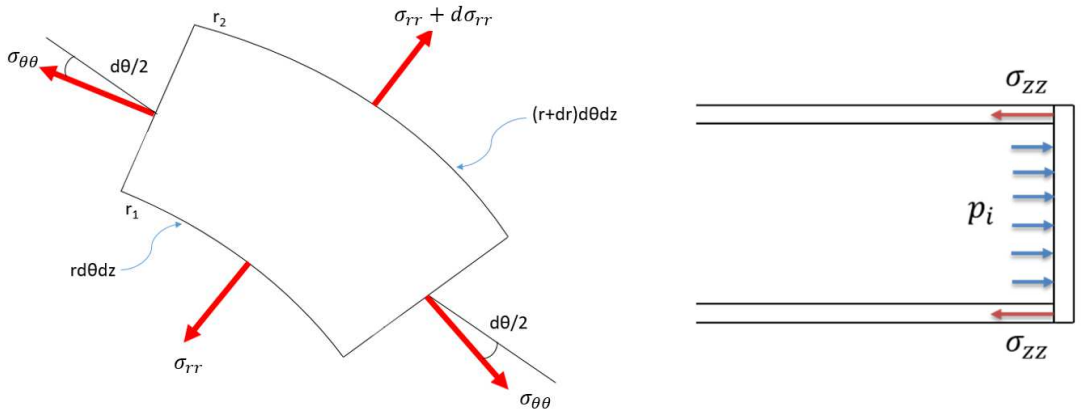

Figure 5. A differential element in cylindric inflation (left) and an enclosed end of the artery (right).

From Figure 4, we see that the circumferential and axial stresses will balance, and the moment summation through the material centroid can be considered negligible. Thus, we are left with only a summation of forces in the radial direction. Manipulation of the radial force balance, allowing dr to approach zero, gives us our equation of momentum equilibrium.

$$\frac{d\sigma_{rr}}{dr} + \frac{(\sigma_{rr}+\sigma_{\theta\theta})}{r} = 0$$

where σ_{rr} is the radial stress, r is the radius, and $\sigma_{\theta\theta}$is the circumferential stress.

Similarly, we sum the axial forces assuming the artery is pressurized and capped at the ends as shown in Figure 4b

$$p_i(\pi r_i^2) = \iint_{0\ r_i}^{2\pi\ r_o} (\sigma_{zz}) r dr d\theta$$

where p_i is the internal pressure on the end cap surface, πr_i^2 and σ_{zz} is the axial stress.

The Cauchy stress for a hyperelastic solid given in general form as a function of Green strain, **E**, and the strain energy density function, W is given as

$$\boldsymbol{\sigma} = \frac{1}{J}\left(\boldsymbol{F} \cdot \frac{\partial W}{\partial \boldsymbol{E}} \cdot \boldsymbol{F^T}\right)\ ;\ \boldsymbol{E} = \frac{1}{2}\left(\boldsymbol{F^T} \cdot \boldsymbol{F} - \boldsymbol{I}\right)$$

Simplifying, we get the radial, circumferential, and axial stresses for the incompressible, viscoelastic cylinder

$$\sigma_{ii} = \lambda_i \frac{dW}{d\lambda_i} - \frac{p}{\lambda_i} \text{ where } i = r, \theta, z$$

where $\lambda_r, \lambda_\theta,$ and λ_z represent the principal stretches corresponding to the diagonal components of the deformation gradient tensor, **F**.

Finally, we solve the cylinder inflation problem by applying our boundary conditions: at $r = r_i\ ;\ \sigma_{rr} = p_i,$ and at $r = r_o\ ;\ \sigma_{rr} = 0$. We then solve the momentum equilibrium equation for our hydrostatic pressure term, p

$$p\ =\ \lambda_r \frac{\partial W}{\partial \lambda_r} + \int_{r_o}^{r} \left(\lambda_r \frac{\partial W}{\partial \lambda_r} - \lambda_\theta \frac{\partial W}{\partial \lambda_\theta}\right)\frac{dr}{r}$$

The simplest case of boundary conditions for a cylindrical domain subject to no residual stresses is the Law of Laplace. To apply the Law of Laplace, we assume the vessel is thin-walled such that the circumferential stress is uniform through the thickness. We then use the

simplification of these two equations for thin-walled cylinders is the Law of Laplace where $\frac{d\sigma_{rr}}{dr} = \frac{P}{h}$ to give

$$\sigma_{\theta\theta} = \frac{Pr}{h} \; ; \; \sigma_{zz} = \frac{Pr}{2h}$$

where P is the internal pressure and h is the wall thickness.

We also note that these equations can be manipulated based on the boundary conditions to give the thick-walled pressure vessel equations proposed by Lamé, which are also commonly used to describe arterial behavior.

Strain Energy Density Functions and Material Constitutive Models

Strain energy density functions are used to describe the energy stored or transmitted in the process of mechanical deformation. A good strain energy density function closely approximates the phenomenological behavior of tissues but also maintains physical meaningfulness. A few key rules exist to maintain physical meaning in strain energy density functions: (1) If $\boldsymbol{F} = \boldsymbol{I}$; $W = 0$, and (2) If $\boldsymbol{F} = \boldsymbol{I}$ and there are no external loads; $\sigma = 0$ where $\boldsymbol{I}$ is the identity tensor. These rules ensure that the equations applied to fit materials within a specified continuum framework satisfy balance laws, specifically conservation of energy and momentum.

Another important concept dealing with strain energy density functions is continuum mixture theory. Continuum mixture theory states that a strain energy function can be made up of multiple different strain energy functions representing multiple different components so long as the continuum conservation laws are satisfied for the sum of all constituents (i.e. a constituent itself does not have to be conservative, but the system must be).

A particularly useful strain energy density function for arteries is that proposed by Holzapfel, Gasser, and Ogden [52, 53]. This model sought to explain the behavior of individual artery layer constituents. In this model, the isotropic, ground matrix is described by a neo-

Hookean term and the anisotropic collagen is described by two separate unit normal vectors a and b that describe the fiber orientation.

$$W = c_1(I_1 - 3) + \sum_{i=1}^{2} \frac{k_1}{2k_2}\left(\exp\left(k_2\left(I_4^i - 1\right)^2\right) - 1\right) ;\ I_1 = tr\left(C_{ij}\right) ;\ I_4^i = C_{ij}a_i a_j$$

where c_1 is the neo-Hookean parameter, I_1 is the first strain invariant, k_1 is the fibrous matrix modulus, k_2 is the fiber nonlinearity, $C_{ij} = F_{iK}F_{Kj}$ is the right Cauchy-Green tensor, I_4^i is the fourth strain invariant of fiber family i, and a_i is the fiber family direction vector.

Another model that is frequently used to describe the same behavior as the Holzapfel-Gasser-Ogden model is the four-fiber family model. This model again describes the isotropic, ground matrix as neo-Hookean but uses four fiber orientations as described by I_4^i instead of two. Using four fibers gives many more parameters to get a suitable fit. It also more closely simulates real arteries since the fiber orientations tend to be distributed and variable, meaning more fibers are better able to approximate the underlying fiber distribution.

These formulations can also be expanded to encompass multiple layers having distinct ground matrix and collagen behavior to better capture the different layers of the artery. One simply needs to provide the boundary condition that the layers remain attached to each other at the interface (i.e. the displacement of the interface is the same for the outside of one layer and the inside of the next layer). Additional studies have described the behavior of other constituents such as SMCs and GAGs by adding additional strain energy terms [77].

Growth and Remodeling Framework:

Our final discussion will be on current vascular growth models. These models tend to expand from the continuum framework and strain energy density discussion above. There are a few nuances to these theories, however. We rewrite the conservation laws for growth below.

1. Conservation of Mass: $\frac{\partial \rho^i}{\partial t} + div(\rho^i \boldsymbol{v}) = \dot{m}^i$ where ρ^i is density of constituent, i, $\boldsymbol{v}$ is the material velocity tensor, and $\dot{m}^i$ is the mass production or decay of constituent, i
2. Balance of Linear Momentum: $div(\boldsymbol{\sigma}^i) = \mathbf{0}$ in a quasi-static process where $\boldsymbol{\sigma}$ is the Cauchy (true) stress tensor of constituent, i.

It is often assumed that the stress follows a rule of mixtures equation (i.e. $\boldsymbol{\sigma} = \sum \phi^i \boldsymbol{\sigma}^i$ where $\phi^i = \rho^i/\rho$). Under this assumption, the balance of linear momentum only must be satisfied globally instead of on a constituent-by-constituent basis [78, 79].

There are two types of growth that are typically modeled in continuum frameworks: volume growth and surface growth [70]. In volume growth, each infinitesimal element is said to gain mass per some prescribed growth rate. Volumetric growth follows the concept of splitting infinitesimal material elements apart, allowing them to grow, deforming them to reassemble the tissue, then loading the tissue with some deformation [62, 65, 70]. This decomposition can be described mathematically by using a growth deformation gradient tensor, $\boldsymbol{F_g}$, an elastic residual stress deformation gradient tensor, $\boldsymbol{F_e}$, and a load deformation gradient tensor, $\boldsymbol{F_l}$. We can then write the overarching deformation gradient for the whole process, $\boldsymbol{F} = \boldsymbol{F_l F_e F_g}$. If we take this concept one step further, we can describe growth and remodeling as a cell trying to maintain some homeostatic stress, σ^*. Then the tissue growth deformation tensor becomes a function of the difference between the local stress, σ, and the theoretical preferred homeostatic stress, σ^*. This type of growth description is typically considered valid for the growth of soft tissues [25, 62].

The other form of growth is surface growth. Surface growth is the product of deposition and resorption of material on a surface. In this type of growth, particles of infinitesimal size are deposited on a surface, and the surface boundary grows. This type of growth can be described by a surface growth velocity tensor, $\boldsymbol{v_g}$, which is a measure of the evolving surface boundary S, at time t, relative to the initial surface, S_0. New particles deposited at time, $0 < \tau < t$, are added to

the boundary so that at time, t, we have all particles adhered or resorbed from the surface [62, 71]. This type of growth is appropriate for describing plaques and calcifications in arteries.

These two techniques for describing growth using continuum mechanics outlined the general form for modeling growth in biological tissues. These relations have been frequently applied to arterial tissues [65, 66, 80–84], where most methods focus on the adaptation of generic cylindrical structures to pressure and stretch. Recent work has focused on applying these models to increasingly complex geometries (e.g. branching structures or nonuniform shapes) or increasingly realistic constitutive relations [25, 26, 93–102, 85, 103, 104, 86–92] accounting for the multi-constituent nature and heterogeneity of the arterial wall. Additionally, recent work has sought to understand the interaction between tissue-engineered constructs and native tissues as in [105], with the idea that such models can be used as a preclinical tool for assessing outcomes of tissue engineered implants [92, 96, 106].

Fiber Network Mechanics:

Continuum models are an excellent framework for understanding arterial mechanics and growth, but they rely on phenomenological constitutive relations which disregard the physics of the fibrous ECM [72]. Therefore, there is a fundamental disconnect between what one would see in the tissue microstructure and the parameters one might extract from a tissue-scale experiment. Continuum mechanics allows us to quantify the change of tissue strength in health and disease (i.e., we can describe cystic medial degradation through the scale of the parameters in our constitutive model). However, with continuum models, we cannot scrutinize the effects of discrete fiber or network changes, like those observed in disease states. Thus, we need better mechanical models of realistic network architectures to serve as the foundation for probing tissue-scale mechanics. We must ensure that we are not blurring discrete effects through time- and space-averaging because we then lose the specificity of our conclusions.

Ideally, we would be able to explain different modes of growth and remodeling by simple adjustment of the network architecture and stress conditions. It is important to model and study vascular mechanics, growth, and remodeling in health and disease using models more rooted in the underlying physiology to discern the mechanisms of aortic aneurysm. There have been many advances in modeling the ECM directly as a fiber network composite [45, 107–112], which will be discussed in more detail in Chapters 5, 6, and 7. Briefly, in constrained mixture theory of continuum mechanics, one defines the mass fractions of individual constituents such that each constituent has its own associated mass fraction (or volume fraction) such that

$$\phi^s = \frac{1}{v}\int dv^i = \frac{1}{v}\sum_i v^i = \sum_i \phi^i$$

where ϕ^s is the total solid volume fraction, v is the tissue volume, v^i is the volume of constituent i, and ϕ^i is the volume fraction of constituent i. It is further assumed that the constituents themselves are independent, but constrained to move together such that

$$\sigma_{kl}(F_{mN}) = \frac{1}{v}\int \sigma^i_{kl}(F_{mN})dv = \frac{1}{v}\sum_i \sigma^i_{kl}(F_{mN})v^i = \sum_i \phi^i\sigma^i_{kl}(F_{mN})$$

where σ_{kl} is the total Cauchy stress, F_{mN} is the deformation gradient, and σ^i_{kl} is the stress of component i. If we further manipulate this relation, such that we account for all constituent fibers, we get the volume average theory relation for Cauchy stress in a fiber network composite

$$\sigma_{kl}(F_{mN}) = \frac{1}{v}\sum_f \sigma^p v^p = \frac{1}{v}\sum_p \frac{f^p}{a^p}a^p l^p = \frac{1}{v}\sum_p f^p l^p$$

where f^p is the force in fiber p, a^p is the deformed cross-section of fiber p, and l^p is the deformed length of fiber p. Further efforts have sought to apply remodeling in ECM networks to discern any multiscale phenomena that continuum models may be unable to capture [113–115].

These past models have focused mainly on networks of one type and have, for the most part, neglected the direct interactions among ECM constituents, which are critical in the remodeling signaling cascade.

CHAPTER 3: MECHANICAL CHARACTERIZATION OF ARTERIES USING THE RING PULL ASSAY

The author acknowledges Springer Nature as the original publisher of the following work which can be attained from Experimental Mechanics at [116].

Summary:

Background: The ring-pull test, where a ring of tissue is hooked via two pins and stretched, is a popular biomechanical test, especially for small arteries. Although convenient and reliable, the ring test produces inhomogeneous strain, making determination of material parameters non-trivial.

Objective: To determine correction factors between ring-pull-estimated and true tissue properties.

Methods: A finite-element model of ring pulling was constructed for a sample with nonlinear, anisotropic mechanical behavior typical of arteries. The pin force and sample cross-section were used to compute an apparent modulus at small and large strain, which were compared to the specified properties. The resulting corrections were validated with experiments on porcine and ovine arteries. The correction was further applied to experiments on mouse aortic rings to determine material and failure properties.

Results: Calculating strain based on centerline stretch rather than inner-wall or outer-wall stretch afforded better estimation of tissue properties. Additional correction factors were developed based on ring wall thickness H, centerline ring radius Rc, and pin radius a. The corrected estimates for tissue properties were in good agreement with uniaxial stretch experiments.

Conclusions: The computed corrections improved estimation of tissue material properties for both the small-strain (toe) modulus and the large-strain (lockout) modulus. When measuring tensile strength, one should minimize H/a to ensure that peak stress occurs at the sample midplane rather than near the pin. In this scenario, tensile strength can be estimated accurately by using inner-wall stretch at the midplane and the corrected properties.

Introduction:

The mechanical characterization of biological soft tissue can be done in many ways (for an overview in the cardiovascular space, see [47]). However, as the scale of the biological samples of interest becomes smaller, numerous challenges arise for most testing modalities (e.g. planar uniaxial and biaxial). The effects of handling and preparation are amplified as it becomes more difficult to make samples of uniform dimensions. Gripping the sample becomes difficult and removes a large portion of tissue from the test. Edge effects become important and can pollute the measurement. The necessary precision of testing machines goes up and costs can rise to prohibitive levels.

As a result, there are two mainstays in the mechanical characterization of very small (mm or smaller) biological tissues: indentation (or atomic force microscopy (AFM)) and ring pull tests. In the case of natural ring shapes, such as arteries, the ring pull test has several distinct advantages: 1. Ring-pull tests load the tissue circumferentially, which is typically in line with the physiologic load state. 2. Ring tests are simple in both gripping and testing, and do not require specialized machinery to do (one can even do such tests on a lab weigh scale). 3. Ring tests are high throughput and repeatable because the sample preparation and test are straightforward.

Ring-pull tests, also called uniaxial ring tests, are appropriate for all types of cylindrical and spherical tissues. A schematic of a ring-pull test is shown in Fig. 5. Ring-pull tests are particularly well suited to small, branched structures because the segmentation of rings allows one to analyze mechanical properties locally without the use of complex inverse finite element (FE) methods. The ring test also lends itself well to assays of passive and active properties of tissues from the cardiovascular, digestive, or respiratory system. A list of systems that ring tests have been used to study, by no means exhaustive, is shown in Table 1 (see Fig. 5 for definition of measures).

Unfortunately, there is no precisely defined strain mapping for the ring pull test, which means one cannot simply fit a material model in a theoretical framework to an experiment [117]. Van Haaften et al. [37] investigated the validity of the uniaxial approximation and proposed a correction factor in the context of linear, isotropic materials. They concluded that the uniaxial approximation breaks down in the case of thick rings and is correctable for linear, isotropic tissues at <5% strain. Although the linear analysis is informative, soft tissues operate at strains much larger than 5% in almost all cases (see Table 1). Tissues also typically exhibit nonlinear, or at least bilinear, material behavior characterized by a small strain (toe) region, a distinct transition strain (or stretch), and a large strain (lockout) region[1]. The nonlinear behavior of tissues can also affect the results because the ring pull test is not a pure extension of the tissue due to bending caused by the pin grip. The typical planar strip uniaxial test is a much better approximation of a pure extension. Additionally, if we consider small samples like the carotid artery or very thick tissues like ventricular rings of the heart, we need corrections that are not extrapolated, but are verified by experiment in the extremes.

Furthermore, the ring test is often used to analyze failure properties of samples [118–120]. It is therefore important to consider the heterogeneity of the ring-pull deformation, along with geometric factors that may concentrate stress. Particularly, when reporting failure strain, one must be aware that the actual strain in the region of failure initiation is often very different than the calculated nominal strain of the sample. The same is true of the failure stress. Failure stress is reported as the mean stress of the sample at failure, which, for a uniaxial test tends to be a good approximation of the maximum stress. However, for a ring test, the deformation is not homogeneous, and we must account for the stress difference across the sample.

[1] The large-strain portion of the stress-strain curve is often called the *linear* regime, but we use *lockout* to avoid confusion with linear material models.

The goal of this work is to create a simple geometry-based strategy for converting force-displacement data from uniaxial ring tests to a corrected uniaxial extension allowing for quantitative assessment of circumferential material and failure properties. To accomplish this goal, we use computational models to assess the uniaxial approximation for rings composed of nonlinear, anisotropic materials under large strains, analyze the effect due to wall thickness and pin (hook) geometry, and propose purely geometric corrections for small-strain modulus, transition strain, and large-strain modulus. We propose a strategy for pin selection and offer an approach for determining failure properties. We then validate our approach using both ring test and uniaxial strip extension experiments on porcine and ovine arterial tissues, and apply our failure approximation to ring tests of murine aortic tissue.

Methods:

Our approach has three primary components outlined in the subsections below. First, we performed finite element analysis of the ring pull test for a range of ring radii, ring thicknesses, and pin radii to assess the behavior of an anisotropic, nonlinear material under a range of geometric conditions. These computational models were used to construct a geometric correction function for converting nominal material properties assessed from ring-pull tests to the equivalent material properties that would be assessed from strip uniaxial extension. Second, we performed ring-pull experiments on various arterial tissues in several animal models using multiple pin sizes when possible. We used these experiments along with the correction function to predict the uniaxial extension behavior. We then assessed and validated our correction by performing uniaxial extensions of the cut and opened ring strips. Third, the computational and experimental data were analyzed and compared as described in the final subsection.

Computational Model

A finite element model (Fig. 6) of the ring pull experiment was created using PreView 2.1.1, solved using FEBio 2.9.1, and visualized using PostView 2.4.4 [121]. Briefly, the model was

created using a ring represented as a quarter of a hollow cylinder sliced in half longitudinally to invoke one-eighth symmetry. A rigid body was created in the ring to mimic the pin. The pin surface was prescribed as a node-on-facet sliding contact with the ring sample inner surface, neglecting friction between the surfaces. An augmented Lagrangian formulation was used with two-pass, automatic penalty for contact. The faces on symmetry planes were held on their respective planes but allowed to slide along the plane. A displacement was prescribed to the ring surface opposite the pin to mimic the experiment. The pin was meshed using 33,600-122,300 hex8 elements depending on pin diameter, and the ring sample was meshed using 42,000-90,000 hex8 elements depending on ring thickness. The material model for the ring was an uncoupled elastic mixture consisting of a nearly incompressible neo-Hookean solid and an exponential fiber family oriented circumferentially around the ring. The strain energy density, W, for this model is:

$$W = C_1(I_1 - 3) + \frac{\xi}{2\alpha}\left[\exp\left(\alpha\left(\lambda_f^2 - 1\right)^2\right) - 1\right] + \frac{1}{2}K(ln(J))^2 \qquad \text{Eq. 1}$$

where: C_1 is the ground matrix modulus, I_1 is the first strain invariant, ξ is the fiber modulus, α is the fiber nonlinearity, K is the ground matrix bulk modulus, and $J = \det(\boldsymbol{F})$ where $\boldsymbol{F}$ is the deformation gradient tensor. In the ring simulations, parameters of $C_1 = 50kPa, \xi = 10kPa, \alpha = 1.0, K = 75\ MPa$ were used. These parameters were taken from assessment of the uniaxial porcine abdominal aortic samples as described in the *Experimental Protocol* subsection. The value of the bulk modulus, K, was chosen to make the material nearly incompressible. It is noted that since the material is nonlinear, the term "modulus" refers to the modulus in the limit of infinitesimal strain.

Sample Preparation

Tissue samples from three animal models were used in this study. Healthy 6-month-old sheep and pig tissue samples (abdominal aorta and carotid) were procured from the Visible Heart Lab (Department of Surgery, University of Minnesota, Minneapolis, MN, USA) immediately following euthanasia for other studies. The samples were trimmed of perivascular connective tissue

then sectioned axially into ~6mm rings. The rings were then equilibrated in 1x PBS for 12 hours to ensure investigation of only passive mechanics of the tissue. Immediately prior to testing the ring dimensions were measured optically using a digital camera and analysis software, FIJI [122].

Wild-type (C57BL/6J) mice were procured from the Provenzano Lab (Department of Biomedical Engineering, University of Minnesota, Minneapolis, MN, USA) immediately following euthanasia as a part of colony maintenance. The heart, lungs, and aorta were excised *en bloc*. The lungs were removed, and the aorta was trimmed of perivascular connective tissue. The aorta was then placed in 1x PBS and allowed to equilibrate for 12 hours as above. Immediately prior to testing, the aorta was sectioned axially into ~1.5mm rings from the descending arch to the renal artery branches. The dimensions of each ring were then measured as above.

Experimental Protocol

Ring-pull tests were performed on all tissues. Sheep and pig tissues were tested using a custom ring pull grip apparatus where the pin diameter could easily be altered by replacing a sleeve (Fig. 7A). This flexibility allowed us to investigate the effect of relative pin to ring size on the overall tissue behavior. Each sample was placed so that both pins passed through the lumen of the vessel (Fig. 7A). The pins were lubricated using canola oil to reduce friction between the tissue and the stainless-steel pins. Lubrication is particularly important for larger pins where more sliding is necessary as the tissue stretches. Samples were kept hydrated during tests by pipetting 1x phosphate-buffered saline solution (PBS) across the sample width. The samples were immersed in 1x PBS between tests. A uniaxial testing machine (TestResources Inc., Shakopee, MN, USA) with a 45N load cell (sheep and pig aorta) or a 5N load cell (carotid artery and mouse aorta) was used to perform the circumferential uniaxial tests. The samples were preconditioned on the largest radius pin for 5 cycles to 50% nominal engineering strain, then uniaxial ring tests were performed for each subsequent pin size at 0.6% strain per second to a nominal engineering strain of 65%. After completion of ring testing, the rings were cut open and allowed to equilibrate for 60 minutes in 1x

PBS. The opening angle was measured immediately before the sample was placed in a uniaxial setup consisting of two grips that clamped the tissue using low-grit sandpaper to prevent slipping (Fig. 7B). The uniaxial experiments were conducted in the same way as the ring-pull tests with preconditioning cycles to 50% engineering strain and a uniaxial pull to 65% engineering strain.

Due to the small size, mouse aortic rings were only tested in the ring test configuration. They were loaded at a strain rate of 1% per second and pulled to failure. Hydration was maintained as above.

For a subset of the sheep aortic rings, ultrasound was used to image the cross-section of the ring samples at several stretches. The samples were submerged in a 1x PBS bath and imaged using a VEVO2100 small animal ultrasound machine (FUJIFILM VisualSonics Inc., Toronto, ON, CA) with a 30MHz transducer.

Data Analysis

For the ring samples, the centerline lengths were used to calculate the kinematics of the tissue. This approach differs from typical measures which use either the pin-to-pin distance from the flattened state to the stretched state, which equates roughly to using the inner luminal surface stretch, or that proposed by Van Haaften et al. [37], which uses the external surface stretch. The deformed thickness, h, was calculated by assuming that the transverse stretches, λ_t, (i.e. in the thickness, H, and width, W, directions) were equal to one another, and that the tissue volume was conserved (i. e. the Jacobian, $J = 1 = \lambda_1\lambda_2\lambda_3 = \lambda_1\lambda_t^2$) (Eq. 2). Under that assumption, the volume conservation can be simplified to a cubic function of λ_t (Eq. 3), which is easily solved using any root finding algorithm.

$$V_0 = V = \pi\left((R_i + H)^2 - R_i^2\right)W = \pi((a + \lambda_t H)^2 - a^2)\lambda_t W + 2d(\lambda_t H)(\lambda_t W) \quad \text{Eq. 2}$$

$$0 = \pi H^2\lambda_t^3 + 2H(\pi a + d)\lambda_t^2 - 2\pi R_c H \quad \text{Eq. 3}$$

Once h and therefore L were determined, the stretch of the centerline was calculated as $\lambda_1 = L/L_0$. The stretch was used to assess the engineering strain, $\varepsilon_1 = \lambda_1 - 1$ for the corresponding PK1 stress ($P_{11} = F_1/A_0$) where P_{11} is the circumferential PK1 stress, F_1 is the force in the direction of stretch, and A_0 is the undeformed sample cross-sectional area. The average PK1 stress was calculated for the midplane region of that sample assuming that each side of the ring held half the total force on the pin.

It should be noted that the analysis performed here uses the assumption of equal transverse stretches and incompressibility which are approximations. It should also be noted that a uniaxial extension cannot elucidate full-field mechanical properties because it only tests one direction at a time. In this case when we refer to the vessel properties, we refer to the circumferential material properties around the vessel wall.

In the assessment of circumferential mechanical properties for this paper we chose to use the small strain (toe) modulus, the large-strain (lockout) modulus, and the transition strain as our metrics of material behavior. The distinct benefit of these properties is that they allow for intuitive assessment of material behavior, as well as allowing one to reconstruct rough stress-strain curves for the material simply. The assessment of these properties was performed by taking the small-strain modulus between 5% to 20% engineering strain for uniaxial cases and 10% to 25% engineering strain for ring tests. The reason for the different limits between the uniaxial and ring tests is that the ring test is that the ring test is characterized by a region of flattening from the ring shape to an ellipsoid where there is very little tissue stretch, and the deformation is mostly bending. This happens typically in the range of 0-5% centerline stretch. The large-strain modulus was taken for average PK1 stress ranges between 200kPa and 350kPa for aortic samples, and between 150kPa and 300kPa for the carotid artery. These ranges were selected based on the stress range of roughly linear modulus at large strains as assessed from preliminary data from uniaxial extensions on the different tissue types. The moduli were fit to a line using MATLAB2019a (Mathworks Inc., Natick,

MA, USA) where the slope is the modulus. The intersection of the small-strain line and the large-strain line is defined as the transition strain (Fig. 8).

Results:

Computational Model

The first question considered was whether the stress-strain curve estimated from the pin force per midplane cross-sectional area and the average tissue strain was a good estimate of the actual stress-strain behavior of the tissue. We started by analyzing luminal surface strain, centerline strain, and exterior surface strain as metrics for stress-strain behavior for the material (Fig. 9). In Fig. 9, the black line is the true material behavior in uniaxial extension, and the colored lines represent the strain estimate for different tissue thicknesses. Using the luminal surface strain shows a much less stiff material behavior than the true behavior because the luminal strain is higher for any given force (Fig. 9A). The centerline strain estimation shows a better approximation, but still consistently underpredicts the tissue stiffness relative to uniaxial (Fig. 9B). The exterior surface strain shows stiffer material behavior than uniaxial because the exterior strains are much lower for any given force (Fig. 9C). All strain measures consistently underpredict small-strain modulus due to the importance of bending, particularly as the tissue thickness increases.

To analyze the stress-strain estimations further, we examined the strains across the sample, as shown in Fig. 10. There was large variability in the strains from exterior (outer) surface to luminal (inner) surface for a given nominal stress. The inner surface begins stretching as the pin begins to move and the ring, viewed from the top, begins to flatten into an oval shape. The stretching begins generating force even before the mean stretch ratio of the tissue departs from $\lambda_1 = 1$. The outer surface lags the inner surface because it requires more pin movement to begin stretching. In fact, as shown in Fig. 10A, the exterior surface goes into compression for a short period as the ring begins to flatten (shown by blue arrows). As the ring deforms there is initial bending that transitions to stretching. Thus, we should expect a stress profile that looks like a

bending deformation (tension on one surface and compression on the other) followed by uniaxial extension (tension on both surfaces albeit of different magnitudes). Furthermore, a volumetric effect arises due to incompressibility, and the tissue in the midplane region deforms from a rectangle to a C-shape. This happens because the higher stretch on the inner surface causes a larger transverse compression on the inner surface relative to the outer surface. As a result, the ring height decreases more on the inner surface causing the cupping shown in Fig. 10B.

Another goal of this work was to investigate the maximum stresses the tissue undergoes during deformation in different ring-pull configurations. Stress concentrations are important because one often wishes to estimate failure properties from the ring-pull test [118–120]. As shown in Fig. 11, for small pin sizes, the stresses concentrate around the back of the pin. This is intuitively demonstrated using Euler beam theory, which we acknowledge is valid neither for large deformations nor for nonlinear material behavior, but which serves for illustration of the principle. For a beam of rectangular cross-section, the bend radius is given by $R_{beam} = EI/M$ where E is the Young's modulus, I is the moment of inertia, and M is the internal moment. The maximum stress in a linear beam subjected to such bending is $\sigma^{max} = M\left(\frac{H}{2}\right)/I$. If we then require that $\sigma^{max} < \sigma^{failure}$, we see there exists a minimum bend radius which gives us a theoretical minimum pin radius where our assumptions of stretch are valid: $a \geq E\left(\frac{H}{2}\right)/\sigma^{failure}$ and $H/a \leq 2\sigma^{failure}/E$. Using this approximate expression, failure properties from [46], and our own values for thickness and large-strain modulus in pig aorta, we get $H/a \leq 2(2.75MPa)/(2.42MPa) = 2.3$. For larger values of H/a, stress concentrates on the back-side of the pin which would likely cause failure at the pin, and not in the midplane region (Fig. 11A & 11B). If one avoids this condition by using $H/a < 1$, the stresses do not concentrate around the pin, but instead reach a maximum on the inner surface of the ring at the midplane region (Fig. 11C & 11D). One can also accurately estimate the luminal stretch at that region as $\lambda^{lumen} = (2\pi a + 2d)/2\pi R_i$. Once one knows the stretch at failure, one can calculate the stress at the luminal surface using our fitted (corrected) material

properties. This approach gives us a much more accurate measure of failure stress than the mean stress over the sample since the initiation of failure happens at the luminal surface.

Experiments

The first objective of the experiments conducted was to determine whether our model was consistent with the behavior of the tissue. We confirmed that qualitative deformation features of our model were also evident in tissue using high resolution ultrasound of a sheep aortic ring sample at different stretches as shown in Fig. 12. Midplane images (Fig. 12, top row) demonstrate how stretching the sample causes the same C-shape cupping as in the simulation (Fig. 12B). The tissue in contact with the pin also compressed in the thickness direction while being stretched circumferentially, forcing the tissue into a trapezoidal shape (Fig. 12, bottom row). The shape change is consistent with what we see near the pins in the model (Fig. 10).

To assess the need for correction, we ran experiments on various arterial tissues in several animal models as shown in Fig. 13. Where applicable, the uniaxial pull is shown in black and each pin size is shown in a different color. Our results indicate that thicker, smaller diameter tissues exhibit markedly different stress-strain behavior in the ring-pull relative to the uniaxial experiment, especially in the small-strain region. We also note that, for sheep aorta and carotid, the transition strain is significantly different for the ring compared to the uniaxial (Fig. 13B & 13C). The mouse aortic rings had no uniaxial equivalent as they were stretched to failure (Fig. 13D).

Material Property Corrections

Correction factors for small-strain modulus, large-strain modulus, and transition strain were obtained from simulations. The rings used in the simulations had dimension in the range of R_c = 0.40-0.70 mm and H = 0.035-0.20 mm. The pins had radii in the range of a = 0.02-0.20 mm. Overall, 50 simulations were performed over this range. For each simulation, the small-strain modulus was calculated. For models using small pins however, the simulation was unable to reach

large deformations due to numerical instability. Therefore, we only used 37 data points for the large-strain modulus and transition strain.

To investigate the role of geometry on the mechanical properties, we use two dimensionless quantities. The first is the ratio of ring thickness to centerline radius: H/R_c. As this ratio approaches zero the bending rigidity of the sample goes to zero and the test approaches a uniaxial stretch in the limit of zero friction. The second quantity is the ratio of ring thickness to pin diameter: H/a. This dimensionless parameter relates to the ability of the ring to form around the pin as discussed above.

We introduce a functional limit and two fundamental limits for dimensions of the ring and pin. The functional limit is that two pins of radius a must fit in the ring lumen so that $R_c - H/2 \geq 2a$. This limit is shown in Fig. 14 as a dashed line. The fundamental limit is if one used two semi-circular D-shaped pins, we must have $R_c - H/2 \geq a$. This limit is shown in Fig. 14 as a greyed area. Since the inner radius of the ring must be greater than zero, an additional limit is that $H/R_c < 2$.

The ratio between ring and uniaxial measurements for the two nondimensionalized parameters, H/R_c and H/a, are shown in Fig. 14. The small strain modulus (Fig. 14A) is consistently underpredicted especially for values of $\frac{H}{R_c} > 0.3$, because of the strain inhomogeneity for ring tests. Furthermore, the small-strain modulus demonstrates strong nonlinear dependence on both nondimensional parameters. In contrast, the large-strain modulus (Fig. 14B) is overestimated when H/R_c is greater than 0.3 for moderate H/a values, but is underestimated for moderate H/R_c values and large H/a values. The large-strain modulus shows similarly strong nonlinear dependence on both quantities. The transition strain (Fig. 14C) shows a consistent increase with increasing H/R_c and a decrease with H/a. The transition strain shows more linear dependence on H/R_c. Thus, the effect of a thick-walled sample (relative to radius) depends on the size of the pins being used to perform the ring pull. There is a window ($H/a \in [0.5,1.5]$ and $H/R_c \in [0.15,0.3]$)

where the estimations are close to the true parameters and the parameter ratios near unity. The ratio H/R_c is out of the experimenter's control, but the choice of pin size can be optimized to estimate the material parameters accurately. Arteries tend to have H/R_c in the range of [0.15-0.35].

Each contour plot in Fig. 14 was fitted to a bivariate cubic function as given in Eq. 4. The parameters which were nearly zero, or whose range at 95% confidence included zero were removed from the fit. Table 2 shows the fitted coefficients along with their 95% confidence intervals. Root mean squared error (RMSE) is shown for the fit and can be interpreted as the fraction of error not accounted for by the geometric correction.

$$f\left(\frac{H}{Rc},\frac{H}{a}\right)=\sum_{i=0}^{3}\sum_{j=0}^{3-i}k_{ij}\left(\frac{H}{R_c}\right)^{i}\left(\frac{H}{a}\right)^{j} \qquad \text{Eq. 4}$$

Thus, we propose the following correction equations for determining material properties from ring-pull tests (Eq. 5A-C).

$$\frac{E_s^{Ring}}{E_s^{uni}}\approx 1-0.042\left(\frac{H}{a}\right)^2+0.214\left(\frac{H}{R_c}\right)\left(\frac{H}{a}\right)^2-1.552\left(\frac{H}{R_c}\right)^2\left(\frac{H}{a}\right) \qquad \text{Eq. 5A}$$

$$\frac{E_L^{Ring}}{E_L^{Uni}}\approx 1+0.094\left(\frac{H}{a}\right)^2-0.627\left(\frac{H}{R_c}\right)\left(\frac{H}{a}\right)^2+2.359\left(\frac{H}{R_c}\right)^2\left(\frac{H}{a}\right) \qquad \text{Eq. 5B}$$

$$\frac{\varepsilon_t^{Ring}}{\varepsilon_t^{Uni}}\approx 1+0.358\left(\frac{H}{R_c}\right)-0.054\left(\frac{H}{a}\right) \qquad \text{Eq. 5C}$$

Validation

We fit each experimental tissue to our bilinear model, and the results are shown in Fig. 15. The uniaxial extension test was treated as the ground truth. The ring-pull small-strain moduli (Fig. 15A) show large errors when compared to the uniaxial data. Particularly, the aortic samples show that the luminal and exterior stretch estimates are poor with the exterior stretch overpredicting the modulus and the luminal stretch underpredicting the modulus. The centerline estimate, however, is

reasonably good. The carotid sample, on the other hand, shows that inner and centerline estimations underpredict the modulus, but the exterior estimate is good. It is important to note these differences because the aortic tissues are thin-walled while the carotid is relatively thick-walled by comparison (i.e. H/R_c is much greater for the carotid than for the aorta). Therefore, no single estimate (luminal, exterior, or centerline) provide correct estimates of small-strain modulus. We were, however, able to correct the small-strain modulus for both the aortic samples and the carotid samples. The correction shows that the error becomes almost constant across all ring sizes indicating that we have removed the geometric effects and are now only left with systemic error. The results for large-strain modulus (Fig. 15B) show that, for aortic samples, the exterior surface stretch tends to overpredict the modulus while the luminal surface stretch tends to underpredict the modulus. In the aortic samples, the centerline tends to be a reasonably good estimate of the modulus. The carotid data shows that the exterior and centerline stretches tend to overestimate the modulus, while the luminal stretch serves as a good approximation. The corrected large-strain modulus showed little change from the uncorrected value (<5%) for both the pig aorta and sheep aorta, but showed a marked improvement (>40%) for the sheep carotid (Fig. 15B). For the transition strain, we saw little change comparing the corrected value to the uncorrected value with large error throughout. We did see a large improvement in the sheep carotid data (>15%), but the corrected transition strain was still 51% above the uniaxial value. We presume the transition strain was polluted by residual stress effects due to testing an intact ring versus an opened, flattened uniaxial sample.

Across all tissue types there is little change in the correction of aortic samples, but there is a significant improvement in modulus estimation for the sheep carotid artery samples shown by the grey arrows in Fig. 15. Particularly, we see that the small-strain modulus for the sheep carotid artery, when corrected, approaches the exterior surface estimate while the large-strain modulus for the sheep carotid artery approaches the interior surface estimate. This shows that our correction,

for a thick-walled tissue such as the carotid, is a vast improvement over any single estimate alone (i.e. using the luminal surface, exterior surface, or centerline without correction).

Failure Property Estimation

The mouse ring pulls had no uniaxial equivalent because of the challenges arising from uniaxial testing of very small tissue samples as described in the *Introduction*. All data in this section are reported as mean±95% confidence interval for n=30 samples. The uncorrected values for small-strain modulus and large-strain modulus were 0.304±0.065 MPa and 1.883±0.209 MPa respectively. The uncorrected transition strain was 0.397±0.048. The values for H/R_c and H/a were 0.159±0.039 and 0.516±0.088 respectively. These values are relatively small meaning the tissue has a relatively thin wall (which places the corrections in the lower left corner of Fig. 16), so the ring-pull is close to a uniaxial test. From our correction equations, we would expect the small-strain modulus to be 0.311 MPa, the large strain modulus to be 1.829 MPa and the transition strain to be 0.385.

The ratio of tissue thickness to pin radius ($H/a = 0.516$) was small enough that we can estimate the failure stress and strain at the midplane (as demonstrated by the computational model and confirmed through experiments). The calculated central strain at rupture was 0.999±0.145 while the luminal strain at rupture was 1.107±0.166. If we look purely at the experiment, we get a mean PK1 stress at failure of 1.254±0.538 MPa. However, if we use the average properties obtained for the mouse aorta as given above, we get a PK1 stress at failure of 1.440±0.591 MPa. These results are in agreement with previously reported values of uniaxial failure for mouse descending thoracic aorta [118]. There is a difference of 14% between the two failure stress values, even though the wall thickness to radius ratio is relatively small ($H/R_c = 0.159$). This would indicate that, even in the case of relatively thin samples, one should use the luminal surface stretch as the metric for failure.

Discussion:

Our model accurately captures the kinematics of the ring pull test, including the unfolding, flattening behavior, and C-shape deformation of the center region shown in ultrasound imaging through the cross section (Fig1. 10, 12). Furthermore, we showed that as an approximation for average strain, one can use the centerline stretch estimated using a transverse stretch calculated by assuming incompressibility. This approximation has distinct advantages over using either the inner surface, which vastly underpredicts the uniaxial stress-strain curve while overpredicting the transition strain, or the exterior surface, which underestimates the small-strain properties, overestimates the large strain properties, and underestimates the transition strain (Fig. 9). The estimation of centerline stress-strain still underpredicts the small-strain modulus and overestimates the transition strain, but the curves are much closer to the uniaxial stress-strain curve than those for either of the other measures (Fig. 9B). Additionally, any of these stretches can be estimated using the assumption of incompressibility with no additional data beyond the force-displacement data one would ordinarily obtain.

To predict failure of ring samples, one needs to know the maximum stress the sample experiences. We have shown that there exist two possible peak stress locations: the luminal side of the central region and the exterior side directly behind the pin (Fig. 11). Additionally, we posit the existence of a minimum bend radius of the material, which greatly changes the kinematics of the ring pull test as we approach it. The problem of bending around the pin is complicated by the fact that the material has some initial curvature, the material is nonlinear, and the material is stretched over the pin rather than being in pure bending. These three issues mean the neutral axis and minimum bend radius are not easily calculated, but we present a simple, albeit oversimplified, analysis that indicates that the minimum bend radius and thus pin size is an important consideration in the testing of ring pull samples.

In this work, we propose several equations for correcting ring pull test properties to uniaxial properties (Eqs. 14A-14C), which show the unaccounted for error from this geometric correction to be from 3% to 9%. Our data show that the small-strain modulus is the most affected property across the range tested (Fig. 14A). We also note that the corrections are most significant when H/R_c is large (Fig. 14A-C). In the cases of the aorta in pig, sheep, and mouse, the corrected properties are very similar to the uncorrected because we are operating in the range of $H/R_c = 0.15 - 0.25$ (Fig. 13). We also show that the overall error in small-strain modulus becomes nearly the same across pin sizes for each tissues tested. This indicates that we have mitigated the error due to these geometric effects, but we are still left with some unaccounted-for error. This error could be due to the material properties, especially the nonlinearity, or due to other factors such as residual stresses. In the correction for the sheep carotid, where $H/R_c = 0.50$, significant improvements are made in matching the uniaxial properties for all extracted parameters. Thus, for thick-walled structures like the ventricle or small arteries, one should use such corrections to attain quantitatively correct properties. In addition, we proposed the use of mean properties assessed in this way to determine a corrected failure stress. We have shown that for a pin of large enough size, one can expect failure to initiate from the midplane region of the ring. Thus, one can estimate the strain at failure on the inner surface and use this strain to give a corrected failure stress from the average material properties.

The most relevant and similar work to this is that of van Haaften et al. [37] for ring tests on linear, isotropic materials. Their proposed correction was validated for small strains (<5%), but they did not address transition strain or lockout modulus. They propose using the exterior ring surface stretch as it becomes linear in strain for tests on linear materials once the ring transitions from the initial bending to the stretch dominated deformation. However, almost all biological soft tissues do not abide by this principle since they are nonlinear and anisotropic. In fact, even the validation tissue used for the experiments of van Haaften et al. are nonlinear. Comparing our data

to those of van Haaften et al., we see that our small-strain and large-strain modulus corrections bookend their proposed correction (Fig. 16). Additionally, the effect of material nonlinearity is quite pronounced, especially for thick-walled tissues where our correction diverges from van Haaften et al.

Finally, we emphasize that this work is designed for arterial samples which have broadly similar behavior to one another. If we attempt to apply this relation to samples that are much stiffer or much more compliant we may expect the relation for correction to change with respect to thickness (i.e. a more compliant material is less affected by the bending than a stiffer material would be especially in thicker rings). However, the trends will remain the same in that as the tissue thickness increases we will observe reduced small-strain modulus and increased large strain modulus. Additionally, this work probes only the passive mechanical behavior of soft biological tissues. We believe that active contractile assays will have similar corrections necessary for ring shaped samples. However, such a study is beyond the scope of this work.

Conclusions:

In this work, we have shown that the uniaxial approximation is only valid in a narrow range of ring geometries. In general, one *does not* need corrections if the sample falls within the range of $H/R_c = 0.15 - 0.3$. However, attention should be paid to the selection of pin size in the range of $H/a = 0.5 - 2.0$ if one intends to investigate failure properties. In these cases, H/a should be near 0.5 because the smaller this value is, the less stress concentrates near the pin. In the limit of $H/R_c \rightarrow 0$, we should note that minimal correction is needed provided that the pin size is in the range of $H/a = 0.25 - 1.0$. In the other limit as $H/R_c \rightarrow 0.5$, correction is necessary regardless of the choice of pin radius. However, we again need to be cognizant of the stress concentration from small pins. In this case, one should minimize H/a subject to the constraints of using circular or D-shaped pins. The correction equations are only valid in the range of $H/R_c = 0 - 0.5$ and $H/a = 0.25 - 3$. As one attempts to extrapolate this phenomenological correction, one should be aware that the

correction may diverge. It is much safer to simply take the value at the extrema in the validated range. It should be emphasized that our proposed correction is for soft collagenous biological tissues that exhibit a bilinear mechanical response to load, and that this correction framework remains valid only under this condition.

Included as a supplement to this work is a MATLAB script designed to take as inputs the sample geometry (radius, thickness, width), pin radius, and force-displacement data. Using these data, the script calculates the centerline strain vs. PK1 stress, fits the small-strain modulus, large-strain modulus, and transition strain, and calculates the luminal strain vs luminal PK1 stress for the assessment of failure properties.

Acknowledgments:

The authors acknowledge funding from the National Science Foundation Graduate Research Fellowship Program (NSF GRFP) under Grant No. 00039202. The authors also acknowledge funding from the National Institutes of Health under Grant No. U01-HL139471. The authors acknowledge and thank the University Imaging Center (UIC) at the University of Minnesota for the use of the small animal ultrasound system, Dr. Paul A. Iaizzo and the Visible Heart Lab for the porcine and ovine tissue used in this study, and Dr. Paulo P. Provenzano and the Provenzano Research Group for the mice used in this study. The authors also thank Drs. Neeta Adhikari and Jennifer L. Hall for their technical advice on dissection and ring testing of mouse tissues, Shannen Kizilski for her assistance in design and fabrication of the ring pull apparatus, and Elizabeth Gacek for her technical assistance in setting up contact in the ring pull simulations.

Tables:

Table 1. Tissues used in ring pull tests including species, nominal stretch range for tests, and sample geometry. Isometric contraction is entered as Iso under "Nominal Stretch".

Tissue	**Species**	**Nominal Stretch**	**a [mm]**	**R_o [mm]**	**R_i [mm]**	**R_c [mm]**	**H [mm]**	**H/R_c**	**H/a**	**Refs.**
Desc. Thoracic Aorta	Murine	1.50	0.35	0.41	0.37	0.39	0.04	0.10	0.11	[123, 124]
Abdominal Aorta	Murine	1.50	0.12	0.32	0.28	0.30	0.04	0.13	0.31	[123, 124]
Thoracic Aorta	Murine	2.0-3.0	0.50	0.37	0.31	0.34	0.06	0.18	0.12	[125]
Neonatal Left Ventricle	Murine	Iso.	0.22	2.17	1.10	1.64	1.07	0.65	4.86	[126]
Cervix	Murine	1.15-6.45	0.40	2.00	1.55	1.78	0.45	0.25	1.13	[127]
Colon	Human	1.30	4.76	18.70	17.20	17.95	1.50	0.08	0.32	[128]
Iris	Bovine	1.18-1.44	<5	16.00	10.00	13.00	6.00	0.46	>1.20	[129]
Lens Capsule	Porcine	1.8	0.74	1.60	1.50	1.55	0.10	0.06	0.14	[130]
Tissue Engineered Construct	-	1.18	0.50	3.20	1.96	2.58	1.24	0.48	2.48	[131]
Tissue Engineered Construct	-	1.15	-	4.00	3.70	3.85	0.30	0.08	-	[132]

Table 2. Parameters fit to the nondimensionalized geometric quantities and the associated 95% confidence intervals of the parameter along with the RMSE for the fit. The other coefficient values were zero and are therefore not included.

Correction	k_{00}	k_{10}	k_{01}	k_{02}	k_{21}	k_{12}	***RMSE***
$E_{ss}^{Ring}/E_{ss}^{Uni}$	1	0	0	-0.042 ±0.005	-1.552 ±0.168	0.214 ±0.027	0.050
$E_{LS}^{Ring}/E_{LS}^{Uni}$	1	0	0	0.094 ±0.046	2.359 ±0.571	-0.627 ±0.203	0.092
$\varepsilon_{t}^{Ring}/\varepsilon_{t}^{Uni}$	1	0.358 ±0.071	-0.054 ±0.013	0	0	0	0.028

Figures:

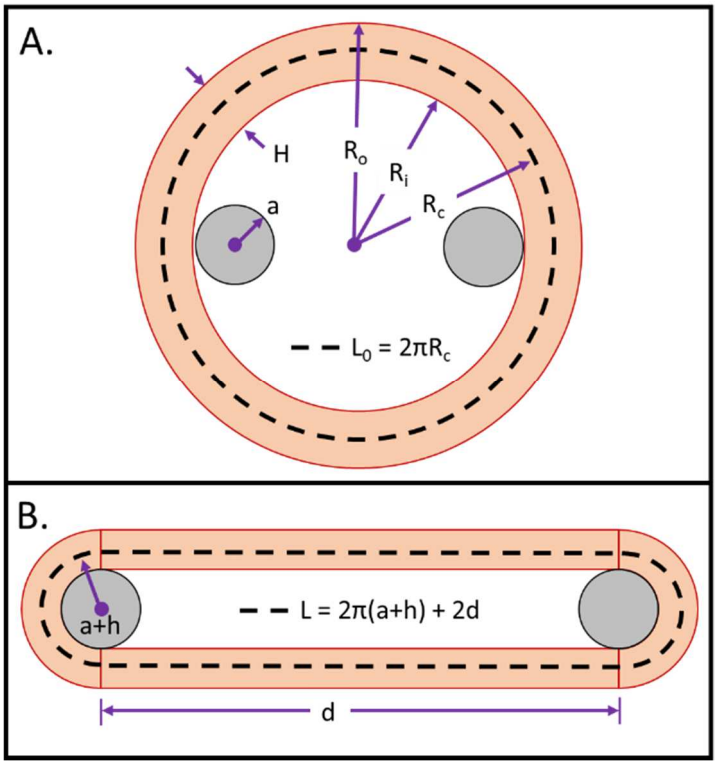

Figure 6. A. Undeformed geometry for the ring pull test where R_c is the centerline radius, R_i is the luminal surface radius, R_o is the outer surface radius, H is the tissue thickness, a is the pin radius, and L_0 is the centerline length. B. Deformed geometry

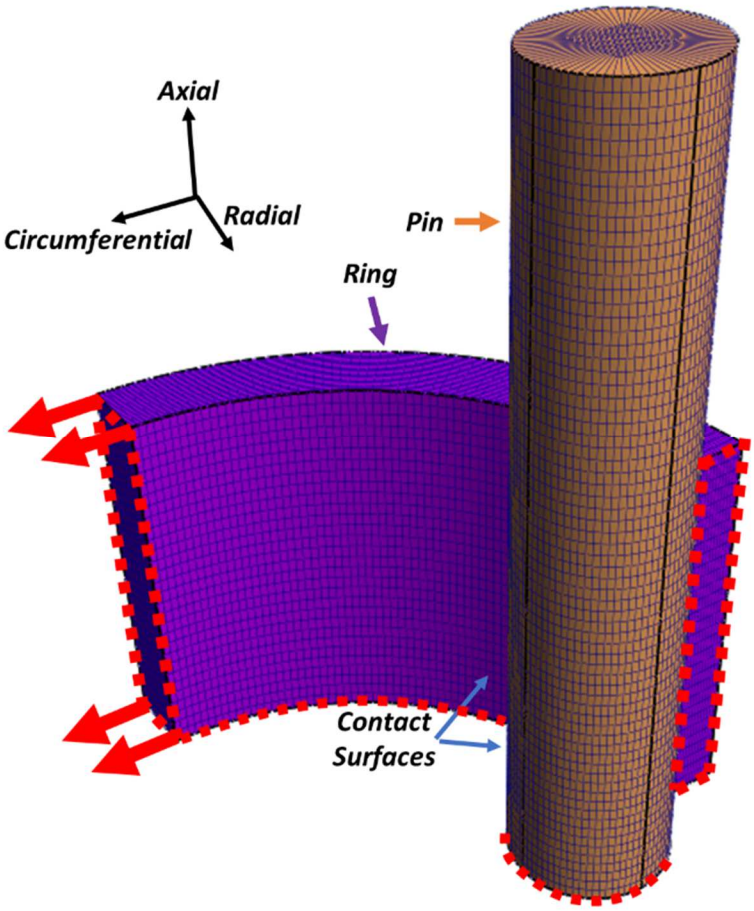

Figure 7. Ring model used for simulations. The ring is shown in purple and the pin in orange. The contact surfaces are indicated by blue arrows. The symmetry planes are shown as red dashed lines. The red arrows show the direction the ring sample is pulled.

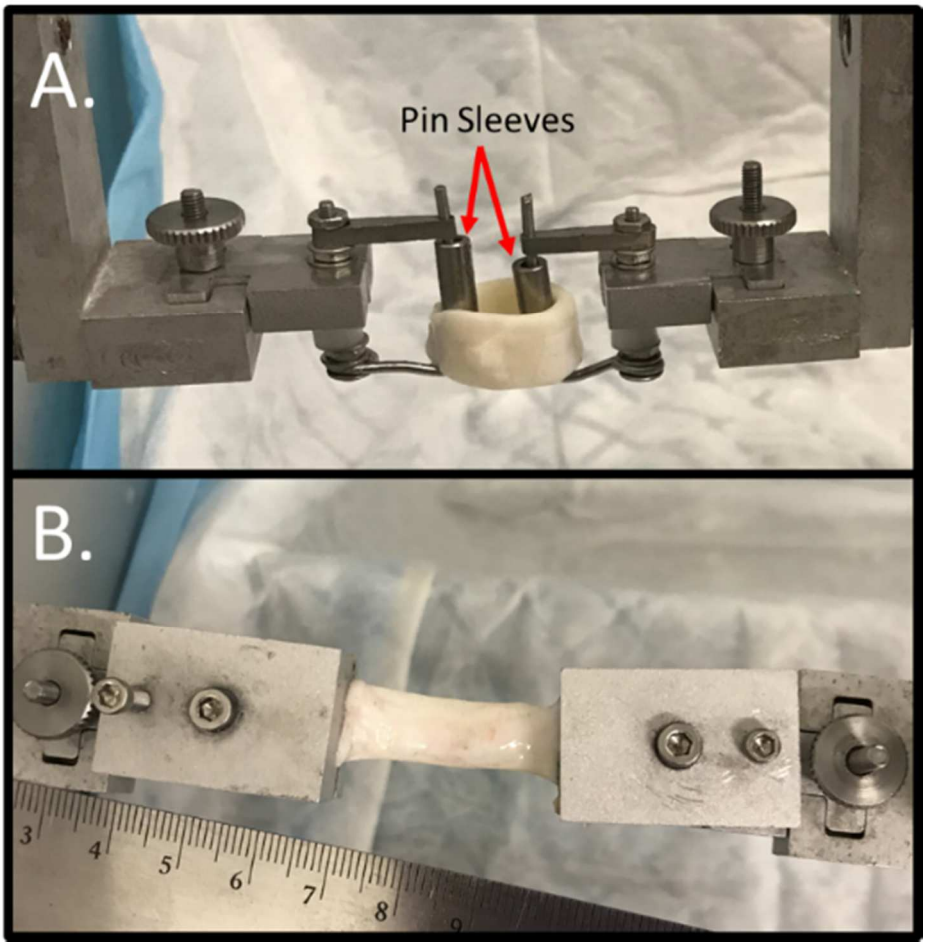

Figure 8. A. Uniaxial ring-pull apparatus showing removable pin sleeves and tissue sample, B. Uniaxial pull apparatus for opened, flattened ring tissue strip.

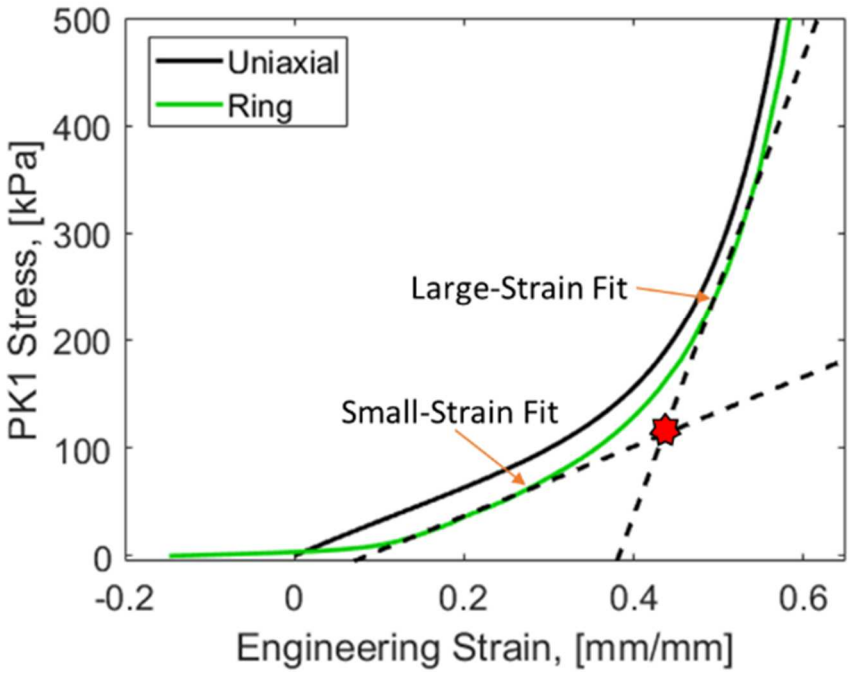

Figure 9. Fit of the small-strain and large-strain modulus (dashed lines) along with the transition strain (red star) for a ring test.

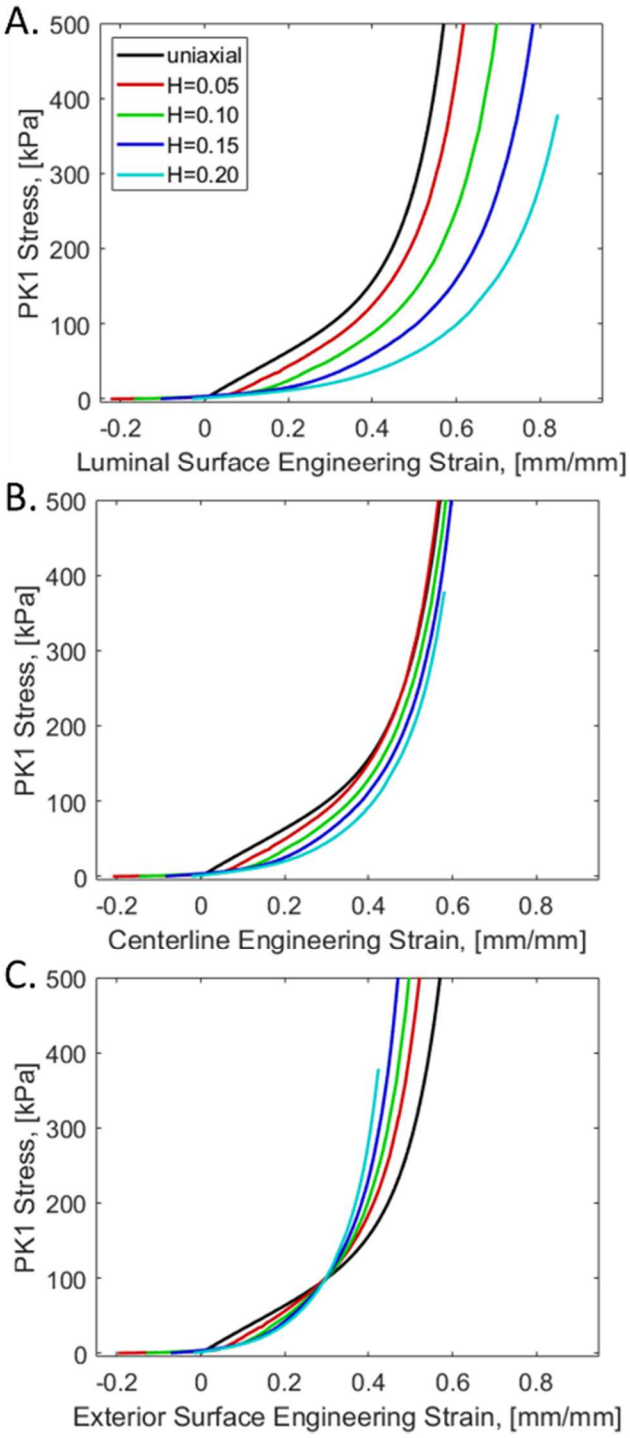

Figure 10. First Piola-Kirchoff stress vs engineering strain curves for uniaxial and ring pull simulations demonstrating the difference between using A. luminal (inner) surface strain, B. centerline strain, and C. exterior (outer) surface strain values for ring

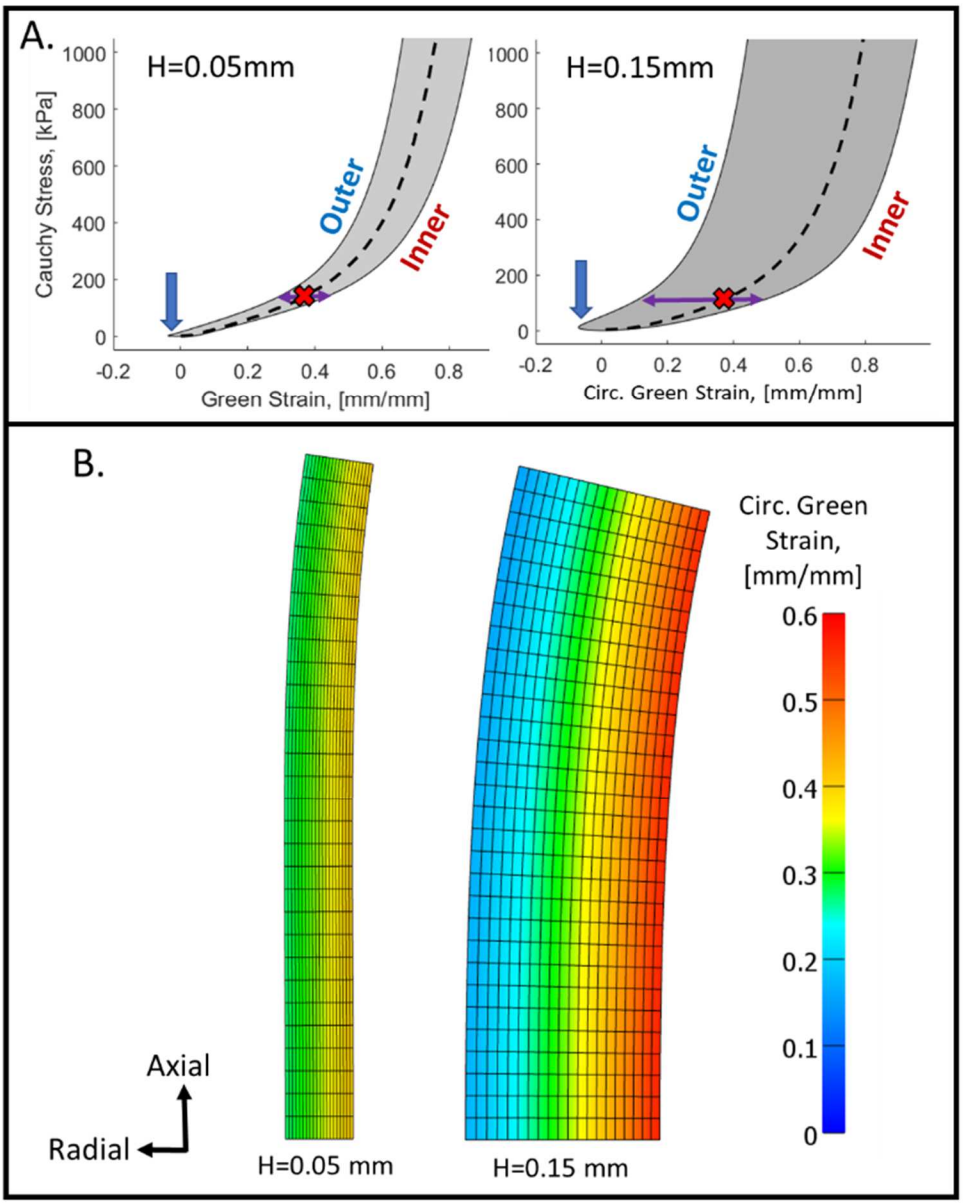

Figure 11. A. Cauchy stress vs Green strain plots for thin (H=0.05mm) and thick (H=0.15mm) ring tests. The shaded area represents the limits of strain at the inner and outer surfaces of the tissue with respect to stress. The dashed line represents the calculated centerline stress-strain curve. shown The red X's in the stress-strain plots show the position of B on the stress-strain curve. The blue arrows show the outer compression. The strain range across the sample at B is represented by the horizontal purple arrow. B. A visualization of the strain across the midplane of thin and thick rings at a nominal Green strain of E_{circ} of 0.35.

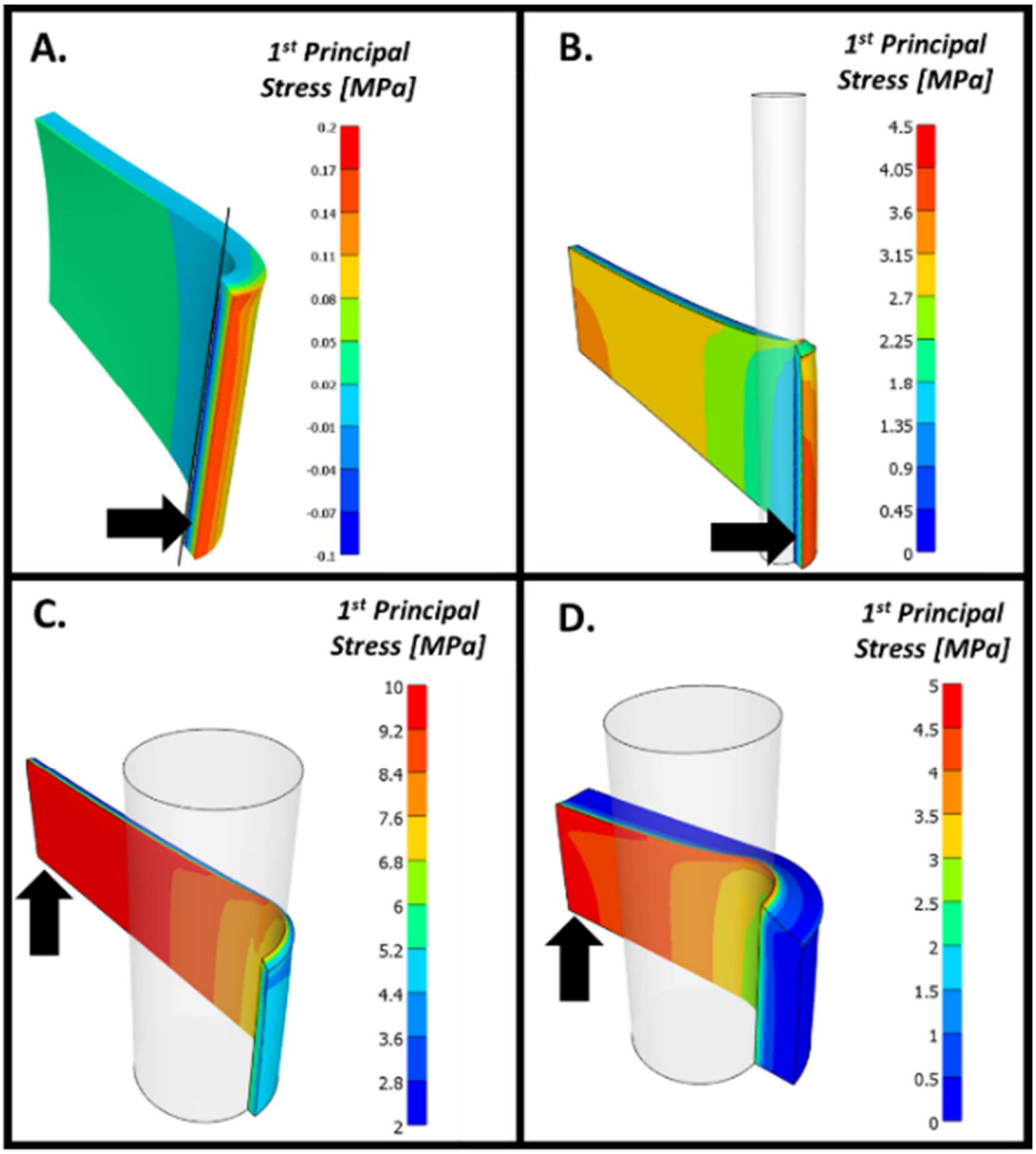

Figure 12. A comparison of the stress concentrations for different pin sizes and wall thicknesses. A. Ring with thickness $H = 0.10\ mm$ and pin size $a \to 0$ (i.e. the nodes on the symmetry plane on the luminal side are fixed in the direction of the pulling force). B. Ring with thickness $H = 0.05\ mm$ and pin size $a = 0.05\ mm$. C. Ring with thickness $H = 0.05\ mm$ and pin size $a = 0.20\ mm$. D. Ring with thickness $H = 0.20\ mm$ and pin size $a = 0.20\ mm$. All rings have centerline radius $R_c = 0.6\ mm$. The black arrows show the area of stress concentration.

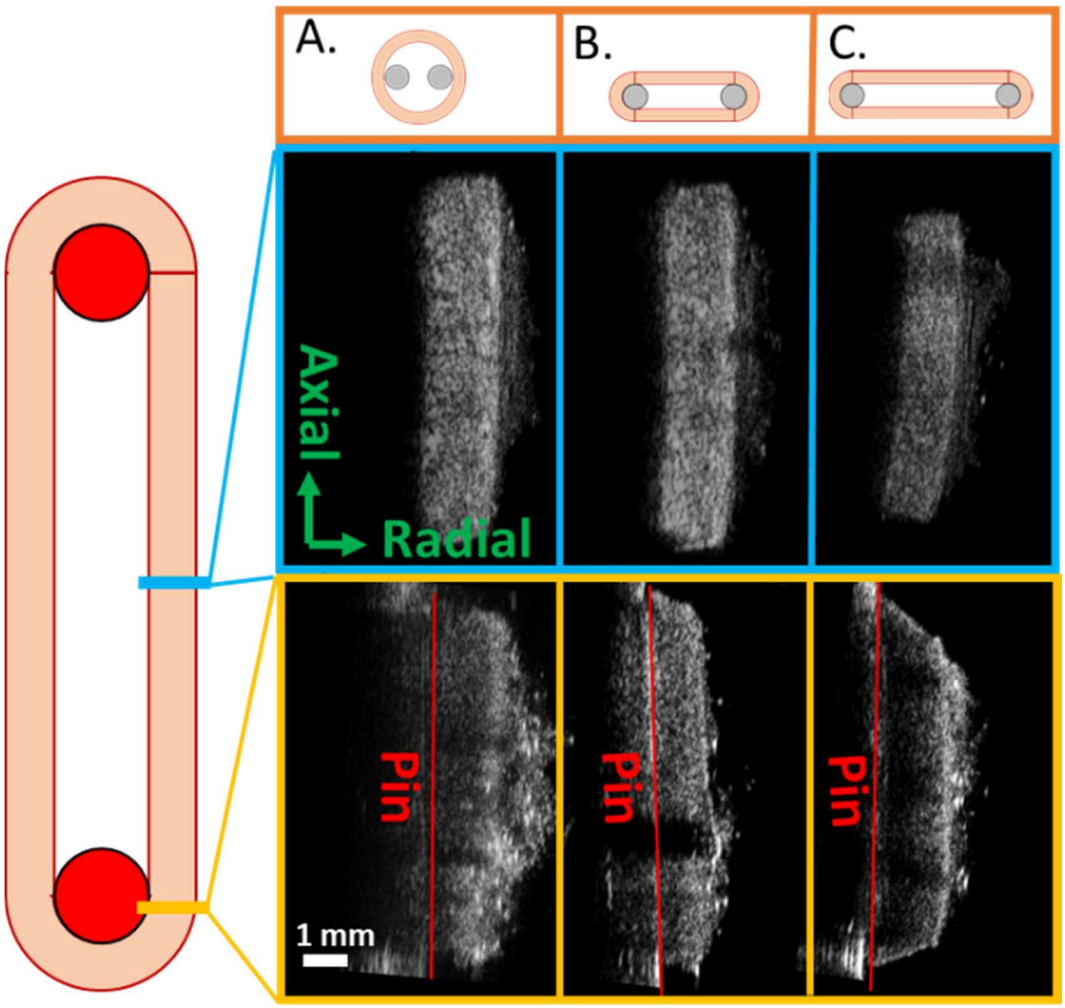

Figure 13. Ultrasound images of porcine abdominal aortic ring cross sections in the center (belly) region (blue) and at the pin (yellow) for A. undeformed ring, B. flattened ring (unstretched centerline) C. stretched ring ($\lambda_{circ} \approx 1.33$). The red line indicates the position of the pin edge along the tissue sample.

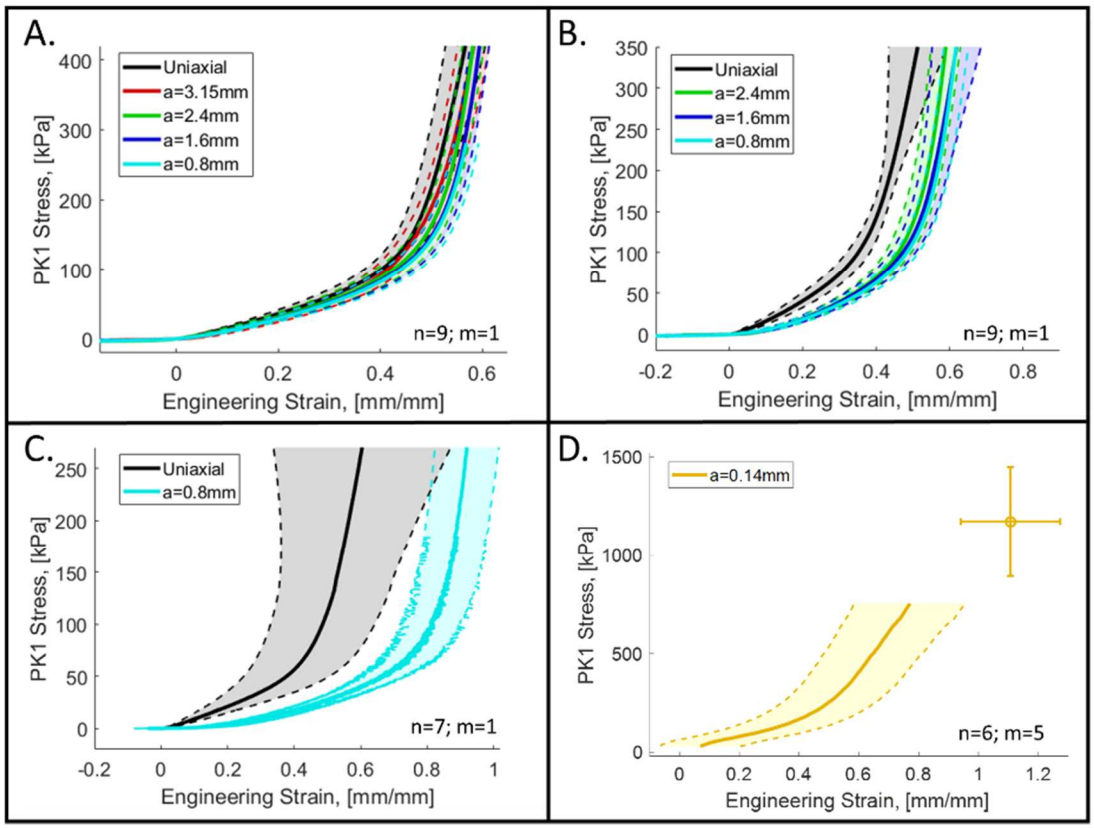

Figure 14. Experimental first Piola-Kirchoff stress vs. engineering strain plots with mean (solid lines), the upper and lower 95% confidence intervals (dashed lines) for uniaxial and ring pull tests with varied pin diameters for A. Porcine abdominal aorta with R_c = 6.84±0.23 mm and H = 1.51±0.24 mm, B. Ovine abdominal aorta with R_c = 5.69±0.28 mm and H = 1.37±0.16 mm, C. Ovine external carotid artery with R_c = 2.21±0.25 mm and H = 1.11±0.39 mm, and D. Mouse thoracic aorta with R_c = 0.450±0.050 mm and H = 0.072±0.012 mm. The final point is the average stress and strain at failure. All values are mean ± 95% CI. The value n is the number of ring samples per animal, and m is the number of animals used.

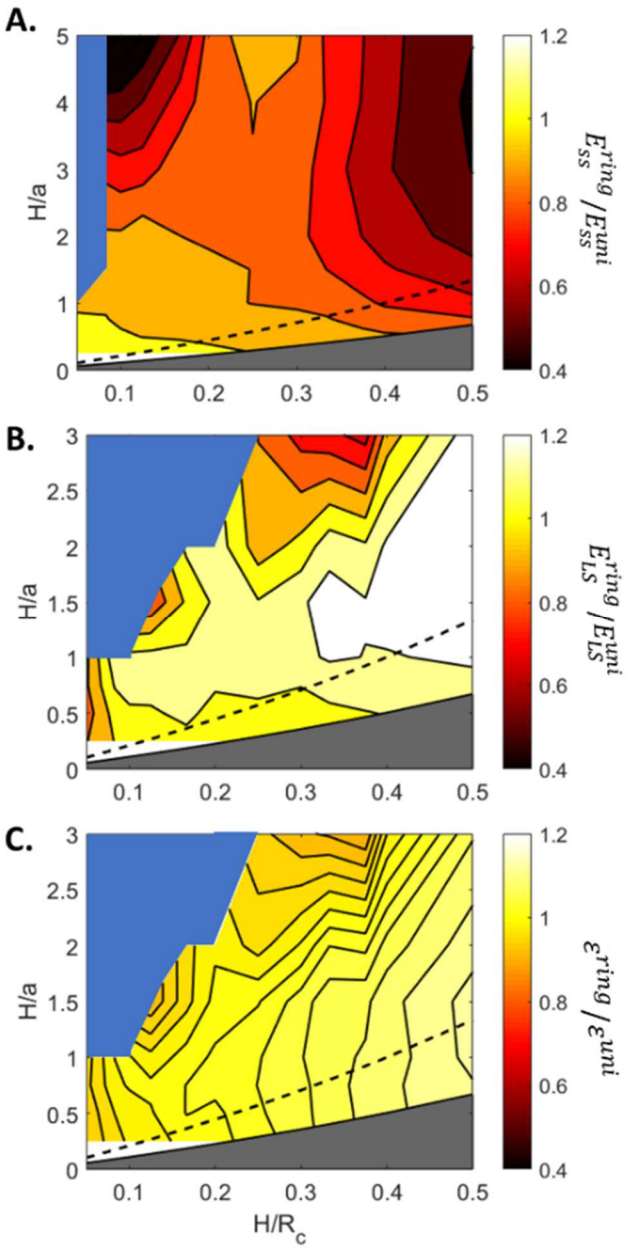

Figure 15. Ratios of the material properties assessed from rings to those assed from uniaxial for A. small strain (toe) region modulus, B. large strain (lockout) modulus, and C. transition strain from small strain regime to large strain regime. The dashed line represents the functional limit for fitting two pins in the ring lumen. The grey area represents the fundamental limit of fitting two D-shaped pins (of radius $R_c - \frac{1}{2}H$) in the lumen. Data was not obtained in the blue regions due to non-convergence of the contact solution for very small pins.

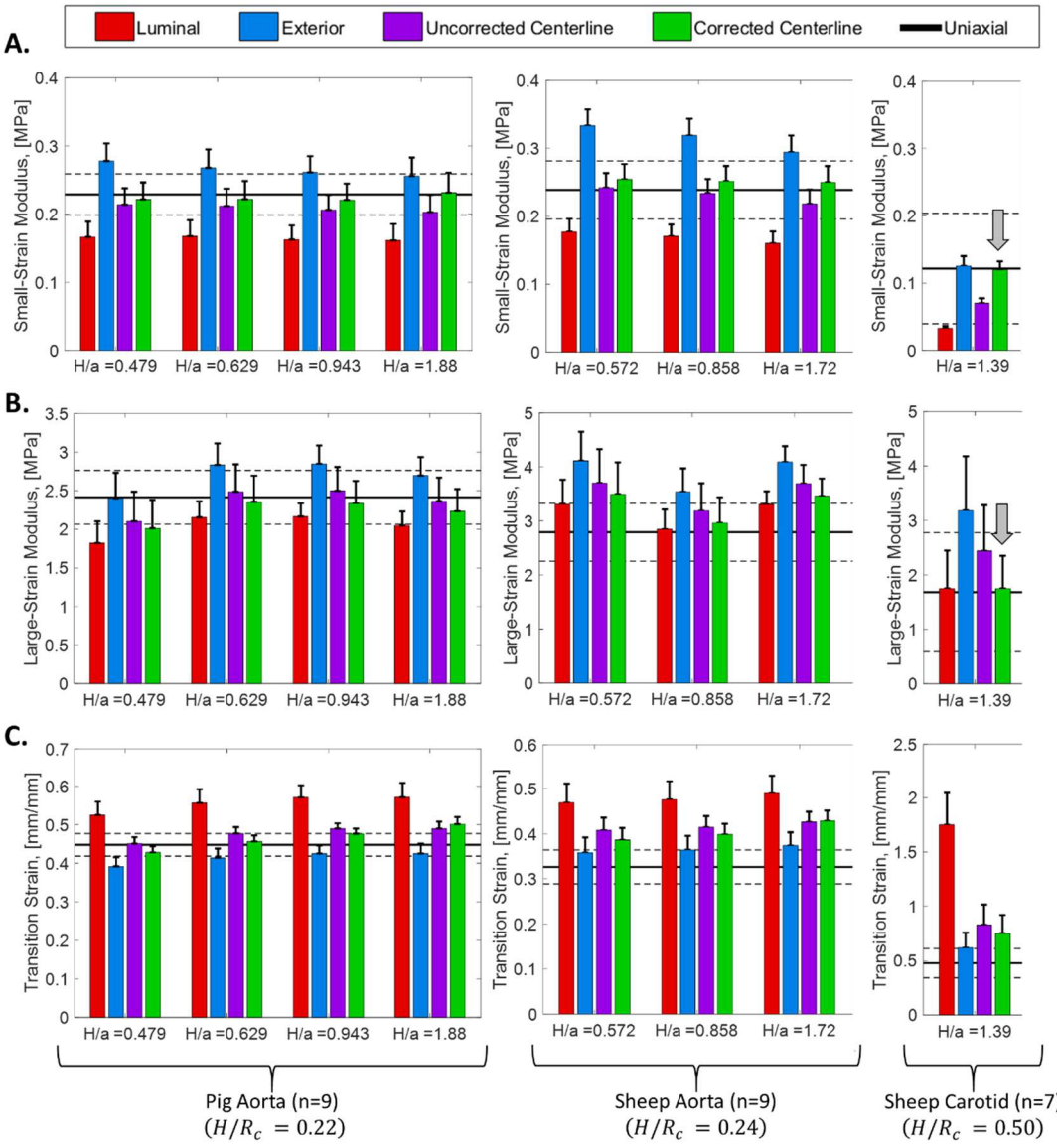

Figure 16. Experimental data for A. Small-strain modulus, B. Large-strain modulus, C. Transition engineering strain estimated from uniaxial (black dashed lines) and ring pull tests using luminal surface stretch (red bars), exterior surface stretch (blue bars), uncorrected centerline stretch (purple bars), and corrected centerline stretch (green bars). Dashed lines and error bars are the 95% confidence interval of the mean. Error bars on the corrected values are the centerline estimate error bars scaled by the correction factor.

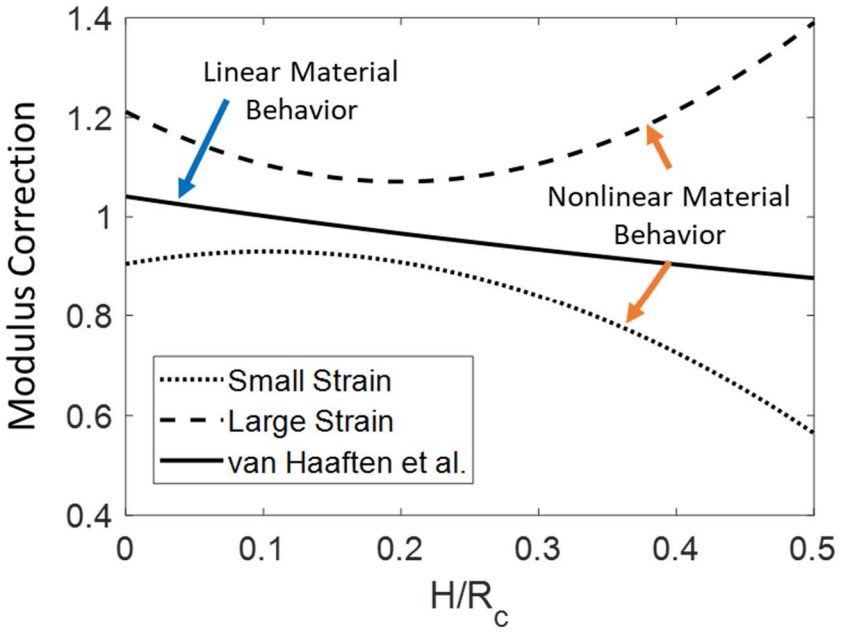

Figure 17. Comparison of the correction for small and large strain proposed in this work compared to that proposed in [37] for $H/a = 1.5$.

CHAPTER 4: ARTERIAL INFLATION TESTING

4.1: SHEEP INNOMINATE ARTERY BIFURCATION INFLATION UNDER ULTRASOUND

Summary:

The arterial tree is a complex geometric structure with many branching vessels. Bifurcations, in particular, tend to be the location for disease formation including atherosclerotic plaques, aneurysm, and, in severe cases, dissection. Thus, it is important to understand how the material properties and the geometry of bifurcations lends itself to disease triggering events. To try to decouple these geometric and material effects, we propose a new test method utilizing inflation of sheep brachiocephalic (innominate) artery bifurcations under ultrasound to visualize precise material responses. Our custom testbed allowed visualization of through-thickness response allowing us to capture the upstream and downstream vessel mechanics of the bifurcation, as well as many novel insights into the behavior of bifurcation region itself. We showed a unique response of the aspect ratio of the bifurcation, changes in wall thickness around the bifurcation, and an assessment of strains within the bifurcation region itself. This test method offers a new technique for assessing complex geometries in a full-field way without the assumption of incompressibility. It gives, not only the same analysis of cylindrical structures in the upstream and downstream regions, but also the ability to assess the bifurcation region itself. Further, this technique could also be used to assess failure properties under burst pressure or complex loadings such as vessel torsion, which could prove insightful in understanding the formation of dissections near bifurcating vessels.

Introduction

The arterial tree is a complex network containing many arterial branches (Fig. 17). The arterial wall is composed of the endothelium, smooth muscle, and elastin and collagen fibers [117]. The components of the layers each contribute to the mechanical properties of the artery, and the interaction of those components, like the arterial structure itself, becomes more complex when the vessel geometry deviates from cylindrical. An example of such an irregular geometry is a bifurcation. The bifurcation's structural and mechanical properties are different from and more complex than those of a straight artery. Particularly, the right common carotid/ right subclavian bifurcation's complex geometry makes it a location for atherosclerotic plaque buildup due to the differences in flow, turbulence, and shear stress [133]. Further, two uncommon, but potentially significant pathologies are innominate artery aneurysm and carotid artery dissection, which tend to happen near bifurcation points [134, 135]. Therefore, the bifurcation is an important area of interest in the study of arterial mechanics. Bifurcations are, however, difficult to study experimentally because the complex architecture and geometry do not lend themselves to standard mechanical testing protocols. Planar biaxial testing is problematic because a planar section of the tissue is difficult to isolate and because properties vary with position within the sample. Inflation is a relatively simple experiment, but it is difficult to analyze the inflation of a bifurcation because the convenience of radial symmetry is lost.

In this work, we develop a test system for inflation of an arterial bifurcation with simultaneous ultrasound scanning, which can then be used to construct 3-D reconstructions of the bifurcating vessel at controlled internal pressures. This system has several advantages over traditional testing methods in that it allows for assessment in a physiologic loading scenario and with through-thickness imaging of both large and complex samples. The advantages of this system are summarized in Table 3.

Table 3. Advantages of Inflation using Ultrasound

Testing Method	*Shape*	*Easy Visualization*	*Physiologic Loading*	*Non-Destructive*	*Wall Thickness*	*Large Samples*	*Interior/Exterior Differences*	*Complex Geometries*
Ring Pull Tests				x	x		x	
Planar (Uniaxial or Biaxial)					x		x	
Optical Inflation		x	x	x		x		x
Ultrasound Inflation		x	x	x	x	x	x	x

Methods:

Sample Preparation:

Ovine carotid artery bifurcations were obtained in accordance with the guidelines outlined by NIH and the University of Minnesota Institutional Animal Care and Use Committee (IACUC). Five samples were obtained from both male and female sheep. Table 1 shows the sample population demographics. The ovine model was chosen because it is a common model for cardiac intervention development. The sample statistics are given in Table 4.

Table 4. Ovine Sample Statistics

Sample	*Gender*	*Mass (kg)*	*Age (mo.)*
1	M (C)	50	8
2	M (C)	44	8
3	F	70	21
4	F	46	6.5
5	F	48	6.5
6	F	66	66

**(C) represents a castrated male*

The samples were cleaned to remove as much of the surrounding connective tissue as possible. The two daughter branches of the sample were cut so that the total length of the sample was approximately 5 cm, ensuring that the sample would fit in the inflation device. The sample was attached to male Luer fittings with suture. The sample was flushed with PBS to ensure there were no clots. One of the daughter branches of the sample was capped to prevent flow out allowing pressurization of the system. The sample was then placed in the artery inflation device

utilizing the attached Luers to connect into a closed fluid system (Fig. 18). The inflation device was submerged in a fluid bath. The system had a bleed-off valve to release any trapped air, a non-torqueing connector, and a pressure monitor. The bath was filled with phosphate-buffered saline (PBS) solution to a level at least 1 cm higher than the artery.

Testing Protocol:

Using a syringe, the system was filled with PBS, the bleed-off valve was closed, and the pressure monitor was zeroed. The sample was stretched to 1.25x its original length prior to inflation to simulate its in vivo length [136]. A 38 MHz ultrasound probe on a VisualSonics Vevo 2100 small animal ultrasound system (FUJIFILM VisualSonics, Inc., Toronto, ON, CA) attached to a track allowed image slices to be obtained under constant motion along the long axis of the sample. The ultrasound probe was placed in the PBS in a position capturing a cross-sectional image of the sample (Fig. 19). Rubber was placed below the sample to reduce echoing off the tank bottom. The probe and imaging software were adjusted until a clear ultrasound image was obtained. The sample was preconditioned by inflating the system with isotonic PBS for 10 cycles from 0 to 100 mmHg internal pressure. The pressure was then increased from 0 to 300 mmHg in increments of 20mmHg capturing cross-sectional ultrasound image stacks along the length of the sample at each pressure.

Data Analysis:

One representative sample was reconstructed from the image stack using Seg3D [137] and analysis was performed long the entire length. For other samples four representative cross-sectional slices were chosen at each pressure step for the mother vessel prior to the bifurcation, the connected region immediately before the bifurcation, the bifurcation region immediately after the bifurcation split, and the daughter vessel (on the stretched side). The images were analyzed using MATLAB R2016A (Mathworks, Inc., Natick, MA). The measurements obtained were the

major and minor axis lengths, the inner and outer diameters, and the inner and outer perimeter. We also estimate the stress-stretch behavior of several regions using the Law of Laplace equation

$$\sigma_{\theta\theta} = P\frac{d}{2t} \qquad \text{Eq. 1}$$

where $\sigma_{\theta\theta}$ is the circumferential stress, P is the transmural pressure, d is the vessel diameter, and t is the vessel wall thickness.

Results:

An example 3-D reconstruction of an undeformed bifurcation including the four representative cross-sectional ultrasound images is displayed in Fig. 19. The reconstruction moves from the mother (proximal) to the daughter (distal) end of the vessel (left to right). The measured cross-sectional luminal perimeter along the length of the bifurcation going from the daughter to the mother end (left to right) at various pressures is displayed in Fig. 20. The daughter section's perimeter increases fairly linearly moving towards the bifurcation from 0 to ~13mm. The bifurcation section's perimeter remains relatively constant from ~13mm to ~18mm, due to the inner septum maintaining the cross-section shape. In the connected section, there is a spike in perimeter at ~19mm, immediately after the bifurcation septum, which then decreases as the vessel approaches the mother branch from ~19mm to ~21mm. The mother section's perimeter remains relatively constant until the end of the sample from ~22mm to ~32mm. The mean normalized wall thickness for each region is shown in Fig. 21. The daughter, bifurcation, and mother regions all show decreased wall thickness with pressure. However, the connected region shows relatively constant wall thickness regardless of increased pressure. The mean adventitial (outer) and luminal (inner) stretch as a function of pressure is given in Fig. 22. The plot shows the characteristic lockout behavior of the circumferential fibers (i.e. the flattening in Figs. 22 or the sharp upturn in Fig. 24) which was observed to occur around 125-150 mmHg. The analyzed regions showed the bifurcation region was the stiffest and the mother region the most compliant, however, the data shows relatively little difference from one another. To further analyze what was happening in the

connected region, we analyzed the aspect ratio (major diameter/minor diameter) of the cross section with respect to pressure (Fig. 23). The aspect ratio of the adventitial side of the connected region shows relatively small decreases in aspect ratio with pressure, maintaining the same relatively elliptical shape (Fig. 23, green). The aspect ratio of the luminal sides of the connected region, however, shows large changes with pressure decreasing from very elliptical to relatively circular (Fig. 23, purple). We further estimated the stress-stretch behavior of the vessel using the Law of Laplace (Fig. 24). We should emphasize that for the bifurcation region, this is an estimate of the outer wall stress, not the septum stress. We see that the mean behaviors are similar, with the mother region being slightly more compliant than the daughter or bifurcation region. Finally, we wish to validate our system compared to systems that use straight sections of vessels. A comparison between our system and other published results [138–140] is given in Fig. 25. We should emphasize that each of Figs. 20-25 are mean behavior with the 95% confidence interval omitted since the regions were never statistically significantly different from one another. The data with plotted confidence intervals are supplied in Appendix B: Supplemental Material (Figs. 63-67).

While it is important that our device recapitulates the bulk behaviors that others have shown, we can also gather more insight because of the ultrasound system. The ultrasound produces a speckle pattern that can be tracked to give local deformation fields throughout the tissue. As an example, we show the 2D strain tracking of a representative bifurcated region (Fig. 26). We see that the inner septum has particularly large strains relative to other regions of the bifurcation. This ability is significant because other experimental techniques lack the ability to visualize such internal structures, which certainly play a significant role in the mechanics and the blood flow characteristics.

Discussion:

The bifurcation's complex geometry has been captured through a circumferential analysis along the long axis of the vessel at varying pressures. This analysis led to several conclusions about the mechanical properties and deformation pattern of the vessel under increasing pressure. The bifurcation section was observed to be the stiffest (Figs. 22 & 24), and the connected region immediately upstream was the most non-circular in cross-section (Fig. 23). However, as pressure increased it moved towards a more circular cross-section, particularly on the luminal side. The thickness of the connected section remained relatively unchanged, which would appear to be a result of the complex geometry as the two daughter vessels merge. The high stiffness and low thickness decrease of this section is likely due to its irregular shape and high fiber density as it is where the two daughter vessels come together. The daughter, mother, and bifurcation sections all had similar properties. This is due to their highly cylindrical nature of these sections, with relatively similar loading. We also showed that the bifurcation septum has large strains (Fig. 26). This is significant because it may well be the initiation point of aneurysm growth or the point of dissection initiation. It is important that we are able to study internal structures like this, which is why ultrasound makes an excellent tool in evaluating arterial mechanics.

In conclusion, we have demonstrated the ability to perform an inflation test on a bifurcating vessel while concurrently imaging the full vessel geometry with ultrasound. We have shown that the region around the bifurcation has complex mechanics, and in fact shows some non-intuitive behavior due to the complex geometry. This apparatus and the resulting combination of pressure and detailed volume imaging has the potential to provide a new level of understanding of bifurcation mechanics. Further, we can combine this apparatus with strain tracking of the ultrasound speckle patterns to visualize local inhomogeneities in the material.

Acknowledgments:

The author acknowledges the efforts of Christopher E. Korenczuk, Carl T. Schoephoester, David Nedrelow, and John P. Carruth who aided immensely in the experimental design and data processing for this work.

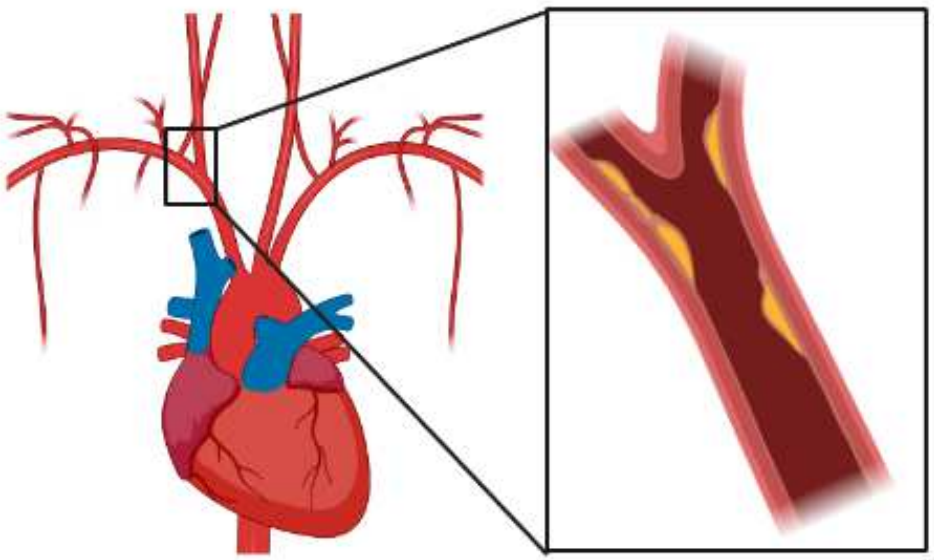

Figure 18. Arterial tree showing the right carotid/subclavian bifurcation. Created with bioRender.com.

Figure 19. Bifurcation test setup showing the sample mounting frame (left) and the full ultrasound setup (right).

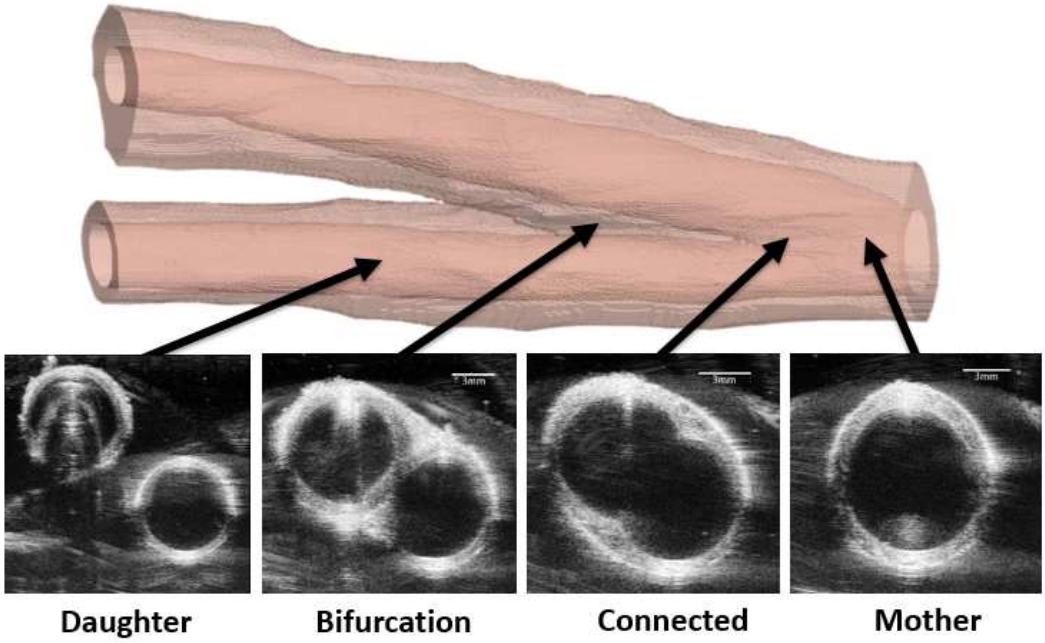

Figure 20. Reconstructed bifurcation with representative ultrasound images.

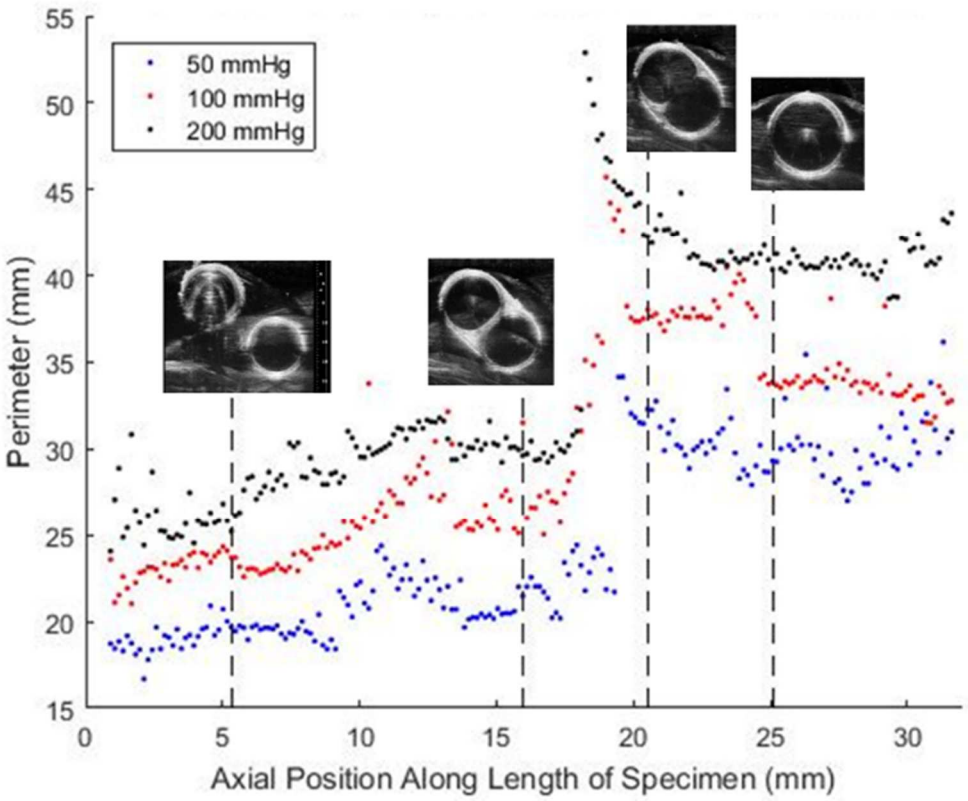

Figure 21. Calculated exterior perimeter along the vessel length at 50mmHg (blue), 100mmHg (red), and 200mmHg (black) pressure.

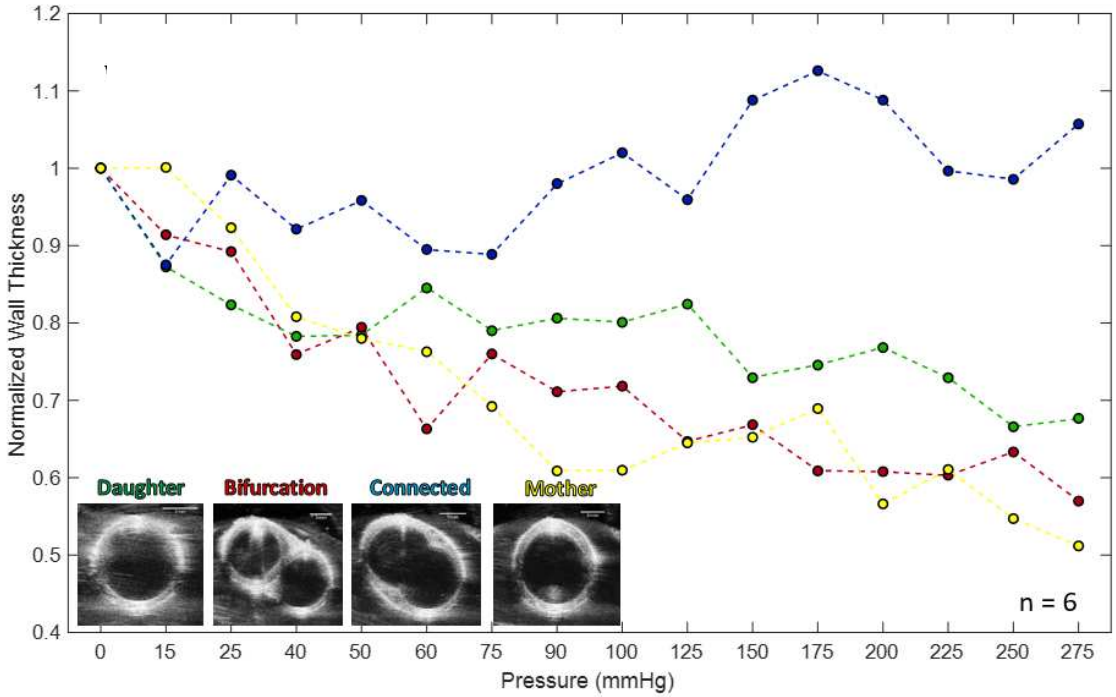

Figure 22. Normalized wall thickness for each sub-section of the vessel with respect to pressure.

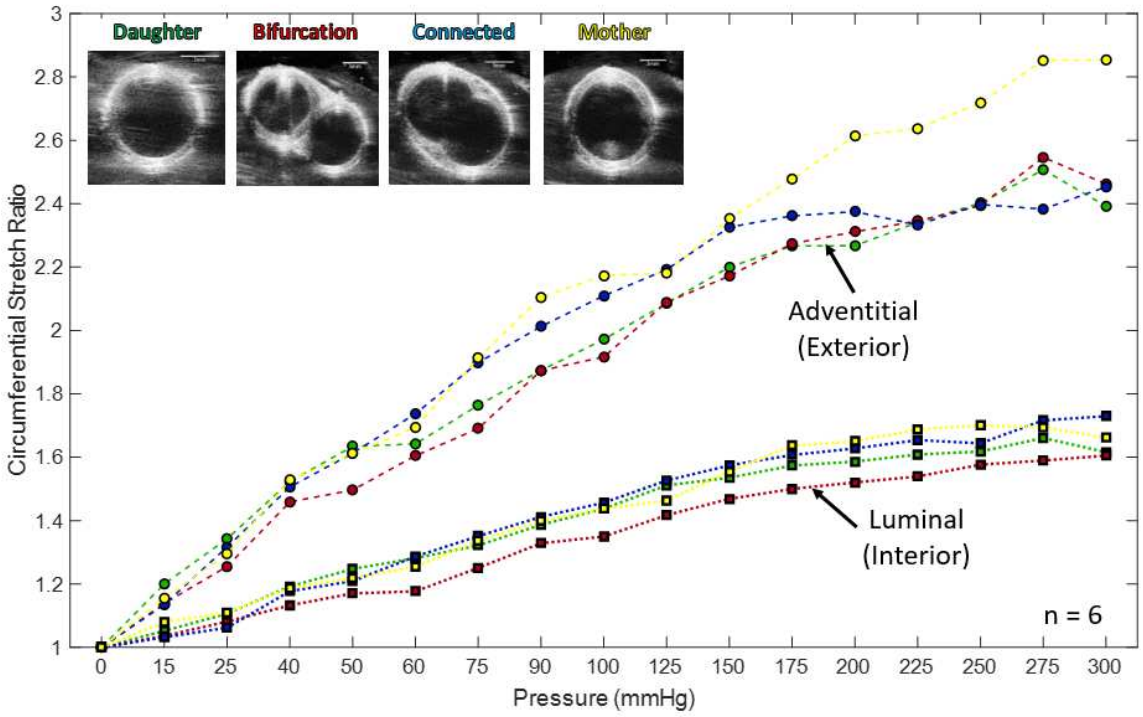

Figure 23. Adventitial and luminal stretch vs. pressure curves for each sub-section of the vessel.

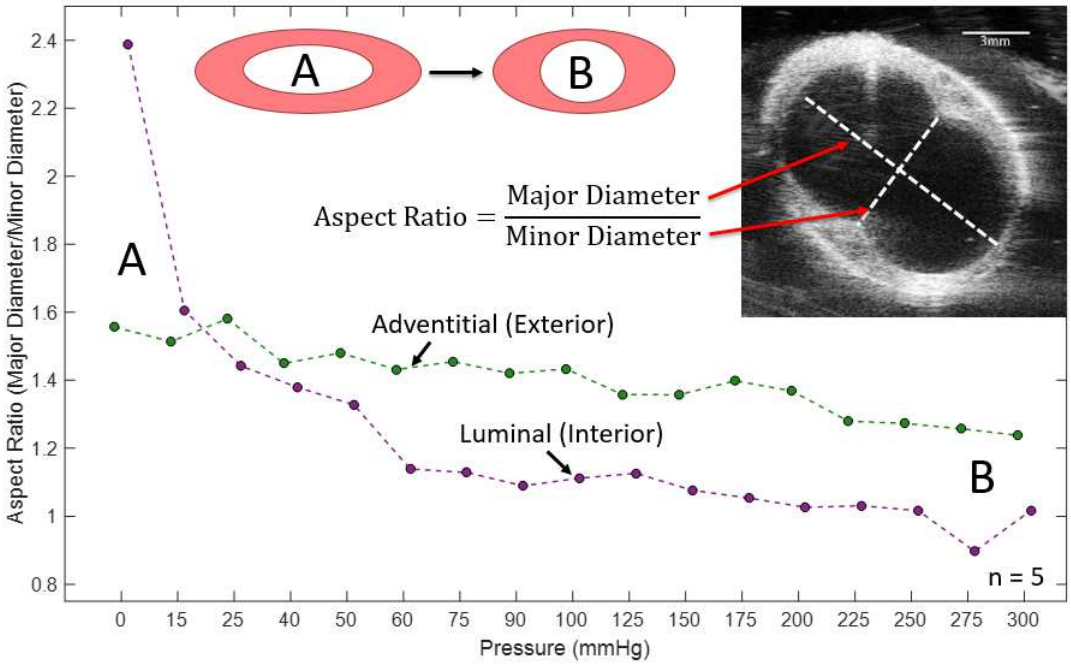

Figure 24. Aspect ratio vs. pressure in the connected region.

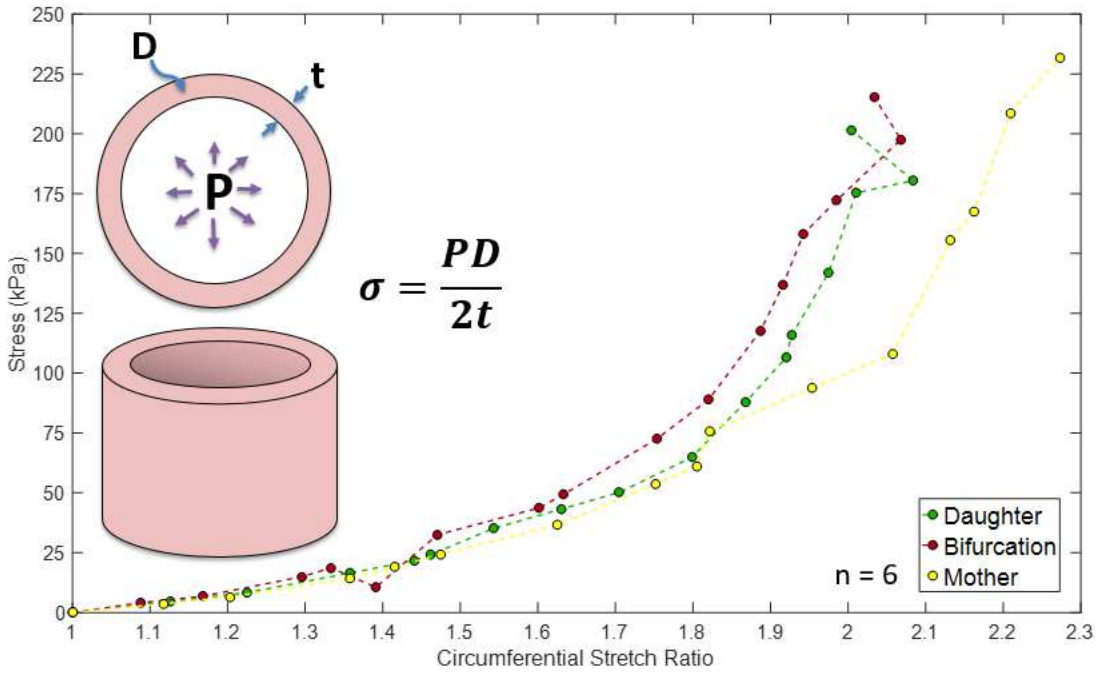

Figure 25. Law of Laplace estimates of stress vs. stretch for each sub-section of the vessel. Note: the estimate for the bifurcation region is for the exterior wall, not the center wall.

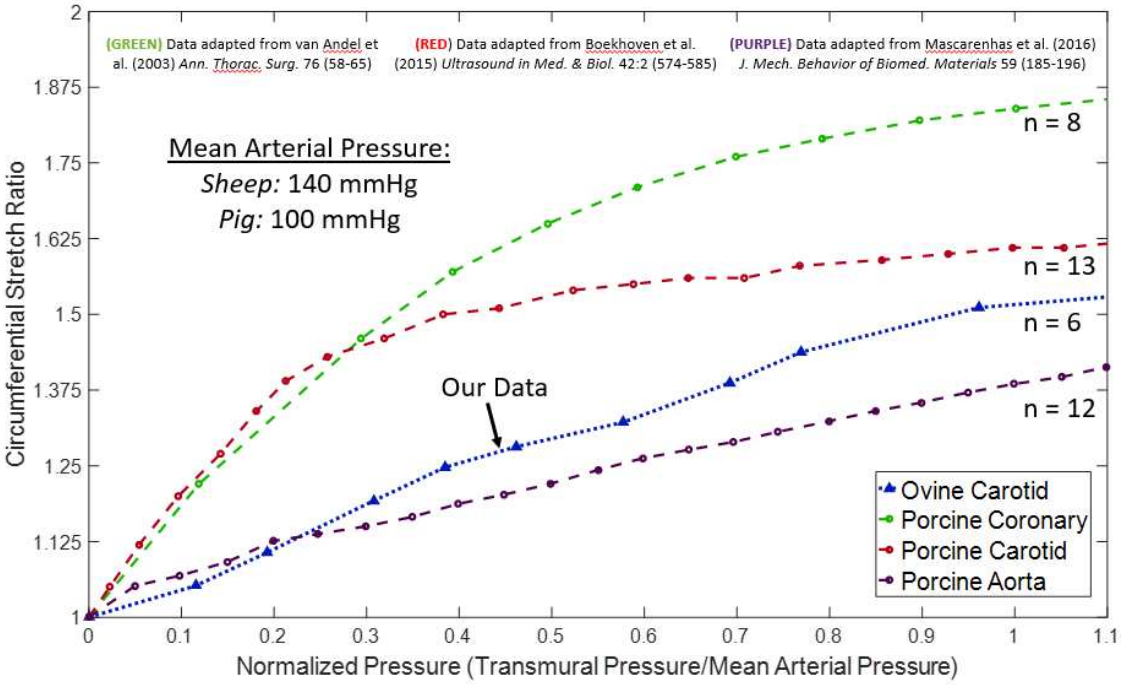

Figure 26. Pressure vs. circumferential stretch comparison for this test and other published tests.

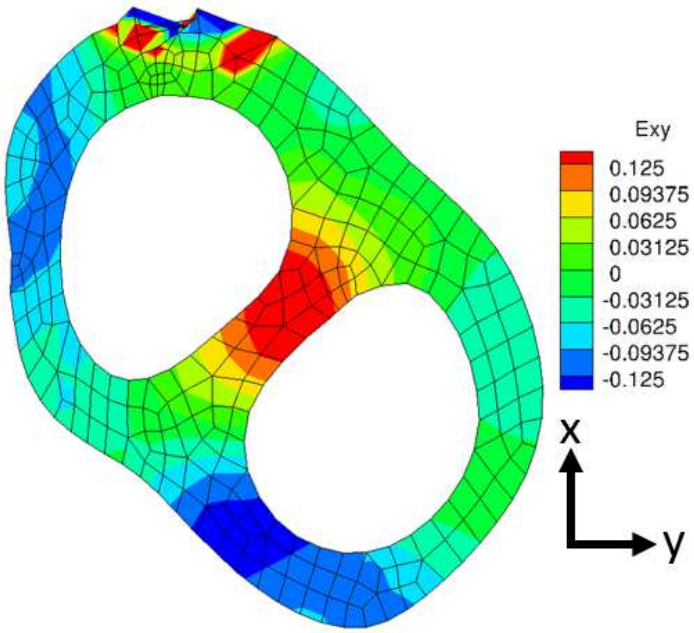

Figure 27. 2D ultrasound strain tracking of inflated bifurcation at 200mmHg

4.2: MOUSE AORTIC INFLATION UNDER ULTRASOUND

Summary:

Mouse models of disease are state of the art for studying disease and therapies. Particularly, mice are the main model for creating and treating genetic disease including those that cause aortic aneurysm such as Marfan Syndrome. Traditionally, the assessment of improved aortic outcomes is aneurysm size and growth rate, however, neither of these is an issue in and of itself [3]. The main feature of aortic aneurysms that we want to study is their stability as failure or dissection can be fatal. Current techniques to assess aortic mechanics and failure focus almost exclusively on straight, cylindrical tubes, but ascending aortic aneurysms from on the arch and near the aortic branches. Therefore, we propose a novel inflation test under high resolution ultrasound utilizing the intact aortic arch to assess mechanical properties. We show that the use of ultrasound allows us to visualize through the thickness and we can assess stretch-stress behavior on the adventitial and luminal surfaces. This technique offers unique insight into the complex geometry of the aortic arch, utilizing a relatively simple mechanical test system. We are able to segment the images obtained to create mouse-specific finite element models, which could be used to regress material properties to the aortic arch. Despite the use of through-thickness imaging, we were unable to strain track the ultrasound speckle due to a combination of lack of resolution and inadequate strain tracking algorithms for this type of problem. Future work should focus on improving the imaging by switching to something like optical coherence tomography and by improving the tracking algorithms to be able to assess strain fields.

Introduction:

The determination of material properties for complex biological tissues continues to be important for understanding both form and function. Knowledge of the underlying tissue is especially important in disease with regards to surgical planning and device design. Aortic aneurysm is one such disease. Aortic aneurysms are dilatations of the aorta which are coincident with aortic dissection or rupture. The aneurysm is typically evaluated by its size and growth rate [3, 6]. However, what we really want to evaluate is the material properties and loading of the aorta to determine how 'risky' or how likely to fail the aneurysm is. It is therefore important that we evaluate the aorta under in vivo loading conditions. This includes maintaining the geometry and the loading conditions. Standard procedure for the determination of aortic properties is to either do planar testing (uniaxial/biaxial) or inflation testing (typically straight cylindrical structures). These two methods work incredibly well for simple tube-like geometries, but are difficult or impossible to perform for small, complex structures like branching vessels or the aortic arch in genetically modified mice.

In this work, we propose a novel inflation methodology for the evaluation of full-field aortic arch mechanics in murine models. We couple a syringe pump with a custom inflation apparatus submerged in saline to overcome the leak-down of pressure due to the branching vessels, and imaging using high frequency ultrasound for real-time through-thickness visualization. This methodology gives us an immense amount of data without requiring the assumption of material incompressibility to ascertain full-field mechanics.

Methods:

Sample Procurement and Preparation

Wild-type mice (C57BL/6J) were procured from either the labs of Jennifer L. Hall (UMN Dept. of Medicine) or Paolo P. Provenzano (UMN Dept. of Biomedical Engineering) following

sacrifice as a part of normal colony maintenance. Immediately following sacrifice, the mice were weighed and the aorta, heart, and lungs were removed bloc.

To remove the heart, aorta, and lungs, the mouse was placed in a supine position and two incisions were made on either side of the mouse along the ribcage. The ribs on either side were then cut. A third incision was made transverse to the midline of the chest wall, and the ribcage was opened up. The arteries feeding the front of the ribcage were then cut and the front of the ribcage removed to expose the thoracic cavity. The cephalic and carotid arteries were then cut above the arch up into the neck and shoulders, thus freeing the top of the aorta. The esophagus and trachea were also cut at this point. The descending aorta and esophagus were cut immediately prior to the diaphragm, and the aorta gently teased away from the posterior ribcage and spine. Once removed, the esophagus, trachea, and lungs were peeled away, and the pulmonary arteries cut to leave the heart and aorta intact. The aorta was then cleaned of perivascular tissue. The major branching vessels on the arch were then tied off and the distal aorta placed on a micropipette and secured using silk suture. The process is shown in Fig. 27.

Inflation Apparatus

A custom submersible test bed was created as shown in Fig. 28. The rubber mat allows the heart to be pinned down, while the syringe pump delivers constant flow through the microcannula. Upstream pressure is measured and internal pressure can be calculated at a specific flowrate as

$$P = P_{canula} + P_{aorta}$$

where P is the indicated pressure, $P_{canula} = f(Q)$ is the pressure drop across the canula which is a function of the flowrate Q, and P_{aorta} is the pressure in the aorta. The canula pressure drop is measured by removing the aorta so that the exit of the canula is zero pressure such that $P = P_{canula}$ which can be obtained for each flowrate, Q.

To create ultrasound coupling, the test bed was submerged in 1x phosphate buffered saline (PBS). A VEVO2100 (FUJIFILM VisualSonics, Inc. Toronto, ON, Canada) small animal ultrasound system with 70MHz transducer (30um axial, 75um lateral resolution) was used with a stepping stage to image the entire vessel. Images were obtained every 32um with z-slice width of 64um. The tests were performed from 9-13mm along the sample length giving between 300-450 image slices.

Testing Protocol

The first step in the testing protocol was preconditioning. Aortas were subjected to 10 cycles of 100-120mmHg aortic pressure. The aorta was then imaged at 0mmHg aortic pressure. The pump was then engaged at a specified flow rate to give ~20mmHg aortic pressure. The aorta was equilibrated for 30s then imaged. The pump rate was then increased by ~20mmHg and imaged again. This procedure was repeated until either the sample pressure could not be increased due to leakiness or the aortic pressure reached 200mmHg. Images for each pressure step were exported as DICOM stacks, segmented using Seg3D2 [137], and analyzed using custom MATLAB2019a (Mathworks Inc., Natick, MA, USA) routines.

Results:

This testbed offers a novel way to study aortic root and whole aortic arch mechanics. The use of ultrasound also allows imaging through the thickness. An example image set at three pressure is shown in Fig 28, where it is clear that we are able to visualize the increased aortic diameter with pressure. Further example images for various locations along the aorta are shown in the inset in Fig. 29 demonstrating that it is possible to process pertinent aortic dimensional parameters. As a proof of concept, we calculated luminal and adventitial stretch vs. pressure for the tested aortas (Fig. 29). These results indicate the aortic stretch increases with pressure, although there is sufficient noise in the data that the general trend is all that is reported here. The expected behavior would be a more defined lockout behavior where the stretch change would be

relatively small compared to increases in pressure. We were also able to segment the aortas into mouse-specific models and simulate the inflation. An example inflation test outside of the ultrasound device is shown in Fig. 30, and the corresponding finite element simulation is shown in Fig. 31.

Discussion:

Using this method we were able to generate longitudinal images of the mouse aortic arch (Fig. 29) which were capable of being segmented into a reasonable reconstruction of the aortic geometry (Fig. 31). The general nature of the test and imaging technique, however, left much to be desired in terms of signal-to-noise due to a combination of limited resolution and variability in pump loading. We can see that the noise in the data (Fig. 29), was such that the general trends in the data were visible, but the material behavior and the relation from one section to the next was impossible to uncover. Despite this, we were able to recreate the bulk behavior of the tissue under pressure loading, where we see a characteristic S-shape in the descending aorta under pressure loading due to the removal of the *in vivo* axial prestretch.

While the testbed shows promise for doing full-arch mechanical tests, the ultrasound lacked sufficient resolution and had too much noise for the mouse aortic mechanics. The hope of this project was to be able to reliably 3D strain-track the ultrasound texture. However, the large displacements and the low resolution lent themselve to difficult, unreliable tracking in existing strain-tracking codes. Further, the data gathered was sufficient for creating 3D models, but the noise in the data means the segmentation was unable to be automated, instead requiring by-hand segmentation to create the 3D reconstruction.

As mentioned, the by-hand nature of much of the analysis presented here is not ideal for this type of experiment. Future work should focus on transitioning this test to a more conducive imaging modality, such as optical coherence tomography (OCT). This higher resolution, higher signal-to-noise imaging modality should provide much more reliable segmentations without as

much user interaction. Further, improvements to tracking algorithms could be made such that the large empty areas where there is simply fluid are removed from the tracking, and compatibility is enforced. Current methods either focus on discrete point tracking (which does not enforce compatibility) or on rectangular slab tracking (which enforces compatibility everywhere). Neither of these algorithms are suitable for this problem as the aorta should have a compatible deformation, while the fluid is not required to be compatible (as it can enter/leave the system) and additionally has no intrinsic speckle to track.

Acknowledgments:

The author acknowledges the labs of Paolo P. Provenzano and Jennifer L. Hall for their generous gift of mouse specimens for this study. The author also acknowledges Dr. Neeta Adhikari for her assistance in dissection and aortic sample preparation. The authors acknowledge funding from the National Science Foundation Graduate Research Fellowship Program (NSF GRFP) under Grant No. 00039202. The authors also acknowledge funding from the National Institutes of Health under Grant No. U01-HL139471.

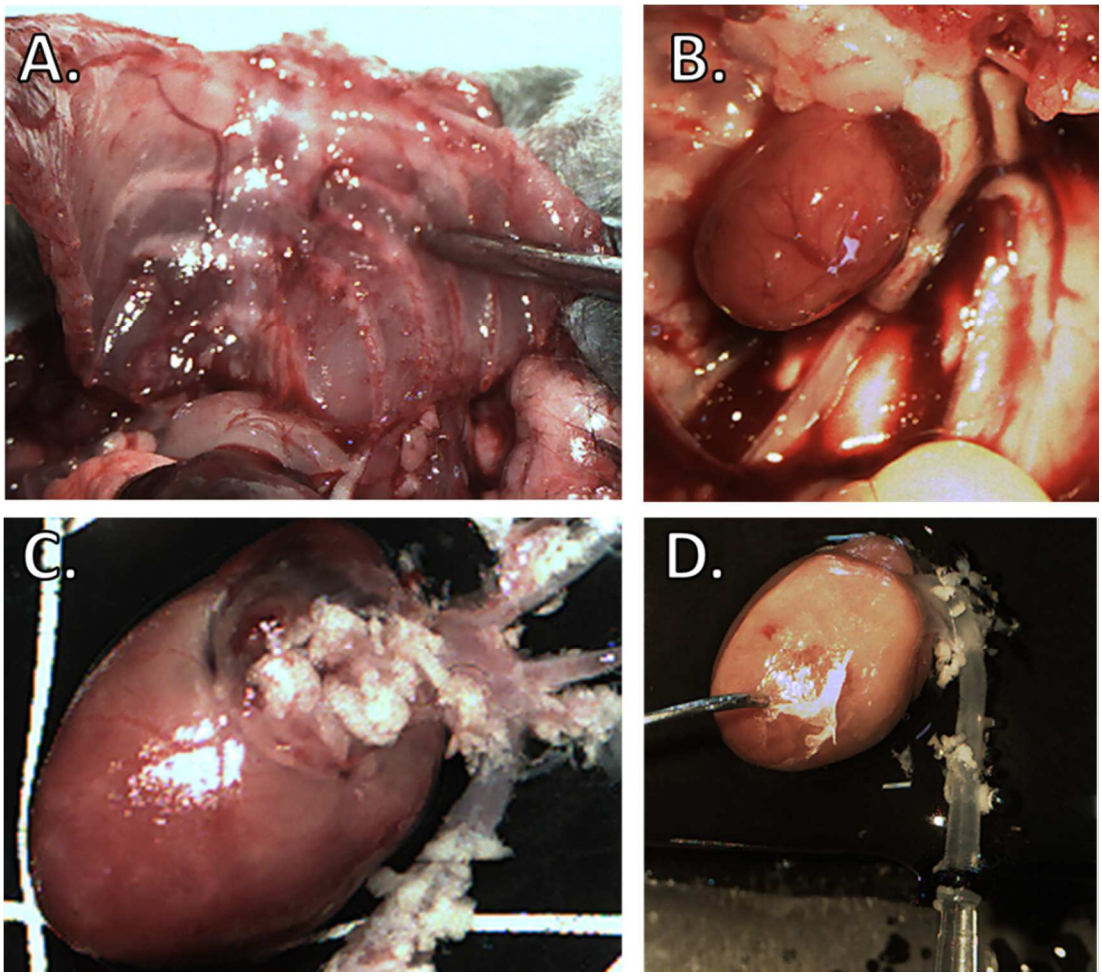

Figure 28. A. Dissection showing opening of the thoracic cavity and the blood vessels feeding the front chest wall. B. The heart and aorta in vivo. C. The heart and aorta ex vivo. D. The aorta fully prepared for inflation.

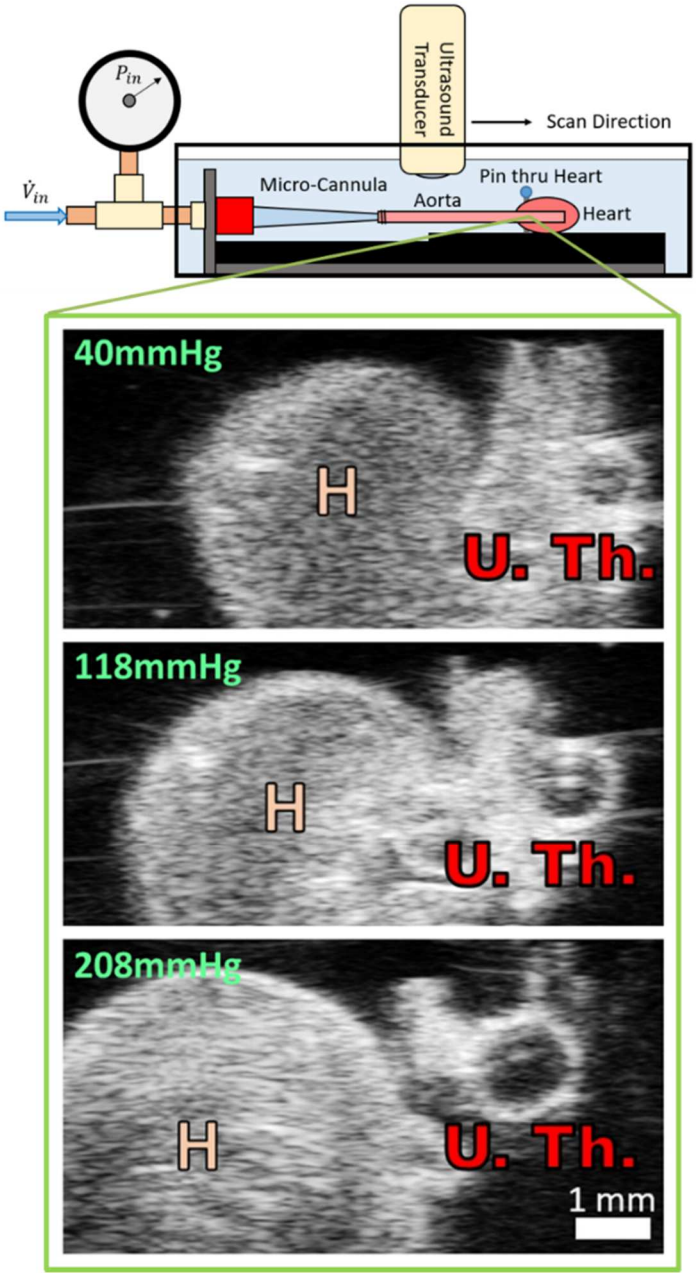

Figure 29. Inflation apparatus diagram and sample images under different internal pressures.

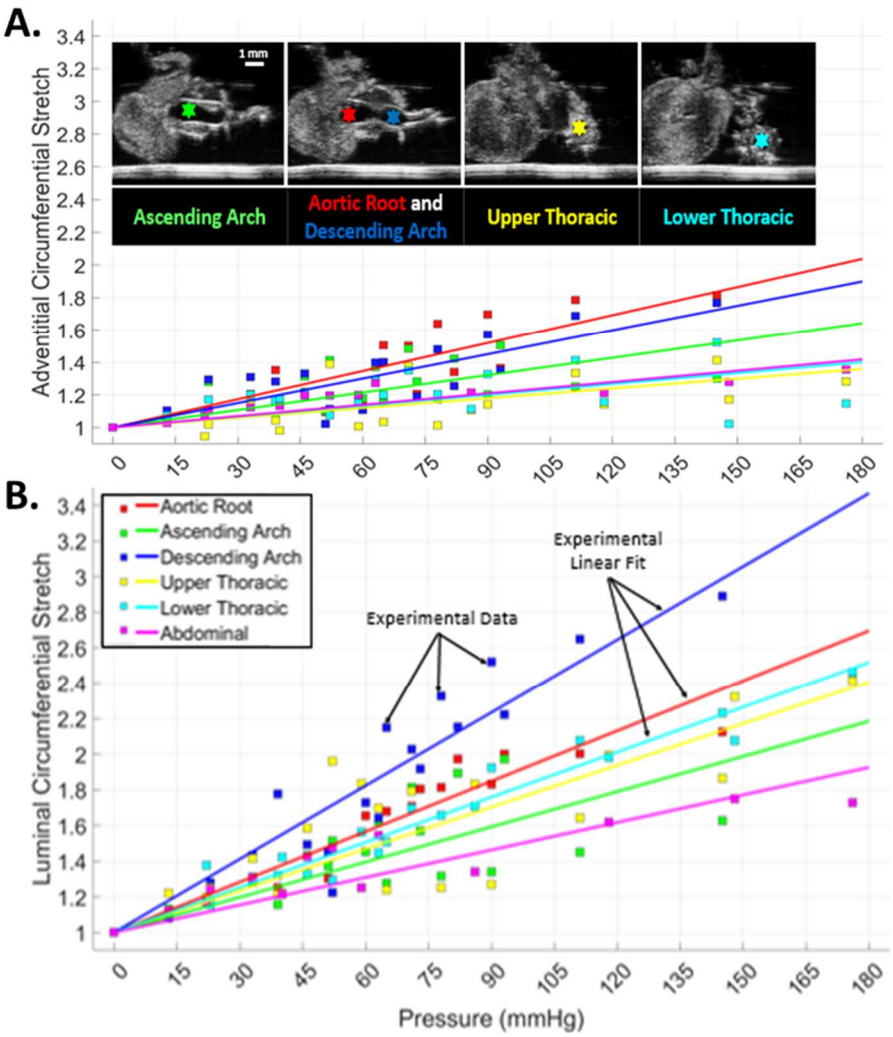

Figure 30. A. Adventitial surface stretch vs luminal pressure at five locations given by the ultrasound images shown. B. Luminal surface stretch vs. luminal pressure at the same 5 locations. N=4 samples.

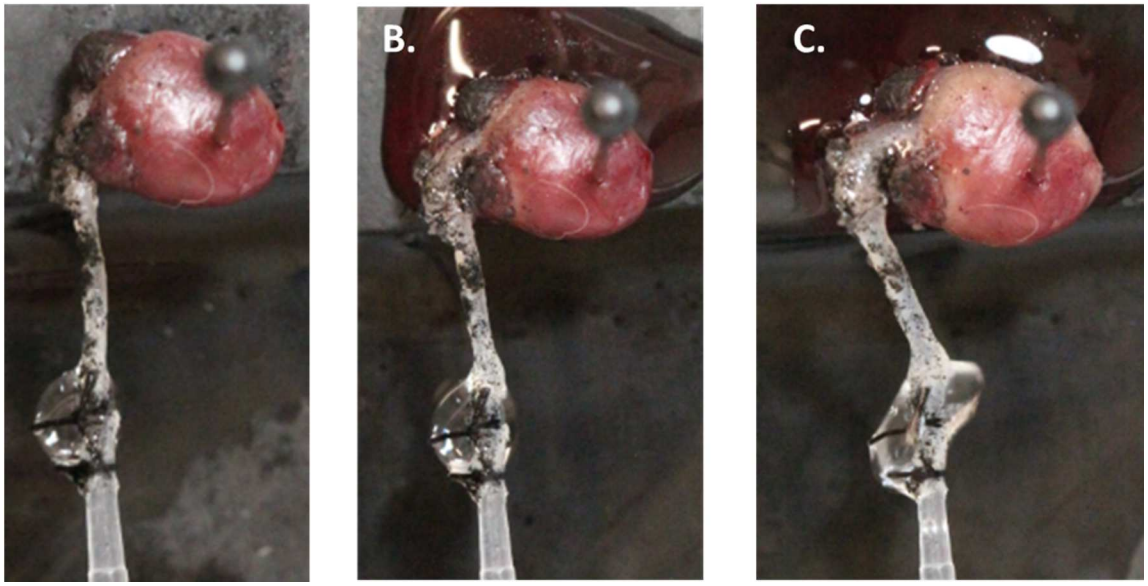

Figure 31. Inflation of the aorta at A. 0 mmHg, B. ~100 mmHg and C. ~150 mmHg

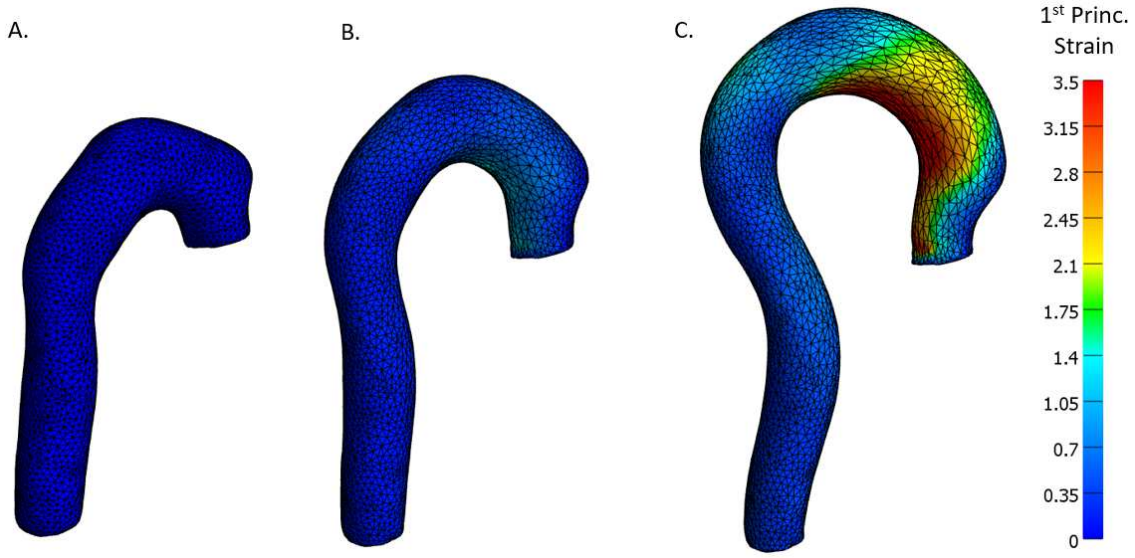

Figure 32. Simulation of aortic reconstruction showing the aorta at A. 0 mmHg, B. 100 mmHg and C. 150 mmHg

CHAPTER 5: MICROSTRUCTURAL GROWTH AND REMODELLING OF THE AORTA IN HEALTH AND DISEASE

Summary:

Aortic aneurysms are inherently unpredictable. One can never be sure whether any given aneurysm may rupture or dissect. Clinically, the criteria for surgical intervention are based on size and growth rate, but it remains difficult to identify a high-risk aneurysm, which may require intervention before the cutoff criteria, vs. an aneurysm than can be treated safely by more conservative measures. In this work, we created a computational microstructural model of a medial lamellar unit (MLU) incorporating (1) growth and remodeling laws applied directly to discrete, individual fibers, (2) separate but interacting fiber networks for collagen, elastin, and smooth muscle, (3) active and passive smooth-muscle cell mechanics, and (4) failure mechanics for all three fiber types. The MLU model was then used to study different pathologies and microstructural anomalies that may play a role in vascular growth and failure. Our model recapitulated many aspects of arterial remodeling under hypertension with no underlying genetic syndrome including remodeling dynamics, tissue mechanics, and failure. Syndromic effects (smooth muscle cell dysfunction or elastin fragmentation) drastically changed the simulated remodeling process, tissue behavior, and tissue strength. Different underlying pathologies were able to produce similarly dilatated vessels with different failure properties, providing a partial explanation for the imperfect nature of aneurysm size as a predictor of outcome.

Introduction:

Aortic aneurysm, or dilatation of the aorta, is a clinically significant pathology as the risk of potentially fatal rupture (through-thickness failure) or dissection (delamination of the layers) is high. In fact, aortic aneurysm and dissection is the fifteenth leading cause of death in the U.S. [1], with just under 10,000 deaths occurring in 2017 [2]. The current diagnostic methods for assessing aneurysm risk are based primarily on dilatation size and growth rate [1]. These criteria, while shown to correlate with aneurysm risk, are not always appropriate, especially for rare disorders involving genetic anomalies (i.e. Familial Thoracic Aortic Aneurism, Marfan Syndrome, Loeys-Dietz Syndrome, or vascular Ehlers-Danlos Syndrome), where population sizes are small and disease severity can vary widely. Thus, it is critical that we understand the underlying pathology that makes one aneurysm different from another, and what properties might point to these differences.

The aorta is a complex, three-dimensional vessel consisting of many interacting constituents [14] that are arranged in a distinct hierarchical structure of three layers [117]. The largest and most structurally important layer is the middle layer, or media. It consists of repeated layers of vascular smooth muscle cells (vSMCs) and extracellular matrix (ECM), primarily type-I collagen and elastin, formed into relatively planar layers radiating outward from the lumen of the vessel (Fig. 32). This repeated structure of vSMCs and ECM is known as the medial lamellar unit (MLU), as shown in Fig. 32. The media consists of ~5-10 MLU layers in rodents and ~50-60 in humans [141]. We focus on the MLU because it is biologically active and serves a major role in the remodeling process. The main structural components of the MLU are collagen, elastin, and vSMCs. The roles of these different components in aortic mechanics have been well studied [142–148]. Viewed simply, collagen is primarily responsible for strengthening the aorta, and giving the aorta its nonlinear "lockout" behavior, while elastin is known to give the aorta its elasticity. These two fibrillar ECM proteins are entirely passive, whereas vSMCs are active,

dynamically adjusting tensile behavior to maintain basal tone and synthesizing protein precursors and proteases that remodel the ECM.

The aorta is constantly being remodeled in response to biological, chemical, and mechanical factors. Collagen is regularly turned over in normal tissue maintenance with a half-life of ~60 days in the aorta [146]. It has been posited that collagen remodels to maintain a homeostatic stress state [149]. This hypothesis is supported by experiments showing strain-related protection of loaded collagen fibers against breakdown [150]. Elastin, on the other hand, is a biologically stable substance, with a half-life on the order of years [151]. It is generally thought to remain relatively unchanged in terms of overall content, but, over timescales on the order of decades, becomes increasingly disrupted and fragmented [143]. The active adjustment of basal tone by vSMCs in response to vessel loading (based on mean arterial pressure and the dynamics of blood flow) happens on the order of seconds to minutes, while the overall growth patterns of cells tend to be on the order of a few days [152, 153]. The aortic vSMCs are able to transition from a contractile to a synthetic phenotype under different conditions, balancing their relative contribution to load bearing with their role in remodeling the ECM.

Two main associations with aortic aneurysm are (1) elastin network disorganization and fragmentation [154] and (2) disruption of vSMCs from normal contractile function (with increases in vSMC apoptosis) [155]. Diseases that coincide with elastin disorganization and fragmentation show increased aortic growth and a propensity toward aneurysm [1, 39]. These observations show that the architecture of biological tissues is complex, and the network structures within the MLU are highly plastic [75, 148, 149, 156–160]. While many computational and theoretical models have explored growth and remodeling in various systems, most have employed a continuum framework [83, 161]. Expanded efforts in the field have sought to apply these methods to increasingly complex physics and realistic geometries [25, 63, 65, 91, 102, 162], but little has been studied in terms of the discrete nature of fiber remodeling. In other words, it

remains unclear what effect the remodeling of individual fibers, and interactions between fibrous constituents may play in tissue-scale growth and remodeling.

Methods:

We propose a novel model of tissue growth applied to a discrete microstructural representative volume element (RVE) in the form of an aortic MLU. The MLU consists of a cellular stress-fiber (actin) network analog representing SMCs and a planar layer of collagen and elastin representing the elastic lamina as shown in Fig. 32. It is worth noting that, what we call actin fibers, are representative of the mechanical contributions of intermediate filaments, microtubules, actin filaments, and myosin motors combined. The application of this discrete model of growth, remodeling, and failure unites the disparate models of growth and failure and allows us to look at how different pathologies, regardless of gross dimensions, may be prone to failure. The model is shown schematically in Fig. 33, and each section of the process is described in a subsection below.

Network Generation:

The selection of an appropriate network type for biological tissues is not a trivial task (as evidenced by [163]). In this model, we chose to use Delaunay networks because of their high degree of mechanical stability. Briefly, a 3D periodic Delaunay network is generated on 100 random nodes in our RVE to serve as our cellular stress-fiber (actin) network. All actin fiber bundles were prescribed an initial radius of 80nm. To create our embedded elastin network, we generate a second periodic Delaunay network on 250 random nodes in our RVE and flatten the resulting network into the circumferential-axial plane. Elastin fibrils were all prescribed a radius of 240nm [164]. To generate a collagen network, we perform a 2D tessellation of the planar elastin network nodes. All collagen fibrils were prescribed an initial radius of 80nm. After the networks are generated, actin network fibers that cross the collagen/elastin lamina layer are connected to the collagen/elastin network node nearest to the point where they cross. This process

approximates an integrin-like connection between the vSMCs and the ECM. An example of a typical network is shown above in Fig. 32.

Boundary Conditions:

The boundary stress values applied to the MLU were chosen using the Law of Laplace for normal (100mmHg) or hypertensive (150mmHg) mean aortic blood pressures and are summarized in Eq. 1.1-1.3. Initial, undeformed dimensions for vessel radius and wall thickness were chosen to mimic the rat aortic wall [12]. The 3-dimensional stresses are prescribed as:

$$\sigma_{\theta\theta} = \frac{P\, r_c}{h};\ \sigma_{zz} = \frac{P\, r_c}{2h};\ \sigma_{rr} = 0 \qquad \text{Eqs. 1.1-1.3}$$

where $\sigma_{\theta\theta}$ is the circumferential stress, P is the mean arterial pressure, $r_c = \lambda_1 R_0$ is the deformed centerline (mid-wall) radius, λ_1 is the circumferential stretch, and $R_0 = 600um$ is the initial vessel centerline radius, $h = \lambda_3 H_0$ where h is the deformed wall thickness, λ_3 is the stretch in thickness (radial direction), and $H_0 = 100um$ is the initial wall thickness, σ_{zz} is the axial stress, and σ_{rr} is the radial stress.

Wall shear stress at the luminal surface of the vessel was calculated using a nominal flow rate of 84 mL/min and a blood viscosity of 3cP [26]. The Poiseuille formula for steady, Newtonian fluid flow, given in Eq. 2, was used to determine an average wall shear stress,

$$\tau_{wall} = -\frac{4\mu Q}{\pi r_i^3} \qquad \text{Eq. 2}$$

where τ_{wall} is the wall shear stress, μ is the kinematic viscosity, Q is the flow rate, and $r_i = \lambda_1 R_0 - \frac{1}{2}\lambda_3 H_0$ is the deformed luminal radius.

Network Solution and Stress Calculation:

The main constituents of mechanical interest in this model are actin-like cellular stress-fibers, collagen, and elastin. Cellular actin fibers were treated as active components with a

characteristic time scale much shorter than the timescale of remodeling. We therefore represent the actin as having two behaviors: a passive bilinear elastic response and an instantaneous active contraction the magnitude of which is driven by wall shear stress (WSS) as given in Eqs. 3.1-3.3:

$$f(\lambda) = 1 - \left(\frac{\lambda - \lambda_{max}}{\lambda_{min} - \lambda_{max}}\right)^2 \; for \; \lambda_{min} < \lambda < 2\lambda_{max} - \lambda_{min} \quad \text{Eq. 3.1}$$

$$S(\tau_{wall}) = S_0 * \tau_\infty / \tau_{wall} \quad \text{Eq. 3.2}$$

$$\sigma_{active} = S(\tau_{wall}) \lambda f(\lambda) \quad \text{Eq. 3.3}$$

where $f(\lambda)$ is the active response function based on the stretch, λ, and $\lambda_{max}$and $\lambda_{min}$are the stretches of maximum and minimum contraction respectively, $S(\tau_{wall})$ is the magnitude of contraction based on WSS τ_{wall}, S_0 and τ_∞ are scaling parameters for contraction and WSS respectively, and σ_{active} is the active contractile stress in the fiber. The gold lines in Fig. 34. show actin fiber mechanics for both active (dotted line) and passive (dashed line) behaviors.

It is well known that collagen tends to take on a crimped conformation which results in a stress-strain behavior consisting of a large toe region followed by a steep lockout. In our model system, we utilize a helical fiber model [165], with parameters fit to single fiber data from [148]. The model is shown by the red line in Fig. 34. Elastin, as the main elastic element, was modeled as a bilinear elastic spring as shown by the black line in Fig. 34. All material parameters used in these models are given in Table 5. Because fibers buckle when compressed, actin and elastin fibers were prescribed a compressive modulus of 1/100 of the tensile modulus in Table 5.

We model the volumetric mechanics of the cell due to the existence of charged fibrous proteins following [166], but scaling the fixed charge density with actin fraction. The overall swelling pressure has two important consequences: first, as the network is compressed, the pressure is increased; and second, as the actin network becomes more dense, through the addition

of fiber, the swelling pressure increases driving growth of the MLU. The osmotic pressure is given by Eqs. 4.1-4.2:

$$c^{FCD} = c_0 \phi^a \quad \text{Eq. 4.1}$$

$$p = RT\left(\sqrt{(c^{FCD})^2 + 4(c^*)^2} - 2c^*\right) \quad \text{Eq. 4.2}$$

where c^{FCD} is the tissue fixed charge density, c_0 is a fixed charge density scaling parameter, ϕ^a is the actin volume fraction, c^* is the extracellular osmolarity, p is the swelling pressure, R is the universal gas constant, and T is the absolute tissue temperature. We note here that the swelling pressure model allows the network to grow over time (i.e. incompressibility is not enforced in the time domain). The swelling pressure does limit compressibility to $\frac{V}{V_0} \sim 0.92$ for the strip biaxial extension test and $\frac{V}{V_0} = 1.08$ for the shear test prior to failure discussed in the *Material Property Calculation and Failure Simulations* subsection below. The compressibility in the strip biaxial test is within the range experimentally measured in [167]. While, to our knowledge, the compressibility of arterial tissue in shear has not been experimentally measured.

We use volume-averaging theory to convert fiber forces in the equilibrated MLU to tissue stress. The physical dimension of the RVE is calculated via a scaling parameter, χ, given in Eq. 5 [168, 169]:

$$\chi = \sqrt{\frac{\sum l_f A_f}{\phi V}} = 10um \quad \text{Eq. 5}$$

where χ is the RVE scaling parameter l_f is the length of fiber f in computational units, A_f is the cross-sectional area of fiber f, ϕ is the fiber volume fraction, and V is the RVE volume in computational units cubed. In Eq. 5, l_f and V are both in computational units, whereas A_f is in physical dimensions. Thus, χ has units of physical length per computational length. It should also

be noted that χ is considered a constant in our simulations, and is simply used to relate computational dimensions of length (for the RVE and fibers) to physical dimensions.

Using the scaling parameter χ and summing the forces for all fibers, we calculate the volume averaged stress that our RVE experiences as shown in Eq. 6:

$$\sigma_{ij} = \frac{1}{\chi^2}\left(\frac{1}{V}\int_V \sigma_{ij}^f dV^f\right) = \frac{1}{\chi^2}\left(\frac{1}{V}\sum_f \left(\sigma^f n_i^f n_j^f\right)V^f\right) \quad \text{Eq. 6}$$

$$= \frac{1}{\chi^2}\left(\frac{1}{V}\sum_f \left(\frac{F^f}{A^f} n_i^f n_j^f\right)\left(A^f l^f\right)\right) = \frac{1}{\chi^2}\left(\frac{1}{V}\sum_f F^f l^f n_i^f n_j^f\right)$$

where σ_{ij} is the tissue stress, χ is the RVE scaling parameter, V is the computational RVE volume, σ_{ij}^f is the fiber stress, V^f is the fiber volume, l^f is the fiber length, A^f is the fiber cross-sectional area, F^f is the fiber force magnitude, and n_i^f is the fiber unit vector. We note that the value set in parentheses for Eq. 6 has units of force per computational unit squared. Thus, we need to scale the stress to real physical dimensions using the scaling parameter.

The Newton-Raphson algorithm is used to find the principal stretches that give us the correct prescribed boundary loads from Eq. 1. A second Newton-Raphson loop is used inside the first to compute the position of each node in the network at static equilibrium given a deformation.

Implementation and Solution Convergence:

The model was implemented in a custom C++ code using the Eigen library [170]. This code is available from a public Github repository (https://github.com/RyanMahutga/JBME_Remodeling1). Convergence of the internal force balance is considered achieved when the residual force norm is less than an absolute threshold of $1e^{-5}nN$ or a relative threshold of $1e^{-5}$ compared to the affine deformation nodal residual for the current stretch step. Convergence of the stress boundary problem is considered achieved if the

absolute magnitude of stress error is less than 100 Pa or the relative stress error is less than 0.1% of the maximum applied boundary stress.

Growth and Remodeling Dynamics:

The dynamics of growth and remodeling (G&R) are handled similarly to [25], but applied to fibers rather than to the tissue as a whole. Fibrils remodel to reach a pre-determined target stress. To reach a specified target stress, fibrils grow radially (effectively adding mass and inter-molecular crosslinks). The equation guiding this growth is given in Eq. 7:

$$\frac{dr}{dt} = \frac{1}{\tau}\left(\frac{\sigma_f}{\sigma_{targ}} - 1\right) r \qquad \text{Eq. 7}$$

where $\frac{dr}{dt}$ is the time rate of change of the fiber radius, τ is the polymerization time constant, r is the fiber radius, σ_f is the fiber stress, σ_{targ} is the fiber target stress. The polymerization time constants, τ, are taken to be 4.5 days for actin [153], and 90 days for collagen [171]. Elastin was not allowed to remodel due to its stability in the aorta. The homeostatic fiber stresses σ_{targ} were taken to be 750kPa for actin and 200kPa for collagen. More information about how target stresses were selected is provided in the Supplemental Material.

The lengthening of fibrils is governed by the assumption that the addition of molecules to the radius of the fibril can be reasonably described as adding a new parallel spring as in [172]. An overall force balance along with algebraic manipulation gives the following relation for the new rest length of the fiber:

$$L' = \frac{\left(\frac{r^2}{M} + 2rdr + dr^2\right)}{\left(\frac{r^2}{M} + \frac{2rdr + dr^2}{\lambda}\right)} L_0 \qquad \text{Eq. 8}$$

where L' is the new rest length of the fiber, r is the pre-existing fiber radius, M is the modulus ratio of the new fiber in compression to the pre-existing fiber in tension, dr is the deposited fiber radius, λ is the fiber stretch at the time of deposition, and L_0 is the pre-existing fiber length when

the new fiber was deposited. The ratio of the pre-existing fiber tensile modulus to the new fiber compressive modulus M is taken to be 1.0.

In this simulation framework, we can decouple the RVE loaded state from the zero-stress state as:

$$F = F_g F_e$$

where F is the current deformation gradient for the current loaded network relative to the unloaded network at time t=0, F_g is the zero-stress network deformation gradient from the unloaded time t=0 network to the unloaded network at the current time, and F_e is the elastic deformation gradient for the network from the current time unloaded network to the current time loaded network. The decoupling of growth and elastic stretch is accomplished by simply running the network through a prescribed zero-stress boundary condition model at every timestep where we already know the loaded total stretch for the network. We can then calculate the elastic deformation as $F_e = F F_g^{-1}$.

Fiber growth and the time evolution of the tissue are modeled using a forward-Euler scheme with variable step size.

Material Property Calculation and Failure Simulations:

Since tissue failure – either by rupture or dissection – is the major clinical threat associated with pathological vessel growth, we looked at two failure scenarios for the MLUs: a strip biaxial and a shear to failure. Each failure scenario treated the test as a passive failure test (as in experiments [44–46, 74, 173–175]) so the actin contractility was removed. The strip biaxial test was meant to serve as an analog for the burst failure of the artery. In the biaxial test, the MLU axial stretch was set to 1.4, and the MLU was stretched to failure in the circumferential direction. The thickness direction was prescribed as zero stress. Properties of small-strain modulus,

transition strain, and large-strain (lockout) modulus were calculated prior to failure. The small-strain modulus is defined as the slope between zero and 50kPa circumferential stress, and the large strain modulus defined as the slope between 200 and 400kPa circumferential stress. The transition strain is defined as the strain where the small-strain line and the lockout modulus line intersect. Rupture failure was defined as the point on the stress-strain curve immediately preceding a drop in stress greater than 50 kPa.

The shear test, in contrast, served as an analog for the dissection failure of the artery. For the shear test, the axial and circumferential stretches were set to 1.4 and 1.6 respectively. The radial direction was prescribed zero stress. The shear was imposed as a circumferential displacement on the radial face. The shear modulus was defined as the slope of the shear stress vs. shear strain curve prior to failure. In each failure scenario, the strain step was adjusted dynamically so that failure occurred in fewer than 15 of the over 3000 total fibers on any given stretch step to maximize the accuracy of the measured bulk failure stress and strain. Dissection failure was defined as the point on the shear-stress vs. strain curve immediately preceding the first drop in stress.

Experimental Design:

The first set of cases we explore consider a vessel subjected to a 50% increase in mean blood pressure. This case has been described extensively in experiments from a gross morphological standpoint [24], from a histological standpoint [176, 177], and from a mechanical standpoint [159, 178, 179]. Furthermore, this case is often used as a validation test for growth and remodeling simulation [25, 26, 103].

The second set of cases we explore are the remodeling of vessels in response to pathological conditions under normotensive blood pressure. As discussed above, two especially common associations with aortic aneurysm are elastin fragmentation [154] and smooth muscle

cell dysfunction [1, 180, 181]. In an attempt to understand these two scenarios, we remodeled our generated networks under normotensive conditions then applied one or both of two perturbations: (1) an instantaneous reduction in elastin (by randomly removing fibers) and/or (2) an instantaneous reduction in smooth muscle cell contractility (by decreasing the parameter, S_0 in Eq. 3.2). The cases that were investigated are summarized in Table 6.

Statistics:

For each scenario outlined above, we used 8 networks generated using the same routine listed in Network Generation. All plots with error bars show mean ± 95% confidence interval on the mean. Comparisons were performed using paired t-tests with significance established at two levels: $p<0.05$ and $p<0.005$.

Results:

Investigation of the Normotensive and Hypertensive Aorta:

The first step in verifying the model was to apply it to a well-studied remodeling case. The standard case is that of a pressure overload where one would expect an initial spike in stress followed by re-equilibration to a new, lower stress state due to growth of the tissue. The expected behavior is seen clearly in the Total Stress line of Fig. 35A, which rises sharply with the introduction of the pressure overload, but then decays to a value close to the initial level. Examining the individual component contributions to the total stress in Fig. 35A, one can see that the load has been shifted from the elastin to the actin during the remodeling process, with the collagen contribution largely returning to its original level. We emphasize that the component's contribution to the overall stress should not be confused with the stress within a component fiber, since the former is a combined effect due to the sum of stresses for each individual component and the volume fraction of that component within the tissue. This effect can be understood by examining the tissue volume fractions in Fig. 35C, starting with two key observations:

1. The total volume fraction of all protein increases slightly, but the volume fraction of actin increases considerably. Thus, the actin contribution to the total stress increases naturally due to the greater actin volume fraction.

2. The elastin volume fraction drops considerably. Since elastin does not remodel, this drop is entirely due to an increase in tissue volume (discussed further in Fig. 35B, D, F). Thus, the elastin contribution to the total stress drops even though the stress on any given fiber increases because the fiber forces are distributed over a much larger area. In contrast, the volume fractions of both collagen and actin increase because remodeling outpaces tissue volume growth.

The effect of remodeling can be seen even more clearly in Fig. 35E, in which the stress for each fiber is shown before and after remodeling. Due to their ability to remodel, the collagen and actin fibers return to the same homeostatic stress levels after remodeling. In contrast, the elastin fibers must stretch more in response to tissue growth and, therefore, go to a higher stress state after remodeling. Thus, based on Figs. 35A, C, and E we conclude the mechanism underlying the remodeling involves a greater portion of load being borne by the actin (i.e., by the smooth muscle), but a higher local fiber stress generated in the elastin.

Turning to the kinematics of tissue growth and remodeling in this base case, there is a substantial increase in tissue volume with increased length in all three directions (Fig. 35B). The volume change is driven primarily by tissue growth (Fig. 35D), as the total volume change due to elastic deformation remains relatively unchanged (Fig. 35F) indicating the tissue in nearly incompressible. The tissue grows in all three directions (Fig. 35D), with the transverse growth driven by the osmotic effect due to increased actin content described in Eq. 4.2. Importantly, the elastic stretch of the tissue in the directions of loading (i.e., circumferential and axial) decreases over time because fibers grow thicker (Fig. 37B) leading to increased force developed for a given strain. The transverse direction of elastic stretch is increased due to the same osmotic effect discussed earlier.

The growth and thickening of the simulated vessel wall can be seen in snapshot in Fig. 36, which shows the vessel at three different stages in the growth and remodeling process in both unloaded (0mmHg luminal pressure) and loaded (100mmHg or 150mmHg luminal pressure) states. The vessel growth is evident in the unloaded-state images of the whole vessel and in the networks themselves. The actin density increase is also evident from these network snapshots.

A distinct feature of this discrete fiber remodeling framework is that we can monitor individual fiber changes. In Fig. 37, we show fiber length and fiber radius for collagen and actin as these fiber types grow during remodeling. The collagen fibers tend to maintain a shorter length than the actin fibers, and each has a unimodal distribution (Fig. 37A). The fiber radii (Fig. 37B) shows that the collagen fibers tend to grow much thicker in response to loading with a unimodal distribution. In contrast, the actin fiber radius is bimodal. It is noted that the fibers that go to zero radius have been removed, and the peak on the low end (shown by green arrows) represents a stable population of fibers with radii in the range of 2-25nm. Examining the network itself, we see that the peak in the distribution at small radius (Fig. 37) corresponds to interlamellar fibers connecting the cell to the ECM, and connecting the adjacent lamellae to one another (Fig. 38). The large radius peak corresponds to fibers falling roughly into the circumferential-axial plane. These two families are interlamellar fibers that resist osmotic pressure and relatively planar fibers that resist the hoop and axial stresses. The alignment of laminar elastin and collagen followed the direction of loading with little discernible change from normotensive to hypertensive cases (Supplement Fig. XXXXXXXXXX1).

Another distinct advantage of a model system using discrete fibers is that we can perform failure simulations and track failed fibers (as performed previously for non-remodeled systems by [45, 182]). An example of a strip biaxial pull to failure test is shown in Fig. 39A. The region of failure initiation is highlighted by the dashed oval. In strip biaxial testing, failure initiates in the collagen/elastin lamina layer. In shear to failure (Fig. 39B), in contrast, failure initiates as the

actin fibers disconnect from the elastic lamina causing delamination of the MLU. Additionally, shear failure occur at a much lower stress, consistent with experimental observations [46]. It should be noted that failures are simplified in that they occur within fibers and not at connections.

The failure simulations of Fig. 39 allow us to quantify the material behavior and failure characteristics for both planar and shear deformations as shown in Fig. 40. The 50% blood pressure overload resulted in a significantly higher small-strain modulus and shear modulus. There was also a statistically significant decrease in the transition strain for the pressure overload case. Taken together, these properties indicate that the tissue stiffness increased as a result of increased mean arterial pressure. In addition, we see statistically significant increases in the stress at rupture and the stress at dissection indicating that the material has remodeled to become stronger in both failure modes.

Investigation of elastin fragmentation and smooth muscle cell dysfunction:

Growth Dynamics:

Simulations used to investigate the independent and coupled roles of elastin fragmentation and smooth muscle cell dysfunction are outlined in Table 6 above. We summarize the results in Fig. 41 for reduction of smooth muscle contractility alone (first column), removal of elastin alone (second column), and combined reduction of contractility and removal of elastin (third column). We define the healthy state as the state immediately before initiation of the insult (i.e. reduction of contractility and/or removal of elastin) at t=135 days (shown by the green arrows in Fig. 41). The circumferential stress for decreased contractility alone (Fig. 41A) shows an instantaneous reduction in actin stress due to the loss of contractility. The resulting reduction in the total circumferential stress in the tissue is gradually regained as collagen and actin remodel. The homeostatic stress state after remodeling is negligibly different than the healthy stress. The circumferential stress for removed elastin fibers (Fig. 41B), however, shows an instantaneous drop in elastin stress but a rise in total stress because the instantaneous loss of elastin makes the

vessel more distensible increasing the tissue stress based on the Law of Laplace. The resulting load on collagen is then redistributed over time onto actin, resulting in increases in both collagen and actin stress at the new, lower total homeostatic stress level compared to the healthy stress. The circumferential stress response for the combination of reduced contractility and removed elastin (Fig. 41C) shows the load from elastin loss redistributes to collagen and actin, with less load borne by the actin compared to the elastin removal alone (Fig. 41B). The result is a homeostatic stress after remodeling below the healthy stress. This counterintuitive result is explained by the fact that the load previously held by elastin is redistributed to collagen and actin. The increase in actin load results in more actin creation, which leads to increased osmotic pressure and more transverse growth. This growth makes the thickness of the tissue larger, so the stress decreases per Eq. 1.

The fiber volume fraction evolution shows that for actin contractility disruption (Fig. 41D), load is primarily redistributed to collagen, which results in increased collagen content. Overall, the total fiber volume fraction increases in this case relative to the healthy level. When elastin is removed (Fig. 41E), the resultant load is redistributed to both collagen and actin resulting in increases in volume fraction of each. The actin and collagen are both stiffer than the elastin, so they add less volume to pick up an equivalent load from the removed elastin, thus, the total fiber volume fraction is decreased relative to the healthy level. In the case of combined actin contractility disruption and elastin fiber removal (Fig. 41F), we again see the disruption of actin contractility driving growth of collagen with total fiber volume recovering more than in the case of removed elastin alone (Fig. 41E). We see relatively little change in overall fiber orientation over the baseline case with changes in elastin or vSMCs (Supplement Fig. 1XXXXXXX).

There is lower total growth for actin disruption alone (Fig. 41G) compared to elastin removal alone (Fig. 41H). However, the combination of reduced contractility and removed elastin (Fig. 41I). results in higher volumetric growth than either alone.

Material and Failure Properties:

Fig. 42A shows the material properties for cases of removed elastin and reduced contractility to the normal baseline networks. Removal of elastin results in a higher small-strain modulus, lower transition strain, and higher shear modulus, but little change to the lockout modulus. In contrast, the reduction of vSMC contractility results in a lower small-strain modulus, higher lockout modulus, higher transition strain, and lower shear modulus. Failure properties were also examined for these cases (Fig. 42B). Removal of elastin results in lower rupture strain and stress, a higher dissection stress, but little change in dissection strain. Reduction in contractility of the vSMCs show increased rupture strain and stress. The reduced contractility cases also show increased dissection strain with little change in dissection stress.

Comparison of Morphologically Similar Dilated Vessels:

After observing the behavioral differences in Fig. 41 & 42, we generated morphologically similar dilated vessels based on inner luminal dimensions, a standard clinical metric measured using CT/MRA/Ultrasound. It has been shown that interobserver error in measurement and measurements taken between different modalities can have high variability [183, 184]. Based on the reported variability in clinical measurement, we set our cutoff for similar pathological vessel sizes at ±4% of the mean of pathological cases (excluding the 30% removed elastin alone case and the 25% contractility alone case). The luminal size for all cases in shown in Fig. 43. The mean is given by the solid line, and the ±4% limit is shown by the shaded box.

Since the standard diagnostic criteria for a risky aneurysm are based on size and a growth rate evaluated in, typically, six month intervals [3], we compared the mechanical behavior and failure properties of vessels of similar lumen diameter and growth rate. The trends in material properties are shown in Fig. 44A. The combined effect of a reduction of contractility and removal of elastin is an increase in small-strain modulus, increase in lockout modulus, decrease in

transition strain, and increase in shear modulus. The effect of changing contractility while keeping the elastin removal the same (gold bar vs purple bar) shows that decreased contractility decreases small-strain modulus, increases lockout modulus, and increases transition strain with little change in shear modulus. The effect of increased elastin removal while maintaining contractility (purple vs green vs light blue bars) shows increases in small-strain modulus, lockout modulus, and transition strain with negligible change in shear modulus.

The failure properties for the comparison of pathological cases are shown in Fig. 44B. The combined effect of reduced contractility and removed elastin decreases rupture strain, but increases rupture stress. There is little change in dissection strain but a significant increase in shear stress at dissection. The role of increased contractility while keeping the elastin removal the same (gold bar vs purple bar) shows that decreased contractility has little effect on any failure parameters. The effect of increased elastin removal while maintaining contractility (purple vs green vs light blue bars) shows increases in strain at rupture with little change in any other failure properties.

Overall variability comparing one pathological vessel to another are summarized in Table 7. The data suggest that vessel behavior and strength are highly dependent on underlying pathologies, and that small perturbations or variations in the underlying pathologies can cause significant changes to underlying material and failure properties for similarly dilated vessels.

Discussion:

Normotensive vs. Hypertensive Aorta:

The general trends for our model in response to a 50% overload in mean arterial pressure are as follows:

1. An initial spike in circumferential stress followed by re-equilibration to a new homeostatic stress state (above the homeostatic stress state at normal blood pressure) (Fig.35A).

2. Growth of the MLU in all dimensions, with particularly pronounced medial thickening (Fig 35B,F), and an increase in luminal diameter under load (Fig, 35B).

3. Fiber remodeling resulting in increased collagen and actin content which coincides with longer fibers with larger radii (Fig. 37), along with less elastin content due to an increase in MLU volume (Fig. 35C).

4. Increased tissue stiffness in both planar and shear tests (Fig. 42).

5. Increased stress at failure for both medial rupture and medial dissection (Fig. 42).

The initial spike in circumferential stress followed by a re-equilibration to a new homeostatic state is consistent with other theoretical models [25, 103]. Our model also shows the homeostatic stress after remodeling with hypertension is greater than that for the normotensive case ($\sigma = 142kPa$ normotensive, $\sigma = 154kPa$ hypertensive), which is consistent with data for hypertensive rats ($\sigma = 120kPa$ normotensive, $\sigma = 164kPa$ hypertensive from [179] and $\sigma = \sim 140kPa$ normotensive, $\sigma = \sim 175kPa$ hypertensive [185]). The observations of [186] show medial thickening and decreased luminal diameter for spontaneously hypertensive rats under *in vivo* load conditions while the data of [187] show the same medial thickening ($\lambda_{medial} = 1.42$) with increased luminal diameter ($\lambda_{luminal} = 1.19$) in hypertensive rats. Our morphological data from the 50% pressure overload scenario show similar medial thickening ($\lambda_{medial} = 1.54$) along with increases in luminal diameter ($\lambda_{luminal} = 1.11$). Additionally, the data of [188] show that the hypertensive rat has a marked decrease in elastin fiber content (~27%) and an insignificant increase in collagen content. Additionally, the estimates for total extracellular fiber fraction is 0.55 in normotensive decreasing to 0.45 in hypertension [188]. Our model indicates similar slight collagen content increase and marked elastin content decrease (~54%) (Fig. 35B). We also show that the total elastin and collagen content decreases from 0.36 in the normotensive case to 0.28 in the hypertensive case. This decrease is similar to the experimental case, although are

tissue ECM is less dense in the simulation. Further, the data of [188] show increased vSMC density of the aortic media in hypertensive rats vs. control rats changing from ~0.27 in normotensive rats to ~0.31 in hypertensive rats. A significant increase in actomyosin content in the aortic media is also shown by [189]. Our model shows a marked increase in the actomyosin density (Fig. 35C) increasing from 0.12 to 0.25 indicating that our cellular network is, again, less dense than actual aortic tissue.

The data of [178, 185] show significant increases in the small-strain modulus (stiffness at 100mmHg in the experiment, 20-50% increase) and statistically insignificant decreases in the lockout modulus (stiffness at 200mmHg in the experiment) for hypertensive rats compared to normotensive controls. Our simulation data shows a large increase in small-strain modulus (93% increase) and moderate increase in lockout modulus (32% increase) (Fig. 40). In addition, we see lower ultimate strains in hypertension and increases in ultimate rupture failure strength, which is consistent with [190].

Unique Insights from this Model:

Some unique insights into the remodeling process emerged that cannot be obtained directly from continuum models. Our model demonstrates that the remodeling process in the 34D actin network formed two distinct fiber populations; one whose radius tended to be relatively large and another that tended to be relatively small. Further investigation showed different microstructural roles for these two fiber families. The two populations were shown to reinforce the network in different directions, with the large-diameter actin fibers aligning in the circumferential-axial plane while the small-diameter fibers aligning radially. This observation suggests the formation of actin struts between layers. Similar struts have been observed experimentally in the rat aortic arch [14], but are formed by interlamellar elastin. The role of these struts in the model is to carry the radial load induced form the osmotic pressure, and

removal of these struts causes large increases in the radial thickness and destabilizes the network itself.

Our model also allowed us to simulate failure onset and propagation (Fig. 39) and showed behavior consistent with histological findings of failed tissues [191]. Our simulated failure data also show large variability within groups, which indicates that structural alterations, that cannot be quantified in the averaged data (i.e. fiber volume content, overall tissue stress, and tissue size), play a critical role in when and how a tissue fails. These types of structural information and discrete phenomena (perhaps only affecting a few fibers), lost in the homogenization of continuum models, are of critical importance in predicting failure, where a cascade of failure can be triggered by a seemingly insignificant local inhomogeneity.

Extension of Results to Other Arterial Tissues:

While the results here are cast in the context of aortic remodeling, many of the observations are also true of other arterial structures affected by hypertension. Of particular note is the pulmonary artery where, although the pressure levels are much lower than that of the aorta, hypertension still causes significant remodeling. Pulmonary hypertension induces dilatation of the vessel [192]. This growth is marked by thickening of the media with pronounced stiffening, increase in collagen content and decrease in elastin content [193]. All of these observations are qualitatively consistent with our model, and could be examined quantitatively by adjusting the model geometry and pressure loads. The same is true of investigating hypertension effects on other vessels such as the carotid or coronary arteries.

Models of Elastin Fragmentation and Smooth Muscle Cell Dysfunction:

The major clinical criteria for assessing aneurysm risk are size and growth rate, which tend to have low temporal resolution and high variability in measurement. We are able to match simulated vessels grown under different pathologic conditions using these criteria for determining

similarity. It is clear from previous studies [1, 154, 181] that aneurysms involve both elastin fragmentation and smooth muscle cell dysfunction or death. These two pathological scenarios are the basis of our comparisons.

Removal of Elastin Fibers:

Tissue stress decreases after equilibration in response to removed elastin (Fig. 41B), which aligns with the murine elastase model in [39]. Remodeling in response to elastin loss shifts the load from elastin to the collagen and actin. The collagen remodels to a lower stress state while the actin adjusts its contraction and remodeling to balance the load shifted from the collagen. This phenomenon results in increases in both actin and collagen fiber content (Fig 41E) and in growth of the MLU network (Fig. 41H). The removal of just elastin leads to increases in luminal diameter with medial thickening, which causes dilatation similar to that observed in elastase models of aneurysms [39, 194], but contrary to what is observed in elastin knockout mice [143]. In addition, the aortic stiffness increased when elastin was removed (Fig. 43), which is consistent with elastin insufficient mice [41] and the elastase-induced aneurysm model [39]. Particularly in [39] we note that the elastic fiber contribution to stress reduces to almost zero, indicating large increases in small-strain stiffness. The collagen contributions to the stress also increase indicating increased lockout stiffness. We limit our discussion here to qualitative results because the mutant mice used to recapitulate these hallmarks of aneurysm do not maintain a normotensive blood pressure.

In a majority of the cases studied here, there was increased tissue strength in response to removal of elastin. The reason for this is that the load previously borne by elastin is transferred to collagen or actin fibers, which thicken in response to overload. Since these constituents are stronger than elastin, the result is a higher failure stress. While this effect is theoretically understandable, it is never observed in aneurysmal tissues. The missing link may be disruption to the collagen or changes in synthesized collagen that arise due to underlying pathologies, or

possible failure occurring at fiber connection junctions rather than in a fiber itself (discussed further in Model Limitations).

Reduced SMC Contractility:

The murine Myh11 model of reduced contractility shows lower homeostatic stress [39], whereas in our model, contractility reduction alone showed little change in homeostatic stress (Fig. 41A). The reduction of actin contractility redistributes load primarily to the collagen, whose remodeling drives subsequent tissue growth. In mouse models of Myh11 mutation, relatively little change in aortic wall diameter or thickness are observed [39], consistent with our model (Fig. 41G). Further, the Myh11 mouse shows decreases in elastin contribution to the material behavior (primarily affecting small-strain modulus) along with increased circumferential collagen/SMC contribution to the material behavior (primarily affecting lockout modulus) [39]. Our model is consistent with these experimental findings. It should be noted that the Myh11 mouse does maintain normotensive blood pressure [195].

Dilated Vessel Mechanics:

The dilated vessels in Fig. 43 show significantly different behaviors from one another both in mechanics and in failure (Table 7), even though they all exhibit nearly the same degree of dilatation and growth rate. Our model showed removal of elastin increased stiffness and shear modulus (Fig. 44), while decreased vSMC contractility lowered small-strain modulus and shear modulus, but increased lockout modulus. The transition strain is also increased with decreased contractility. These relatively small perturbations to dilated vessels make a significant difference in material behavior and failure.

We acknowledge that none of these growth scenarios reach the 50% increase in luminal diameter that is typically associated with an aneurysm, despite relatively large changes to the constituents. The modest changes in vessel size are due to the specification of the fiber growth

model. The modulus ratio in Eq. 8, for example, could be tuned to bring the magnitudes of these changes closer to experimental findings. Further, this model treats the growth and decay processes as coupled (i.e. there is only one remodeling equation) when, in reality, the processes of fiber decay through protease activity and fiber growth through fiber deposition occur through very different, and still largely unknown, mechanisms.

Model Limitations:

As with all models of complex systems, there are several limitations associated with this model. First, as discussed earlier, we use a Delaunay network, which tends to be more affine than one might observe of biological networks, especially collagen. Additionally, our structure of smooth muscle stress fibers and a coupled elastic lamina is a simplification of what is observed in arterial tissue. The actual arterial structure contains additional collagen surrounding the SMCs and elastin struts that protrude radially [14]. It is likely that altering the collagen-elastin lamella to be a 3D structure would reproduce these structures as we have already seen the same type of structures emerge from our model, albeit made from actin rather than ECM components. Nevertheless, the structural model here is significantly more representative than a purely continuous model.

A second limitation is the use of osmotic pressure to describe bulk intracellular properties. While it is true that cells use osmotic pressure for various processes including movement, it is naïve to think that the osmotic pressure is the only bulk material model needed. One may well expect that the cell volume is controlled through numerous other biological mechanisms in addition to osmolarity differences.

We assumed that fibers remodel toward a target stress. The fibers themselves are passive elements and cannot sense their surroundings. One could hypothesize that if the fibers are at higher stress, then the cell is also at higher stress, and its response is to release more procollagen and enzyme (peptidase), which causes fibers to grow. If we then add the experimental

observations of [148], a mechanism arises whereby loaded fibers grow, but unloaded fibers decay due to innate matrix metalloprotease (MMP) activity. An approximation of this process is the fiber growth model used in these simulations.

An additional assumption in the fiber remodeling is that the fiber growth and decay processes are coupled (i.e. can be described through a single equation). However, it is clear that the mechanisms for fiber deposition and decay are very different from one another, and are linked in a complex way through cell signaling. The decoupling of these two processes could give us a much improved model allowing for more growth and fundamental changes in fiber properties. Additionally, the use of this single remodeling equation forces the remodeling process in a quasi-static system (like the one we use) to approach a steady-state value. This simplification does not account for the continuous turnover of the ECM, and limits the predictive capabilities of this model in long-term growth (e.g. studying aneurysmal growth over the course of many years).

An additional limitation in the model is that it currently does not capture the decreased strength of aneurysmal tissue. We believe this is due to the fact that we are not modulating the decay of collagen as a cell might in response to insult. The model does not account for many structural alterations that arise from SMC apoptosis or glycosaminoglycan (GAG) pooling. Both of these aspects could result in changes to tissue strength based on composition. Further, we believe that there are significant structural changes to the underlying networks (beyond just changes in constituent content, fiber radii, and fiber lengths), as opposed to our current simplified remodeling of the fibers in the network. Additionally, our current model does not distinguish failure strengths of bonds between constituents (nodes in the model). It is likely that strengths of constituent bonds are important in failure, and may be changed in disease states.

Conclusions:

The data presented here demonstrate that this model can capture a majority of experimental observations in the simple case of pressure overload (hypertension), and that it can be used to elucidate both bulk material mechanics and failure properties for many pathological scenarios. Further, our data have demonstrated that structural details, such as the interlamellar struts, can be identified and justified from this model. Discrete-fiber structural models, with increased detail, can be used to predict changes or disruptions in tissue architecture such as those coincident with aneurysm. Further, models of this type allow us to investigate the risk associated with certain pathological aneurysms.

This model system allows us to simulate an extremely complex process. We can simulate experiments that are incredibly difficult to perform such as stimulating or inhibiting elastin, collagen, or actin production, altering mechanical loading during development, altering fiber architecture during the growth process, or changing the maturation process of fibers. Each of these aspects could be insightful in understanding disease pathogenesis for aneurysm formation.

Acknowledgments:

The authors acknowledge funding from the National Science Foundation Graduate Research Fellowship Program (NSF GRFP) under Grant No. 00039202 and from the National Institutes of Health under Grant No. U01-HL139471.

Table 5: Constituent Models and Parameters

Constituent:	***Model:***	***Material Parameters:***	***Failure:***	***References:***
Actin	Linear Elastic - Passive	$E = 4\ MPa$	$\lambda_{crit} = 2.0$	[196]
	Active	$S_0 = 200\ kPa;\ \lambda_{min} = 0.65;\ \lambda_{max} = 1.4;\ \tau_\infty = 5.0\ Pa$		[197]
Collagen	Helical Spring	$E = 700\ MPa; R_0 = 5.8\ nm; r_0 = 1.6\ nm; H_0 = 67.4\ nm$	$\lambda_{crit} = 1.43$	[150, 198, 199]
Elastin	Linear Elastic	$E = 1\ MPa$	$\lambda_{crit} = 2.35$	[200]
Intracellular Space	Osmotic Pressure	$c_0 = 280 mEq/L;\ T = 310\ K;\ c^* = 150\ mEq/L;$	N/A	[166]

Table 6. Pathological remodeling cases summarized in results. Tested cases are denoted with an X.

		vSMC Contractility		
		100% of normal	25% of normal	0% of normal
Elastin Fiber Removal	0% removal	*Baseline*	X	-
	20% removal	-	X	X
	25% removal	-	X	-
	30% removal	X	X	-

Table 7. Comparison of inter-sample pathological vessel differences showing properties with $p<0.05$. The upper right of the matrix shows material properties: small-strain modulus (E_0), lockout modulus (E_∞), transition strain (ε_{tran}), and shear modulus (G). The lower left of the matrix shows failure properties: rupture strain (ε_{rup}), rupture stress (σ_{rup}), dissection strain (γ_{dis}), and dissection stress (τ_{dis}).

% of Normal Contractility/ % Removed Elastin	Overload	0%/20%	25%/20%	25%/25%	25%/30%
Overload		E_0, E_∞ ε_{tran}, G	E_0, E_∞ ε_{tran}, G	E_0, E_∞ ε_{tran}, G	E_0, E_∞ ε_{tran}, G
0%/20%	ε_{rup}, τ_{dis}		E_0, E_∞ ε_{tran}	E_0, ε_{tran}	E_0, ε_{tran}
25%/20%	ε_{rup}, τ_{dis}	–		E_0, E_∞ ε_{tran}	E_0, E_∞ ε_{tran}
25%/25%	ε_{rup}, γ_{dis}, τ_{dis}	γ_{dis}	ε_{rup}		E_0, ε_{tran}
25%/30%	ε_{rup}, γ_{dis}, τ_{dis}	$\varepsilon_{rup}, \gamma_{dis}$	ε_{rup}	ε_{rup}	

% of Normal Contractility/% Removed Elastin

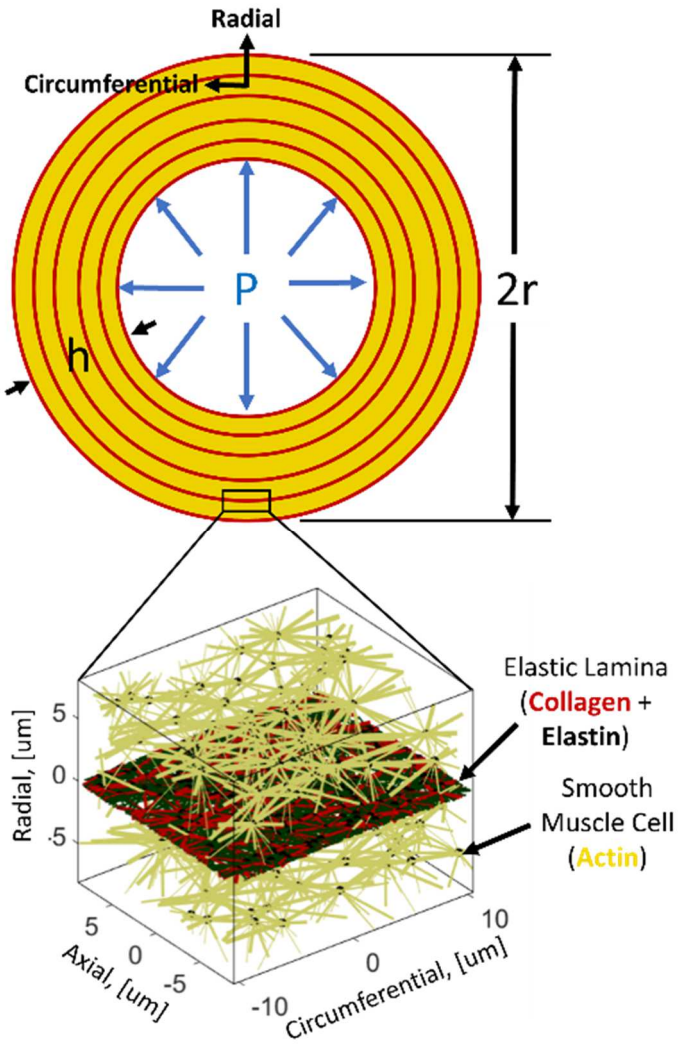

Figure 33. Aortic vessel geometry and repeated medial lamellar unit.

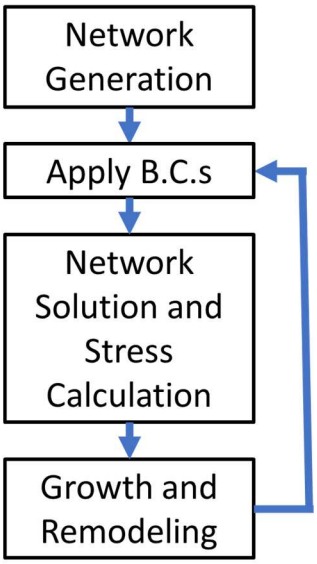

Figure 34. Computational model flowchart.

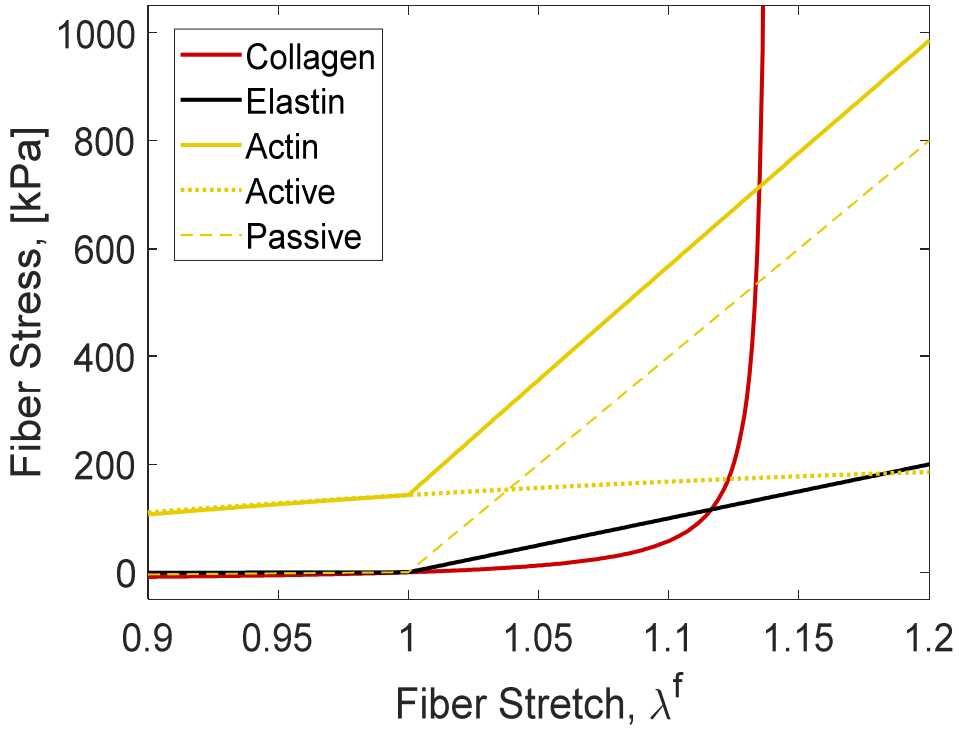

Figure 35. Mechanical behavior of fiber constituents.

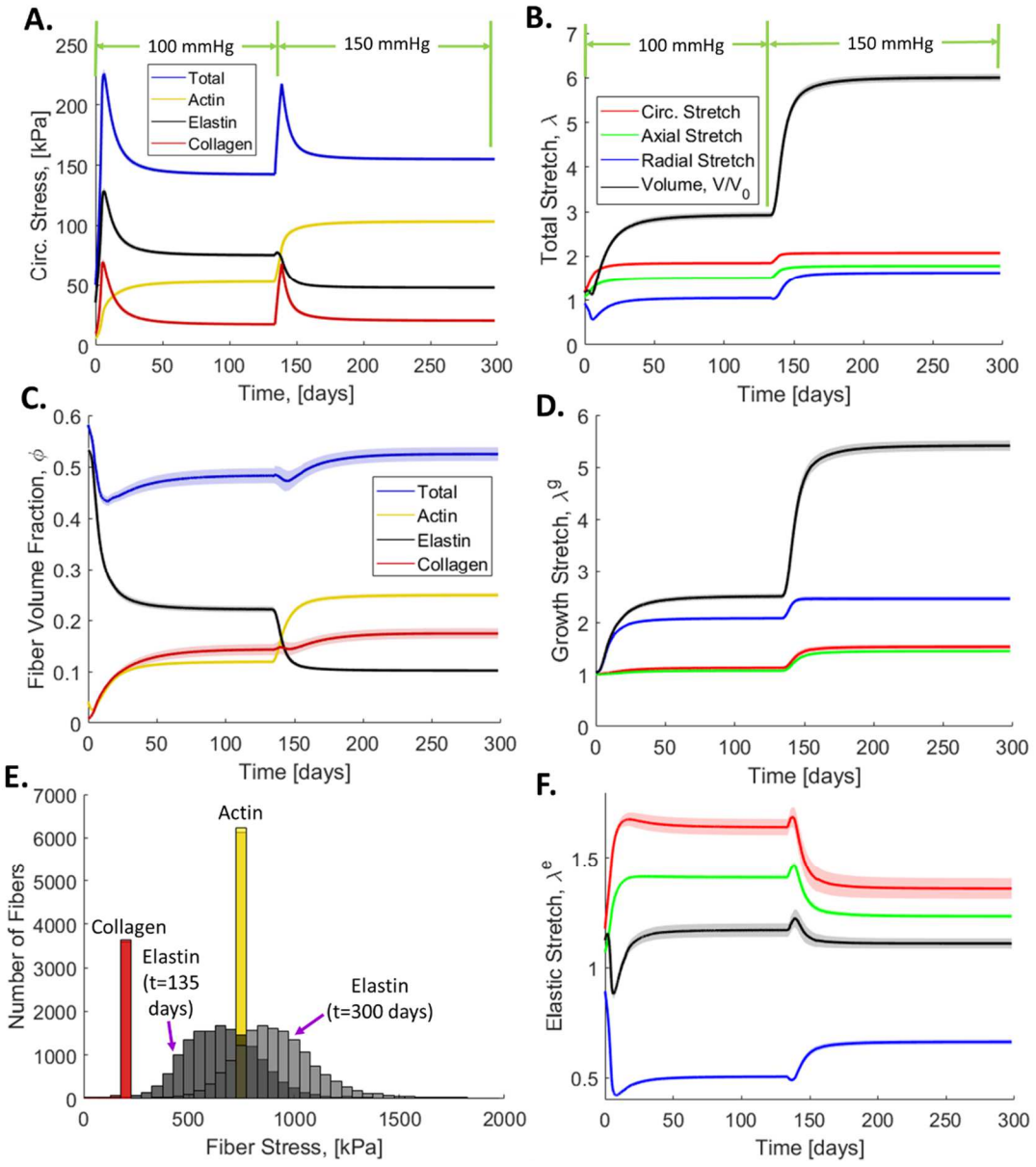

Figure 36. A. Circumferential stress evolution with normal blood pressure (100mmHg) and hypertension (150mmHg). B. Overall tissue stretch evolution. C. Fiber volume fraction evolution. D. Growth contribution of stretch evolution. E. Histogram of fiber stresses for each fiber type at t=135 days and t=300 days. F. Elastic contribution of stretch evolution. Solid lines are means and the shaded region is 95% confidence interval for N=8.

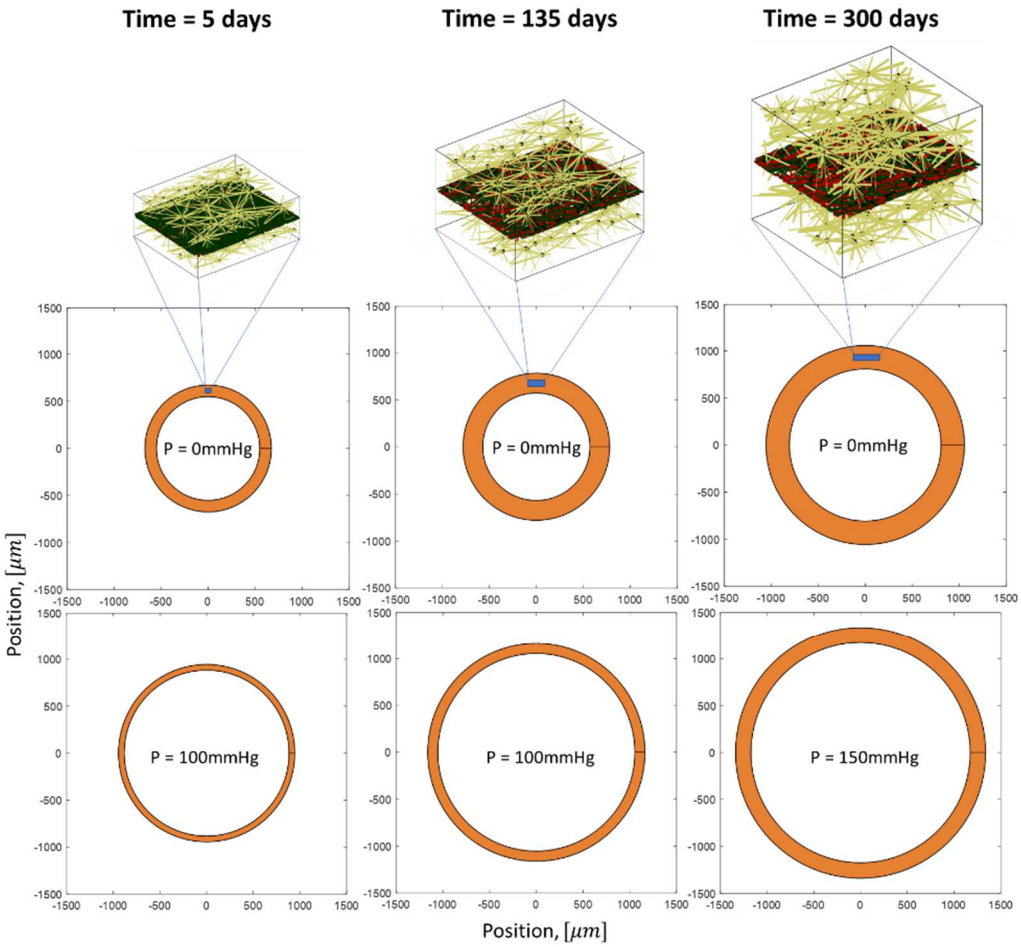

Figure 37. Representative arterial networks and overall size during the remodeling process showing actin in gold, collagen in red, and elastin in black.

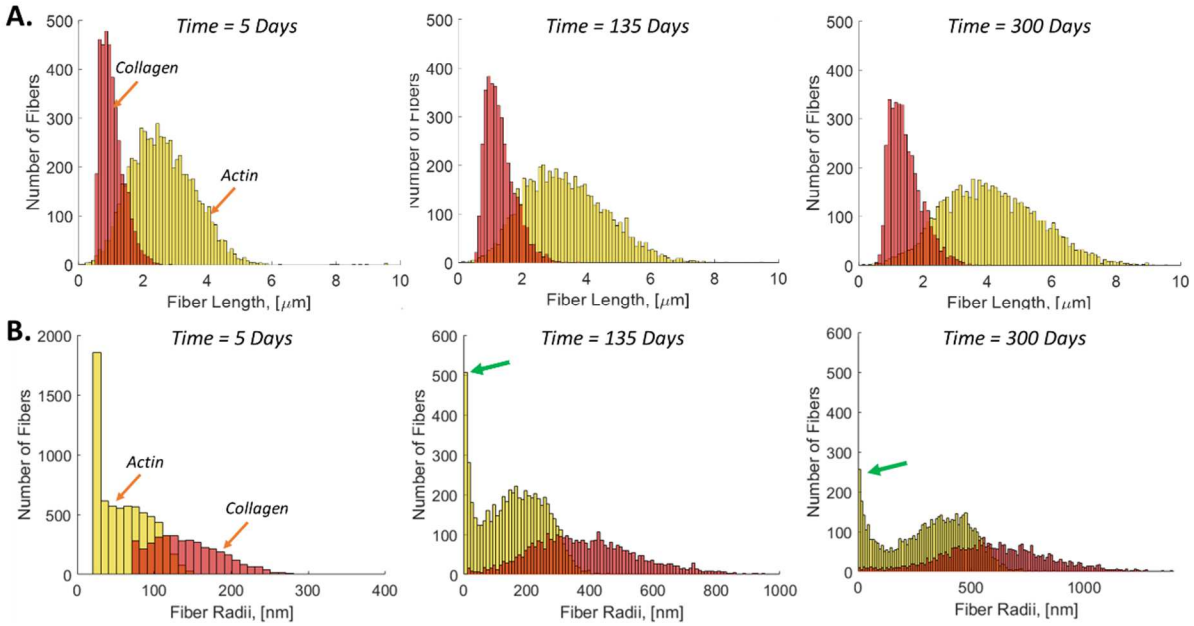

Figure 38. Pooled histograms of all fibers in all networks (N=8) for A. fiber length evolution of actin and collagen. B. fiber radius evolution of actin and collagen. The green arrows show the actin fiber peak at small radii.

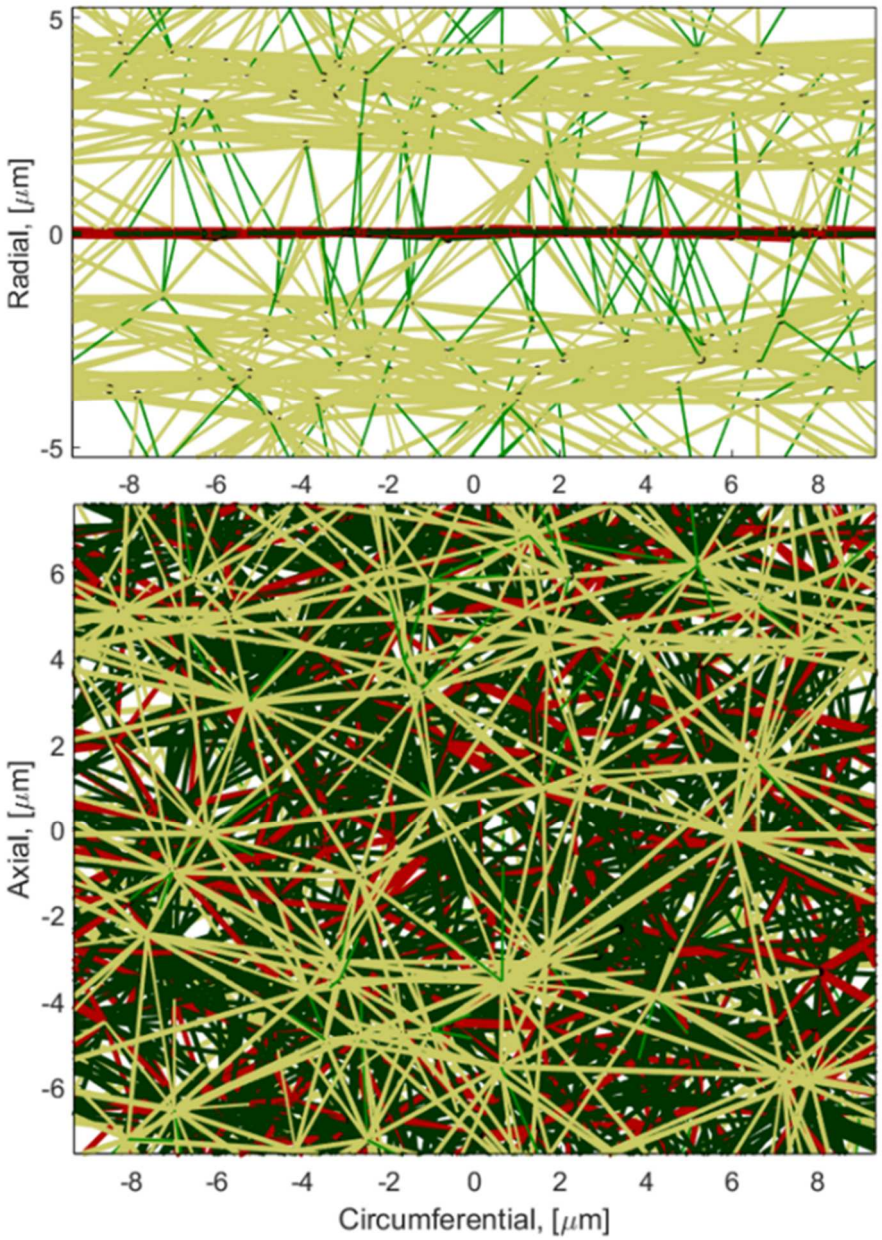

Figure 39. Homeostatic hypertensive MLU showing small diameter (r<25um) actin fibers in green, large diameter actin fibers (r>25um) in gold, collagen in red, and elastin in black.

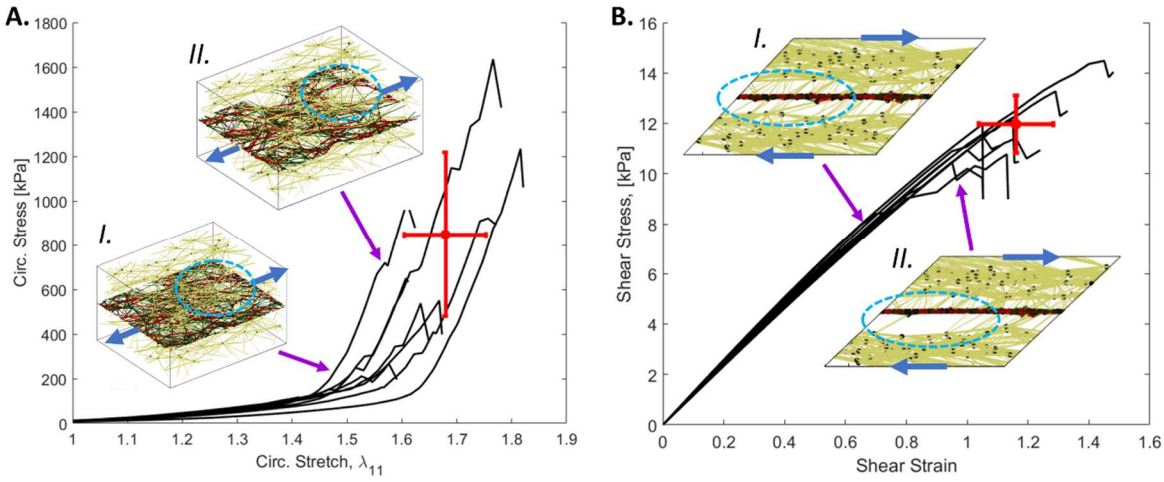

Figure 40. Representative failure curves (black lines) and networks before (I) and after (II) failure for A. circumferential failure and B. shear failure. The red dot shows the mean failure behavior and the cross shows the 95% confidence interval. The blue arrows show the direction of loading, and the light blue dashed ovals show tear formation in A, and delamination in B.

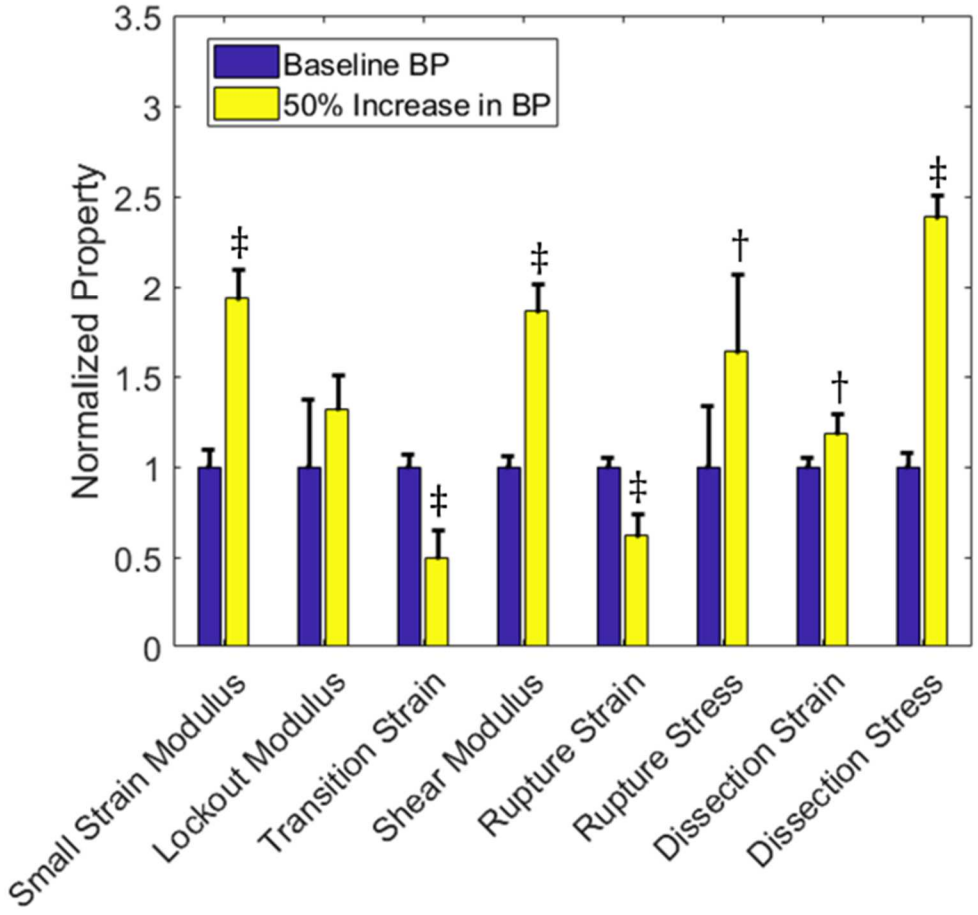

Figure 41. Material and failure properties for baseline normal blood pressure (blue) and a 50% increase in baseline blood pressure (yellow). Solid bars are means and the error bars are 95% confidence interval for N=8. The symbol † represents $p<0.05$ and the symbol ‡ represents $p<0.005$ relative to the baseline vessel.

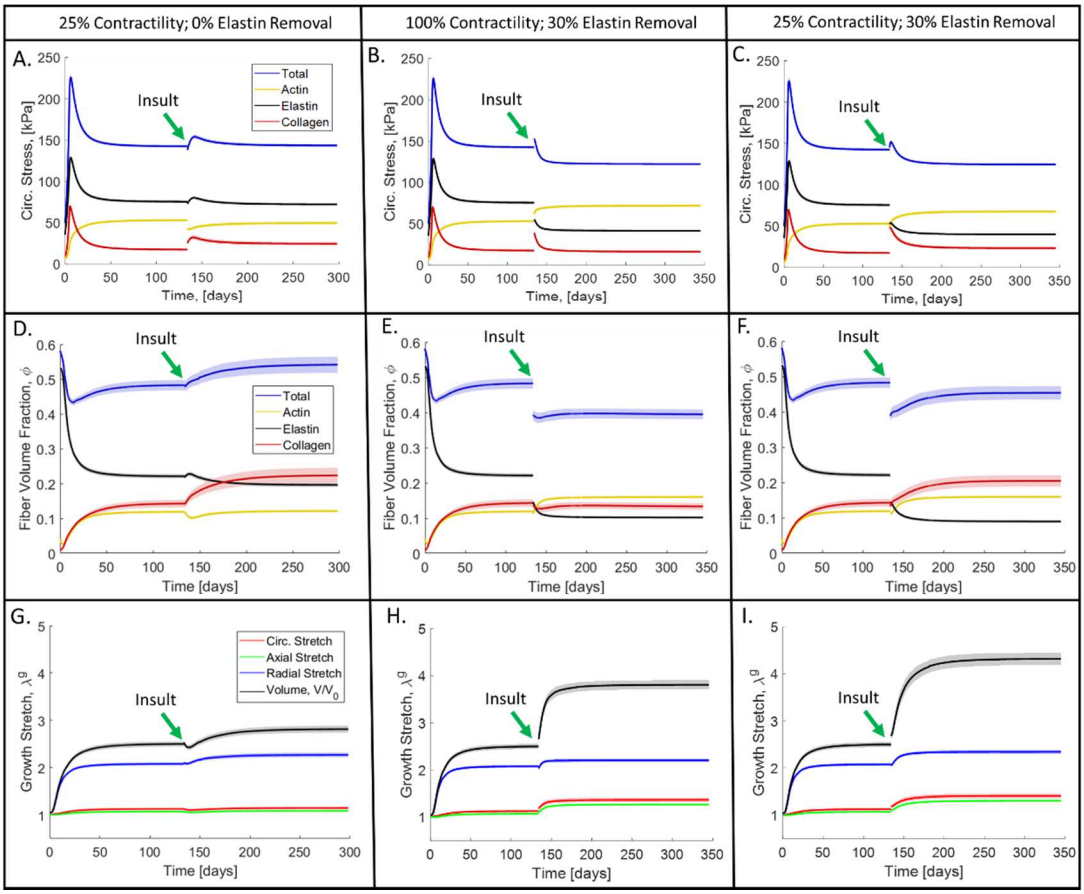

Figure 42. A. Circumferential stress evolution for contractility reduced to 25% of normal with no elastin removal. B. Circumferential stress evolution for normal contractility with 30% elastin removal. C. Circumferential stress evolution for contractility reduced to 25% of normal with 30% elastin removal. D. Fiber volume fraction evolution for contractility reduced to 25% of normal with no elastin removal. E. Fiber volume fraction evolution for normal contractility with 30% elastin removal. F. Fiber volume fraction for contractility reduced to 25% of normal with 30% elastin removal. G. MLU growth for contractility reduced to 25% of normal with no elastin removal. H. MLU growth for normal contractility with 30% elastin removal. I. MLU growth for contractility reduced to 25% of normal with 30% elastin removal. Solid lines are means and the shaded region is 95% confidence interval for N=8.

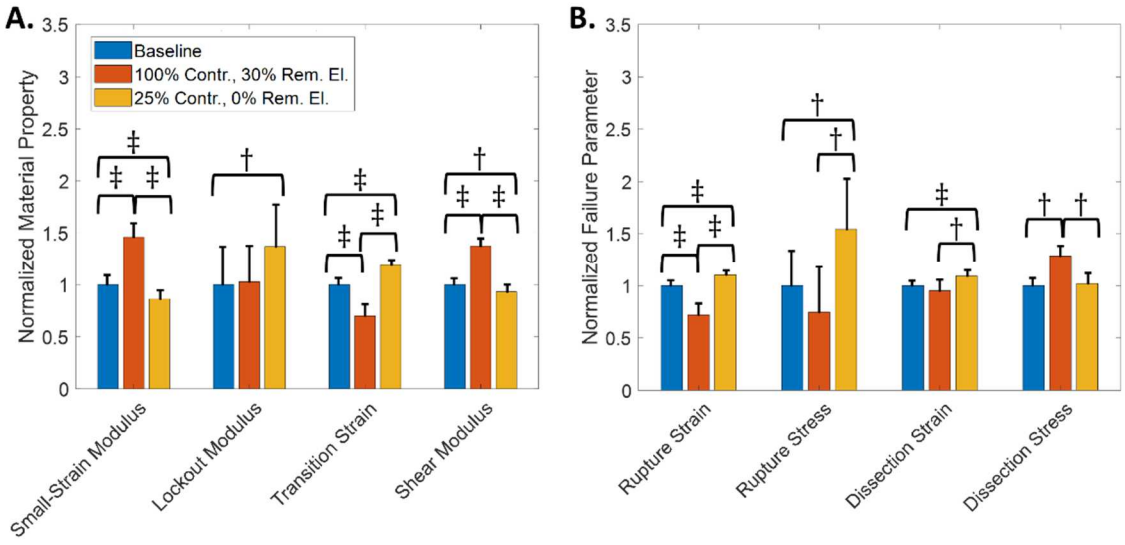

Figure 43. A. Normalized material properties and B. Normalized failure properties for baseline (blue), normal (100%) contractility with 30% removed elastin (orange), and 25% of normal contractility with normal elastin (0% removed) (gold). Solid bars are means and the error bars are 95% confidence interval for N=8. The symbol † represents $p<0.05$ and the symbol ‡ represents $p<0.005$.

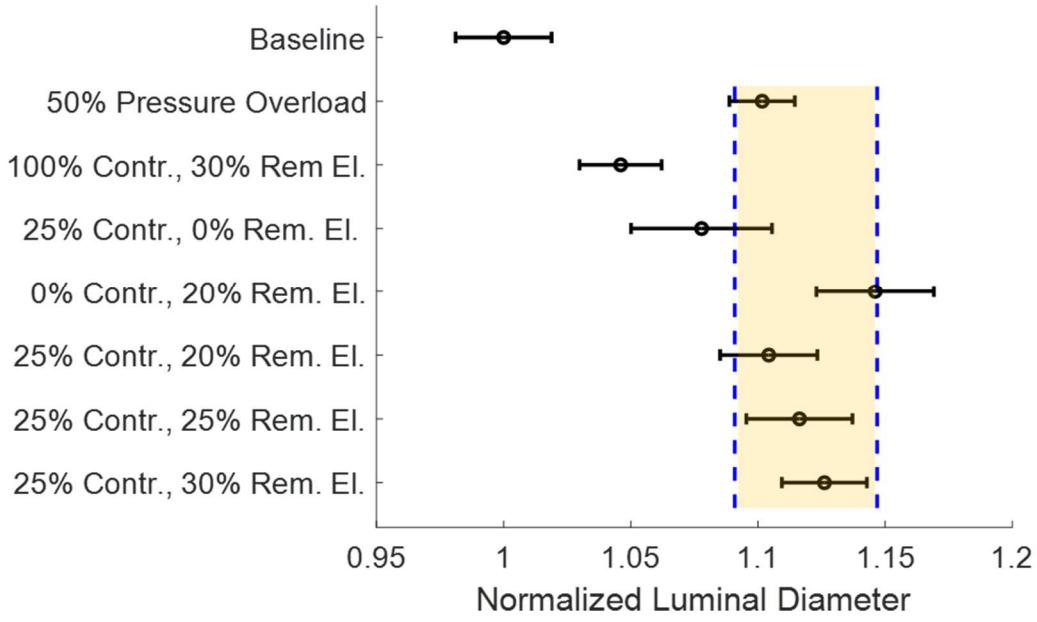

Figure 44. Normalized homeostatic luminal diameter at load for all tested cases. The highlighted cases are within ±2.5% (dashed lines) of the mean for pathological growth cases. Circles are means and the error bars are the 95% confidence interval for N=8.

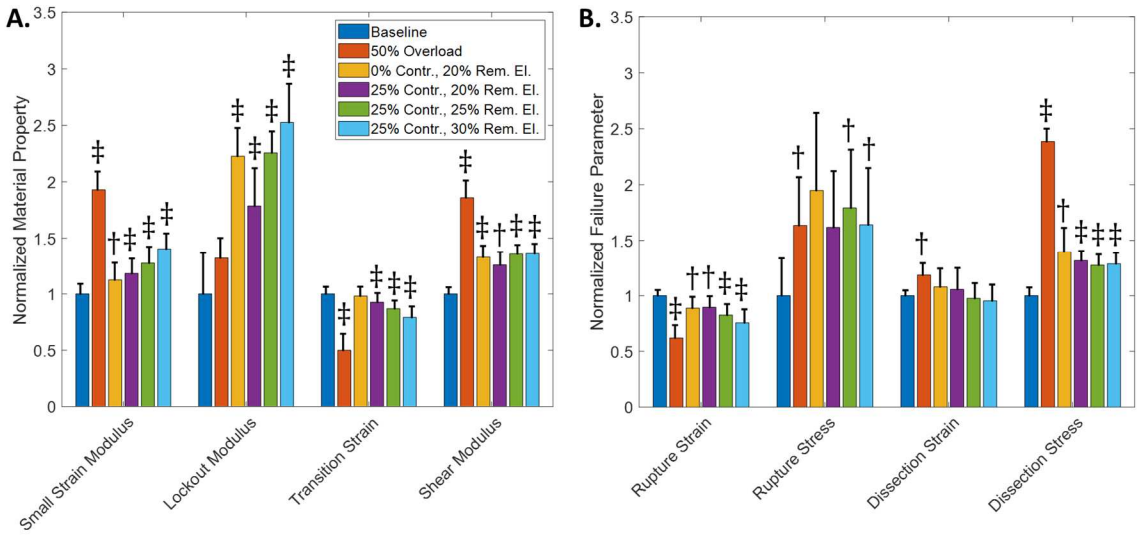

Figure 45. A. Mechanical properties of baseline and pathological vessels. B. Failure properties of baseline and pathological vessels. Solid bars are means and the error bars are 95% confidence interval for N=8. The symbol † represents $p<0.05$ and the symbol ‡ represents $p<0.005$ relative to the baseline vessel.

CHAPTER 6: THE HOLZAPFEL-GASSER-OGDEN MODEL FOR NETWORK MECHANICS

Summary:

The heterogenous, nonlinear, anisotropic material behavior of biological tissues makes precise definition of an accurate constitutive model difficult. One possible solution to this issue would be to define microstructural elements and perform fully coupled multiscale simulation. However, for complex geometries and loading scenarios, the computational costs of such simulations can be prohibitive. Ideally then, we should seek a method that contains microstructural detail, but leverages the speed of classical continuum-based finite-element (FE) modeling. In this work, we demonstrate the use of the Holzapfel-Gasser-Ogden (HGO) model [201, 202] to fit the behavior of microstructural network models. We show that Delaunay microstructural networks can be fit to the HGO strain energy function by calculating fiber network strain energy and average fiber stretch ratio. We then use the HGO constitutive model in a FE framework to improve the speed of our hybrid model, and demonstrate that this method, combined with a material property update scheme, can match a full multiscale simulation. This method gives us flexibility in defining complex FE simulations that would be impossible, or at least prohibitively time consuming, in multiscale simulation, while still accounting for microstructural heterogeneity.

Introduction:

Biological soft tissues are hyperelastic materials exhibiting a broad range of behaviors. This behavior is largely dictated by the presence of both basal gel-like substance and composite networks of fibers (Fig. 45). To date, most mathematical descriptions of material behavior rely on constitutive relations in the continuum mechanics framework. Many of these material models are drawn from an average over the microstructure. The benefit of material models of this form, like the Holzapfel-Gasser-Ogden (HGO) model (also known as the Gasser-Ogden-Holzapfel (GOH) model) is that the calculations of both stress and elasticity are simplified into a straightforward mathematical form. The alternative, then, is the multiscale model, where one precisely defines the microstructure, then passes microstructural information up a scale to the macroscopic geometry. The benefit of multiscale models is one extracts much information on the material at the fiber composite level. However, such models are computationally expensive. On the other hand, what continuum constitutive models lack in material detail, they more than make up for in computational savings over their multiscale counterparts. Therefore, perhaps the most ideal option would be a hybrid approach, leveraging the speed of continuum constitutive relations when the microstructural detail is not needed, and using a multiscale model when we seek information on the cellular scale. In this work, we propose a simple solution for coupling a microscale fiber-network model to a macroscale continuum constitutive model of the HGO type with the goal of improving computational efficiency of the multiscale model while maintaining microstructural detail.

Methods:

Mathematical Preliminaries:

Kinematic quantities important in the following analysis are given here. The first important descriptor is the deformation gradient, $\boldsymbol{F}$, which maps the deformation from the undeformed domain to the deformed domain. Out of the deformation gradient comes the Jacobian, $\boldsymbol{J}$ which is

given as the determinant of $\boldsymbol{F}$, and represents the volume change due to the deformation. Additional important kinematic variables are the right Cauchy-Green tensor $\boldsymbol{C}$, defined by $C_{IJ} = F_{jK}F_{iK}$, and the Green-Lagrange strain tensor $\boldsymbol{E}$, defined by $E_{IJ} = \frac{1}{2}(C_{IJ} - \delta_{IJ})$ where δ_{IJ} is the Kronecker delta. In this work, we also use several strain invariants. The isotropic first strain invariant, $I_1 = C_{II}$, and the transverse isotropic fourth strain invariant, $I_4 = a_I^0 C_{IJ} a_J^0$, dictated by a direction vector, $\boldsymbol{a^0}$. We further define the fourth strain invariant as the square of the averaged fiber stretch $\langle I_4 \rangle = H_{IJ}C_{IJ} = \hat{\lambda}_f^2$, where H_{IJ} is the generalized structure tensor (defined below) and $\hat{\lambda}_f$ is the averaged fiber stretch. A number of mechanics quantities are also addressed in the following analysis. The first is the concept of stress. The Cauchy stress carries the physical interpretation of force per current cross-sectional area and is defined as $\boldsymbol{\sigma} = \frac{2}{J}\boldsymbol{F}\frac{\partial W}{\partial \boldsymbol{C}}\boldsymbol{F}^T$ where W is the strain energy density function for the material. The second Piola-Kirchoff stress is defined as $\boldsymbol{S} = \frac{\partial W}{\partial \boldsymbol{E}} = J\boldsymbol{F}^{-T}\boldsymbol{\sigma}\boldsymbol{F}^{-1}$, which carries no meaningful physical interpretation, but does represent a useful quantity for purposes of calculation due to both force and area being mapped to the reference configuration.

Our goal is to convert a discrete fiber network model, which allows a high degree of structural fidelity but is computationally intensive, into an HGO model, which is computationally much more tractable. Because our goal is computational simplicity, we use the simple form of the HGO model shown above in Eq. 1. It is routinely assumed in affine models of this type that the constitutive equation can be written in terms of independent contributions from a non-fibrous matrix and the fiber network. The non-fibrous matrix is often incompressible or includes a volume-dependent term to limit material compressibility. Similarly, in multiscale models [107, 203, 204], a separate neo-Hookean matrix is introduced in parallel to the network. For the present analysis, it is therefore assumed that the fiber network contribution is distinct from the neo-Hookean, incompressible non-fibrillar matrix, and the current work focuses on the fiber network contribution only. The

fundamental challenge to be addressed is to convert a fiber network model into one based on the fiber stretch via I_4 (i.e. $a_I^0 C_{IJ} a_J^0$ in a model of the classical HGO form

$$W = C_1(I_1 - 3) + W^f(I_4) \qquad \text{Eq. 1}$$

where W is the total strain energy, C_1 is the neo-Hookean ground matric material constant, I_1 is the first strain invariant of the right Cauchy-Green tensor, and $W^f(I_4)$ is the strain energy density of the tissue fibers). That is, the problem is to determine parameters C_2 and C_3 such that the model

$$W^f = C_2/(2C_3)\,[exp(C_3(\langle I_4\rangle - 1)^2) - 1] \qquad \text{Eq. 2}$$

yields a fiber-network strain energy density function W^f that matches the results from the network computations. Here we delineate the difference between the square stretch, I_4, in a given direction $\boldsymbol{a^0}$, and the square stretch in the average fiber direction $\langle I_4\rangle = H_{IJ}C_{IJ}$. The invariant $\langle I_4\rangle$ is calculated as the double contraction of a generalized structure tensor H_{IJ} with the right Cauchy-Green tensor C_{IJ}. The generalized structure tensor H_{IJ} is defined as

$$H_{IJ} = \frac{1}{V}\int_\Omega N_I^m N_J^m dV = \frac{\sum_{m=1}^k V^m N_I^m N_J^m}{\sum_{m=1}^k V^m} \qquad \text{Eq. 3}$$

where $\boldsymbol{N}^m$ is the unit vector in the direction of fiber m, and $V^m = \pi(R^m)^2 L^m$ is the volume of a fiber with radius, R^m and length, L^m. The calculation of the generalized structure tensor and its use to calculate $\langle I_4\rangle$ are based on the underlying assumption that, in general, the network behaves affinely. This calculation does not account for different properties of fibers such as the tension-compression asymmetry of fiber response, or the different fiber types that might occur (e.g., collagen and elastin). There are also differences incurred because the fibers are exponential and the deformation in a network is not affine, meaning the apparent modulus of any given fiber need not be the same as any other or, in fact, the average fiber. There are several ways one could approach this problem, including calculating the end-state $h_{ij} = F_{iK}H_{KL}F_{Lj}$ for the network and mapping it back to the undeformed domain with or without those fibers that are in compression. This strategy, however, would rely on an accurate representation of the deformation, which is often unknown *a*

priori. A second option would be to not calculate the structure tensor from the fiber network, but instead treat its components as additional fitting parameters. Doing so, however, would leave the underlying structural information we have from the microstructural networks unutilized.

One of the challenges with a structure-tensor-based model is the so-called tension-compression switch. Fibers are very stiff in tension but buckle and support almost no load in compression. If the structure tensor and the resulting calculated $\langle I_4 \rangle$ do not exclude fibers in compression, then the model is at risk of overpredicting the stress response, especially if the model has been fitted to data from a different strain field. This issue has received much discussion (e.g., [205, 206]), and variations have been proposed in which compressed fibers are excluded [207, 208]. In the current work, we chose to use a simpler, all-fiber structure tensor. As noted earlier, the tension-compression switch is approximated smoothly in the discrete-fiber model by the exponential fiber constitutive equation; the specific representation of the switch has relatively little effect on the overall network mechanics [209]. We refer the reader to the in-depth discussions on structure tensors and tension-compression asymmetry in biological tissues given by Holzapfel et al. [206] and Melnik et al. [208].

To define the network behavior of biological soft tissue, Delaunay networks were generated using the Delaunay triangulation function, *delaunay*, in MATLAB R2019a (MathWorks, Natick, MA). Briefly, randomly generated seed points in the 3D space were used to generate a Delaunay tetrahedral network. The seed points represent network nodes, and the edges of the tetrahedral regions represent the fibers. After initial generation, the number of the seed points was adjusted to obtain a defined final volume fraction for each network, holding the fiber cross-sectional areas constant. The fiber volume fraction in a network is given by

$$\phi^f = \frac{V^f}{V} = \frac{\chi \sum_{m=1}^{k} \pi (R^m)^2 L^{*m}}{\chi^3 V^*} \qquad \text{Eq. 4}$$

where ϕ^f is the fiber volume fraction, V^f is the total fiber volume, V is the network volume, χ is a scale factor converting from computational length units to real length unit [m], R^m is the radius of

fiber m, L^{*m} is the length of fiber m in computational space, and V^* is the network volume in computational space.

The fibers in these networks were modeled as one-dimensional nonlinear springs connected at freely rotating pin joints (nodes) at two ends. The fibers are subjected to moderate to large strains and have negligible bending stiffness. The governing equation describing the *fibers in the network* was adapted from [210] and is defined as

$$f = \frac{kA}{B}(exp[BE] - 1) \qquad \text{Eq. 5}$$

where f is the force generated within the fiber, A is the fiber undeformed cross-sectional area, k and B are constant and represent fiber stiffness and nonlinearity, respectively, and $E = \frac{1}{2}(\lambda_m^2 - 1)$ is the Green strain of the fiber, m, stretched to stretch ratio λ_m. The values for k and B in Eq. 6 and the fiber radius were set to 10 MPa, 2.5, and 100nm, respectively, following Dhume et al. [211]. We emphasize that the function in Eq. 6 represents a single fiber in the network, where the function itself is chosen so that the force is zero at zero strain, with large magnitude forces developed in tension and low magnitude forces developed in compression, simulating the tension-compression switch seen in native collagen fibers. The solution of the network state given a prescribed deformation was calculated using Newton iteration to balance all forces on internal nodes. The overall Cauchy stress state for the network was then calculated as

$$\sigma_{ij} = \frac{1}{V}\int_{\Omega} \sigma_{ij} dV \approx \frac{1}{V}\sum_{m=1}^{k} \sigma^m V^m = \frac{1}{V}\sum_{m=1}^{k} \left(\frac{f_i^m}{A^m}\right) n_j^m (A^m l^m) = \frac{1}{V}\sum_{m=1}^{k} f_i^m n_j^m l^m \qquad \text{Eq. 6}$$

where σ_{ij} is the network volume averaged Cauchy stress, V is the network volume, σ_{ij}^m is the Cauchy stress of fiber m, V^m is the volume of fiber m, f_i^m is the force from fiber m, A^m is the instantaneous cross-sectional area of fiber m, $\boldsymbol{n^m}$ is the fiber normal direction in the deformed state, and l^m is the current length of fiber m.

There are, of course, infinitely many possible deformations, but a material property fitting problem can be reduced conveniently by considering the fiber network strain energy W^f as a function of $\hat{\lambda}^f = \sqrt{\langle I_4 \rangle} = \sqrt{\mathrm{H_{IJ}C_{IJ}}}$, which represents an averaged fiber stretch in the affine, continuous model. Although the product $\mathrm{H_{IJ}C_{IJ}}$ does not have any physical meaning within the context of the non-affine discrete fiber model, it is easily calculated and convenient for use in the fitting process. Likewise, W^f can be calculated either from computing an average stress in the domain [109] and integrating it with respect to its energy conjugate in the continuum sense to determine a strain energy, or by summing the total strain energy of all fibers and dividing by the domain volume. These two methods are given by

$$W^f = \int_{E_{IJ}=0}^{E_{IJ}} S_{IJ} dE_{IJ} = \frac{1}{V}\int_{\Omega} w^m dV \approx \frac{1}{V}\sum_{m=1}^{k} w^m V^m \qquad \text{Eq. 7.1}$$

where W^f is the total strain energy density of the fiber network, S_{IJ} is the second Piola-Kirchhoff stress, E_{IJ} is the Green strain, w^m is the strain energy density of fiber m, V is the domain volume, and V^m is the volume of fiber m. The individual strain energy of a fiber is given by

$$w^m = \int_{E_{IJ}^m=0}^{E_{IJ}^m} S_{IJ}^m dE_{IJ}^m \qquad \text{Eq. 7.2}$$

The results from a network simulation of any macroscopic deformation can then be represented as W^f vs. $\hat{\lambda}^f$. This method is further summarized in the flowchart in Fig. 46. With W^f vs. λ^f from the network determined, the total-fiber constitutive law can be fit to the aggregated network-scale simulation results. Although in principle any fiber constitutive law could be used, a continuum model in an exponential format that is similar to the fiber's qualitative behavior is an intuitive choice to predict fibers' overall behavior. Therefore, throughout this work we use the expression of Eq. 2 and fit C_2 and C_3 to the W^f vs. λ^f curve.

One can fit the behavior of a network by subjecting it to many potential deformations and fitting the total data, or one could simply fit one single deformation of interest. The former will give a better rough estimate if the actual deformation of the material is unknown, while the latter will be

more accurate if there is confidence in the magnitude and type of deformation the network will undergo. We henceforth refer to the initial average fit to many deformations as the ***HGO fit*** and to the later fit to a single deformation as the ***refit***. Care must be taken when refitting to a single deformation, as not all deformations will cause the average stretch to be greater than one. In these cases, the fit will not capture the behavior of the network, and an alternative fit should be used. In our model, we use two methods for dealing with this issue: 1. If the average stretch never exceeds one, we simply make the fiber modulus zero, thereby removing the fiber contribution, and 2. If the average stretch does eventually exceed one, but the fit is poor due to the behavior of the strain energy curve (i.e., Fig. 48), we attempt to fit only the slope of the strain energy curve for which the average stretch is greater than one. This effectively allows us to fit something closer to the stress, as the stress is directly related to the slope of the W^f vs. λ^f curve.

Hybrid Microstructural-Continuum Multiscale Approach

The novelty of this approach is that it removes much of the computational overhead needed in fully coupled multiscale approaches. Particularly, the use of the network model to fit a continuous material model (HGO) lets us leverage the increased speed in calculating both stress and the material (or spatial) elasticity tensor of the continuum material model over the micro-network model. Take, for example, a network consisting of Q fibers and R nodes where we have Cauchy stress given by Eq. 7 converted to the PK2 stress to calculate the material elasticity tensor

$$C_{IJMN} = \frac{\partial S_{IJ}}{\partial C_{MN}} = \frac{\partial}{\partial C_{MN}}\left[\frac{1}{V_0} F_{Im}^{-1}\left(\sum_{k=1}^{Q} f_m^k l^k n_n^k\right) F_{Jn}^{-1}\right] \qquad \text{Eq. 8}$$

where S_{IJ} is the network PK2 stress, and C_{MN} is the right Cauchy-Green tensor, V_0 is the undeformed network volume, $\boldsymbol{F^{-1}}$ is the inverse deformation gradient tensor, $\boldsymbol{f^k}$ is the fiber force vector, $\boldsymbol{n^k}$ is the fiber direction vector, and l^f is the fiber current length. If we examine these equations, it becomes clear that, at a minimum, we would need to calculate the fiber force, $\boldsymbol{f}$ for each fiber, k, and we would need to calculate something akin to the fiber elasticity,

$\frac{\partial}{\partial C_{MN}}\left(\left(\sum_{k=1}^{N} f_m^k l_n^k\right)\right)$ for each fiber, *k*. For each network at each Gauss point in each element (i.e. 8 networks per hex element), we would have to calculate both of these quantities. That means we would have to run one network simulation per Gauss point and make Q calculations for the stress and Q calculations for the elasticity per network, if there existed an analytical solution to the elasticity tensor, which, in the case of non-affine networks, is not necessarily the case. Additionally, the network solution relies on determining the static force balance of internal nodes, which, if solved explicitly, would yield another *R* calculations. However, this solution typically involves implicit solution via Newton iteration, resulting in between 5-10 iterations to achieve static equilibrium for a well-conditioned network. Thus, in the best case scenario, we would have $2Q+R$ calculations per Gauss point. If we contrast this with the HGO model, which involves one stress calculation and one elasticity calculation per Gauss point, we might well expect a decrease in computational cost on the order of $Q + \frac{1}{2}R$ per Gauss point.

Once the HGO properties are fitted to the network simulations, we can use those material inputs in a finite element (FE) framework as shown in Fig. 47a. This allows us to rely on the constitutive relation to solve the FE simulation rather than having to use costly microscale network simulations. Further, once we have the solution from the FE simulation, we can extract the deformation gradient at any point of interest and run the networks to evaluate any microstructural quantities such as fiber orientation or fiber stresses. This offers us the ability to evaluate discrete quantities in regions of interest, or to pass strains down to the microstructure to evaluate fiber remodeling or failure.

In an FE simulation, one often is concerned with an imposed deformation that occurs in a series of small steps. In this case, one can choose whether to iterate at a given step until the deformation field and model are consistent, or to adjust the model based on a given step and use the updated parameters for *the next* step. The latter approach introduces some error in that the continuum model does not match the microscopic model at the end of the step, but it has the considerable efficiency

advantage of allowing an update at relatively low computational cost. The lagging update errors can also be further mitigated by imposing smaller deformation steps where in the limit of an infinitesimally small step the error becomes zero. If one only cared about the end state of the deformation, then this method would introduce little error, especially if the state or states of interest are iterated to match microscopic and macroscopic stress. For this work, we chose the less costly approach of allowing the continuum model correction to proceed with the previous step update, and only iterate the state of interest, which in our example (2.7) is the final step. This process is shown in Fig. 47b.

In this study, we compared the fit of the HGO model to an array of deformations and the fit of an HGO model to a specific deformation. To do this, we first fit the network to x-uniaxial (magnitude 1.25), xy-biaxial, xz-biaxial (magnitude 1.1), xy- shear and xz-shear (magnitude 0.15). Once the HGO model had been fit, we tested it on a deformation that differed from the ones used in fitting the model parameters. Specifically, we modeled an element from complex motion of the stretching and three-point bending of a facet capsular ligament as in [212]. We imposed the deformation gradient of an element experiencing maximum stretch during the simulated experiment:

$$\boldsymbol{F} = \begin{bmatrix} 1.239 & 0 & 0.0035 \\ 0 & 1.048 & -0.0014 \\ -0.0080 & 0.102 & 0.770 \end{bmatrix} \qquad \text{Eq. 9}$$

which was dissimilar to the uniaxial, biaxial, and shear deformations used to fit the initial HGO model. The deformation was imposed on the discrete network model, and the volume-averaged Cauchy stress was determined. Concurrently, the Cauchy stress was calculated by the HGO model using the parameters fitted to the suite of deformations (given above as ***HGO fit***). In addition, in keeping with the ***refit*** update strategy discussed above, after the simulation was done, we refit the HGO model to W^f vs. λ^f giving us stress estimates for the deformation imposed in Eq. 9.

Comparison between Network-to-HGO Model and Full Multiscale Model

The goal of the proposed method is to facilitate higher-efficiency multiscale simulations based on network structure. To evaluate its potential, we performed a full multiscale simulation of a representative L4-L5 facet capsular ligament (FCL) sample during spinal flexion (reproducing the model of Zarei et al. [213]). The model boundary conditions are defined through application of nodal displacements based on the bone surface from the kinematic simulation of Bermel et al. [214]. Additional details of the simulation setup are available in [213]. The same micro-networks used in [213] were applied in the network-to-continuum scheme, and the resulting continuum biomechanics problem was solved using the open-source finite-element platform FEBio [121]. Because FEBio does not support the HGO model, the ligament was modeled as a coupled solid mixture of a Mooney-Rivlin (effectively reduced to a neo-Hookean) ground matrix with three fiber families, leading to the strain energy density function

$$W = W^m + W^f \qquad \text{Eq. 10A}$$

where W is the total strain energy density. The first term in the total strain energy density is the non-fibrillar matrix component of the strain energy density W^m given by

$$W^m = C_1(I_1 - 3) - 2C_1 \ln J + \frac{\lambda}{2}(\ln J)^2 \qquad \text{Eq. 10B}$$

where C_1 is half the second Lamé parameter relating to the neo-Hookean material parameter, I_1 is the first strain invariant of the right Cauchy-Green tensor, C_{IJ}, $J = \det(\boldsymbol{F})$ is the differential volume change of the deformation, and λ is the first Lamé parameter relating to the bulk modulus. The tissue was considered as a compressible material with a matrix modulus and bulk modulus that matched those used by Zarei et al. [213]. The compressibility of the FCL was experimentally observed by Little et al., who suggest that the Poisson's ratio is as low as 0.3 [215]. The second half of the strain energy density is the fiber component of the strain energy density W^f given by

$$W^f = C_2/(2C_3)\sum_{p=1}^{3} h^p \left(exp\left(C_3(I_4^p - 1)^2\right) - 1\right) \quad \text{Eq. 10C}$$

where C_2 represents the fiber modulus, C_3 captures fiber nonlinearity, h^p is the weighting factor for fiber family p, $I_4^p = C_{IJ}N_I^p N_J^p = (\lambda^p)^2$ is the fourth strain invariant of the right Cauchy-Green tensor, C_{IJ}, $\boldsymbol{N}^p$ is the unit vector pointing in the direction of fiber family p in the undeformed state, and λ^p is the average fiber stretch of fiber family p. The undeformed direction vectors $\boldsymbol{N}^p$, were generated directly from the structure tensors H_{IJ} by taking the eigenvectors, which, since H_{IJ} is a symmetric positive definite matrix, give three orthogonal fiber directions. For the current work, we use these three orthogonal fiber families pointing in the principal directions of H_{IJ} and assign the weight h^p to each family based on the eigenvalues of H_{IJ} corresponding to each eigenvector $\boldsymbol{N}^p$. Fiber material parameters C_2 and C_3 were fit to the W^f vs. λ^f plots using the method described above. The neo-Hookean material parameter, C_1, and the bulk modulus parameter, λ, were set to 0.025 MPa and 0.417 MPa, respectively, to match [213]. The analogous stress for this strain energy function can be found in the FEBio manual [216] under compressible materials Fiber with Exponential Power Law (4.1.3.8) and Coupled Mooney-Rivlin (4.1.3.17).

Briefly, to generate the finite-element simulation, we imported the L4-L5 FCL geometry mesh of hexahedral elements [213], and applied HGO parameters to each individual element corresponding to the microstructural networks applied in [213]. To simulate flexion, the displacement of the nodes at the entheses (left and right sides of Fig. 4a) were specified based on the the L4-L5 motion segment model [214] as further described in [213].

Initially, micro-networks from the full multiscale model were fit to the HGO using multiple deformations, as described previously. A FEBio model of the representative FCL sample bending in flexion was then simulated using the initial HGO fit for fiber material parameters in Eq. 7C. For added accuracy, the deformation gradient tensor for each element in the FEBio HGO model was then used to refit the fiber material parameters. For comparison, maximum shear stress and

maximum shear strain fields were computed for the full multiscale model, the FEBio initial HGO model, and the FEBio refit HGO model.

Results:

A simple validation of the initial HGO fit and refit process is shown in Fig. 48. The initial HGO fit of uniaxial, biaxial, and shear deformations produces stresses of a similar magnitude as the network simulation under the deformation given in Eq. 9 (Fig. 48a). However, the results show large discrepancies in the shape of the curve (Fig. 48a), which are largely corrected in the refit process (Fig. 48b). The study presented indicates the viability of ftting an HGO model using the underlying orientation and a generated W^f vs. λ^f for many deformations to give a rough estimate of parameters, while highlighting importance of the refit process to producing the proper behavior. Further, this case study demonstrates how network mechanics vary significantly from the extrapolated HGO model under different deformations.

The trouble with extrapolating network mechanics can be partly explained by the non-affine nature of fiber networks. As a simple verification, suppose we have the network shown in Fig. 49a having $H_{IJ} = \begin{bmatrix} 2/3 & 0 \\ 0 & 1/3 \end{bmatrix}$. If we stretch in the direction of fibers as shown in Fig. 49b where $F_{iJ} = \begin{bmatrix} 3/2 & 0 \\ 0 & 2/3 \end{bmatrix}$ and $C_{IJ} = \begin{bmatrix} 9/4 & 0 \\ 0 & 4/9 \end{bmatrix}$, we have an estimated average fiber stretch of $\langle \lambda_f \rangle = \sqrt{H_{IJ}C_{IJ}} = \sqrt{3/2 + 4/27} = 1.284$. If we simply compute the average stretch of the three fibers we have $\lambda_1 = 2/3$ and $\lambda_2 = \lambda_3 = 3/2$ which gives us a mean stretch of $\bar{\lambda} = 1.222$. Now if we take the same network and stretch transverse to the direction of alignment as shown in Fig. 49c where $F_{iJ} = \begin{bmatrix} 2/3 & 0 \\ 0 & 3/2 \end{bmatrix}$ and $C_{IJ} = \begin{bmatrix} 4/9 & 0 \\ 0 & 9/4 \end{bmatrix}$, we get an estimated average stretch of $\langle \lambda_f \rangle = \sqrt{8/27 + 3/4} = 1.023$. If we then compute the actual stretches by computing the equilibrium positions assuming that the fiber forces are linear in strain such that sum of vertical forces is zero:

$$\sum f_y = 0 = (L_1/l - 1) - 2(L_2/l - 1)\cos(\theta) \qquad \text{Eq. 11}$$

and enforcing the geometric constraints that $L_2\cos(\theta) + L_1 = 1.5/2$ and $2L_2\sin(\theta) = 1/1.5$, we can solve giving $L_1 = 0.439$, $L_2 = 0.456$, and $\theta = 47.0^o$. Thus, the stretches are $\lambda_1 = 0.88$ and $\lambda_2 = \lambda_3 = 0.91$ giving an average stretch of $\bar{\lambda} = 0.900$. This example leads us to two observations: 1. The estimated stretch transverse to the direction of alignment is far from that in the direction of alignment, and 2. The estimated behavior of the stretch transverse to the direction of alignment is not representative of the true average, and is, in fact, indicating the network is in tension when the true behavior of the network shows all the fibers in compression. This simple example drives home the point that the networks estimated using the structure tensor, H_{IJ} can be quite different from the real network behavior when the network is loaded transverse to its preferred direction of alignment. This issue one can encounter when trying to fit the network behavior to the HGO model where the network itself develops almost no stress (effectively zero since the fibers buckle in compression) despite the fact that the HGO model using the structure tensor and calculating $\langle I_4 \rangle$ indicates the fibers should be in tension. This results in a fitted HGO fiber stiffness of ~0, which is clearly unphysical in general, but may be true for certain deformations. This effect is one that we must account for in our fitting method (e.g. by using a fit/refit process).

Maximum shear stress and strain fields are shown for the multiscale model, initial HGO model, and refit HGO model (Fig. 50). The maximum shear stress and strain distribution of the HGO model compared to the multiscale model are visually similar, and the HGO model was able to predict the regions of high shear stress and strain. The initial HGO model parameters underpredicted the magnitude of the maximum shear stress and overpredicted the max shear strains in these regions, but the accuracy of the tissue's stress prediction improved with a refit of the HGO parameters with each element's average deformation gradient tensor. The refit HGO model more accurately localized regions of high tissue shear stress, at the cost of a small increase in the tissue's strain, when compared to the initial HGO model. This observation is supported by the improvement of RMS error of the refit HGO model maximum shear stress compared to the initial HGO model.

The RMS errors for the initial HGO model maximum shear stress and strain are 0.074 MPa, and 3.28%, respectively. The RMS errors for the refit HGO model maximum shear stress and strain are 0.062 MPa, and 4.12%, respectively. Further, the computation time for the entire HGO simulation including the final step refit is shown in Table 8. The time to run the HGO simulation is orders of magnitude decreased over the full multiscale simulation.

Table 8. Computation Time for Multiscale vs HGO FE model

Task	***Multiscale***	***HGO***
	Time [CPU hour]	
Initial Simulation and Fit of 900 Networks (x 5 deformations x 20 steps)	NA	1.12
Re-simulation and Refit of 900 Networks (x 1 deformation x 20 steps)	NA	0.34
FE Simulation	2622.69	0.02
Total	2622.69	1.48

Discussion:

In this work, we developed a hybrid microstructural-continuum multiscale model to reproduce the macroscopic constitutive behavior of a structure-based multiscale simulation. This paper presents methods to speed up the model construction and full analysis of a discrete-fiber multiscale model while accounting for the microstructural details of a heterogeneous tissue such as FCL. The proposed work uses the structural parameters of discrete fiber networks in a continuous-fiber model such as HGO to decrease the computational cost of a full multiscale simulation of a heterogeneous tissue from 2622.69 to 1.48 CPU-hours as is shown in Table 8.

The results of Fig. 48 suggest that extrapolating beyond the fitting range can give an overall rough estimate of behavior, but it is important to update the parameters based on the deformation. If the deformation of interest is known (e.g., one knows that the system will be loaded in equibiaxial extension), then one can simply fit a model to that deformation and use the model, but the deformation of interest is almost never known *a priori*. Even if the type of deformation or the boundary conditions are known, however, the magnitude of the deformation is often unknown, and tissue heterogeneity virtually assures that the local deformation is different from the applied

(global) deformation, so it is essential to have a procedure that can be used to provide a good initial guess of the continuum model parameters one needs, as well as a method for updating the parameters. This work demonstrates reasonable methods for selection of initial parameters via fitting multiple deformations, and a refitting process based on the simulation deformation gradient.

These results indicate that the HGO model itself does not fully capture the change in network behavior with the generalized structure tensor, H_{IJ}. One issue with this structure tensor is that, to properly capture the behavior of a dispersed fiber population with a tension-compression switch, one needs to recalculate the tensor using only the tensile fibers. In an ideal case, this would be done for each deformation step (alternative approaches are not given here, but are discussed in [206, 208]). Such an approach could help alleviate some of these differences observed in the current study, but the cost of performing a spherical integration over 3D distributions of fibers might well prove greater than that of the simple refit process, especially for multiple fiber families or multiple fiber types. Some network models, might be better fit, to a certain extent, by a compressed-fiber-excluding macroscopic model, and a more thorough testing regimen achievable via computational vs. experimental tests may provide more insight into exactly what behaviors are captured or lost by such models. Future in-depth studies of on the translation of a discrete, fiber-level tension-compression switch to a macroscopic fiber compression exclusion model are merited.

As discussed above, we do not account for the fiber tension-compression asymmetry in the calculation of H_{IJ}. That is, H_{IJ} is calculated based on all fibers in the initial state. We instead capture the fiber tension-compression switch through the fiber constitutive law, which is much stiffer in tension than in compression. The tension-compression switch of fibers is intrinsic to the microstructural model, so we remove the requirement for fiber exclusion from the structure tensor [206, 217]. The HGO parameters C2 and C3, which are fit to the results of the microstructural simulations, are thus informed by the tension-compression asymmetry inherent to the model. It may

be possible that a better fit of the microstructural model could be obtained by an HGO model with a tension-compression switch, but that possibility was not explored in the current work.

We further described how a curve-fit of multiple simulations could allow one to select continuous model parameters to represent Delaunay networks with arbitrary orientation without rerunning simulations (Fig. 48). The construction of such databases of properties for networks can further simplify the assessment of material parameters that describe network behavior. While the equations show a high degree of variance, construction of a broad curve-fit of parameter values can give us a reasonable starting point for a wide range of networks. The initial fitting of the network behavior to multiple deformations is the largest contribution to the overall time spent on simulation for the HGO FE model (Table 8). Thus, if one can select starting parameters based on network orientation and some other metric of network construction like network type (Delaunay, Voronoi, etc.), one can greatly reduce the time to produce simulations. In fact, this method of reproducing network parameters from pre-defined relations rather than having to generate and run the networks could have a significant impact on creation and simulation of multiscale tissue models, allowing for many hypotheses to be tested quickly with regards to fiber orientations, tissue composition, or localized defects. If such a strategy is to be pursued, however, it is imperative that the starting parameter values be based on networks similar to the ones being used in the simulation.

We describe the application of the microstructural-to-HGO modelling strategy to a finite-element simulation. This simulation shows similar results to a full multiscale simulation (Fig. 50) while reducing the model construction and simulation time by orders of magnitude over a full multiscale approach (Table 8). As mentioned previously, this approach, combined with estimation of material parameters without generating and simulating networks, could enable multiscale simulations without the need for a supercomputing cluster. Eliminating the necessity of bridging micro- to mm-scale could also open up opportunities to take tissue multiscale approaches up

another scale level to organ or full-body kinematics, further helping us identify things like the role local FCL defects play in the spine or elucidating the role of microstructure in aneurysm mechanics.

Model Limitations

As with all models, the proposed system has several limitations. First, because the HGO model is an imperfect estimator of actual network behavior, there will be intrinsic errors even after the proposed refitting procedure. One could perform this analysis with other constitutive models that may capture specific behavior differently as compared to the HGO model (take for example the Blatz-Ko material for compressible materials like collagen gels [218], or any of a number of actively contracting models for vascular tissues such as [219–221]). The proposed technique is adaptable to different constitutive models, and could be fit to multiple affine models to select the best choice.

As noted above, the HGO model did not fully capture the observed network behavior. We observe that a strength of our approach is that the computational experiments are not limited by the physical realities of equipment design and sample damage, so one can perform any experiment desired and as many experiments as desired. As a result, any inability of the continuum-scale model to capture the micro-scale network model's behavior will be apparent. Whether this effect is a positive or negative feature depends on the perspective of the user: it virtually guarantees inconsistency between the micro- and macro-scale models in some deformation, but it enables the user to see exactly where and how severe such inconsistency is, which could be valuable. For example, one could decide that the inaccuracy is in a range of deformations that are not physiologically relevant, or the inconsistency could inspire the development of new constitutive models at the continuum scale.

Another limitation of the approach in current form is the restriction to a single, non-evolving network. A major advantage of the full multiscale approach is the ability to accommodate changes in the network due to, e.g., failure [45, 222, 223] or remodeling [110, 113]. In the case of an

evolving network, the macroscale parameters would necessarily have to be refit at each step. Knowing the deformation state at the previous step could allow for efficient re-fitting, but there is much work still to be done to identify the optimal strategy for such problems. Similarly, in particular in the case of the arterial wall, multicomponent models are important at both the microstructural [10, 45, 223] and macrostructural [224–227] scales, and the best strategy to fit a multicomponent, discrete-fiber microstructural model is by no means clear and has not been explored in this work.

Lastly, compressing the network in the direction in which most fibers are aligned might result in average of fiber stretch ($\hat{\lambda}_f$) less than one. In this case, some fibers are still stretched leading to a rise in the strain energy. The fitting procedure will be unable to capture these behaviors, and such artifacts will cause an increase in the stiffness of the model, since the slope of W^f vs. λ^f curve, i.e. stress, will be artificially increased as the fit attempts to match the network when average stretch becomes greater than one (i.e. W_f has been increasing from the network model since some fibers are in tension, but the overall average $\hat{\lambda}_f$ is still less than one, thus the fit must be stiffer than the network in order to minimize the distance between the curves). Conversely, as observed in the example given in Fig. 49, it is also possible for the average fiber stretch $\hat{\lambda}_f$ to give a value greater than one, while the true average is less than one. This would indicate that the fibers themselves have a negligible effect on the behavior. While this might be true for a specific deformation, it is, in general, not an accurate representation of the material, and thus requires special care to be taken in the fitting process. These problems are mostly theoretical, since tissues are almost always loaded in the direction that their fibers are aligned, but it is nonetheless important to make sure there is a method for dealing with this issue in this framework. We offer one solution in this work, but it is by no means the only way to deal with this issue.

Acknowledgments:

This work was supported by the National Institutes of Health through the grants U01 AT010326, U54 CA210190, T32 AR050938, and U01 HL139471. Ryan R. Mahutga and Lauren M. Bersie-Larson are supported by University of Minnesota Doctoral Dissertation Fellowships. Ryan R. Mahutga was supported by National Science Foundation Graduate Research Fellowship Program (NSF GRFP) under Grant No. 00039202. Any opinion, findings, and conclusions or recommendations expressed in this material are those of the authors(s) and do not necessarily reflect the views of the National Science Foundation.

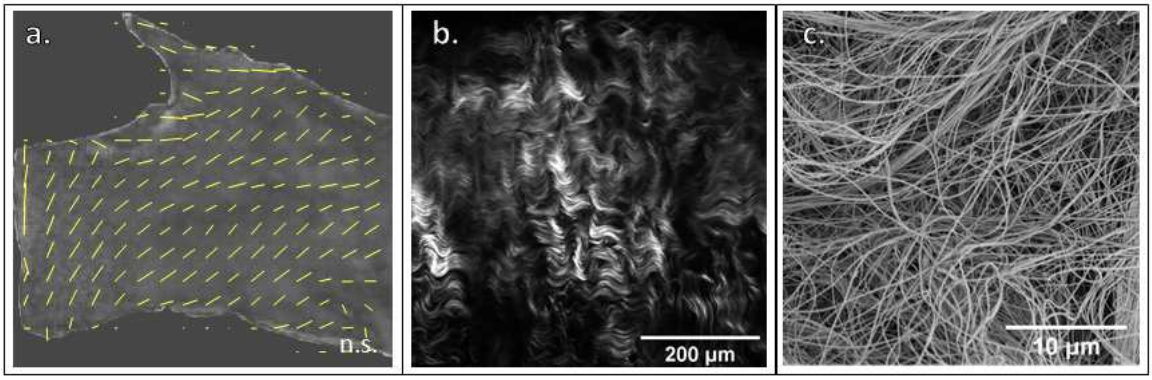

Figure 46 a. Quantitative Polarized Light Imaging (QPLI) of the brachiocephalic artery bifurcation showing macro-scale fiber orientation vectors. b. Second Harmonic Generation (SHG) imaging of collagen microstructure in the Facet Capsular Ligament (FCL). c. Scanning Electron Microscopy (SEM) of the collagen microstructure in the FCL

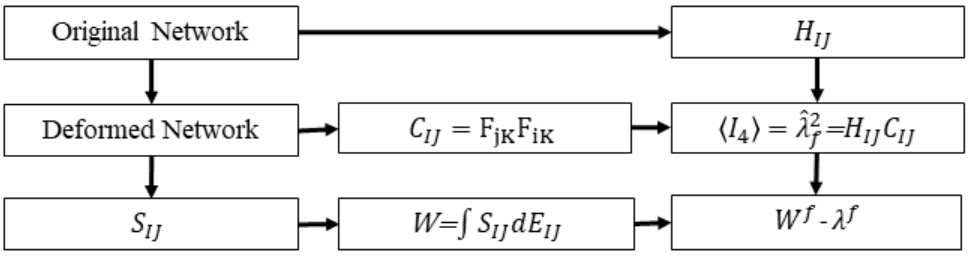

Figure 47. Flowchart for converting fiber network model to affine model

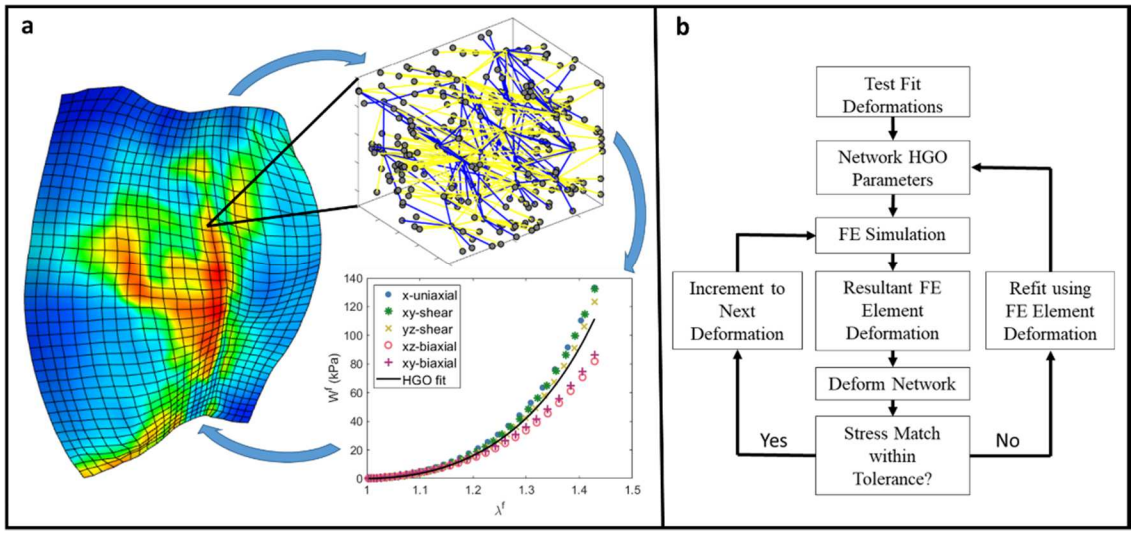

Figure 48. Schematic of the hybrid continuum-discrete multiscale approach. b. Flowchart for the hybrid continuum-discrete multiscale approach.

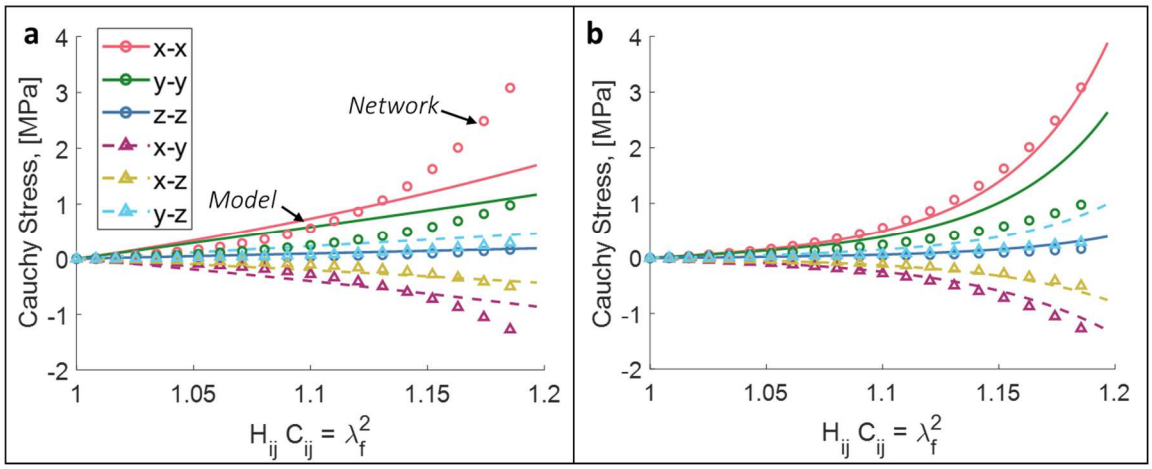

Figure 49. Comparison between HGO model and network simulation under complex deformation for a. initial fit and b. refit

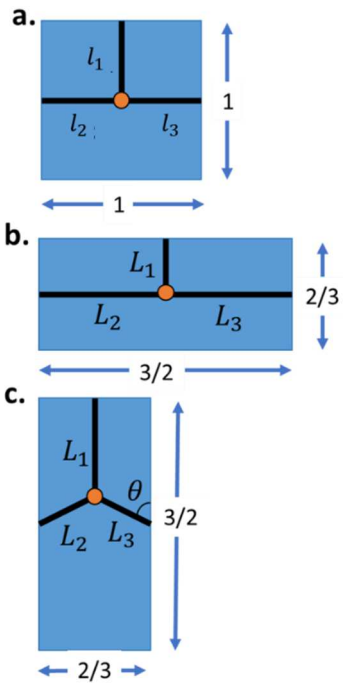

Figure 50. **a.** Undeformed network where $l_1 = l_2 = l_3 = l = 1/2$. **b.** Network stretched in the direction of strongest alignment where $L_2 = L_3 = 3/4$ and $L_1 = 1/3$. **c.** Network stretched transverse to the direction of stongest alignment where $L_2 = L_3$.

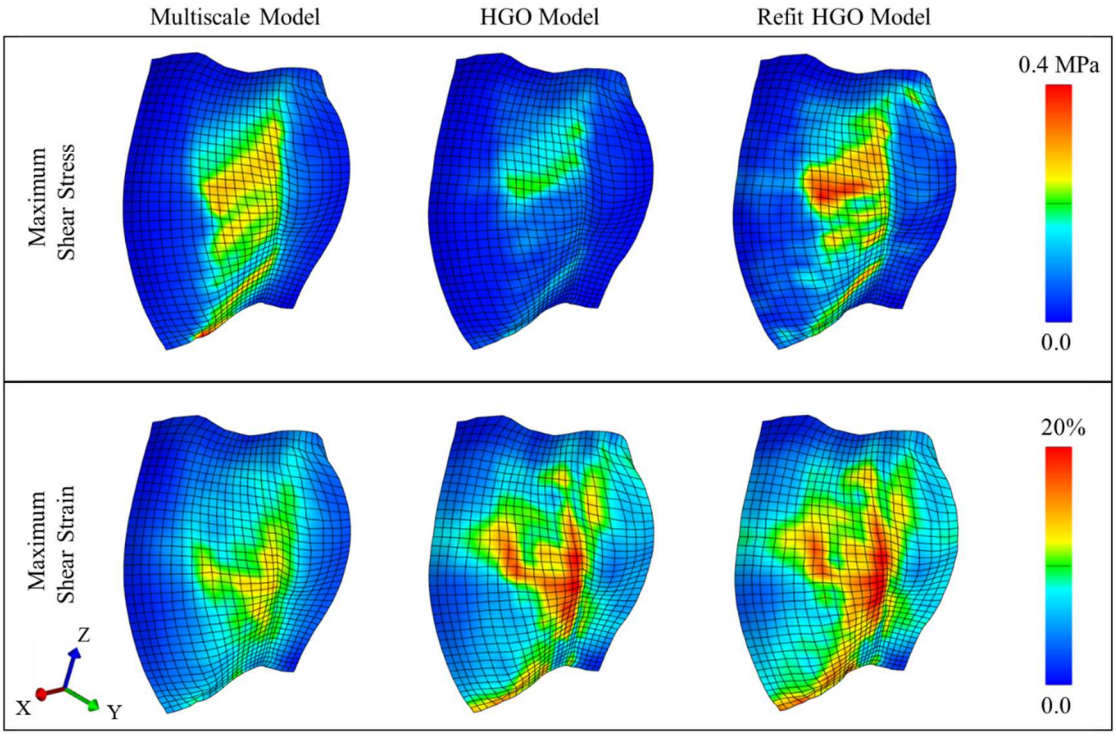

Figure 51. Maximum Shear Stresses and Strains of the multiscale, HGO, and refit HGO models for a single representative FCL sample during spinal flexion. The HGO model predicted the location of high shear stresses and strains while the refit HGO model improved the accuracy of magnitude of the maximum shear stress

CHAPTER 7: MULTISCALE REMODELLING OF TISSUE-ENGINEERED CONSTRUCTS

Summary:

The evolution of biological tissues as they grow and adapt remains of vital importance for understanding disease states from aortic aneurysm to low back pain. Understanding how cells, as the active component of tissues, modulate their environment through the manipulation, addition, and removal of constituents is significant, not only from the aspect of understanding disease progression, but also for creating therapeutics such as tissue-engineered grafts. In this work, we demonstrate a technique for performing multiscale fiber-network remodeling simulations utilizing existing finite-elements codes and discrete-fiber networks. This technique offers unique insights into fiber remodeling and subcellular structural mechanics. We are able to verify the technique using a simple geometric case, and further validate it against simple existing tissue engineered constructs. We recapitulate macroscopic measurables including mechanics and fiber orientation, while also tracking fiber length and radius changes.

Introduction:

Recently there has been a move toward computational validation of medical devices in early development, preclinical testing, and in U.S. Food and Drug Administration (FDA) approval [228, 229]. However, despite the amount of data one can gather from classical finite element models, many still fall short in predicting both failure and growth/remodeling. These two aspects are particularly important in trying to understand impacts on the body while trying to optimize long-term outcomes. Researchers and companies expend many resources on preclinical trials of devices, many of which end up with devices underperforming and requiring redesign. One example of the successes one can make by simply refining designs in computational tools is that of Sanders et al. and Emmert et al. where heart valves were redesigned following computational analysis using growth and remodeling, and the redesign validated in a preclinical trial in sheep [92, 106]. While this study demonstrates how effective computational modelling can be in design of medical devices, we propose taking the idea a step farther in order to understand what happens at the microstructural level and predict abhorrent remodeling or failure modes the tissue may undergo based on the underlying extracellular matrix (ECM).

Previous work in the field has been performed using continuum models of growth beginning with the work of Skalak [161]. This outlined the general form for modeling continuum growth in biological tissues which was expanded to arterial tissues [65, 66, 80–84]. These methods focus on the adaptation of generic cylindrical structures to pressure and stretch. Recent work has focused on taking these models and applying them to increasingly complex geometries or increasingly realistic constitutive relations [85, 86, 95–100, 87–94]. In our analysis, we focus on the simulation of an aortic valve implanted in adolescent sheep [230, 231]. Others have approached similar problems using continuum remodeling [105], but our technique offers unique insight into failure modes and specific ECM structure [10].

Methods:

Growth Preliminaries:

Modeling tissue growth and remodeling has been performed in many ways. Traditionally, the material undergoing growth and remodeling is treated as a continuum. There are two ideas that intersect in the area of tissue growth and remodeling one is the idea of kinematic growth, as in [71, 80–82, 161], where one can have the reference configuration grow based on some underlying remodeling law, and the growth of the tissue can be prescribed as a deformation tensor. This is show schematically in Fig. 52, and is given mathematically as

$$F_{iJ} = F^{g}_{iK} F^{e}_{KJ} \qquad \text{Eq. 1}$$

where F_{iJ} is the total deformation tensor, F^{g}_{iK} is the growth tensor which is the mapping from the initial reference configuration to the grown reference configuration, and is typically a function of stress or strain (stretch), and F^{e}_{KJ} is the elastic deformation tensor, which is the elastic deformation from the growth reference configuration to the deformed reference configuration. It is important to note here that even in lieu of any prescribed boundary conditions, F^{e}_{KJ} is not, in general, the identity because the growth must be rectified by the compatibility equation, such that, in the absence of body forces,

$$\sigma_{ij,j} = \mathbf{0} \qquad \text{Eq. 2}$$

where σ_{ij} is the Cauchy stress.

The other is the idea of a constrained mixture, as in [64–66, 68, 84–86, 88–90]. In constrained mixture theory, one defines the mass fractions of individual constituents such that each constituent has its own associated mass fraction (or volume fraction) such that

$$\phi^{s} = \frac{1}{v}\int dv^{i} = \frac{1}{v}\sum_{i} \; v^{i} = \sum_{i} \; \phi^{i} \qquad \text{Eq. 3}$$

where ϕ^{s} is the total solid volume fraction, v is the volume of the tissue, v^{i} is the volume of constituent i, and ϕ^{i} is the volume fraction of constituent i.

It is further assumed that the constituents themselves are independent, but constrained to move together such that

$$\sigma_{kl}(F_{mN}) = \frac{1}{v}\int \sigma^i_{kl}(F_{mN})dv = \frac{1}{v}\sum_i \ \sigma^i_{kl}(F_{mN})v^i = \sum_i \ \phi^i\sigma^i_{kl}(F_{mN}) \quad \text{Eq. 4}$$

If we combine this idea with the kinematic growth theory, we can have each constituent evolve such that

$$F_{mN} = \left(F^g_{mK}\right)^i (F^e_{KN})^i \quad \text{Eq. 5}$$

So that the overall deformation gradients are the same, but the growth and elastic stretch of any given constituent need not be. We also note that $\sigma^i_{kl}(F_{mN})$ when $F_{mN} = \delta_{mN}$ does not necessarily mean $\sigma^i_{kl}(\delta_{mN}) = \mathbf{0}$ since the reference, strain-free configuration is $\left(F^g_{mK}\right)^i$ which is not, in general, equal to F_{mN}.

The benefit of using this method is the computational efficiency of being able to limit the behavior to a specified number of constituents (i.e. i=3 for tissues composed primarily of cells, collagen and elastin), and treating those constituents as independent so that for a specified deformation each may remodel with no effect on the other constituents.

Clearly this is an approximation since cells are constantly interacting with their microenvironment. If we return to Eq. 4, we can manipulate it such that we account for all constituent fibers, which gives us

$$\sigma_{kl}(F_{mN}) = \frac{1}{v}\sum_f \ \sigma^p v^p = \frac{1}{v}\sum_p \ \frac{f^p}{a^p}a^p l^p = \frac{1}{v}\sum_p \ f^p l^p \quad \text{Eq. 6}$$

where σ^p is the stress of fiber p, v^p is the volume of fiber p, f^p is the force in fiber p, a^p is the deformed cross-sectional area of fiber p, and l^p is the deformed length of fiber p.

Microscale Mechanics and Remodeling:

In this work, we utilize microstructural discrete-fiber networks. The networks are generated using a periodic Delaunay tessellation using the tetrahedron edges as fibers. These fibers are linked at the nodes of the tessellation tetrahedrons via pin joint. The fibers in this model are of one type – collagen – which is represented as a helical spring [165] having parameters of spring radius $r_0 = 1.6nm$, helical radius $R_0 = 5.8nm$, helical separation $h_0 = \ 67.6nm$, and

modulus $E = 20MPa$. This model simulates the waviness of collagen with high modulus in tension and low modulus in compression. To solve for the internal equilibrium of the network subject to a deformation, we solve a Newton iteration to minimize the forces on all nodes.

The fibers are remodeled relative to the fiber stress. This model simulates the assumption that the cells remodel the microstructure to approach a defined target stress. The model for the remodeling of each fiber is given by

$$\frac{dR}{dt} = \frac{1}{\tau}\left(\frac{\sigma}{\sigma_\infty} - 1\right) R \; ; \frac{dL}{dt} = k\frac{dR}{dt} \qquad \text{Eq. 7}$$

where R is the fiber radius, t is time, τ is the remodeling time constant, σ is the fiber stress, σ_∞ is the homeostatic fiber stress, L is fiber initial length, and k is a parameter relating fiber lengthening to fiber thickening. As the fibers are remodeled, the network zero-stress state is updated by finding a new deformation such that the stresses are zero. More precisely, we reduce the problem to finding F_{ii}^g where $\sigma_{ii} = 0$ since the shear stresses are relatively small throughout the remodeling process. Further, to maintain network stability, we enforce an osmotic (or hydrostatic) pressure to prevent the network from collapsing. The expression for the osmotic pressure is

$$c_{fcd} = c_0\phi \; ; P = RT\left(\sqrt{c_{fcd}^2 + 4c_*^2} - 2c_*\right) \qquad \text{Eq. 8}$$

where c_{fcd} is fixed charge density, c_0 is a fixed charge scaling factor (70 M), ϕ is the fiber volume fraction, P is the osmotic pressure, R is the universal gas constant, T is the tissue temperature (310K), and c_* is the external osmolarity (150 M).

Macroscale Mechanics and Remodeling:

The macroscale models in this work were simulated using FEBio2.5 [121]. The verification model was created using FEBio Studio. The geometry is meshed using 8 node hex elements. The finite element model for the cruciform validation case was created by using a 2D segmentation of the geometry in [232] and extruding the thickness. The geometry was meshed

using 8 node hex elements. For either case, each element was prescribed a unique constitutive model based utilizing the solid mixture model with a neo-Hookean ground matrix with embedded exponential-power fibers [216]

$$W = c_1(I_1 - 3) + \frac{K}{2}(ln\ (J)\ )^2 + \sum_{i=1}^{3} \frac{c_2^i}{2c_3^i}\left[exp\ \left(c_3^i\left(I_4^i - 1\right)^2\right) - 1\right] \quad \text{Eq. 9}$$

where W is strain energy density, c_1 is the modulus of the ground matrix, $I_1 = tr(C_{ij})$ is the first strain invariant of the right Cauchy-Green tensor $C_{ij} = F_{iM}F_{jM}$, K is the bulk modulus, c_2^i is the fiber modulus of family i, c_3^i captures the nonlinearity of fiber family i, $I_4^i = C_{ij}N_iN_j$ is the fourth strain invariant C where N is the fiber direction vector.

The undeformed reference state for each element was defined using the growth deformation tensor, and the compatibility of the overall geometry was enforced using the FEBio Prestrain material [233]. This allowed for each element to have a unique reference configuration, with compatibility enforced on the geometry to visualize the development of residual stresses within the material.

Micro-to-Macro Coupling:

The microscale network model was coupled to the macroscale geometry by defining a stress-strain relationship for each network. This was achieved by creating a stress-strain curve for a prescribed subset of deformations. For the first iteration, in the absence of any prior knowledge of macroscale deformations, we perform a suite of uniaxial, biaxial, and shear tests to generate a characteristic behavior for the material. After the first iteration, we utilize the deformation from the finite element simulation to perform a simple linear ramping from the undeformed network configuration to the deformed configuration. We then fit the behavior subject to the applied deformation. This resulted in the ability to define the strain energy density function in Eq. 9 such that it would approximate the behavior of the discrete-fiber networks.

Functionality:

The code operates by calculating the material properties and zero-stress state (growth) from the networks then using that as inputs into the FEBio simulation. The simulation is run and the results for the element deformations and the element stresses are used for the network remodeling simulation. Briefly, the network is either remodeled using deformation control or stress control, which is user defined. The code also operates using a forward Euler approach with the user defining the time step length and the duration of remodeling for each FE simulation. The code begins by calculating the zero-stress state for the network using Newton's method with a numerical Jacobian calculation. The code then deforms the network either to the given deformation or to the given stress (which is also solved using Newton iteration) depending on the selected control type. The code then calculates the internal equilibrium of fibers and remodels the fibers based on Eq. 7. The time is then incremented and the code continues remodeling the network until it reached the defined time duration. The end state network material properties and the ending zero-stress state are calculated and used as input to the next iteration FE simulation. The overall FE-network remodeling algorithm is summarized in the flowchart in Fig. 53A. The network remodeling code is summarized in the flowchart in Fig. 53B.

Verification Case Study:

To verify the simulation framework, we performed a suite of simple remodeling cases. We define a simple eight element cube macroscale geometry (Fig. 54A). Each element of the cube is represented by an eight fiber, one node periodic network (Fig. 54B). The network behavior was fit (Fig. 54C) to the strain energy density function in Eq 9 to define the materials for each element of Fig. 54A. Test cases utilizing boundary conditions of free in all dimensions and fixed in all dimensions were used to validate the code and compare to the results of a single network remodeled under the same conditions.

Experimental Case Study:

To test our remodeling framework, we simulate a simple collagen gel-based cruciform seeded with fibroblasts as in [232]. We perform loading scenarios of free contraction, holding the biaxial sample fixed, and strip biaxial increase 20% load and decrease 20% load shown schematically in Fig. 55A. During remodeling, we track the grip force and the overall geometric changes to compare to experimental results [232]. We also track fiber realignment and changes in mechanics to compare to experimental observation [234]. This case study served as a proof-of-concept for our simulation design, and also allowed us to fit the fiber homeostatic stress level.

Results:

Verification Case Study:

To verify the results of our simulation framework, we addressed two network remodeling methods one using deformation control (i.e., fixing the deformation, then remodeling) and one using stress control (i.e., deforming the network to match the stress, then remodeling). We also performed two multiscale simulation scenarios with the geometry shown in Fig. 54. We consider boundary conditions of all faces fixed and all faces free.

With all faces fixed, we see very good agreement between the single network simulation, the deformation control multiscale simulations, and the stress control multiscale simulations (Fig. 56). In the first column, we show that the stress approaches the same target stress for all simulation types. In the stress control multiscale simulation we do steps in the stress profile of the stress-control simulation (last row) due to the nature of the network deformation changing with remodeling as the stress is matched. In both growth (second column) and fiber volume evolution (third column), we show almost not difference between the various simulation types.

With all faces free, we show good agreement between the single network simulations and the force-control and stress-control multiscale simulations (Fig. 57). In the stress evolution (first column), we see that the deformation control simulation (second row) at each multiscale step begins at zero stress, but then ramps up. This is to be expected as the deformation is fixed so the

network naturally tends to remodel to develop some level of stress. We do note that as time progresses the amount of stress developed in remodeling does decrease, indicating the simulation is closing in on a solution. The growth in the simulations (second column) also shows good agreement, with the deformation-control simulations (second row) showing slight differences in the remodeling profile. The fiber volume fraction profiles also show good agreement (third column), with the deformation-control simulations (second row), again, showing slight differences in the remodeling profile.

Experimental Case Study:

To understand the utility of this approach, we simulate a simple tissue-engineering example shown in Fig. 58. We simulated the grip force from the experiments of Eichinger and Paukner et al. including both +20% load at 28h (Fig. 57A) and -20% at 28h (Fig. 58B).

In addition, we demonstrate changes in stress (Fig. 59). The initial homeostatic stress immediately prior to 28h is shown in Fig. 59A and 59E. The stress immediately following the 28h jump is shown in Fig. 59B (+20% force) and Fig. 59F (-20% force). The new homeostatic stress state at 42h is shown in Fig. 59C and 59G for +20% and -20% force respectively. In addition to analyzing the stress, we also show the fiber orientations which began isotropic, and at the end of test aligned in the arms while remaining relatively isotropic in the center region (Fig. 59D and 59H).

One major benefit of this framework is we are capable of looking at microstructural details during remodeling. Shown in Fig. 60 are the fiber lengths (top row) and fiber radii (bottom row) for the left arm (left column), the center arm (center column), and the top arm (right column). We see that in all cases the fibers get shorter (Fig. 60 A,B,C; purple-pink lines vs. light blue line). We also see that there is a letter degree of fiber radial growth in the center region than in either arm regions (Fig. 60D/F vs Fig. 60E)

Discussion:

This work demonstrates a novel method for multiscale simulation of remodeling in biological tissues. We couple network microstructural elements to finite element modeling via FEBio by using simple constitutive modeling. The finite element code solves the compatibility of the growth, and determines the stress-strain state, while the remodeling is handled by the microstructural model given the stress-strain state. Being able to apply the remodeling directly to the network level allows for gathering architectural information along with local material inhomogeneities. Further, the multiscale microstructural modeling also allows us to assess failure mechanics.

Verification Case Study:

The verification problem sets demonstrate the ability to match single-network remodeling using the FE multiscale framework (Fig. 56 and 57). We are able to show that two different methods (deformation control and stress control) can match the single network simulation provided we use small enough time steps (Fig. 57). This is important because it illuminates the importance of selecting the number of remodeling time steps relative to the finite-element steps. We note that the closer the network remodeling boundary conditions are to the imposed finite element boundary conditions, the more accurate the remodeling results. Thus, careful consideration should be given the setting up the microscale remodeling to maximize the accuracy of the technique.

Experimental Case Study:

Our experimental case study shows that our model is capable of matching simple experimental remodeling cases (Fig. 58) [232]. Our data also showed fiber directionality mimicking other cruciform experiments (Fig. 59D and 59H) [234]. Further, we are able to demonstrate alterations in individual fibers (Fig. 60), which allow us to visualize tissue heterogeneity.

Limitations:

The constitutive coupling using this method is an approximation of the network behavior, and, therefore, should be carefully considered. For example, the eight fiber networks used in the Verification Case Study showed very linear behavior, and was subjected to little shear deformation. Thus, it was reasonable to use the neo-Hookean constitutive model for the material. However, if out macroscale geometry was subject to compressive loads or shear loads, we may consider other constitutive models to accurately represent the network material behavior.

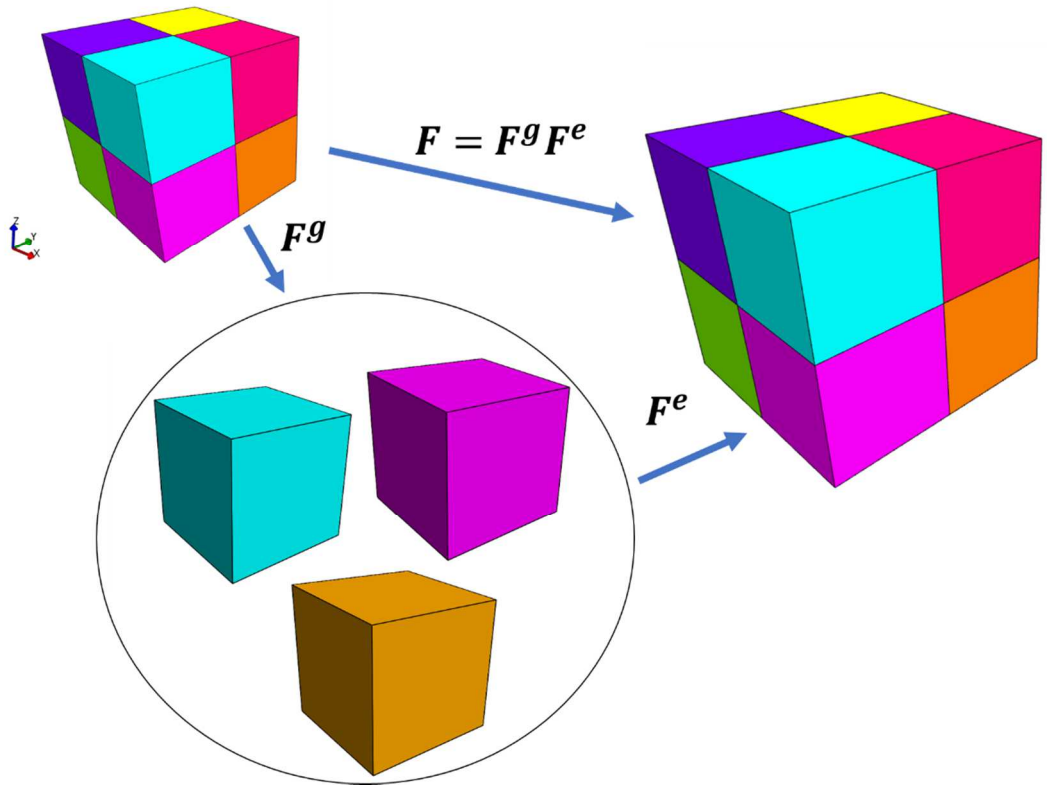

Figure 52. Growth theory schematic

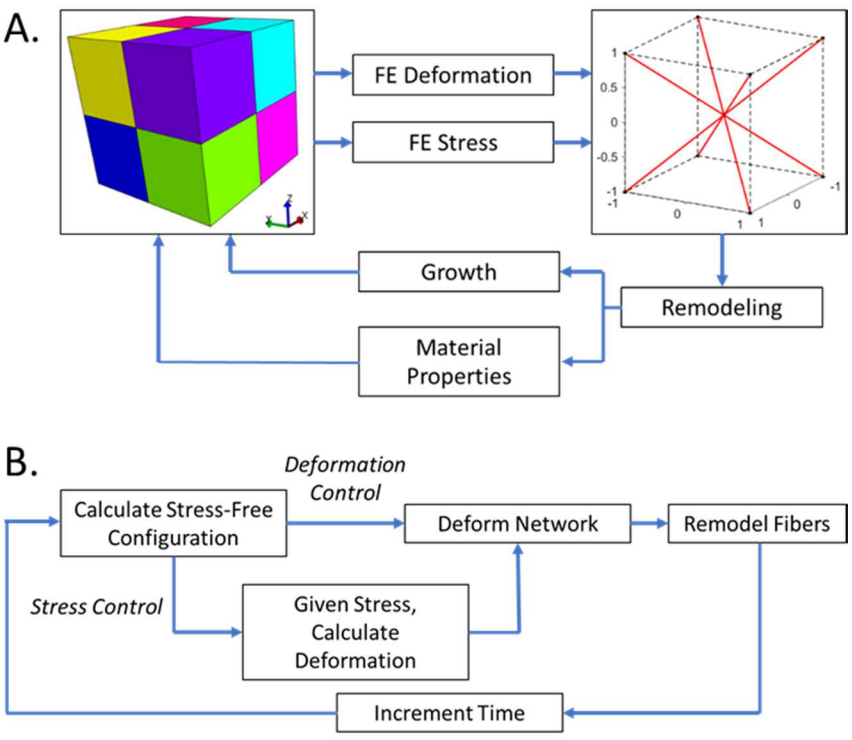

Figure 53. A. Multiscale Framework Flowchart. B. Network Remodeling Flowchart.

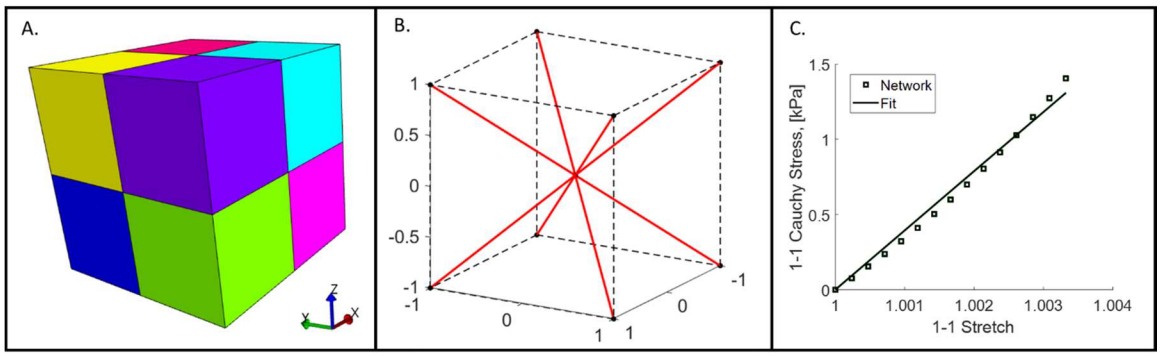

Figure 54. Verification Problem. A. Macroscale Geometry, B. Network Stucutre, C. Network Constitutive Fit.

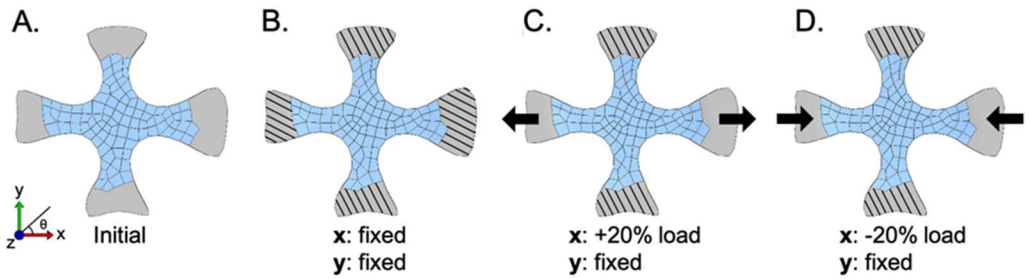

Figure 55. A. Unconstrained cruciform, B. Fully constrained cruciform followed by C. uniaxial stretch of +20% baseline force or by D. uniaxial compression of 20% baseline force.

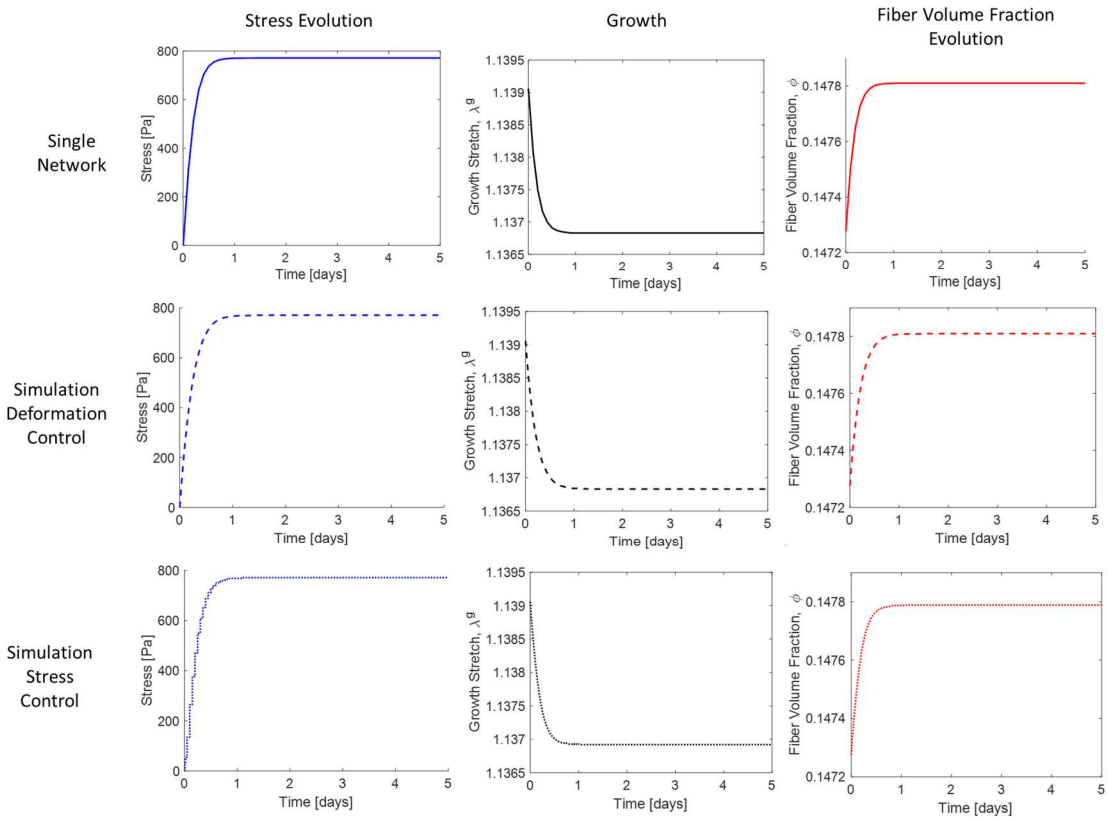

Figure 56. Fixed boundary verification problem. Top row: single network data. Second row: deformation control multiscale simulation. Third row: stress control simulation. Left column: stress evolution. Middle column: Network growth evolution. Right column: fiber volume fraction.

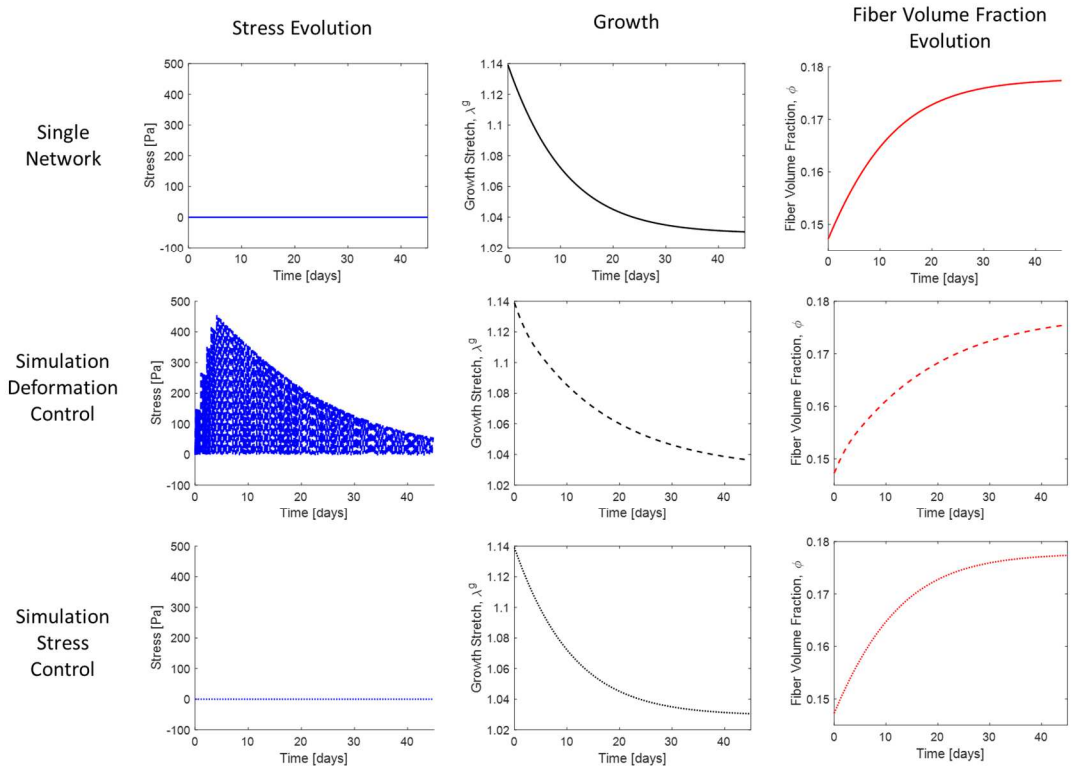

Figure 57. Free boundary verification problem. Top row: single network data. Second row: deformation control multiscale simulation. Third row: stress control simulation. Left column: stress evolution. Middle column: Network growth evolution. Right column: fiber volume fraction.

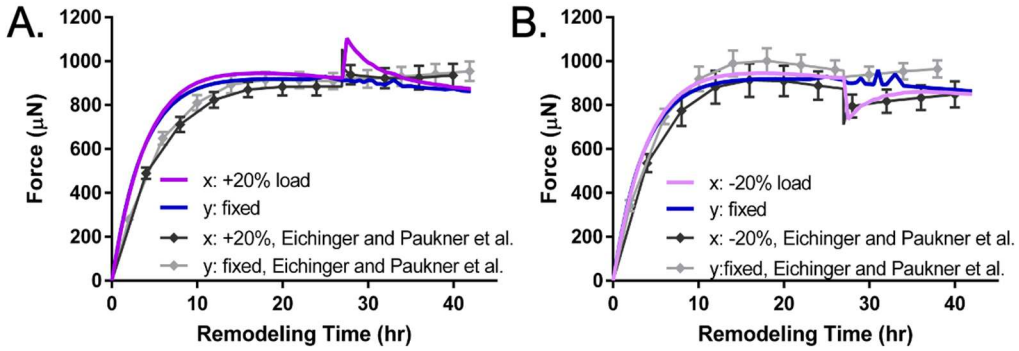

Figure 58. Measured cruciform grip loads over 42 hours with A. a 20% increase in or B. a 20% decrease in grip load at 28 hrs.

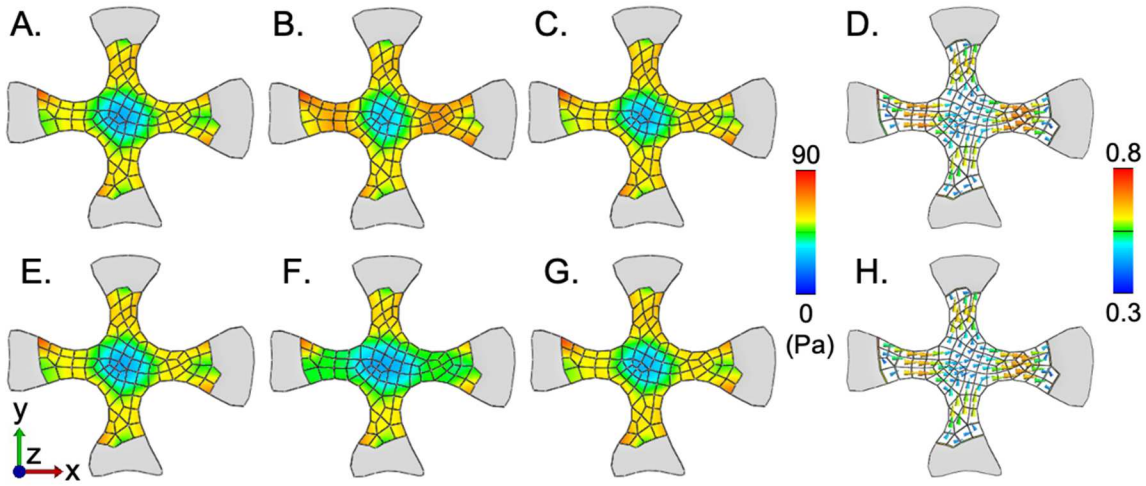

Figure 59. The 1st principal stress at remodeling time of A. 27h, B. 28h and C. 42h with 20% increase in load at hour 28, and the 1st principal stress at time E. 27h, F. 28h, and G. 42h with 20% decrease in load at hour 28. Principal in-plane fiber orientation (theta) at hour 42 for D.) 20% increase in load and H. 20% decrease in load. Color bar indicates strength of alignment (maximum Eigenvalue of the orientation tensor).

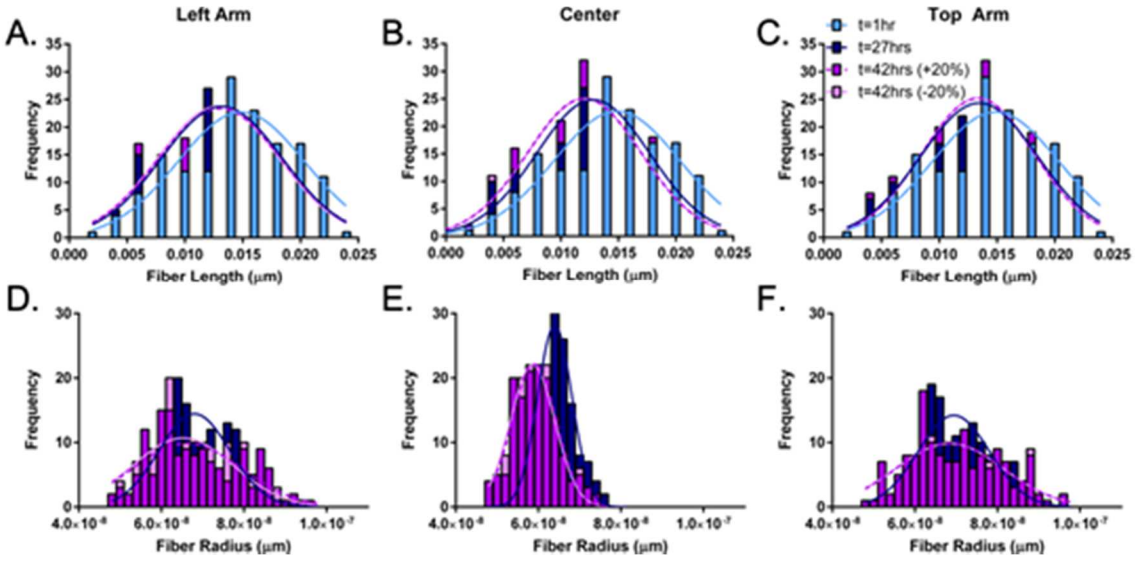

Figure 60. Length of every network fiber within a representative element shown for the A. left arm, B. center, and C. top arm of the cruciform at 1, 27 and 42 hrs of remodeling. Similarly, fiber radii are shown for the D. left arm, E. center, and F. top arm at 27 and 42hrs. The initial fiber radius for all fibers was 8.0 x 10-8 m.

CHAPTER 8: CONCLUSIONS AND FUTURE WORK

8.1: MAJOR FINDINGS AND IMPACT

The Ring Pull Assay:

The ring pull assay offers a high-throughput, repeatable method for testing arterial tissues. This test requires minimal tissue prep and a relatively simple testing protocol/apparatus. Our work has indicated that this test can be used to determine circumferential material behavior repeatably. Our work has also shown that this apparatus can also be used to determine failure properties of the tissue in question. Overall, this technique stands to be used as a simple indicator of tissue properties and failure to assess changes due to genetics or therapies. This technique offers much improved insight over standard *in vivo* imaging and requires less expertise than traditional inflation-type experiments. Taken together, this technique may be used for therapy screenings in mouse models helping with the development of pharmaceuticals for the treatment of arterial diseases like aneurysm and dissection.

Arterial Inflation under Ultrasound:

Ultrasound offers specific unique insights that many other imaging techniques for inflation do not. Ultrasound allows for a full-field visualization of the artery both along the length and through the thickness. Many current methods use simple optical tracking under the assumption of incompressibility to assess luminal and exterior stretches. Ultrasound allows for direct measurement of these stretch values as well as the ability to precisely evaluate compressibility. This is especially important and significant in tissues such as bifurcations or the aortic arch, as the geometry does not lend itself well to assessment of stretches through the thickness. These complex geometries are often important as they tend to coincide with tissue malformations (such as aneurysm) or tissue failure initiation (as in dissection). Our experimental

apparatus allowed us to visualize complex geometries and the ultrasound imaging proved to have enough resolution to broadly visualize the deformation. However, for small tissues, ultrasound resolution can be inadequate, and the better choice would be optical coherence tomography (OCT).

Micromechanical Modeling or Arterial Growth and Remodeling:

In this work, we developed a unique micromechanical model of growth and remodeling utilizing discrete fibers and a periodic network. The model showed the ability to capture many experimental observables including recovery of a homeostatic stress. We were also able to assess the failure mechanics using our model, which is not possible with most continuum models. Additionally, we were able to demonstrate different pathological remodeling cases and assess changes in microstructural strength, even under the same macroscopic growth levels. This is important because clinically the current assessment criteria are based on size and growth rate, which have been shown to be imperfect indicators of failure. Our model demonstrates direct differences between pathologies which could contribute to understanding of when aneurysms require surgical intervention.

Multiscale Modeling in Growth and Remodeling:

In this work, we created a unique multiscale coupling technique to allow for assessment of growth on the macroscopic scale from microscale discrete fiber networks. The purpose of this approach is to be able to describe a discrete fiber network as a continuum solid in order to increase computational efficiency while maintaining microstructural detail. We were able to apply this technique to garner significant computational gains, and further utilized the technique to investigate growth and remodeling of tissues. We showed the ability to match macroscopic observables from a simple collagen gel/fibroblast system including magnitudes of force generated from remodeling as well as fiber re-orientation and overall tissue mechanics. We further applied

our technique to a tissue engineered valve that was implanted in sheep to attempt to predict the experimental findings. The model showed results similar to experimental observations in terms of tissue remodeling and valve insufficiency. We also tracked changes in both material properties and failure behavior that were broadly similar to the explanted tissue.

8.2: FUTURE DIRECTIONS

The Ring Pull Assay:

As mentioned, the ring pull assay represents an excellent mechanical test for assessing mechanical properties and failure of circumferential tissue sections. There are certainly opportunities to utilize this technique and our observations to perform high-throughput screenings of pharmaceuticals for treatment of diseases like aortic aneurysm. Further, the use of computational techniques to garner insight and even relate one mechanical test to another has utility in mechanics particularly if we think of using in-tact tissues in complex geometries. It is often difficult to assess material properties from such structures, but the use of computational models can help with approximation of pertinent mechanical properties through simple observation. For instance, the identification of stress concentrators or the tissue geometry on behavior can help dissect geometric influences from material behavior, perhaps without performing complex inverse mechanics models.

Arterial Inflation under Ultrasound:

Inflation testing offers a more physiological testing environment for arterial tissues. Ultrasound imaging allows tissues to be imaged through thickness. The benefit of experiments using these two in conjunction is that we have full-field information without the assumption of incompressibility. With the addition of computational models, we have a technique to assess and decouple geometric effects from material effects through inverse finite element methods. In

addition, ultrasound produces a distinct speckle pattern, which can be tracked. The major issue currently is that inflation of cylindrical cross-sections produces a relatively small amount of speckle relative to the dead space around and within the vessel. Current tracking algorithms tend to focus on roughly cubic slabs of tissue or through tracking discrete points. The rectangular slab allows for tracking by enforcing compatibility in the deformation, which results in much more robust and reliable tracking for biological soft tissues. This method, however, does not work for tissues with dead space around them or within them, as the space is generally water and therefore need not necessarily deform subject to the same compatibility constraint. The tracking of discrete points shows promise, but is prone to mis-tracking and without the additionally constraint of compatibility, can be unreliable. Thus, we would want something akin to a mesh within our image space that could be tracked and deformed in order to maximize the cross-correlation of the speckle pattern while also enforcing compatibility within the tissue. However, creation of such a mesh would require segmentation of large image stacks which can be prohibitively time consuming. Another option could be recasting the inflated geometry in a parameter space such that the images form rectangles. Take, for example a cane-like shape (i.e. an aorta), we can define the aorta based on an centerline axial coordinate in the longitudinal direction and a radius and angle coordinate in the cross-section. This means we could create image stacks by using radius and angle rather than x and y-coordinates in the cross-section and a distance along the centerline rather than a z-coordinate. This would effectively remap the x-y-z images into polar coordinates along the axis and allow a standard tracking algorithm designed for tissue slabs to track the images.

Micromechanical Modeling or Arterial Growth and Remodeling:

The micromechanical model of growth and remodeling proposed in this work represents one option for trying to understand growth on the cellular level. Our technique offers many advantages over continuum-based approaches, and has broad utility, however we still lack

sufficient experimental detail to inform the model, so it is difficult to draw any conclusions with certainty. In particular, it still remains unclear what the process of fiber turnover exactly looks like and the role the cell and the self-assembly of fibrous components (particularly collagen) play. Further, we also don't understand the exact nature of the cells' interaction with the matrix and how this interaction changes over time (i.e. with maturity or with phenotypic changes). This lack of data is particularly detrimental to understanding disease states where we have even less available data to draw from. Thus, there is ample room to try to understand and model these phenomena, and to perform micro-scale experiments utilizing tissue-equivalents and various phenotypes of vSMCs and fibroblasts to try to uncover how the cells and matrix interact and exactly what fiber turnover looks like in tissue development.

Multiscale Modeling in Growth and Remodeling:

Multiscale approaches are necessary for understanding the growth and remodeling process as we must be able to understand how the individual fibrous subunits are formed into fibers and how those fibers link to other ECM components or cells to assess, not only growth, but also tissue properties and strength. Further, there is a need for improved simulation techniques to predict the behavior of implanted tissue-engineered constructs including not only functional growth, but also failure modes. There are also opportunities to apply techniques like this to predict the behavior of tissues in response to surgical interventions, even without the addition of new tissue. The benefit of being able to predict these processes is that the time and effort to create a model of a tissue implant are much lower than performing animal studies, especially if the implant ends up failing. Multiscale growth models should slot into the design process between the benchtop and preclinical trials.

APPENDIX A: MODELLING TISSUE-ENGINEERED CARDIAC MECHANICS

Summary:

The ability to predict the behavior of tissue-engineered constructs is of critical importance to experimental design and the successful adaptation of such technologies to clinic. In this work, we create a model representative of a tissue engineered human-chambered muscle pump (hChaMP), which is a scaled down geometry of a human heart. We created a finite element model of the geometry and applied various layer thicknesses of actively contracting elements representative of semi-mature cardiomyocytes. With this model, we predicted the experimental stroke volume of the cardiac construct using the observed muscle layer thickness. We also gathered additional information to try to improve the next generation of the construct. Unsurprisingly, we show that the layer thickness directly affects the stroke volume of the construct. However, we demonstrate that the location of the layer directly impacts the function of the heart showing that cell migration into the inner walls of the chambers creates a much better function than cell migration into the outer surface, even with the same wall thicknesses. Further, we show that maintaining cell thickness, but attaining patent cell layers on both the inner chamber walls and exterior of the construct nearly recovers full function of the heart relative to full thickness cells. This result highlights the importance of making the next generation construct have inner chamber muscle, which will guide the cell culture technique for follow up experiments.

Introduction:

Tissue engineering continues to show promise in treating many diseases. In particular, cellularized constructs for cardiovascular applications are beginning to show promise for everything from myocardial infarction therapies to heart valve replacements, and even whole heart transplants. One issue that continues to plague these therapies is the inability to emulate mature healthy cardiomyocytes in vivo, especially in large, complex structures. We therefore need a method for evaluating organ-scale function based on cardiomyocyte infiltration and maturation in such constructs not only to evaluate the performance of the current construct, but also to guide how we approach making better constructs.

In this work, we developed a model of cardiac contraction of a novel human chambered muscle pump (hChaMP) miniaturized from a patient scan and seeded with human induced pluripotent stem cells (hiPSCs). Using data on cell infiltration and hiPSC contractility based on maturation we evaluate the current hChaMP, and deliver insight into making a more effective second iteration of this construct.

Methods:

To create the geometry of the hChaMP, a MRI scan of the printed structure was segmented using SimVascular [236]. Once the geometry was segmented, analysis was performed using the FEBio software suite [121]. The geometry was imported into PreView 2.1.5, refined, and meshed using 10 node tetrahedral elements. The outer surface and ventricular surfaces were partitioned in order to find elements on each to allow the generation of properly sized muscle layers (i.e. 200-250um, 600-650um).

The ground substance used in this simulation was the bioink material which was assigned a neo-Hookean strain energy density as follows: $W = c_1(I_1 - 3)$ where c_1 is the neo-Hookean material constant and I_1 is the first invariant of the right Cauchy-Green deformation tensor. The neo-Hookean constant of the bioink was derived from its shear modulus as: $c_1 \approx G(1 + \upsilon)$ where

G is the shear modulus, and υ is the Poisson's ratio. The hiPSC-derived cardiomyocytes were modeled as a transversely isotropic contractile stress relative to the normal direction from the ventricular inner surfaces to the exterior surface. The maximum stress magnitude was taken to be 3.5 kPa based on the underlying bioink stiffness and the age of the hiPSC-derived cells [237].

A single node on the apex of the heart was fixed in all directions to stabilize the structure during contraction. Once the materials were defined and the boundary condition implemented, the simulation was solved using FEBio 2.9.1. Results and videos were exported from PostView 2.5. A custom routine was created in MATLAB2019a (Mathworks Inc., Natick, MA, USA) for calculating right and left ventricular volume during the contraction using the built-in *convhull* function to find the convex hull volume for the ventricular surface nodal positions.

Results:

From experiments, it was determined that the volume moved through the hCHaMP chambers was ~0.5 uL and maximum volume moved through the chambers was ~5.0 uL, which is approximately 17% of that of the average stroke volume of an adult murine heart [15]. To verify the accuracy of these values and determine the effect of wall cellularization on stroke volume, we developed an *in silico* finite element model using the hChaMP digital template. Using this model, changes in chamber volume were assessed under three different assumptions: 1) The entirety of the wall thickness is occupied by cells, 2) Approximately half of the wall thickness (600-650 μm) is occupied by cells, and 3) The cellularization is limited to the outer 200-250 μm of the structure (Figure XX). Based on the underlying substrate bioink stiffness and the age of cultured hiPSC-derived cardiomyocytes, a maximum contraction stress of 3.5 kPa was prescribed for this model [237]. The stroke volume calculated for the 200-250 μm wall thickness (most similar to the level of cellularization we observed) was 1.7 μL. The experimentally determined stroke volume is slightly lower than this, likely due to an uneven distribution of cardiomyocytes across the hChaMP surface. Based on the *in silico* model, we expect that fully cellularized hChaMP under

the same conditions would produce a stroke volume of approximately 14 μL which is ~47% of the adult murine heart. However, with increased maturation of SMCs that stroke volume could increase adult murine heart output. Based on this model, to achieve normal adult murine cardiac output, we would need cell contractility of ~13kPa.

The major limitation with this hChaMP construct is the ability of the hiPSCs to integrate into the bioink. The cells only attach and integrate onto the outer surface, which is less than optimal. In fact, in Figure Y we see that the ideal scenario is to have the inner surface cellularize in addition to the outer surface. This gives us stroke volume greater than even half the thickness from the outside.

Discussion:

This model system shows similar behavior to the experiments on the hChaMP construct. We show that this model can bridge the gap between single-cell experiments and the overall construct based on cardiomyocyte maturity [237]. Based on our model in Figure XX, we see that we can improve stroke volume by increasing layer thickness. This is challenging because of the diminishing ability to diffuse differentiation agents and required media into the construct. We do however, demonstrate an alternative for improving the stroke volume by achieving cardiomyocyte infiltration from the inner surface in addition to the outer surface (Fig Y). This has challenges itself, but is likely more feasible than increasing layer thickness, because of the ability to flow media and differentiation agents through the hChaMP. In fact, sustained pressure internal to the hChaMP ventricles could aid in media diffusion and cardiac maturation. Based on Figure XX, we see that we need increased cardiomyocyte maturation regardless of hiPSC cardiomyocyte thickness. This is a challenge in vitro due to the relative fragility of hiPSC-derived cardiomyocytes, but appears to be necessary to reproduce functionality.

Acknowledgments:

The authors acknowledge funding from the National Science Foundation Graduate Research Fellowship Program (NSF GRFP) under Grant No. 00039202. The author also acknowledges guidance from his thesis advisor Victor H. Barocas on design and implementation of this model system.

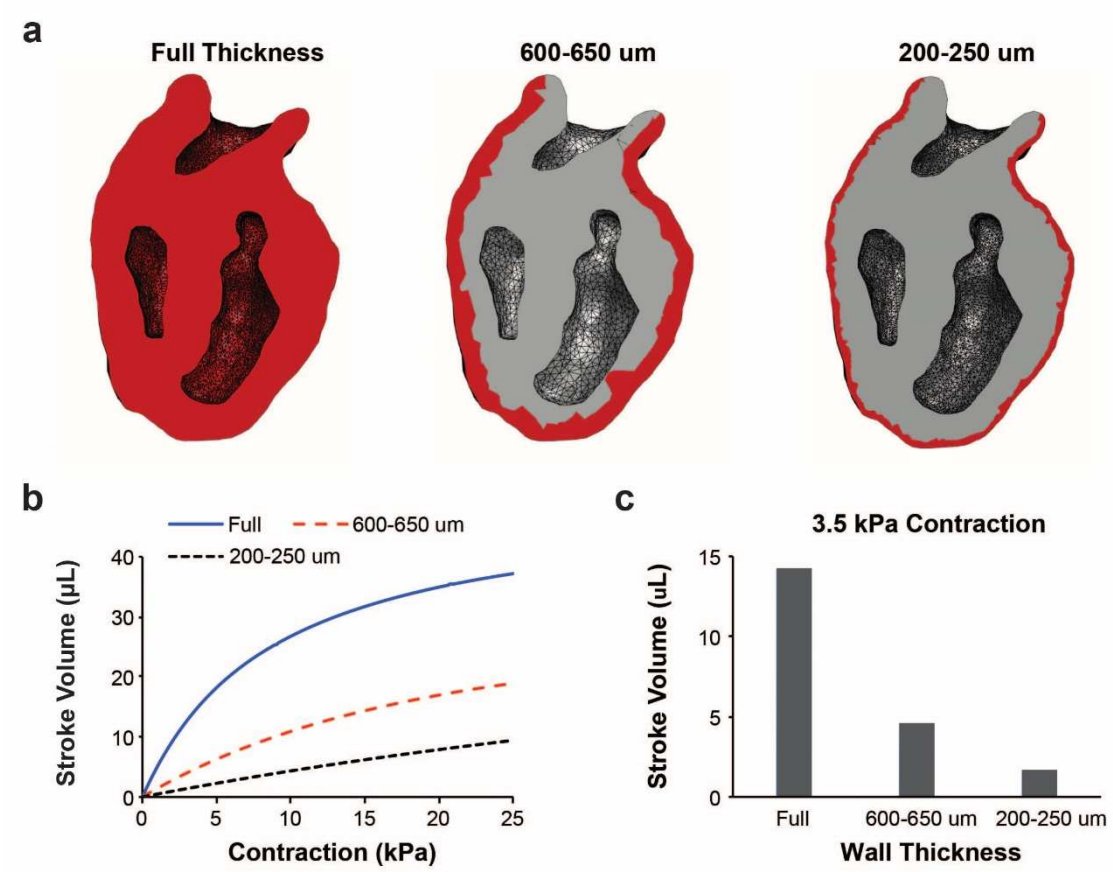

Figure 61. *In silico* model of stroke volume in hChaMPs of varying wall thicknesses. a) Cross-sectional views of the hChaMP digital model with full cellular wall thickness (~ 1mm), 600-650 µm thickness, or 200-250 µm thickness. Gray color indicates bio-ink material, and red color indicates cellularized regions. **b)** Stroke volume versus contraction stress quantified *in silico* for three cell layer thicknesses. **c)** Stroke volume associated with a 3.5 kPa contraction for three cell layer thicknesses.

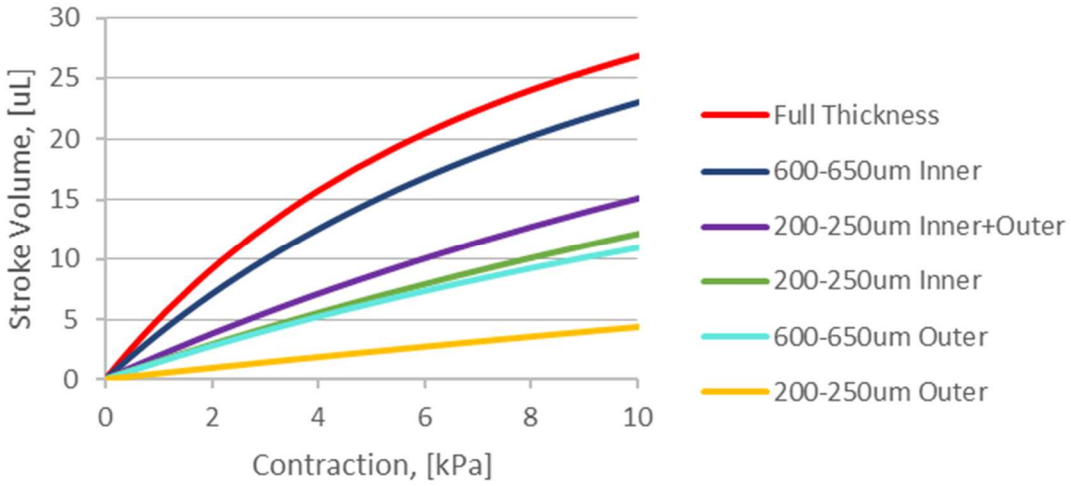

Figure 62. Stroke volume with respect to various cell infiltration thicknesses and locations.

APPENDIX B: SUPPLEMENTAL MATERIAL

Chapter 4.1 Supplemental Figures:

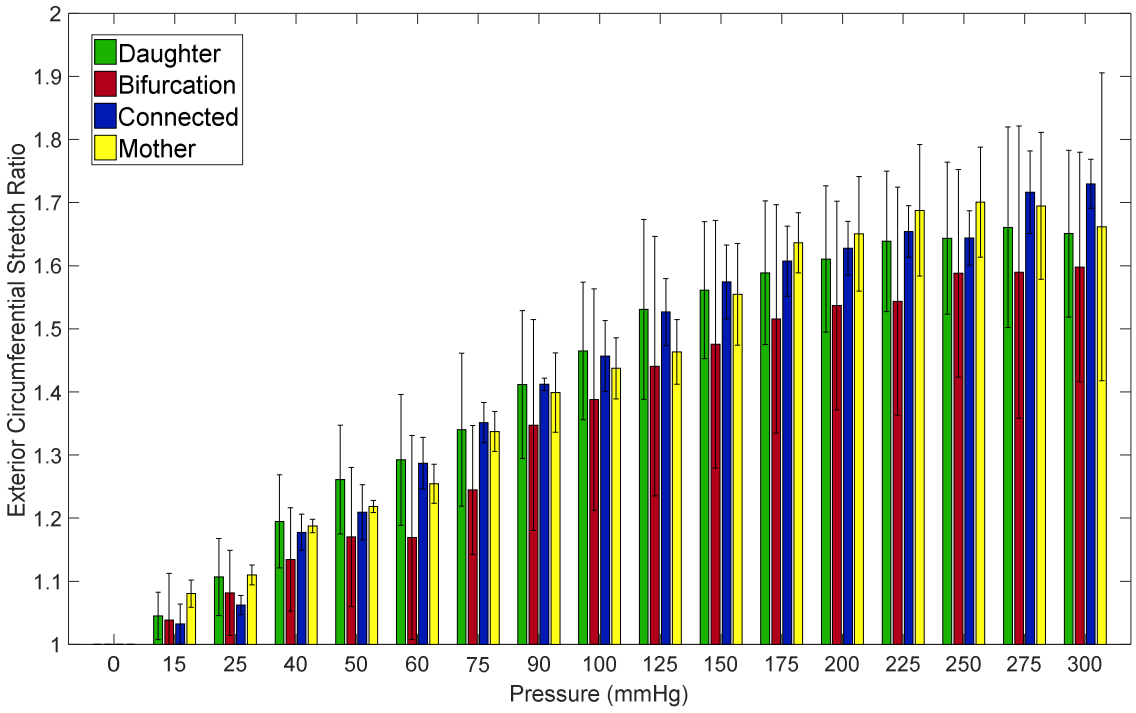

Figure 63. Exterior circumferential stretch vs. pressure

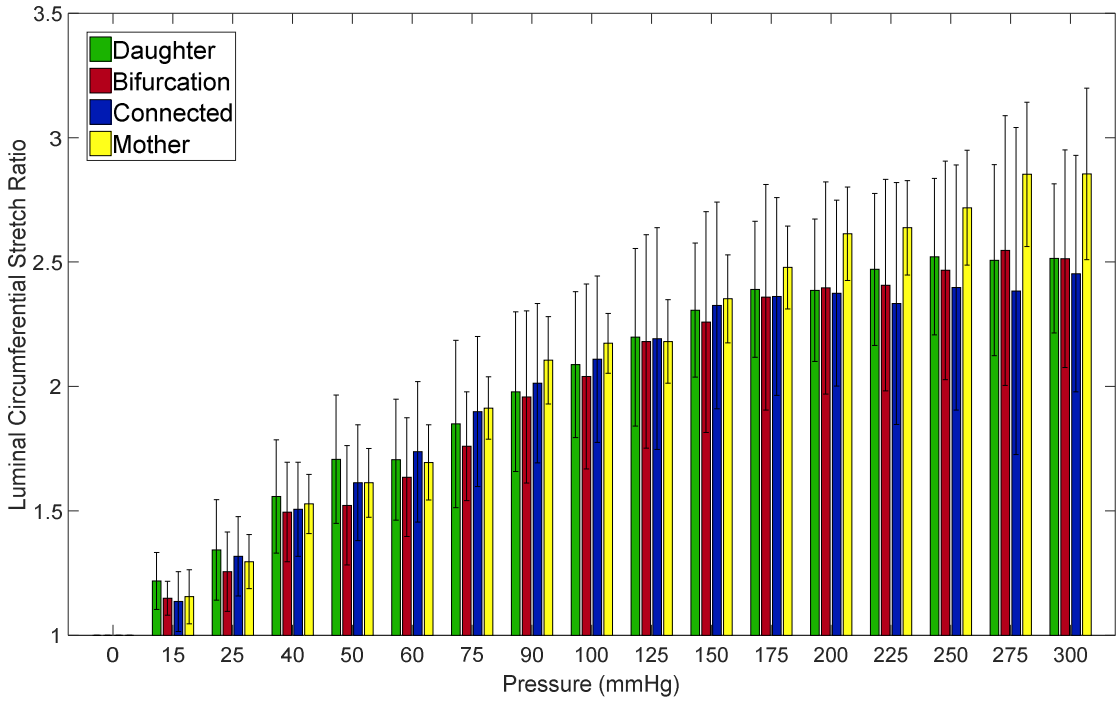

Figure 64. Luminal circumferential stretch vs. pressure

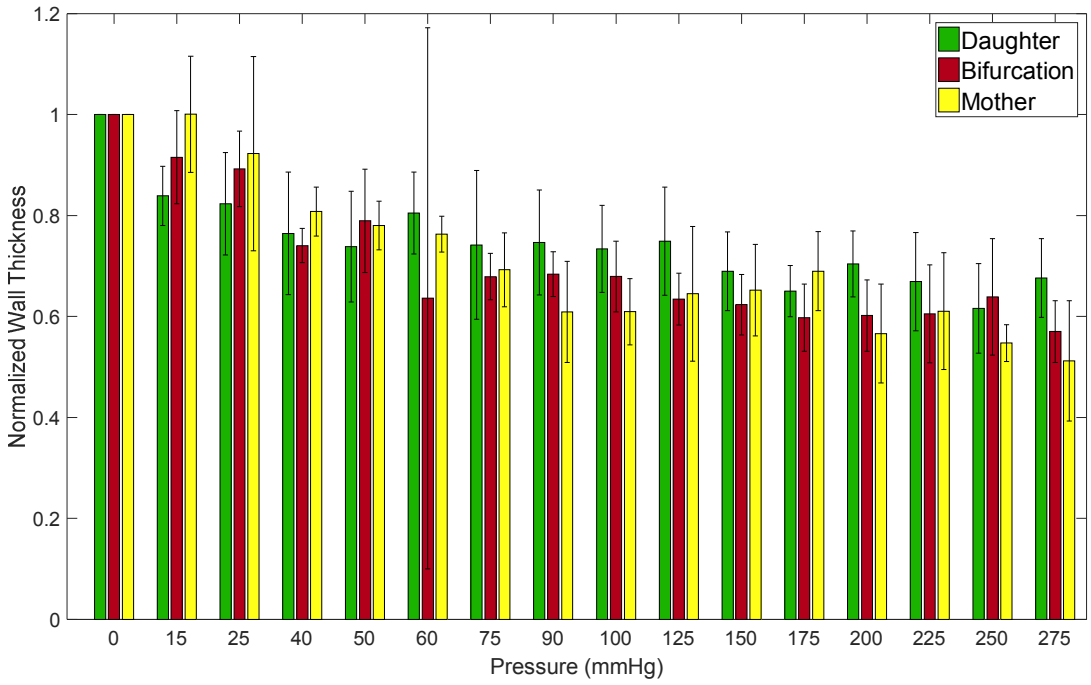

Figure 65. Normalized wall thickness vs. pressure

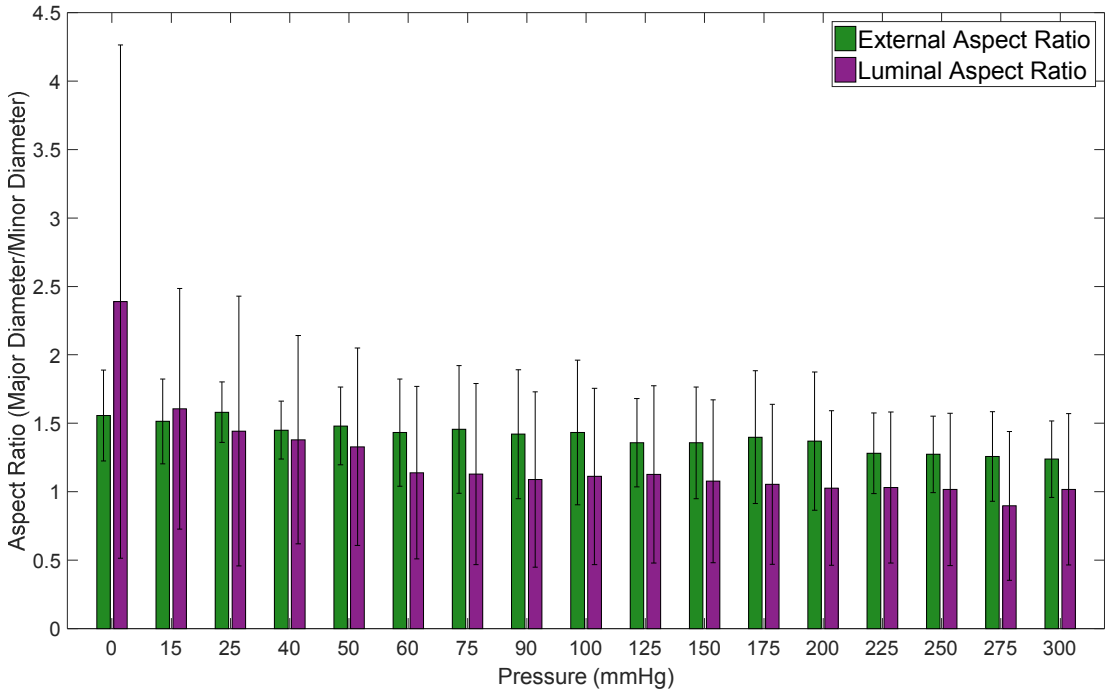

Figure 66. Connected region aspect ratio vs. pressure

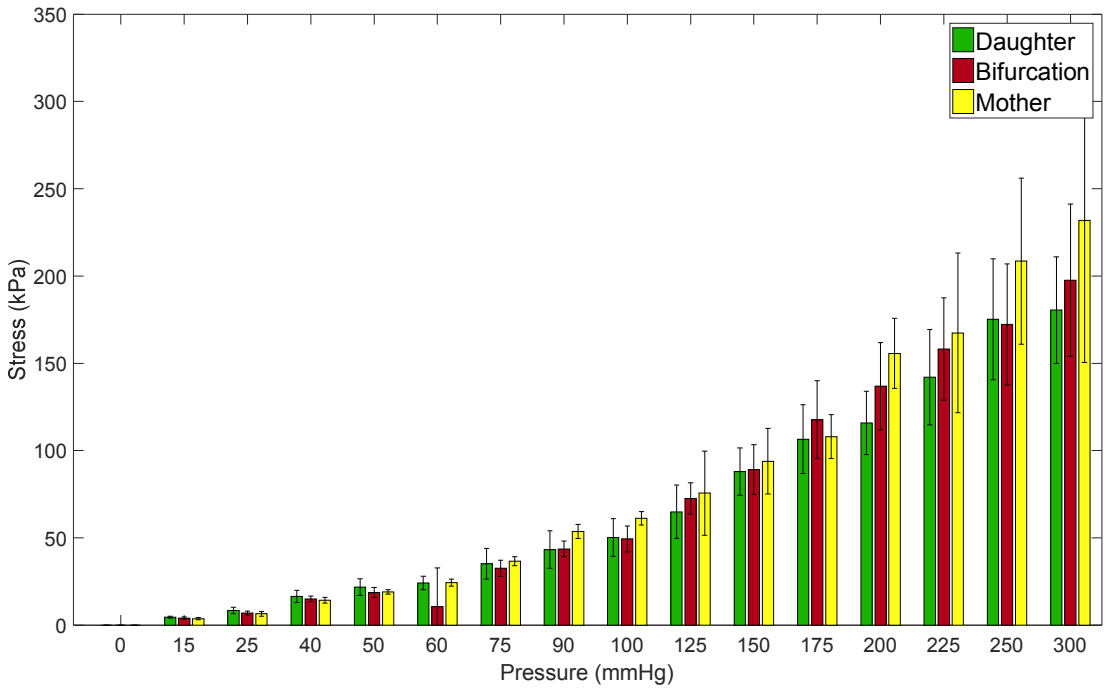

Figure 67. Law of Laplace circumferential stress vs. pressure

Chapter 5 Supplement:

Estimation of Actin Time Constant, τ:

From [153] we see: $k = 1\ MPah\ and\ \sigma_\infty = 9.7kPa$ for $\frac{d\lambda}{dt} = \frac{1}{k}(\sigma - \sigma_\infty)\lambda$

For our model: $\frac{dr}{dt} = \frac{1}{\tau}\left(\frac{\sigma}{\sigma_\infty} - 1\right)r$ and we approximate using the above to give: $\tau = \frac{1MPah}{9.7kPa} = 103.1h = 4.3\ days$

Estimation of Equilibrium Actin Stress, σ_∞^S :

From [238] we see approximate basal force of an SMC is 7.5 uN. If we then say a SMC cell has approximate cross-section of $100um^2$ ($r = 5.6um$), we get $\sigma_\infty^{Cell} = 75kPa = \sigma_\infty^S \phi^S$. If we then assume $\phi^S = 0.1$ then we get $\sigma_\infty^S = 750kPa$

Estimation of Collagen Time Constant:

From [171], we estimate the half life of collagen at 60-90 days. Then: $\frac{1}{2}N_0 = N_0 \exp\left(-\frac{60\ days}{\tau}\right)$ so $\tau = \frac{60\ days}{\ln(2)} \approx 90\ days$

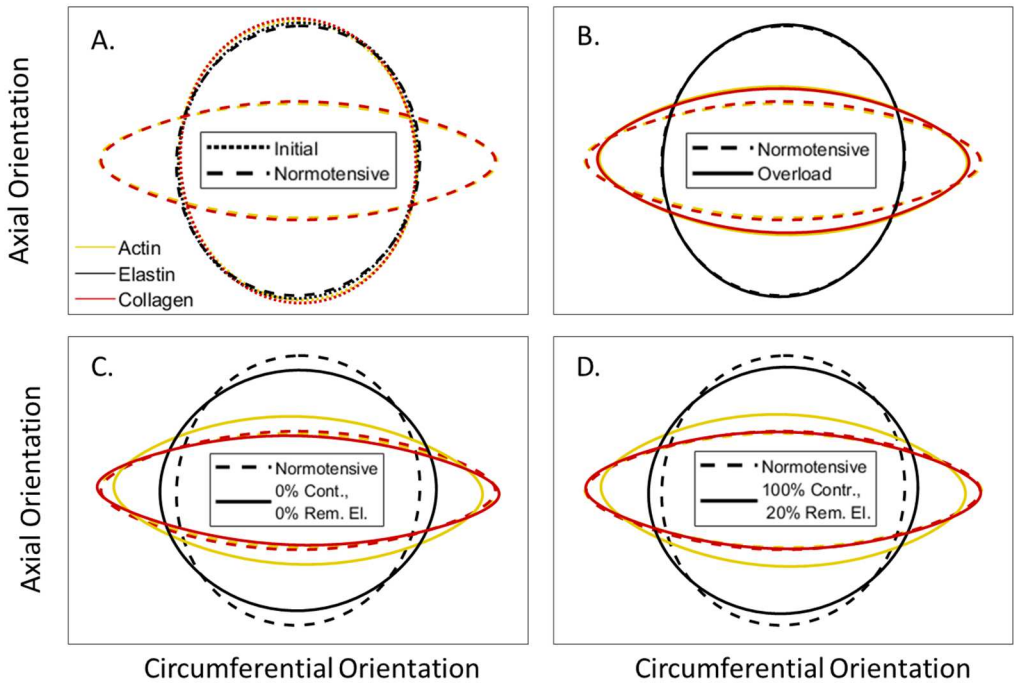

Figure 68. Fiber orientation plotted as an ellipse with major axis and minor axis lengths corresponding to strength of alignment and principle fiber orientation shown as major axis direction corresponding to the tilt of the ellipse for A. initial vs normotensive, B. normotensive vs 50% overload, C. normotensive vs vSMC contractility dysfunction (0% of normal contractility), and D. normotensive vs 20% removed elastin fibers. *Note: A circle represents an isotropic network.*

BIBLIOGRAPHY

1. Milewicz, D.M., Guo, D.-C., Tran-Fadulu, V., Lafont, A.L., Papke, C.L., Inamoto, S., Kwartler, C.S., Pannu, H.: Genetic Basis of Thoracic Aortic Aneurysms and Dissections: Focus on Smooth Muscle Cell Contractile Dysfunction. Annu. Rev. Genomics Hum. Genet. 9, 283–302 (2008). https://doi.org/10.1146/annurev.genom.8.080706.092303
2. Aortic Aneurysm | cdc.gov, https://www.cdc.gov/heartdisease/aortic_aneurysm.htm
3. Nardi, P., Ruvolo, G.: Current Indications to Surgical Repair of the Aneurysms of Ascending Aorta. J. Vasc. Endovasc. Surg. 01, (2016). https://doi.org/10.21767/2573-4482.10009
4. Roth, G.A., Mensah, G.A., Johnson, C.O., Addolorato, G., Ammirati, E., et al. ; Global Burden of Cardiovascular Diseases and Risk Factors, 1990–2019: Update From the GBD 2019 Study, https://doi.org/10.1016/j.jacc.2020.11.010, (2020)
5. Xu, J., Murphy, S., Kochanek, K., Bastian, B.: Deaths: Final Data for 2013. Natl. Vital Stat. Reports. 64, (2016)
6. Dean, J.C.S.: Marfan syndrome: Clinical diagnosis and management. Eur. J. Hum. Genet. 15, 724–733 (2007). https://doi.org/10.1038/sj.ejhg.5201851
7. Iaizzo, P.A.: Handbook of cardiac anatomy, physiology, and devices: Second edition. Humana Press (2005)
8. Walther, F.J., Siassi, B., King, J., Wu, P.Y.K.: Normal values of aortic root measurements in neonates. Pediatr. Cardiol. 6, 61–63 (1985). https://doi.org/10.1007/BF02282739
9. Mahutga, R.R., Schoephoerster, C.T., Barocas, V.H.: The Ring-Pull Assay for Mechanical Properties of Fibrous Soft Tissues – an Analysis of the Uniaxial Approximation and a Correction for Nonlinear Thick-Walled Tissues. Exp. Mech. 61, 53–66 (2021). https://doi.org/10.1007/s11340-020-00623-3
10. Mahutga, R., Barocas, V.H.: Investigation of Pathophysiological Aspects of Aortic Growth, Remodeling, and Failure Using a Discrete-Fiber Microstructural Model. J. Biomech. Eng. 142, (2020). https://doi.org/10.1115/1.4048031
11. Saladin, K.S.: Human Anatomy 2nd Ed. McGraw-Hill Companies, Inc. (2008)
12. Fornieri, C., Quaglino Jr, D., Mori, G.: Role of the exracellular matrix in age-related modifications of the rat aorta. Art.Thromb. 12, 1008–1016 (1992)
13. Yu, X., Suki, B., Zhang, Y., Zhang, Y., Zhang, Y.: Avalanches and power law behavior in aortic dissection propagation. Sci. Adv. 6, eaaz1173 (2020). https://doi.org/10.1126/sciadv.aaz1173

14. O'Connell, M.K., Murthy, S., Phan, S., Xu, C., Buchanan, J.A., Spilker, R., Dalman, R.L., Zarins, C.K., Denk, W., Taylor, C.A.: The three-dimensional micro- and nanostructure of the aortic medial lamellar unit measured using 3D confocal and electron microscopy imaging. Matrix Biol. 27, 171–181 (2008). https://doi.org/10.1016/j.matbio.2007.10.008
15. Trueting, P., Dintzis, S.: Comparative Anatomy and Histology - A Mouse and Human Atlas 1st Ed. Elsevier, Inc. (2012)
16. Humphrey, J.D.: Cardiovascular Solid Mechanics: Cells, Tissues, and Organs. Springer-Verlag New York, Inc, New York, NY (2002)
17. Halper, J.: Progress in Heritable Soft Connective Tissue Diseases Introduction. Prog. Heritable Soft Connect. Tissue Dis. 802, 1–3 (2014). https://doi.org/10.1007/978-94-007-7893-1_1
18. Bennett, M.R., Sinha, S., Owens, G.K.: Vascular Smooth Muscle Cells in Atherosclerosis. Circ. Res. 118, 692–702 (2016). https://doi.org/10.1161/CIRCRESAHA.115.306361
19. Theocharis, A.D., Manou, D., Karamanos, N.K.: The extracellular matrix as a multitasking player in disease. FEBS J. 286, 2830–2869 (2019). https://doi.org/10.1111/febs.14818
20. Isselbacher, E.M.: Thoracic and Abdominal Aortic Aneurysms. Circulation. 111, 816–828
21. LaValley, D.J., Reinhart-King, C.A.: Matrix Stiffening in the Formation of Blood Vessels. Adv. Regen. Biol. 1, (2014)
22. Lyle, A.N., Raaz, U.: Killing Me Unsoftly Causes and Mechanisms of Arterial Stiffness. Arterioscler. Thromb. Vasc. Biol. 37, E1–E11 (2017). https://doi.org/10.1161/ATVBAHA.116.308563
23. Verma, S., Siu, S.C.: Aortic Dilatation in Patients with Bicuspid Aortic Valve. N. Engl. J. Med. 370, 1920–1929 (2014). https://doi.org/10.1056/NEJMra1207059
24. Saleh, F.H., Jurjus, A.R.: A comparative study of morphological changes in spontaneously hypertensive rats and normotensive Wistar Kyoto rats treated with an angiotensin converting enzyme inhibitor or a calcium channel blocker. J. Pathol. 193, 415–420 (2001). https://doi.org/10.1002/1096-9896(2000)9999:9999<::AID-PATH796>3.0.CO;2-F
25. Taber, L.A.: A Model for Aortic Growth Based on Fluid Shear and Fiber Stresses. J. Biomech. Eng. 120, 348 (1998). https://doi.org/10.1115/1.2798001
26. Alford, P.W., Humphrey, J.D., Taber, L.A.: Growth and Remodelling in a Thick-Walled Artery Model: Effects of Spatial Variations in Wall Constituents. Biomech. Model. Mechanobiol. 7, 245–262 (2008). https://doi.org/10.1007/s10237-007-0101-2.Growth
27. Herrmann, J., Samee, S., Chade, A., Porcel, M.R., Lerman, L.O., Lerman, A.: Differential

effect of experimental hypertension and hypercholesterolemia on adventitial remodeling. Arterioscler. Thromb. Vasc. Biol. 25, 447–453 (2005). https://doi.org/10.1161/01.ATV.0000152606.34120.97

28. Nakashima, Y., Wight, T.N., Sueishi, K.: Early atherosclerosis in humans: role of diffuse intimal thickening and extracellular matrix proteoglycans. Cardiovasc. Res. 79, 14–23 (2008). https://doi.org/10.1093/cvr/cvn099
29. Porterfield, S.P., Calhoon, T.B., Weiss, H.S.: Changes in Connective Tissue Colloidal Charge Density With Atherosclerosis and Age. Am. J. Physiol. 215, 324-+ (1968). https://doi.org/10.1152/ajplegacy.1968.215.2.324
30. Pancheri, F.Q., Peattie, R.A., Reddy, N.D., Ahamed, T., Lin, W., Ouellette, T.D., Iafrati, M.D., Dorfmann, A.L.: Histology and Biaxial Mechanical Behavior of Abdominal Aortic Aneurysm Tissue Samples. J. Biomech. Eng. Asme. 139, (2017). https://doi.org/10.1115/1.4035261
31. Shahmansouri, N., Alreshidan, M., Emmott, A., Lachapelle, K., Cartier, R., Leask, R.L., Mongrain, R.: Evaluating ascending aortic aneurysm tissue toughness: Dependence on collagen and elastin contents. J. Mech. Behav. Biomed. Mater. 64, 262–271 (2016). https://doi.org/10.1016/j.jmbbm.2016.08.006
32. Witzenburg, C.M., Dhume, R.Y., Shah, S.B., Korenczuk, C.E., Wagner, H.P., Alford, P.W., Barocas, V.H.: Failure of the Porcine Ascending Aorta: Multidirectional Experiments and a Unifying Microstructural Model. J. Biomech. Eng. Asme. 139, (2017). https://doi.org/10.1115/1.4035264
33. Korenczuk, C.E., Dhume, R.Y., Liao, K.K., Barocas, V.H.: Ex Vivo Mechanical Tests and Multiscale Computational Modeling Highlight the Importance of Intramural Shear Stress in Ascending Thoracic Aortic Aneurysms. J. Biomech. Eng. 141, (2019). https://doi.org/10.1115/1.4045270
34. Pham, T., Martin, C., Elefteriades, J., Sun, W.: Biomechanical characterization of ascending aortic aneurysm with concomitant bicuspid aortic valve and bovine aortic arch. Acta Biomater. 9, 7927–7936 (2013). https://doi.org/10.1016/j.actbio.2013.04.021
35. Cox, R.H.: Comparison of mechanical and chemical properties of extra- and intralobar canine pulmonary arteries. Am. J. Physiol. - Hear. Circ. Physiol. 11, (1982). https://doi.org/10.1152/ajpheart.1982.242.2.h245
36. Adebayo, O., Hookway, T.A., Hu, J.Z., Billiar, K.L., Rolle, M.W.: Self-assembled smooth muscle cell tissue rings exhibit greater tensile strength than cell-seeded fibrin or collagen gel rings. J. Biomed. Mater. Res. - Part A. 101 A, 428–437 (2013).

https://doi.org/10.1002/jbm.a.34341

37. Van Haaften, E.E., Van Turnhout, M.C., Kurniawan, N.A.: Image-based analysis of uniaxial ring test for mechanical characterization of soft materials and biological tissues. Soft Matter. 15, 3353–3361 (2019). https://doi.org/10.1039/c8sm02343c
38. FitzGibbon, B., McGarry, P.: Development of a test method to investigate mode II fracture and dissection of arteries. Acta Biomater. 121, 444–460 (2021). https://doi.org/10.1016/j.actbio.2020.11.023
39. Bellini, C., Bersi, M.R., Caulk, A.W., Ferruzzi, J., Milewicz, D.M., Ramirez, F., Rifkin, D.B., Tellides, G., Yanagisawa, H., Humphrey, J.D.: Comparison of 10 murine models reveals a distinct biomechanical phenotype in thoracic aortic aneurysms. J. R. Soc. Interface. 14, (2017). https://doi.org/10.1098/rsif.2016.1036
40. Wagenseil, J.E., Ciliberto, C.H., Knutsen, R.H., Levy, M.A., Kovacs, A., Mecham, R.P.: The importance of elastin to aortic development in mice. Am J Physiol Hear. Circ Physiol. 299, H257–H264 (2010)
41. Le, V.P., Knutsen, R.H., Mecham, R.P., Wagenseil, J.E.: Decreased aortic diameter and compliance precedes blood pressure increases in postnatal development of elastin-insufficient mice. Am. J. Physiol. - Hear. Circ. Physiol. 301, H221–H229 (2011). https://doi.org/10.1152/ajpheart.00119.2011
42. Hu, J.J., Baek, S., Humphrey, J.D.: Stress-strain behavior of the passive basilar artery in normotension and hypertension. J. Biomech. 40, 2559–2563 (2007). https://doi.org/10.1016/j.jbiomech.2006.11.007
43. Boekhoven, R.W., Peters, M.F.J., Rutten, M.C.M., van Sambeek, M.R., van de Vosse, F.N., Lopata, R.G.P.: INFLATION AND BI-AXIAL TENSILE TESTING OF HEALTHY PORCINE CAROTID ARTERIES. Ultrasound Med. Biol. 42, 574–585 (2016). https://doi.org/10.1016/j.ultrasmedbio.2015.09.019
44. Kim, J.H., Avril, S., Duprey, A., Favre, J.P.: Experimental characterization of rupture in human aortic aneurysms using a full-field measurement technique. Biomech. Model. Mechanobiol. 11, 841–853 (2012). https://doi.org/10.1007/s10237-011-0356-5
45. Witzenburg, C.M., Dhume, R.Y., Shah, S.B., Korenczuk, C.E., Wagner, H.P., Alford, P.W., Barocas, V.H.: Failure of the porcine ascending aorta: Multidirectional experiments and a unifying microstructural model. J. Biomech. Eng. 139, (2017). https://doi.org/10.1115/1.4035264
46. Korenczuk, C.E., Votava, L.E., Dhume, R.Y., Kizilski, S.B., Brown, G.E., Narain, R., Barocas, V.H.: Isotropic Failure Criteria Are Not Appropriate for Anisotropic Fibrous

Biological Tissues. (2017). https://doi.org/10.1115/1.4036316
47. Macrae, R.A., Miller, K., Doyle, B.J.: Methods in Mechanical Testing of Arterial Tissue: A Review. Strain. 52, 380–399 (2016). https://doi.org/10.1111/str.12183
48. Fung, Y.C., Fronek, K., Patitucci, P.: Pseudoelasticity of arteries and the choice of its mathematical expression. Am. J. Physiol. 237, H620–H631 (1979)
49. Fung, Y.C.: Biomechanics: Mechanical Properties of Living Tissues. Springer-Verlag New York, Inc. (1993)
50. Holzapfel, G.A., Gasser, T.C., Ogden, R.W.: Comparison of a multi-layer structural model for arterial walls with a fung-type model, and issues of material stability. J. Biomech. Eng. Asme. 126, 264–275 (2004). https://doi.org/10.1115/1.1695572
51. Holzapfel, G.A.: Determination of material models for arterial walls from uniaxial extension tests and histological structure. J. Theor. Biol. 238, 290–302 (2005)
52. Holzapfel, G.A., Gasser, T.C., Ogden, R.W.: A New Constitutive Framework for Arterial Wall Mechanics and a Comparative Study of Material Models. J. Elast. 61, 1–48 (2000)
53. Gasser, T.C., Ogden, R.W., Holzapfel, G.A.: Hyperelastic modelling of arterial layers with distributed collagen fibre orientations. J. R. Soc. Interface. 3, 15–35 (2006). https://doi.org/10.1098/rsif.2005.0073
54. Ferruzi, J., Bersi, M.R., Humphrey, J.D.: Biomechanical Phenotyping of Central Arteries in Health and Disease: Advantages of and Methods for Murine Models. Ann. Biomed. Eng. 41, 1311–1330 (2013)
55. Bersi, M.R., Ferruzi, J., Eberth, J.F., Gleason jr, R.L., Humphrey, J.D.: Consistent Biomechanical Phenotyping of Common Carotid Arteries from Seven Genetic, Pharmacological, and Surgical Mouse Models. Ann. Biomed. Eng. 42, 1207–1223 (2014)
56. Wilson, J.S., Bersi, M.R., Li, G., Humphrey, J.D.: Correlation of Wall Microstructure and Heterogeneous Distributions of Strain in Evolving Murine Abdominal Aortic Aneurysms. Cardiovasc. Eng. Technol. (2017)
57. Ferruzzi, J., Collins, M.J., Yeh, A.T., Humphrey, J.D.: Mechanical assessment of elastin integrity in fibrillin-1-deficient carotid arteries: implications for Marfan syndrome. Cardiovasc. Res. 92, 287–295 (2011)
58. Collins, M.J., Bersi, M., Wilson, E., Humphrey, J.D.: Mechanical properties of suprarenal and infrarenal abdominal aorta: Implications for muse models of aneurysms. Med. Eng. Phys. 33, 1262–1269 (2011)
59. Eberth, J.F., Taucer, A.I., Wilson, E., Humphrey, J.D.: Mechanics of Carotid Arteries in a Mouse Model of Marfan Syndrome. Ann. Biomed. Eng. 37, 1093–1104 (2009)

60. Humphrey, J.D., Holzapfel, G.A.: Mechanics, mechanobiology, and modeling of human abdominal aorta and aneurysms. J. Biomech. 45, 805–814 (2012)
61. Bellini, C., Ferruzzi, J., Roccabianca, S., Di Martino, E.S., Humphrey, J.D.: A Microstructurally Motivated Model of Arterial Wall Mechanics with Mechanobiological Implications. Ann. Biomed. Eng. 42, 488–502 (2014)
62. Taber, L.A.: Biomechanics of Growth, Remodeling, and Morphogenesis. Appl. Mech. Rev. 48, 487 (1995). https://doi.org/10.1115/1.3005109
63. Alford, P.W., Taber, L.A.: Computational study of growth and remodelling in the aortic arch. Comput. Methods Biomech. Biomed. Engin. 11, 525–538 (2008). https://doi.org/10.1080/10255840801930710
64. Baek, S., Rajagopal, K.R., Humphrey, J.D.: Competition between radial expansion and thickening in the enlargement of an intracranial saccular aneurysm. J. Elast. 80, 13–31 (2005). https://doi.org/10.1007/s10659-005-9004-6
65. Humphrey, J.D., Rajagopal, K.R.: A Constrained Mixture Model For Growth And Remodelling Of Soft Tissues. Math. Model. Methods Appl. Sci. 12, 407–430 (2002). https://doi.org/10.1142/S0218202502001714
66. Humphrey, J.D., Rajagopal, K.R.: A constrained mixture model for arterial adaptations to a sustained step change in blood flow. Biomech. Model. Mechanobiol. 2, 109–126 (2003). https://doi.org/10.1007/s10237-003-0033-4
67. Baek, S., Rajagopal, K.R., Humphrey, J.D.: A Theoretical Model of Enlarging Intracranial Fusiform Aneurysms. J. Biomech. Eng. 128, 142 (2006). https://doi.org/10.1115/1.2132374
68. Gleason, R.L., Humphrey, J.D.: Effects of a sustained extension on arterial growth and remodeling: A theoretical study. J. Biomech. 38, 1255–1261 (2005). https://doi.org/10.1016/j.jbiomech.2004.06.017
69. RODRIGUEZ, E.K., HOGER, A., MCCULLOCH, A.D.: STRESS-DEPENDENT FINITE GROWTH IN SOFT ELASTIC TISSUES. J. Biomech. 27, 455–467 (1994). https://doi.org/10.1016/0021-9290(94)90021-3
70. SKALAK, R., DASGUPTA, G., MOSS, M., OTTEN, E., DULLEMEIJER, P., VILMANN, H.: ANALYTICAL DESCRIPTION OF GROWTH. J. Theor. Biol. 94, 555–577 (1982). https://doi.org/10.1016/0022-5193(82)90301-0
71. Skalak, R., Farrow, D.A., Hoger, A.: Kinematics of surface growth. J. Math. Biol. 35, 869–907 (1997). https://doi.org/10.1007/s002850050081
72. Tadmor, E.B., Miller, R.E., Elliott, R.S.: Continuum Mechanics and Thermodynamics:

From Fundamental Concepts to Governing Equations. Cambridge University Press (2012)
73. Tadmor, E.B., Miller, R.E.: Modeling Materials: Continuum, Atomistic and Multiscale Techniques. Cambridge University Press (2015)
74. Sherifova, S., Holzapfel, G.A.: Biomechanics of Aortic Wall Failure with a Focus on Dissection and Aneurysm: A Review. Acta Biomater. (2019). https://doi.org/10.1016/J.ACTBIO.2019.08.017
75. Fung, Y.C., Liu, S.Q.: Change of Residual Strains in Arteries due to Hypertrophy Caused by Aortic Constriction.
76. FUNG, Y.C., LIU, S.Q.: CHANGE OF RESIDUAL STRAINS IN ARTERIES DUE TO HYPERTROPHY CAUSED BY AORTIC CONSTRICTION. Circ. Res. 65, 1340–1349 (1989)
77. Roccabianca, S., Ateshian, G.A., Humphrey, J.D.: Biomechanical roles of medial pooling of glycosaminoglycans in thoracic aortic dissection. Biomech. Model. Mechanobiol. 13, 13–25 (2014). https://doi.org/10.1007/s10237-013-0482-3
78. Ateshian, G.A.: On the theory of reactive mixtures for modeling biological growth. Biomech. Model. Mechanobiol. 6, 423–445 (2007). https://doi.org/10.1007/s10237-006-0070-x
79. Valentín, A., Humphrey, J.D.: Evaluation of fundamental hypotheses underlying constrained mixture models of arterial growth and remodelling. Philos. Trans. R. Soc. A Math. Phys. Eng. Sci. 367, 3585–3606 (2009). https://doi.org/10.1098/rsta.2009.0113
80. Taber, L.A.: Biomechanics of growth, remodeling, and morphogenesis. Appl Mech Rev. 48, 487–545 (1995)
81. Taber, L.A., Eggers, D.W.: Theoretical study of stress-modulated growth in the aorta. J. Theor. Biol. 180, 343–357 (1996). https://doi.org/10.1006/jtbi.1996.0107
82. Taber, L.A.: A model for aortic growth based on fluid shear and fiber stresses. J. Biomech. Eng. Asme. 120, 348–354 (1998). https://doi.org/10.1115/1.2798001
83. Rodriguez, E.K., Hoger, A., McCulloch, A.D.: Stress-dependent finite growth in soft elastic tissues. J. Biomech. 27, 455–467 (1994). https://doi.org/10.1016/0021-9290(94)90021-3
84. Humphrey, J.D.: Remodeling of a collagenous tissue at fixed lengths. J. Biomech. Eng. Asme. 121, 591–597 (1999). https://doi.org/10.1115/1.2800858
85. Alford, P.W., Humphrey, J.D., Taber, L.A.: Growth and remodeling in a thick-walled artery model: effects of spatial variations in wall constituents. Biomech. Model. Mechanobiol. 7, 245–262 (2008). https://doi.org/10.1007/s10237-007-0101-2

86. Alford, P.A., Taber, L.A.: Computational study of growth snd remodelling in the aortic arch. Comput. Methods Biomech. Biomed. Engin. 11, 525–538 (2008)
87. Bellini, C., Ferruzzi, J., Roccabianca, S., Di Martino, E.S., Humphrey, J.D.: A Microstructurally Motivated Model of Arterial Wall Mechanics with Mechanobiological Implications. https://doi.org/10.1007/s10439-013-0928-x
88. Baek, S., Rajagopal, K.R., Humphrey, J.D.: A theoretical model of enlarging intracranial fusiform aneurysms. J. Biomech. Eng. Asme. 128, 142–149 (2006). https://doi.org/10.1115/1.2132374
89. Horvat, N., Virag, L., Holzapfel, G.A., Sorić, J., Karšaj, I.: A finite element implementation of a growth and remodeling model for soft biological tissues: Verification and application to abdominal aortic aneurysms. Comput. Methods Appl. Mech. Eng. 352, 586–605 (2019). https://doi.org/10.1016/j.cma.2019.04.041
90. Hariton, I., deBotton, G., Gasser, T.C., Holzapfel, G.A.: Stress-driven collagen fiber remodeling in arterial walls. Biomech. Model. Mechanobiol. 6, 163–175 (2007). https://doi.org/10.1007/s10237-006-0049-7
91. Kuhl, E., Holzapfel, G.A.: A continuum model for remodeling in living structures. J. Mater. Sci. 42, 8811–8823 (2007). https://doi.org/10.1007/s10853-007-1917-y
92. Emmert, M.Y., Schmitt, B.A., Loerakker, S., Sanders, B., Spriestersbach, H., Fioretta, E.S., Bruder, L., Brakmann, K., Motta, S.E., Lintas, V., Dijkman, P.E., Frese, L., Berger, F., Baaijens, F.P.T., Hoerstrup, S.P.: Computational modeling guides tissue-engineered heart valve design for long-term in vivo performance in a translational sheep model. Sci. Transl. Med. 10, (2018). https://doi.org/10.1126/scitranslmed.aan4587
93. Roccabianca, S., Bellini, C., Humphrey, J.D.: Computational modelling suggests good, bad and ugly roles of glycosaminoglycans in arterial wall mechanics and mechanobiology. J. R. Soc. Interface. 11, (2014). https://doi.org/10.1098/rsif.2014.0397
94. Ateshian, G.A., Nims, R.J., Maas, S., Weiss, J.A.: Computational modeling of chemical reactions and interstitial growth and remodeling involving charged solutes and solid-bound molecules. Biomech. Model. Mechanobiol. 13, 1105–1120 (2014). https://doi.org/10.1007/s10237-014-0560-1
95. Latorre, M., Bersi, M.R., Humphrey, J.D.: Computational modeling predicts immuno-mechanical mechanisms of maladaptive aortic remodeling in hypertension. Int. J. Eng. Sci. 141, 35–46 (2019). https://doi.org/10.1016/j.ijengsci.2019.05.014
96. Loerakker, S., Ristori, T.: Computational modeling for cardiovascular tissue engineering: the importance of including cell behavior in growth and remodeling algorithms. Curr.

Opin. Biomed. Eng. (2019). https://doi.org/10.1016/j.cobme.2019.12.007

97. Figueroa, C.A., Baek, S., Taylor, C.A., Humphrey, J.D.: A computational framework for fluid-solid-growth modeling in cardiovascular simulations. Comput. Methods Appl. Mech. Eng. 198, 3583–3602 (2008). https://doi.org/10.1016/j.cma.2008.09.013
98. Sáez, P., Peña, E., Tarbell, J.M., Martínez, M.A.: Computational model of collagen turnover in carotid arteries during hypertension. Int. j. numer. method. biomed. eng. 31, e02705 (2015). https://doi.org/10.1002/cnm.2705
99. Sankaran, S., Humphrey, J.D., Marsden, A.L.: An efficient framework for optimization and parameter sensitivity analysis in arterial growth and remodeling computations. Comput. Methods Appl. Mech. Eng. 256, 200–210 (2013). https://doi.org/10.1016/j.cma.2012.12.013
100. Buskohl, P.R., Jenkins, J.T., Butcher, J.T.: Computational simulation of hemodynamic-driven growth and remodeling of embryonic atrioventricular valves. Biomech. Model. Mechanobiol. 11, 1205–1217 (2012). https://doi.org/10.1007/s10237-012-0424-5
101. Comellas, E., Comellas, E., Gasser, T.C., Bellomo, F.J., Oller, S.: A homeostatic-driven turnover remodelling constitutive model for healing in soft tissues A Homeostatic-Driven Turnover Remodelling Constitutive Model for Healing in Soft Tissues. (2016). https://doi.org/10.1098/rsif.2015.1081
102. Ateshian, G.A., Humphrey, J.D.: Continuum Mixture Models of Biological Growth and Remodeling: Past Successes and Future Opportunities. Annu. Rev. Biomed. Eng. 14, 97–111 (2012). https://doi.org/10.1146/annurev-bioeng-071910-124726
103. Karsaj, I., Humphrey, J.D.: A Multilayered Wall Model of Arterial Growth and Remodeling. Mech Mater. 44, 110–119 (2012). https://doi.org/10.1016/j.mechmat.2011.05.006.A
104. Ambrosi, D., Ateshian, G.A., Arruda, E.M., Cowin, S.C., Dumais, J., Goriely, A., Holzapfel, G.A., Humphrey, J.D., Kemkemer, R., Kuhl, E., Olberding, J.E., Taber, L.A., Garikipati, K.: Perspectives on biological growth and remodeling. J. Mech. Phys. Solids. 59, 863–883 (2011). https://doi.org/10.1016/j.jmps.2010.12.011
105. Loerakker, S., Ristori, T., Baaijens, F.P.T.: A computational analysis of cell-mediated compaction and collagen remodeling in tissue-engineered heart valves. J. Mech. Behav. Biomed. Mater. 58, 173–187 (2016). https://doi.org/10.1016/j.jmbbm.2015.10.001
106. Sanders, B., Loerakker, S., Fioretta, E.S., Bax, D.J.P., Driessen-Mol, A., Hoerstrup, S.P., Baaijens, F.P.T.: Improved Geometry of Decellularized Tissue Engineered Heart Valves to Prevent Leaflet Retraction. Ann. Biomed. Eng. 44,. https://doi.org/10.1007/s10439-015-

1386-4

107. Stylianopoulos, T., Barocas, V.H.: Multiscale, structure-based modeling for the elastic mechanical behavior of arterial walls. J. Biomech. Eng. 129, 611–618 (2007). https://doi.org/10.1115/1.2746387

108. Cao, X., Ban, E., Baker, B.M., Lin, Y., Burdick, J.A., Chen, C.S., Shenoy, V.B.: Multiscale model predicts increasing focal adhesion size with decreasing stiffness in fibrous matrices. Proc. Natl. Acad. Sci. U. S. A. 114, E4549–E4555 (2017). https://doi.org/10.1073/pnas.1620486114

109. Chandran, P.L., Barocas, V.H.: Deterministic Material-Based Averaging Theory Model of Collagen Gel Micromechanics. (2007). https://doi.org/10.1115/1.2472369

110. Hadi, M.F.F., Sander, E.A.A., Ruberti, J.W.W., Barocas, V.H.H.: Simulated remodeling of loaded collagen networks via strain-dependent enzymatic degradation and constant-rate fiber growth. Mech. Mater. 44, 72–82 (2012). https://doi.org/10.1016/j.mechmat.2011.07.003

111. Korenczuk, C.E., Dhume, R.Y., Liao, K.K., Barocas, V.H.: Ex Vivo Mechanical Tests and Multiscale Computational Modeling Highlight the Importance of Intramural Shear Stress in Ascending Thoracic Aortic Aneurysms. J. Biomech. Eng. 141, (2019). https://doi.org/10.1115/1.4045270

112. Hatami-Marbini, H., Shahsavari, A., Picu, R.C.: Multiscale modeling of semiflexible random fibrous structures. CAD Comput. Aided Des. 45, 77–83 (2013). https://doi.org/10.1016/j.cad.2011.10.002

113. Bersie-Larson, L.M., Lazarina Gyoneva, ·, Daniel, ·, Goodman, J., Dorfman, K.D., Segal, · Yoav, Barocas, V.H.: Glomerular filtration and podocyte tensional homeostasis: importance of the minor type IV collagen network. Biomech. Model. Mechanobiol. https://doi.org/10.1007/s10237-020-01347-y

114. Sander, E.A., Stylianopoulos, T., Tranquillo, R.T., Barocas, V.H.: Image-based multiscale modeling predicts tissue-level and network-level fiber reorganization in stretched cell-compacted collagen gels. Proc. Natl. Acad. Sci. 106, 17675–17680 (2009)

115. Gyoneva, L., Hovell, C.B., Pewowaruk, R.J., Dorfman, K.D., Segal, Y., Barocas, V.H.: Cell-matrix interaction during strain-dependent remodelling of simulated collagen networks. Interface Focus. 6, (2016). https://doi.org/10.1098/rsfs.2015.0069

116. Mahutga, R.R., Schoephoerster, C.T., Barocas, V.H.: The Ring-Pull Assay for Mechanical Properties of Fibrous Soft Tissues – an Analysis of the Uniaxial Approximation and a Correction for Nonlinear Thick-Walled Tissues. Exp. Mech. 1–14 (2020).

https://doi.org/10.1007/s11340-020-00623-3
117. Humphrey, J.D.: Cardiovascular Solid Mechanics. Springer New York (2002)
118. Sokolis, D.P.: Passive mechanical properties and structure of the aorta: Segmental analysis. Acta Physiol. 190, 277–289 (2007). https://doi.org/10.1111/j.1748-1716.2006.01661.x
119. Stoiber, M., Messner, B., Grasl, & C., Gschlad, V., Bergmeister, & H., Bernhard, & D., Schima, & H.: A Method for Mechanical Characterization of Small Blood Vessels and Vascular Grafts. https://doi.org/10.1007/s11340-015-0053-x
120. Rahn, D.D., Ruff, M.D., Brown, S.A., Tibbals, H.F., Word, R.A.: Biomechanical properties of the vaginal wall: effect of pregnancy, elastic fiber deficiency, and pelvic organ prolapse. Am. J. Obstet. Gynecol. 198, 590.e1-590.e6 (2008). https://doi.org/10.1016/j.ajog.2008.02.022
121. Maas, S.A., Ellis, B.J., Ateshian, G.A., Weiss, J.A.: FEBio: Finite elements for biomechanics. J. Biomech. Eng. 134, (2012). https://doi.org/10.1115/1.4005694
122. Schindelin, J., Arganda-Carreras, I., Frise, E., Kaynig, V., Longair, M., Pietzsch, T., Preibisch, S., Rueden, C., Saalfeld, S., Schmid, B., Tinevez, J.Y., White, D.J., Hartenstein, V., Eliceiri, K., Tomancak, P., Cardona, A.: Fiji: An open-source platform for biological-image analysis, (2012)
123. Clark, T.E., Lillie, M.A., Vogl, A.W., Gosline, J.M., Shadwick, R.E.: Mechanical contribution of lamellar and interlamellar elastin along the mouse aorta. J. Biomech. 48, 3599–3605 (2015). https://doi.org/10.1016/j.jbiomech.2015.08.004
124. Clark, T.E.: Stiffness of mouse aortic elastin and its possible relation to aortic media structure. (2013). https://doi.org/10.14288/1.0073921
125. Vouyouka, A.G., Pfeiffer, B.J., Liem, T.K., Taylor, T.A., Mudaliar, J., Phillips, C.L.: The role of type I collagen in aortic wall strength with a homotrimeric [α1(I)]3 collagen mouse model. J. Vasc. Surg. 33, 1263–1270 (2001). https://doi.org/10.1067/mva.2001.113579
126. Pillekamp, F., Halbach, M., Reppel, M., Rubenchyk, O., Pfannkuche, K., Xi, J.-Y., Bloch, W., Sreeram, N., Brockmeier, K., Hescheler, J.: Neonatal Murine Heart Slices. A Robust Model to Study Ventricular Isometric Contractions. Cell. Physiol. Biochem. 20, 837–846 (2007). https://doi.org/10.1159/000110443
127. Yoshida, K., Mahendroo, M., Vink, J., Wapner, R., Myers, K.: Material properties of mouse cervical tissue in normal gestation. Acta Biomater. (2016). https://doi.org/10.1016/j.actbio.2016.03.005
128. Watters, D.A.K., Smith, A.N., Eastwood, M.A., Anderson, C., Elton, R.A., Mugerwa,

J.W.: Mechanical properties of the colon: comparison of the features of the African and European colon in vitro. (1985)

129. Heys, J., Barocas, V.H.: Mechanical characterization of the bovine iris. J. Biomech. 32, 999–1003 (1999). https://doi.org/10.1016/S0021-9290(99)00075-5
130. Krag, S., Andreassen, T.T.: Biomechanical measurements of the porcine lens capsule. Exp. Eye Res. 62, 253–260 (1996). https://doi.org/10.1006/exer.1996.0030
131. Shazly, T., Rachev, A., Lessner, S., Argraves, W.S., Ferdous, J., Zhou, B., Moreira, A.M., Sutton, M.: On the Uniaxial Ring Test of Tissue Engineered Constructs. https://doi.org/10.1007/s11340-014-9910-2
132. Girton, T.S., Oegema, T.R., Grassl, E.D., Isenberg, B.C., Tranquillo, R.T.: Mechanisms of stiffening and strengthening in media-equivalents fabricated using glycation. J. Biomech. Eng. 122, 216–223 (2000). https://doi.org/10.1115/1.429652
133. Paukovits, T.M., Lukács, L., Bérczi, V., Hirschberg, K., Nemes, B., Hüttl, K.: Percutaneous endovascular treatment of innominate artery lesions: A single-centre experience on 77 lesions. Eur. J. Vasc. Endovasc. Surg. 40, 35–43 (2010). https://doi.org/10.1016/j.ejvs.2010.03.017
134. Rao, A.S., Makaroun, M.S., Marone, L.K., Cho, J.S., Rhee, R., Chaer, R.A.: Long-term outcomes of internal carotid artery dissection. J. Vasc. Surg. 54, 370–375 (2011). https://doi.org/10.1016/j.jvs.2011.02.059
135. Kieffer, E., Chiche, L., Koskas, F., Bahnini, A.: Aneurysms of the innominate artery: Surgical treatment of 27 patients. J. Vasc. Surg. 34, 222–228 (2001). https://doi.org/10.1067/mva.2001.115807
136. Tong, J., Sommer, G., Regitnig, P., Holzapfel, G.A.: Dissection Properties and Mechanical Strength of Tissue Components in Human Carotid Bifurcations. Ann. Biomed. Eng. 39, 1703–1719 (2011)
137. CIBC: No Title, (2016)
138. Van Andel, C.J., Pistecky, P. V., Borst, C.: Mechanical properties of porcine and human arteries: Implications for coronary anastomotic connectors. Ann. Thorac. Surg. 76, 58–64 (2003). https://doi.org/10.1016/S0003-4975(03)00263-7
139. Boekhoven, R.W., Peters, M.F.J., Rutten, M.C.M., van Sambeek, M.R., van de Vosse, F.N., Lopata, R.G.P.: Inflation and Bi-Axial Tensile Testing of Healthy Porcine Carotid Arteries. Ultrasound Med. Biol. 42, 574–585 (2016). https://doi.org/10.1016/j.ultrasmedbio.2015.09.019
140. Mascarenhas, E.J.S., Peters, M.F.J., Nijs, J., Rutten, M.C.M., van de Vosse, F.N., Lopata,

R.G.P.: Assessment of mechanical properties of porcine aortas under physiological loading conditions using vascular elastography. J. Mech. Behav. Biomed. Mater. 59, 185–196 (2016). https://doi.org/10.1016/j.jmbbm.2015.12.009

141. Treuting, P.M., Dintzis, S.M., Montine, K.S.: Comparative Anatomy and Histology. Elsevier Inc. (2012)
142. Wheeler, J.B., Mukherjee, R., Stroud, R.E., Jones, J.A., Ikonomidis, J.S.: Relation of Murine Thoracic Aortic Structural and Cellular Changes With Aging to Passive and Active Mechanical Properties. https://doi.org/10.1161/JAHA.114.001744
143. Wagenseil, J.E., Mecham, R.P.: Elastin in large artery stiffness and hypertension. J. Cardiovasc. Transl. Res. 5, 264–273 (2012). https://doi.org/10.1007/s12265-012-9349-8
144. Aaron, B.B., Gosline, J.M.: Elastin as a random-network elastomer: A mechanical and optical analysis of single elastin fibers. Biopolymers. 20, 1247–1260 (1981). https://doi.org/10.1002/bip.1981.360200611
145. Mouw, J.K., Ou, G., Weaver, V.M.: Extracellular matrix assembly: A multiscale deconstruction. Nat. Rev. Mol. Cell Biol. 15, 771–785 (2014). https://doi.org/10.1038/nrm3902
146. Nissen, R., Cardinale, G.J., Udenfriend, S.: Increased turnover of arterial collagen in hypertensive rats. Proc. Natl. Acad. Sci. U. S. A. 75, 451–3 (1978). https://doi.org/10.1073/PNAS.75.1.451
147. Revenko, I., Sommer, F., Minh, D.T., Garrone, R., Franc, J.-M.: Atomic force microscopy study of the collagen fibre structure. Biol. Cell. 80, 67–69 (1994). https://doi.org/10.1016/0248-4900(94)90019-1
148. Flynn, B.P., Bhole, A.P., Saeidi, N., Liles, M., Dimarzio, C.A., Ruberti, J.W.: Mechanical strain stabilizes reconstituted collagen fibrils against enzymatic degradation by mammalian collagenase matrix metalloproteinase 8 (MMP-8). PLoS One. 5, 21–23 (2010). https://doi.org/10.1371/journal.pone.0012337
149. Ruberti, J.W., Hallab, N.J.: Strain-controlled enzymatic cleavage of collagen in loaded matrix. Biochem. Biophys. Res. Commun. 336, 483–489 (2005). https://doi.org/10.1016/j.bbrc.2005.08.128
150. Flynn, B.P., Tilburey, G.E., Ruberti, J.W.: Highly sensitive single-fibril erosion assay demonstrates mechanochemical switch in native collagen fibrils. Biomech. Model. Mechanobiol. 12, 291–300 (2013). https://doi.org/10.1007/s10237-012-0399-2
151. Martyn, C., Greenwald, S.: Impaired synthesis of elastin in walls of aorta and large conduit arteries during early development as an initiating event in pathogenesis of

systemic hypertension. Lancet. 350, 953–955 (1997). https://doi.org/10.1016/S0140-6736(96)10508-0

152. Win, Z., Buksa, J.M., Steucke, K.E., Gant Luxton, G.W., Barocas, V.H., Alford, P.W.: Cellular Microbiaxial Stretching to Measure a Single-Cell Strain Energy Density Function. J. Biomech. Eng. 139, 071006 (2017). https://doi.org/10.1115/1.4036440
153. Steucke, K.E., Win, Z., Stemler, T.R., Walsh, E.E., Hall, J.L., Alford, P.W.: Empirically determined vascular smooth muscle cell mechano-adaptation law. J. Biomech. Eng. 139, (2017). https://doi.org/10.1115/1.4036454
154. Vorp, D.A., Tsamis, A., Krawiec, J.T.: Elastin and collagen fibre microstructure of the human aorta in ageing and disease: a review. https://doi.org/10.1098/rsif.2012.1004
155. Collins, M.J., Dev, V., Strauss, B.H., Fedak, P.W.M., Butany, J.: Variation in the histopathological features of patients with ascending aortic aneurysms: a study of 111 surgically excised cases. J. Clin. Pathol. 61, 519–23 (2008). https://doi.org/10.1136/jcp.2006.046250
156. Fung, Y.C., Liu, S.Q.: Determination of the mechanical properties of the different layers of blood vessels in vivo. Proc. Natl. Acad. Sci. U. S. A. 92, 2169–73 (1995). https://doi.org/10.1073/PNAS.92.6.2169
157. Liu, S.Q., Fung, Y.C.: Relationship Between Hypertension, Hypertrophy, and Opening Angle of Zero-Stress State of Arteries Following Aortic Constriction. J. Biomech. Eng. 111, 325 (1989). https://doi.org/10.1115/1.3168386
158. Jackson, Z.S., Gotlieb, A.I., Langille, B.L.: Wall tissue remodeling regulates longitudinal tension in arteries. Circ. Res. 90, 918–925 (2002). https://doi.org/10.1161/01.RES.0000016481.87703.CC
159. Matsumoto, T., Hayashi, K.: Stress and Strain Distribution in Hypertensive and Normotensive Rat Aorta Considering Residual Strain. J. Biomech. Eng. 118, 62 (1996). https://doi.org/10.1115/1.2795947
160. Bendeck, M.P., Langille, B.L.: Rapid accumulation of elastin and collagen in the aortas of sheep in the immediate perinatal period. Circ. Res. 69, 1165–1169 (1991). https://doi.org/10.1161/01.RES.69.4.1165
161. Skalak, R., Dasgupta, G., Moss, M., Otten, E., Dullemeijer, P., Vilmann, H.: Analytical description of growth. J. Theor. Biol. 94, 555–577 (1982). https://doi.org/10.1016/0022-5193(82)90301-0
162. Hariton, I., deBotton, G., Gasser, T.C., Holzapfel, G.A.: Stress-driven collagen fiber remodeling in arterial walls. Biomech. Model. Mechanobiol. 6, 163–175 (2007).

https://doi.org/10.1007/s10237-006-0049-7
163. C. Picu, R.: Mechanics of random fiber networks—a review. Soft Matter. 7, 6768–6785 (2011). https://doi.org/10.1039/C1SM05022B
164. Green, E.M., Mansfield, J.C., Bell, J.S., Winlove, C.P.: The structure and micromechanics of elastic tissue. Interface Focus. 4, (2014). https://doi.org/10.1098/rsfs.2013.0058
165. Freed, A.D., Doehring, T.C.: Elastic Model for Crimped Collagen Fibrils. J. Biomech. Eng. 127, 587 (2005). https://doi.org/10.1115/1.1934145
166. Ateshian, G.A., Rajan, V., Chahine, N.O., Canal, C.E., Hung, C.T.: Modeling the Matrix of Articular Cartilage Using a Continuous Fiber Angular Distribution Predicts Many Observed Phenomena. J. Biomech. Eng. 131, 061003 (2009). https://doi.org/10.1115/1.3118773
167. Nolan, D.R., McGarry, J.P.: On the Compressibility of Arterial Tissue. Ann. Biomed. Eng. 44, 993–1007 (2016). https://doi.org/10.1007/s10439-015-1417-1
168. Chandran, P.L., Barocas, V.H.: Affine Versus Non-Affine Fibril Kinematics in Collagen Networks: Theoretical Studies of Network Behavior. J. Biomech. Eng. 128, 259 (2005). https://doi.org/10.1115/1.2165699
169. Stylianopoulos, T., Barocas, V.H.: Volume-averaging theory for the study of the mechanics of collagen networks. Comput. Methods Appl. Mech. Eng. 196, 2981–2990 (2007). https://doi.org/10.1016/j.cma.2006.06.019
170. Guennebaud, G., Jacob, B.: Eigen v3, (2010)
171. Nissen, R., Cardinale, G.J., Udenfriend, S.: Increased turnover of arterial collagen in hypertensive rats. Proc. Natl. Acad. Sci. U. S. A. 75, 451–3 (1978). https://doi.org/10.1073/PNAS.75.1.451
172. Jia, Z., Nguyen, T.D.: A micromechanical model for the growth of collagenous tissues under mechanics-mediated collagen deposition and degradation. J. Mech. Behav. Biomed. Mater. 98, 96–107 (2019). https://doi.org/10.1016/j.jmbbm.2019.06.004
173. Tong, J., Cheng, Y., Holzapfel, G.A.: Mechanical assessment of arterial dissection in health and disease: Advancements and challenges. J. Biomech. 49, 2366–2373 (2016). https://doi.org/10.1016/j.jbiomech.2016.02.009
174. Sommer, G., Sherifova, S., Oberwalder, P.J., Dapunt, O.E., Ursomanno, P.A., DeAnda, A., Griffith, B.E., Holzapfel, G.A.: Mechanical strength of aneurysmatic and dissected human thoracic aortas at different shear loading modes. J. Biomech. 49, 2374–2382 (2016). https://doi.org/10.1016/j.jbiomech.2016.02.042
175. Vorp, D.A., Vande Geest, J.P.: Biomechanical determinants of abdominal aortic aneurysm

rupture, (2005)

176. Benetos, A., Lacolley, P., Safar, M.E.: Prevention of aortic fibrosis by spironolactone in spontaneously hypertensive rats. Arterioscler. Thromb. Vasc. Biol. 17, 1152–1156 (1997). https://doi.org/10.1161/01.ATV.17.6.1152
177. Koffi, I., Lacolley, P., Kirchengaast, M., Pomiès, J.P., Laurent, S., Benetos, A.: Prevention of arterial structural alterations with verapamil and trandolapril and consequences for mechanical properties in spontaneously hypertensive rats. Eur. J. Pharmacol. 361, 51–60 (1998). https://doi.org/10.1016/S0014-2999(98)00691-8
178. Matsumoto, T., Hayashi, K.: Mechanical and dimensional adaptation of rat aorta to hypertension. J. Biomech. Eng. 116, 278–283 (1994). https://doi.org/10.1115/1.2895731
179. Bézie, Y., Lamaziè, J.-M.D., Laurent, S., Challande, P., Cunha, R.S., Bonnet, J., Lacolley, P.: Fibronectin Expression and Aortic Wall Elastic Modulus in Spontaneously Hypertensive Rats. (1998)
180. Perrucci, G.L., Rurali, E., Gowran, A., Pini, A., Antona, C., Chiesa, R., Pompilio, G., Nigro, P.: Vascular smooth muscle cells in Marfan syndrome aneurysm: the broken bricks in the aortic wall, (2016)
181. Guo, D.C., Pannu, H., Tran-Fadulu, V., Papke, C.L., Yu, R.K., Avidan, N., Bourgeois, S., Estrera, A.L., Safi, H.J., Sparks, E., Amor, D., Ades, L., McConnell, V., Willoughby, C.E., Abuelo, D., Willing, M., Lewis, R.A., Kim, D.H., Scherer, S., Tung, P.P., Ahn, C., Buja, L.M., Raman, C.S., Shete, S.S., Milewicz, D.M.: Mutations in smooth muscle α-actin (ACTA2) lead to thoracic aortic aneurysms and dissections. Nat. Genet. 39, 1488–1493 (2007). https://doi.org/10.1038/ng.2007.6
182. Deogekar, S., Picu, R.C.: On the strength of random fiber networks. J. Mech. Phys. Solids. 116, 1–16 (2018). https://doi.org/10.1016/j.jmps.2018.03.026
183. Lederle, F.A., Wilson, S.E., Johnson, G.R., Reinke, D.B., Littooy, F.N., Acher, C.W., Messina, L.M., Ballard, D.J., Ansel, H.J.: Variability in measurement of abdominal aortic aneurysms. J. Vasc. Surg. (1995). https://doi.org/10.1016/S0741-5214(95)70222-9
184. Wilmink, A.B.M., Forshaw, M., Quick, C.R.G., Hubbard, C.S., Day, N.E.: Accuracy of serial screening for abdominal aortic aneurysms by ultrasound. J. Med. Screen. 9, 125–7 (2002). https://doi.org/10.1136/jms.9.3.125
185. Hayashi, K., Sugimoto, T.: Biomechanical response of arterial wall to DOCA-salt hypertension in growing and middle-aged rats. J. Biomech. 40, 1583–1593 (2007). https://doi.org/10.1016/j.jbiomech.2006.07.021
186. Van Gorp, A.W., Van Ingen Schenau, D.S., Hoeks, A.P.G., Struijker Boudier, H.A.J.,

Reneman, R.S., De Mey, J.G.R.: Aortic wall properties in normotensive and hypertensive rats of various ages in vivo. In: Hypertension. pp. 363–368. Lippincott Williams and Wilkins (1995)

187. Marque, V., Kieffer, P., Atkinson, J., Lartaud-Idjouadiene, I.: Elastic properties and composition of the aortic wall in old spontaneously hypertensive rats. Hypertension. 34, 415–422 (1999). https://doi.org/10.1161/01.HYP.34.3.415
188. Hayashi, K., Shimizu, E.: Composition of connective tissues and morphometry of vascular smooth muscle in arterial wall of DOCA-salt hypertensive rats - In relation with arterial remodeling. J. Biomech. 49, 1225–1229 (2016). https://doi.org/10.1016/j.jbiomech.2016.02.044
189. Seidel, C.L.: Aortic actomyosin content of maturing normal and spontaneously hypertensive rats. Am. J. Physiol. - Hear. Circ. Physiol. 6, (1979). https://doi.org/10.1152/ajpheart.1979.237.1.h34
190. Kochová, P., Tonar, Z., Matejka, V.M., Svíglerová, J.: Morphology and mechanical properties of the subrenal aorta in normotensive and hypertensive rats. Biomed Pap Med Fac Univ Palacky Olomouc Czech Repub. 152, 239–245 (2009). https://doi.org/10.5507/bp.2008.037
191. Sommer, G., Gasser, T.C., Regitnig, P., Auer, M., Holzapfel, G.A.: Dissection properties of the human aortic media: An experimental study. J. Biomech. Eng. 130, (2008). https://doi.org/10.1115/1.2898733
192. Kobs, R.W., Muvarak, N.E., Eickhoff, J.C., Chesler, N.C.: Linked mechanical and biological aspects of remodeling in mouse pulmonary arteries with hypoxia-induced hypertension. Am J Physiol Hear. Circ Physiol. 288, 1209–1217 (2005). https://doi.org/10.1152/ajpheart.01129
193. Golob, M.J., Tabima, D.M., Wolf, G.D., Johnston, J.L., Forouzan, O., Mulchrone, A.M., Kellihan, H.B., Bates, M.L., Chesler, N.C.: Pulmonary arterial strain-and remodeling-induced stiffening are differentiated in a chronic model of pulmonary hypertension. https://doi.org/10.1016/j.jbiomech.2017.02.003
194. Thompson, R.W., Curci, J.A., Ennis, T.L., Mao, D., Pagano, M.B., Pham, C.T..: Pathophysiology of Abdominal Aortic Aneurysms: Insights from the Elastase-Induced Model in Mice with Different Genetic Backgrounds. Ann. N. Y. Acad. Sci. 1085, 59–73 (2006). https://doi.org/10.1196/annals.1383.029
195. Bellini, C., Bersi, M.R., Caulk, A.W., Ferruzzi, J., Milewicz, D.M., Ramirez, F., Rifkin, D.B., Tellides, G., Yanagisawa, H., Humphrey, J.D.: Comparison of 10 murine models

reveals a distinct biomechanical phenotype in thoracic aortic aneurysms. J. R. Soc. Interface. 14, 1–12 (2017). https://doi.org/10.1098/rsif.2016.1036

196. Holmes, K.C., Popp, D., Gebhard, W., Kabsch, W.: Atomic model of the actin filament. Nature. 347, 44–49 (1990). https://doi.org/10.1038/347044a0
197. Rachev, A., Hayashi, K.: Theoretical Study of the Effects of Vascular Smooth Muscle Contraction on Strain and Stress Distributions in Arteries. (1999)
198. Shen, Z.L., Dodge, M.R., Kahn, H., Ballarini, R., Eppell, S.J.: Stress-strain experiments on individual collagen fibrils. Biophys. J. 95, 3956–3963 (2008). https://doi.org/10.1529/biophysj.107.124602
199. Buehler, M.J.: Nanomechanics of collagen fibrils under varying cross-link densities: Atomistic and continuum studies. J. Mech. Behav. Biomed. Mater. 1, 59–67 (2008). https://doi.org/10.1016/j.jmbbm.2007.04.001
200. Gosline, J., Lillie, M., Carrington, E., Guerette, P., Ortlepp, C., Savage, K.: Elastic proteins: biological roles and mechanical properties. https://doi.org/10.1098/rstb.2001.1022
201. Holzapfel, G.A., Gasser, T.C., Ogden, R.W.: A new constitutive framework for arterial wall mechanics and a comparative study of material models. J. Elast. 61, 1–48 (2000). https://doi.org/10.1023/A:1010835316564
202. Gasser, T.C., Ogden, R.W., Holzapfel, G.A.: Hyperelastic modelling of arterial layers with distributed collagen fibre orientations. https://doi.org/10.1098/rsif.2005.0073
203. Sander, E., Stylianopoulos, T., Tranquillo, R., Barocas, V.: Image-based biomechanics of collagen-based tissue equivalents. IEEE Eng. Med. Biol. Mag. 28, 10–18 (2009). https://doi.org/10.1109/MEMB.2009.932486
204. Zarei, V., Liu, C.J., Claeson, A.A., Akkin, T., Barocas, V.H.: Image-based multiscale mechanical modeling shows the importance of structural heterogeneity in the human lumbar facet capsular ligament. Biomech. Model. Mechanobiol. 16, 1425–1438 (2017). https://doi.org/10.1007/s10237-017-0896-4
205. Li, K., Ogden, R.W., Holzapfel, G.A.: A discrete fibre dispersion method for excluding fibres under compression in the modelling of fibrous tissues. J. R. Soc. Interface. 15, 20170766 (2018). https://doi.org/10.1098/rsif.2017.0766
206. Holzapfel, G.A., Ogden, R.W., Sherifova, S.: On fibre dispersion modelling of soft biological tissues: A review, (2019)
207. Li, K., Ogden, R.W., Holzapfel, G.A.: Modeling fibrous biological tissues with a general invariant that excludes compressed fibers. J. Mech. Phys. Solids. 110, 38–53 (2018).

https://doi.org/10.1016/j.jmps.2017.09.005

208. Melnik, A. V., Borja Da Rocha, H., Goriely, A.: On the modeling of fiber dispersion in fiber-reinforced elastic materials. Int. J. Non. Linear. Mech. 75, 92–106 (2015). https://doi.org/10.1016/j.ijnonlinmec.2014.10.006
209. Chandran, P.L., Barocas, V.H.: Affine Versus Non-Affine Fibril Kinematics in Collagen Networks: Theoretical Studies of Network Behavior. J. Biomech. Eng. 128, 259–270 (2006). https://doi.org/10.1115/1.2165699
210. Billiar, K.L., Sacks, M.S.: Biaxial mechanical properties of the native and glutaraldehyde-treated aortic valve cusp: Part II - A structural constitutive model. J. Biomech. Eng. 122, 327–336 (2000). https://doi.org/10.1115/1.1287158
211. Dhume, R.Y., Shih, E.D., Barocas, V.H.: Multiscale model of fatigue of collagen gels. Biomech. Model. Mechanobiol. 18, 175–187 (2019). https://doi.org/10.1007/s10237-018-1075-y
212. Gacek, E., Bermel, E.A., Ellingson, A.M., Barocas, V.H.: Through-thickness Regional Variation in the Mechanical Characteristics of the Lumbar Facet Capsular Ligament. Biomech. Model. Mechanobiol. In Review, (2020)
213. Barocas, V.H., Zarei, V., Dhume, R.Y., Ellingson, A.M.: Multiscale modelling of the human lumbar facet capsular ligament: analysing spinal motion from the joint to the neurons. https://doi.org/10.1098/rsif.2018.0550
214. Bermel, E.A., Barocas, V.H., Ellingson, A.M.: The role of the facet capsular ligament in providing spinal stability. Comput. Methods Biomech. Biomed. Engin. 21, 712–721 (2018). https://doi.org/10.1080/10255842.2018.1514392
215. Little, J.S., Khalsa, P.S.: Material Properties of the Human Lumbar Facet Joint Capsule. J. Biomech. Eng. 127, 15–24 (2005). https://doi.org/10.1115/1.1835348
216. Maas, S.A., Rawlins, D., Weiss, J.A., Ateshian, G.A.: FEBio User Manual v2.8, https://help.febio.org/FEBio/FEBio_um_2_8/
217. Volokh, K.Y.: On arterial fiber dispersion and auxetic effect. J. Biomech. 61, 123–130 (2017). https://doi.org/10.1016/j.jbiomech.2017.07.010
218. Lane, B.A., Harmon, K.A., Goodwin, R.L., Yost, M.J., Shazly, T., Eberth, J.F.: Constitutive modeling of compressible type-I collagen hydrogels. Med. Eng. Phys. 53, 39–48 (2018). https://doi.org/10.1016/j.medengphy.2018.01.003
219. Böl, M., Reese, S., Parker, K.K., Kuhl, E.: Computational modeling of muscular thin films for cardiac repair. Comput. Mech. 43, 535–544 (2009). https://doi.org/10.1007/s00466-008-0328-5

220. Eriksson, T., Prassl, A., Plank, G., Holzapfel, G.: Influence of myocardial fiber/sheet orientations on left ventricular mechanical contraction. Math. Mech. Solids. 18, 592–606 (2013). https://doi.org/10.1177/1081286513485779
221. Win, Z., Buksa, J.M., Alford, P.W.: Architecture-Dependent Anisotropic Hysteresis in Smooth Muscle Cells. Biophys. J. 115, 2044–2054 (2018). https://doi.org/10.1016/j.bpj.2018.09.027
222. Vanderheiden, S.M., Hadi, M.F., Barocas, V.H.: Crack Propagation Versus Fiber Alignment in Collagen Gels: Experiments and Multiscale Simulation. (2015). https://doi.org/10.1115/1.4031570
223. Korenczuk, C.E., Dhume, R.Y., Liao, K.K., Barocas, V.H.: Ex Vivo Mechanical Tests and Multiscale Computational Modeling Highlight the Importance of Intramural Shear Stress in Ascending Thoracic Aortic Aneurysms. J. Biomech. Eng. 141, (2019). https://doi.org/10.1115/1.4045270
224. Zeinali-Davarani, S., Wang, Y., Chow, M.J., Turcotte, R., Zhang, Y.: Contribution of collagen fiber undulation to regional biomechanical properties along porcine thoracic aorta. J. Biomech. Eng. (2015). https://doi.org/10.1115/1.4029637
225. Smoljkić, M., Fehervary, H., Van den Bergh, P., Jorge-Peñas, A., Kluyskens, L., Dymarkowski, S., Verbrugghe, P., Meuris, B., Vander Sloten, J., Famaey, N.: Biomechanical Characterization of Ascending Aortic Aneurysms. Biomech. Model. Mechanobiol. (2017). https://doi.org/10.1007/s10237-016-0848-4
226. Holzapfel, G.A., Ogden, R.W.: Modelling the layer-specific three-dimensional residual stresses in arteries, with an application to the human aorta. J. R. Soc. Interface. 7, 787–799 (2010). https://doi.org/10.1098/rsif.2009.0357
227. Baek, S., Valentin, A., Humphrey, J.D.: Biochemomechanics of cerebral vasospasm and its resolution: II. Constitutive relations and model simulations. Ann. Biomed. Eng. 35, 1498–1509 (2007). https://doi.org/10.1007/s10439-007-9322-x
228. Morrison, T.M., Dreher, M.L., Nagaraja, S., Angelone, L.M., Kainz, W.: The role of computational modeling and simulation in the total product life cycle of peripheral vascular devices. J. Med. Devices, Trans. ASME. 11, (2017). https://doi.org/10.1115/1.4035866
229. Morrison, T.M., Pathmanathan, P., Adwan, M., Margerrison, E.: Advancing Regulatory Science With Computational Modeling for Medical Devices at the FDA's Office of Science and Engineering Laboratories. Front. Med. 5, 241 (2018). https://doi.org/10.3389/fmed.2018.00241

230. Reimer, J., Syedain, Z., Haynie, B., Lahti, M., Berry, J., Tranquillo, R.: Implantation of a Tissue-Engineered Tubular Heart Valve in Growing Lambs. Ann. Biomed. Eng. 45, 439–451 (2017). https://doi.org/10.1007/s10439-016-1605-7
231. Reimer, J.M., Syedain, Z.H., Haynie, B.H.T., Tranquillo, R.T.: Pediatric tubular pulmonary heart valve from decellularized engineered tissue tubes. Biomaterials. 62, 88–94 (2015). https://doi.org/10.1016/j.biomaterials.2015.05.009
232. Eichinger, J.F., Paukner, D., Szafron, J.M., Aydin, R.C., Humphrey, J.D., Cyron, C.J.: Computer-controlled biaxial bioreactor for investigating cell-mediated homeostasis in tissue equivalents. J. Biomech. Eng. 142, (2020). https://doi.org/10.1115/1.4046201
233. Maas, S.A., Erdemir, A., Halloran, J.P., Weiss, J.A.: A general framework for application of prestrain to computational models of biological materials. J. Mech. Behav. Biomed. Mater. 61, 499–510 (2016). https://doi.org/10.1016/j.jmbbm.2016.04.012
234. Sander, E.A., Barocas, V.H., Tranquillo, R.T.: Initial fiber alignment pattern alters extracellular matrix synthesis in fibroblast-populated fibrin gel cruciforms and correlates with predicted tension. Ann. Biomed. Eng. 39, 714–729 (2011). https://doi.org/10.1007/s10439-010-0192-2
235. Kupfer, M.E., Lin, W.-H., Ravikumar, V., Qiu, K., Wang, L., Gao, L., Bhuiyan, D., Lenz, M., Ai, J., Mahutga, R.R., Townsend, D., Zhang, J., McAlpine, M.C., Tolkacheva, E.G., Ogle, B.M.: In Situ Expansion, Differentiation and Electromechanical Coupling of Human Cardiac Muscle in a 3D Bioprinted, Chambered Organoid. Circ. Res. CIRCRESAHA.119.316155 (2020). https://doi.org/10.1161/CIRCRESAHA.119.316155
236. Updegrove, A., Wilson, N.M., Merkow, J., Lan, H., Marsden, A.L., Shadden, S.C.: SimVascular: An Open Source Pipeline for Cardiovascular Simulation, (2017)
237. Wheelwright, M., Win, Z., Mikkila, J.L., Amen, K.Y., Alford, P.W., Metzger, J.M.: Investigation of human iPSC-derived cardiac myocyte functional maturation by single cell traction force microscopy. PLoS One. 13, (2018). https://doi.org/10.1371/journal.pone.0194909
238. Ye, G.J.C., Aratyn-Schaus, Y., Nesmith, A.P., Pasqualini, F.S., Alford, P.W., Parker, K.K.: The contractile strength of vascular smooth muscle myocytes is shape dependent. Integr. Biol. (United Kingdom). 6, 152–163 (2014). https://doi.org/10.1039/c3ib40230d